Geological and kinematic evolution of the western part of the North Anatolian Fault system: an analogue modelling investigation

---

A thesis submitted for the degree of Doctor of Philosophy

Sibel Bulkan

Department of Earth Sciences
Royal Holloway University of London

November, 2020

“If one day, my
words are against science,
choose science.”

Mustafa Kemal Atatürk

Declaration of Authorship

I, Sibel Bulkan, hereby declare that this thesis and the work contained within are entirely my own, unless stated otherwise. Chapters 4 is a co-authored paper which is submitted for publication or awaiting submission for publication. Chapter 5 is a co-authored manuscript has published in the *Journal of Tectonophysics.* Chapter 6 is also a manuscript that is currently in preparation to be submitted for publication in a peer-reviewed journal. I am responsible for the data collection and analysis throughout this thesis, and for primary authorship of all 3 of the included papers.

Signed: Sibel Bulkan

Dated: 17th November 2020

Abstract

The right-lateral North Anatolian Fault (NAF) appears to be an exceptional example of a continental strike-slip fault that extends in an east-west direction for more than 1200 km dividing the Eurasian and Anatolian plates. To the east the plate boundary is localized along a single fault system while toward the west the fault branches into three segments. The Sea of Marmara lies along the western part of the NAF, and it is a key geodynamical region characterised by transtension accommodating both the strike-slip motion between Anatolia and Eurasia and the extensional deformation present in the adjacent Aegean region. Although it has been, and still is an intensively studied area, the NAF geometry and kinematics, and their relationship with the geology and geodesy within the Sea of Marmara are not entirely constrained.

To investigate the geometry and the evolution of pull-apart basins and of the Sea of Marmara in particular, I used crustal-scale 3D analogue models and GPS-derived strain rate field. The analogue models consisted of two different rheological layers, upper and lower crust, while the geometry of the fault was reproduced by a releasing bend adjacent to a restraining bend subject to dextral movement. The crustal thickness and the length and orientation of the releasing-restraining bend pair in the analogue model were scaled according to the western part of the NAF. In the experiments, we used dry-quartz sand and silicon putty to simulate the rheological behaviour of the upper and lower crust, respectively. The experimental methods further illustrate the characteristics of the analogue models and techniques used to elaborate their data. We compared the models to different regions in the Sea of Marmara at different scales. The analogue models reproduced the overall basin characteristics and showed how the basin evolved to attain subsidence along the releasing bend and uplift over the restraining bend. Topography and slip transfer along different parts of the fault system were analysed. The

findings of this study contribute to the understanding of the geometry of each segment of western NAF that influences the overall geodynamic evolution of the area of the Sea of Marmara.

In the last years dense campaign GPS – Global Positioning System - measurements constrained modern deformation in western Anatolia and the Sea of Marmara. I elaborated these data to obtain the strain rate pattern over this area, including the orientation and the magnitude of its principal horizontal components and dilation. This last analysis allowed us to gain an overall perspective on the deformation trend of the Sea of Marmara resulting from the interaction of Anatolia with the Nubian slab rollback in the Aegean Sea. The result showed the different strain accumulation in the Anatolia and Eurasia plates, but also an extensional neotectonics regime possibly linked to the Aegean extension.

In this thesis, the analogue models are compared with the western part of the North Anatolian Fault -Sea of Marmara. However, these models also have general applicability to complex strike slip fault systems where the interaction of restraining/releasing bend (double-bend) are even less clearly understood than in the Sea of Marmara. This general applicability is the result of our "geometrical" approach which can be compared to other natural examples that show a reasonable fit.

Acknowledgements

Firstly, I would like to express my special appreciation and respect to my supervisor, Paola Vannucchi, who has supported me throughout my research. Paola continuously provided encouragement, was always willing and enthusiastic to assist in any way she could throughout this thesis. She has inspired me to become an independent researcher and helped me realize the power of critical reasoning. Without her guidance and constant feedback this PhD would not have been achievable. I also would like to thank Ian Watkinson, my second supervisor, for his constructive feedbacks and advices that he provided at critical times. I would like to extend my sincere thanks to Jason Morgan for his support, encouragement and credible ideas which have been great contribution in the completion of the thesis.

I greatly appreciate the support that I received from Fabrizio Storti and Cristian Cavozzi through the collaborative work undertaken in the University of Parma, Italy, during the first phase of my research. They enabled me to use the lab facilities in their department and guided me in performing all the models presented in this thesis. It was a great pleasure for me to work with them. I am grateful to Pierre Henry for his crucial contribution to my first manuscript, as well as the guidance on the numerical part of my research. The support I received from him during the collaborative work I undertook in the Aix-Marseille University, CEREGE, Aix-en-Provence, France was invaluable. I also would like to thank many other researchers in both France and Italy for their great hospitality and enjoyable coffee breaks that we had during my visits. I would like to extend my gratitude to Luca Gasperini and Alina Polonia for their insightful suggestions in my second manuscript and giving me unwavering support to achieve it.

I would like to thank the people, without whom I would not have been able to handle this uphill battle. I am blessed with incredible friends, Semra Bakkaloğlu, Rafika Ismail, Ania Preiss, Sandy Kyriaki and Alex Clarke, who have been such a great support by providing positive distractions which always helped me rest my mind. Special thanks to İnci Doğan for our enjoyable long distance conversations when I needed her the most.

I gratefully acknowledge the funding I received for my PhD from the RHUL Earth Sciences Department Research Committee and the “FLOWS” by the COST Action ES1301. I am also indebted to Margaret Collinson for her great support in my times of need. I am very thankful to the staff of the Department of the Earth Sciences for all their considerate guidance.

I will always be grateful towards Celâl Şengör who keeps inspiring me through everything he teaches me. His insights and wisdom have helped pave my way at Royal Holloway.

This journey would not have been possible without the support of my family. I deeply thank them for their unconditional support, love and encouragement. Special thanks to my beloved nieces Aylin, Eda, Zeynep and Lale for making me always smile.

Table of Contents

List of Figures

CHAPTER 4

CHAPTER 5

CHAPTER 6

List of Tables

Definition of Terms

Areal strain: It defines how much compression and extension take place in each area. In this thesis it is represented by sum of the diagonal components of the strain tensors $(Exx + Eyy)$.

Material derivative topography: Material derivative topography is the rate of change of topography for a portion over a time step that follows surface motions.

Releasing bend: A curve localised in a strike-slip fault where the orientation of the fault changes, it becomes oblique to the regional slip vector and it accommodates local extension (for example a dextral fault steps to the right). It is responsible for transtensional deformation forming pull-apart basins or negative flower structures (i.e. Cunningham and Mann, 2007).

Restraining bend: A curve localised in a strike slip fault where the orientation of the fault changes, it becomes oblique to the regional slip vector and it accommodates local compression (for example a dextral strike-slip fault steps to the left). It is responsible for transpressional deformation forming areas of uplift or positive flower structures (i.e. Cunningham and Mann, 2007).

Releasing and restraining bend pairs (Paired bends): A situation where a releasing bend is adjacent to a restraining bend structure – o viceversa. This term was first used by Mann et al. (1985).

Shear rate : Velocity gradient, the rate of change of shear strain with time. In this thesis, it is represented by the velocity gradient perpendicular to the velocity discontinuity applied at the base of the model ($\partial u/\partial y$).

Shear strain: Tangent of the change in angle between lines that were initially perpendicular. This may be expressed as an angle of shear, in radians.

Vorticity: Vorticity is a vector field defined as the curl of velocity. The angular velocity of lines between known points in a rock undergoing strain, described as rotational strain.

Chapter 1: Introduction

Transform faults constitute conservative plate boundaries: they are lithospheric strike-slip faults that allow lateral surface movements between plates. Whether they develop on continental or oceanic lithosphere, they are characterised by strong morphological or topographic expressions. In continental settings transform faults are often accompanied by a complex system of en-echelon fractures, faults and folds (Sylvester, 1988).The fault pattern and geometry can range from single, pure strike-slip shear zones to complex domains with lateral offsets at branches, resulting from bends, oversteps or flower structures that partition and diffuse tectonic deformation both horizontally and vertically throughout the lithosphere.

Typical structural expressions of vertical displacement along transform faults are rhomboid-shaped depressions such as pull-apart basins and elongated depressions, and uplifted pressure ridges that are usually accompanied by faults and drag folds (Sylvester, 1988).

The topic of this thesis focuses on the transform plate boundary that comprises the western part of the North Anatolian Fault (NAF) (Sengor et al., 2014). Within the study area, the NAF is characterised by a complex geometry with several sub-parallel splays and structural expressions involving depressions such as the Sea of Marmara, and uplifted regions such as the Ganos Mountain (Fig. 1.1).

The NAF itself is a remarkable example of a continental right-lateral strike-slip fault that extends more than 1200 km while separating the Eurasian and Anatolian plates (McKenzie, 1972). This plate boundary is localised within a single fault system in its east, and branches into two major segments towards its west. The western part of the NAF and the Sea of Marmara occupy a critical geodynamic region where the NAF strike-slip system is perturbed by the

Aegean extensional regime (Straub et al., 1997; Kahle et al., 1999; Reilinger et al. 2010). Consequences of this interference appear as a bending of the NAF trace (Le Pichon et al., 2001; Imren et al., 2001]) that induces significant transtensional and transpressive deformation in this region. This geodynamic setting makes the Marmara region an ideal site to evaluate both how and through what steps transpressive and transtensional faults interact to create topographic relief.

In western Turkey the NAF splays into two principal branches called the northern and the southern branches. From GPS data, most of the overall lateral motion appears to be transferred from the main trace to the east to the northern branch in the west across the Sea of Marmara (Ergintav et al., 2014)(Fig. 1.1a). However, the relationship between the Sea of Marmara basin and the kinematics of the submerged part of the NAF beneath the Sea of Marmara continues to be debated.

Transform faults are typically seismically active; the NAF has produced a series of large and devastating earthquakes during the 20th century. These started (in the west) with the 1912 Mw 7.4 Ganos earthquake, followed in 1939 Mw 7.4 by the Erzincan earthquake in eastern Anatolia (Toksöz 1979; Barka 1996; Stein 1997; Nalbant 1998). After these events, subsequent earthquakes have systematically propagated westwards towards Istanbul. The two most recent earthquakes, both M>7, occurred in 1999 to the east of Istanbul, near Izmit and Düzce, and both caused major societal disruptions and fatalities.

The co-seismic rupture zones of the 1912 Ganos earthquake and the 1999 Izmit earthquake bound a seismic gap along the northern branch of the NAF that lies within the Sea of Marmara. If this seismic gap were to rupture during a single event, it would produce a massive earthquake near the metropolis of

Istanbul and its surrounding area (Hubert-Ferrari et al., 2000). Therefore, the NAF is the largest seismic hazard within the Marmara region.

From this brief introduction is already clear how important it is to improve our understanding of the seismo-tectonics and geo-hazard potential of the NAF near Istanbul. My research has been inspired by this overall goal.

During this research, I started by defining the fault geometries, kinematics and strain accumulation between each of the western segments of the NAF over the last few Myr. I generated several maps describing 1) the present geometry and kinematics of the fault system both at surface and depth and 2) the morphology of the area and strain localisation patterns for the northern branch of the NAF around the Sea of Marmara region. These maps served as the first step to investigate the characteristics of active tectonics with the aim to link these with the lithosphere dynamics in the Sea of Marmara region.

The second step of my research was to build analogue laboratory models that could reproduce the fault systems of the Sea of Marmara. These models were created and run in the Analogue Modelling Laboratory "E. Costa" of the Department of Chemistry, Life Sciences and Environmental Sustainability, at University of Parma, Italy. The models were purposely designed to document the propagation of a transform system characterized by bends along the faults that create restraining and releasing segments. The geometry reproduced in the analogue models is a simplified version of the actual NAF geometry. We intentionally simplified the geometry of the NAF to focus on the causal links between fault bends and their influence on the distribution of deformation at crustal scale. This study used Particle Image Velocimetry (PIV) analysis applied to analogue modelling to quantify the distribution of incremental shear rates, topographic changes and strain distributions. High-resolution PIV analysis provides us with much better measurements that allow comparison between these models and GPS data and reflection seismic data within the Marmara region. Finally, I used additional complimentary data collected by the scientific cruise "SEISMARMARA". These data sets contain multibeam bathymetry and shallow seismic reflection data that were downloaded from the IFREMER web site (https://campagnes.flotteoceanographique.fr). With these analyses we "closed the circle" by allowing the NAF-inspired analogue models to inform us on the possible fault characteristics that could be responsible for neo-tectonic deformation associated with the propagation and distribution of deformation along the northern branch of the NAF in the Sea of Marmara.

A set of thirteen experiments were performed to test variations in potential model configurations. Here I discuss in detail the results from the most representative experiments for the problems contained in this thesis. A complete overview of all analogue models is provided in Appendix I.

Finally, continuous GPS velocity measurements collected over the last three decades (see Ayhan et al. (2002) and Bulut et al. (2019)) were used to calculate strain rate patterns and dilation over northwest Anatolia and the Sea of Marmara region in particular. The goal of this study was to evaluate the strain distribution related to seismic slip and the interference between the strike-slip regime linked to the Anatolia-Eurasia plate boundary and the extensional regime linked to the Nubian slab rollback in the Aegean.

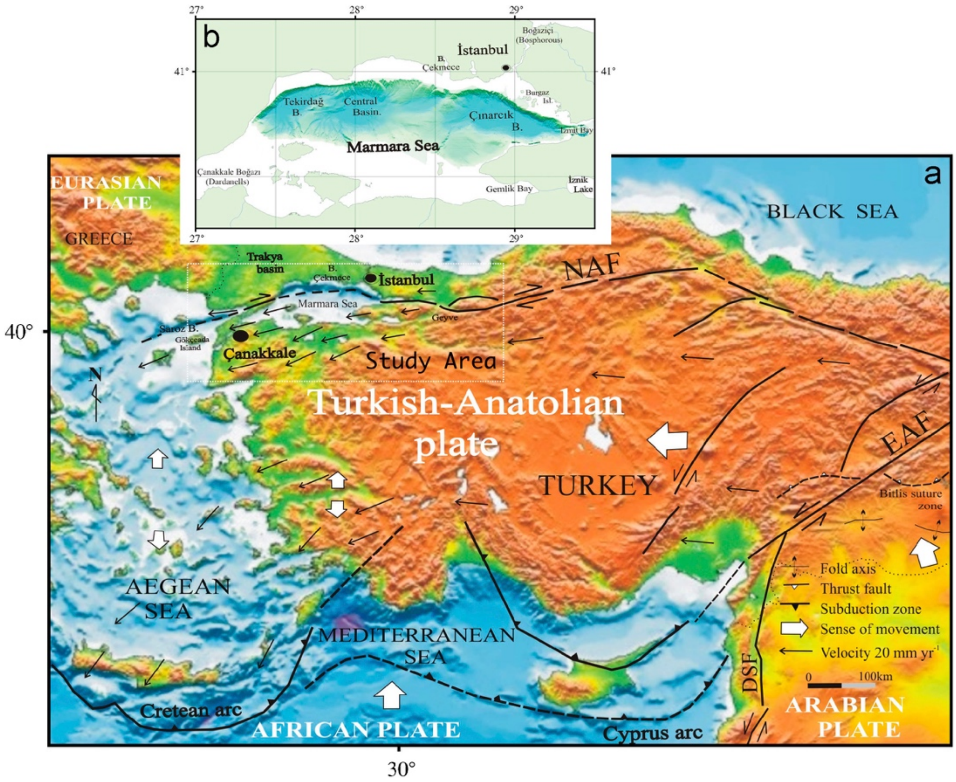

***Figure 1-1** (from Koral et al., 2007) The location of the study area at the eastern Mediterranean. The principal active tectonic features, which are connected to the Sea of Marmara. The North and East Anatolian Faults, that accommodate the westward escape of the Anatolian block, and an active subduction zone along the southwestern boundary of the Anatolian block GPS velocity field relative to a Europe-fixed reference as in Straub and Kahle (1994), Reilinger et al. (1997), and Kahle et al. (1998) is indicated by arrows. The small rectangle with white outline indicates study area of this thesis . NAF: North Anatolian Fault; EAF: East Anatolian Fault; DSF: Dead Sea Fault. (b) The Sea of Marmara comprises three deep basins from east to west: the Çınarcık, Central, and Tekirdağ Basins. Each basin is separated from each other by ridges several hundred meters high.*

1.1 Aims and Outline of This Thesis

While the Sea of Marmara has been thoroughly studied in terms of surface fault maps (Armijo et al., 1999, 2005; LePichon et al., 2001; Imren et al., 2001; Seeber et al.,2004, 2006; Okay et al., 2004; Carton et al., 2007; Laigle et al., 2008; Becel et al., 2010; Gasperini et al., 2011; Sorlien, et al.,2012; Kurt et al., 2013; Grall et al., 2012), topographic maps (LePichon et al., 2001), horizon depth maps (Becel et al., 2010, Grall et al., 2012) and fault rate estimations (Ergintav et al., 2014), its overall tectonic setting remains a matter of debate. The two end-member scenarios are the “single fault” model (LePichon, 2001) and the "pull-apart" model (Armijo et al., 2002), whether the Sea of Marmara is characterised by a master strike-slip fault that could rupture in a single large event or by smaller faults that could rupture in multiple smaller events has significant implications for the seismic hazard of the region, Istanbul in particular. This study aims to address this problem by studying physical models that explore the kinematics of the area. These models will provide insights to better characterize the structures and dynamics of the Sea of Marmara, to analyse and quantify strain along the northern branch of the NAF, and to investigate the topographic response that results from this deformation. Specifically, this study aims to answer the following questions related to the region of the Sea of Marmara:

1. Can a releasing-restraining bend pair along the strike-slip fault reproduce the structures observed in the Sea of Marmara?
2. How is the evolution of the strain localisation in different fault segments, and which fault segments tend to remain active over time?
3. To what extent does fault localization control the development of subsidence or uplift?
4. Restraining and releasing bends along transform-type faults can either work as barriers or help earthquake propagation (Cunningham and Mann, 2007). Does the co-seismic strain release on the Izmit segment directly affect the strain accumulation on the Prince Island segment?
5. The Izmit segment is oriented at an angle relative to the Central High segment, that we measure as 10°. Could this difference in orientation be responsible for the compressive deformation observed at the NW edge of the Çınarcık basin?
6. How does the spatial pattern of strain rate change going from the east to the west of the Sea of Marmara, as it is located at the

transition between a pure strike-slip region to its east and the extensional regime of the Aegean Sea to its west?

    a. How is this correlated to changes in stress?

7. To what extent is the strain rate linked to recent earthquakes?

The work presented in this thesis is organized into seven individual chapters. One of these - Chapters 4 is copy of manuscript that has already been submitted to international peer-review journal. Also, it (Chapter 4) has been published as a preprint in the Earth and Space Science Open Archive - ESSOAr (https://doi.org/10.1002/essoar.10502140.1). Chapter 5 has been published in Tectonophysics journal. Chapter 6 is also a manuscript that is currently in preparation to be submitted for publication in a peer-reviewed journal.

Chapter 1 defines the objectives and research questions to be addressed by this thesis.

Chapter 2 provides information background of the study area of this thesis.

Chapter 3 gives an outline for the methodological approach, including experimental setups used for this study.

Chapter 4 presents a manuscript entitled "The evolution of restraining and releasing fault segments pairs caused by fault bends: analogue modelling investigation and application to the Sea of Marmara". This manuscript is currently under review in Journal of Tectonics.

A copy of the manuscript has been published in the ESSOAr archive (https://doi.org/10.1002/essoar.10502140.1). This chapter examines the evolution of a releasing-restraining fault segment pair caused by bending along a strike-slip fault using scaled analogue model simulations. The manuscript further proposes a model for the major fault within the Sea of Marmara as a fault which evolved from a single to a multi-branch fault system, with different branches active and dominant at different times. It also proposes that the western portion of the basin may be characterized by a fault shortcut associated with both a compressional regime and the uplift of Ganos Mountain.

Chapter 5 is entitled "Modelling tectonic deformation along the North-Anatolian Fault in the Sea of Marmara". This manuscript has published in *Tectonophysics*. This chapter also uses the results of analogue simulations in order to investigate the tectonic deformation in the eastern sub-basin of the Sea of Marmara, the Çınarcık Basin. Here the results of the experiments were compared with the morpho-bathymetric map and seismic reflection profiles acquired during the "SEISMARMARA" campaign. This chapter proposes that most of the deformation observed in the Çınarcık Basin is controlled by the changing geometry of the fault with sharp variations in its orientation. From east to west, the NAF in the Çınarcık Basin changes from; 1) almost pure strike-slip deformation in the westernmost part of the Izmit segment; 2) transtension deformation along the central Çınarcık basin segment; 3) transpressive deformation along the easternmost part along the Istanbul segment, where compressive features are observed, both in models and in seismic reflection data.

Chapter 6 is entitled "Strain variation along the western part of the North Anatolian Fault based on GPS data". In this chapter I investigate how the Sea of Marmara strain rate pattern might be influenced by short-term seismic slip, or, as an alternative, by the long-term interaction between the strike-slip regime between Anatolia and Eurasia and the Aegean extensional system. This analysis shows how deformation is distributed at the transition from the NAF to the more complex Aegean boundary and how this transition occurs within the Sea of Marmara and its adjacent regions. To do this, we used strain rates and strain tensor rates derived from GPS data. This chapter proposes that the deformation trend in north-western Anatolia where the NAF network becomes more complex might be associated with a weak lithospheric zone influenced by the extensional Aegean system.

Chapter 7 discusses the parameters that shaped the overall modelling approach, and then it summarises the contributions analysed in Chapter 4, Chapter 5, and Chapter 6.

Chapter 8 provides a summary and conclusion of this thesis.

Chapter 2: Regional Background

2.1 North Anatolian Fault

The North Anatolian Fault (NAF)[1] is an intracontinental, dextral strike-slip fault that is >1200 km in length and in places is characterized by a wide deformation zone of up to 100 km in width (Şengör et al., 2005) (Fig. 2.1a)[2]. The fault goes from Karlıova triple junction in eastern Turkey to the Aegean Sea to the west (Fig. 2.1a). The NAF is the plate boundary between the Eurasian and Anatolian plates; it formed to accommodate the westward motion of the Anatolian plate that resulted from the collision between Arabia and Eurasia during the Miocene (Fig. 2.1a) (Şengör, 1979; Şengör et al., 1985). Additionally, northwest Anatolia is influenced by the convergence between the Nubian (African) and the Eurasian plates. This convergence is responsible for subduction processes in the Hellenic trench. Nubian slab rollback, in particular, is responsible for widespread extension in the Aegean Sea (Flerit et al., 2003). This extension results in a westward pulling force on the Anatolian plate which adds complexity to the western sectors of the NAF system (e.g., Le Pichon, 1982; Le Pichon and Kreemer (2010); Royden, 1993). The NAF's geometry, for example, changes from a single strike-slip fault to the east, to multiple branches to the west in the region of the Sea of Marmara (Fig. 2.1a). GPS velocity data show the effect of the Aegean "pulling" very well: the eastern part of the Anatolian plate moves at a rate of ~20 mm/yr with respect to Eurasia (Reilinger et al., 2006); this velocity increases progressively in western Anatolia (from ~32°E) to about 30 mm/yr near the Hellenic trench (Nocquet, 2012) (Fig. 2.1a).

The NAF trace, clearly visible in the topography across eastern and central Turkey, is close to being the small circle predicted by rigid plate tectonics. The

[1] In this chapter I will use both NAF and NAFZ depending on the characteristics of the fault in the area that I am describing.

best fitting Euler pole of rotation that describes Anatolia/Eurasia motion is located in the Nile delta (McClusky et al.,2000).

Since the discovery of the NAF as a geological feature (Ketin, 1948) there have been a large number of studies (McKenzie and Parker, 1967; Le Pichon, 1968; McClusky et al., 2000 and references therein) resulting in extensive discussions and debates about the evolution, timing of initiation, geological long-term slip-rate and cumulative-offset along the NAFZ.

The latest review of the North Anatolian Fault Zone (NAFZ)[1] evolution by Şengör et al. (2005) suggests that the NAFZ initiated near the Karliova region in the east in the late Miocene (~12 Ma) and propagated to the west, reaching the Sea of Marmara region in the middle Pleistocene (~200 ka). As already mentioned, the NAFZ is formed by a single main fault strand in most of eastern Anatolia, where it behaves as pure strike-slip fault, but it changes to a mostly transtensional setting to the northwest where it becomes more complex and splits into two major splays, called "northern" and "southern" branches of the NAF (Le Pichon et al. 2014). The northern branch enters through the Gulf of Izmit to the Sea of Marmara (Fig. 2.1b). Here the Sea of Marmara takes the form of a large rhomboid that has been interpreted to be a pull-apart strike-slip depression resulting from transtensional shear (Okay et al., 1999) (Fig. 2.1b). The southern branch runs to the SW of the Sea of Marmara: it crosses south of the Iznik Bay and the Sea of Marmara, makes a left bend near Erdek, and then runs in a SW direction until it enters the Aegean Sea (Fig. 2.1b).

According to GPS observations, most of the lateral motion measured on the NAF to the east of the splay appears to be transferred to the northern branch. Reilinger and McClusky (2011) quantified this to be ~80% of the total slip. The segment of the northern NAF that takes in most of the slip runs below the Sea of Marmara and it is called the Main Marmara Fault (MMF) (Le Pichon, X. et al. 2001) (2.1a) Main Marmara Fault connects the Gulf of Izmit with the

Ganos fault established by Le Pichon et al. (2001), included the segments from east to west; Prince Island Fault, Central High Fault, Tekirdağ Segment (Table 2.1).

***Table 2-1** Summary and categorization of the NAF branches.*

<table>
<tr><td rowspan="3">NAF or NAFZ</td><td rowspan="2">Northern strand or Northern Branch</td><td rowspan="2">Great Marmara Fault</td><td>Main Marmara Fault[a]</td><td>Princes’ Island segment or Cinarcik Segment + Central High Fault or Central Segment +Tekirdag Segment</td></tr>
<tr><td colspan="2">Ganos Fault + Izmit Fault</td></tr>
<tr><td colspan="4">Southern strand or Southern Branch</td></tr>
</table>

[a]Le Pichon, X. et al. 2001

Note. This table summarizes and categorises the NAF branches as they are used in this thesis. The Main Marmara Fault includes the segments of Princes’ Island segment or Cinarcik Segment, Central High Fault or Central Segment, Tekirdag Segment; the Great Marmara Fault includes the previous segment, the Ganos Fault and the Izmit Fault; the Northern Segment or Northern Branch includes all previous segments; NAF or NAFZ includes all previous segments and Southern Strand or Southern Branch.

Strike-slip deformation along the eastern part of the NAF has been constrained by several techniques. Geodetic measurements indicate ≈25 mm/yr of slip (Reilinger et al., 2006), while geologically-inferred displacements are on the order of ≈18 mm/yr over the last 10k years (Hubert-Ferrari et al., 2002; Kozacı et al., 2009). This difference suggests that some plate deformation is also being accommodated away from the main fault. Estimates of the total offset along the NAF in eastern and central Anatolia range between 30 and 75 km (Barka and Gülen, 1989; Herece and Akay, 2003; Ferrari, et al. 2002; Şengör, et al. 2005). On the entire Sea of Marmara fault, Şengör (2014) proposed 55 km left-lateral offset with 26 km seen along the Pamukova strand that leads to the main southern strand (Şengör et al. 2005). Armijo et al. (1999) has reported 70 ± 2 km offset on the northern branch of NAF and additional 15+10 km on faults farther south at the west of the Sea of Marmara (Armijo et. al. 2002). Recently, Akbayram et. al. (2015) proposed 52+1 km cumulative dextral displacement along the northern branch of NAF by the Middle Eocene volcanic belt east of the Marmara and additional 15 km on the second strand of the Düzce Fault, total offset estimated as ~67 km in the Eastern Marmara region.

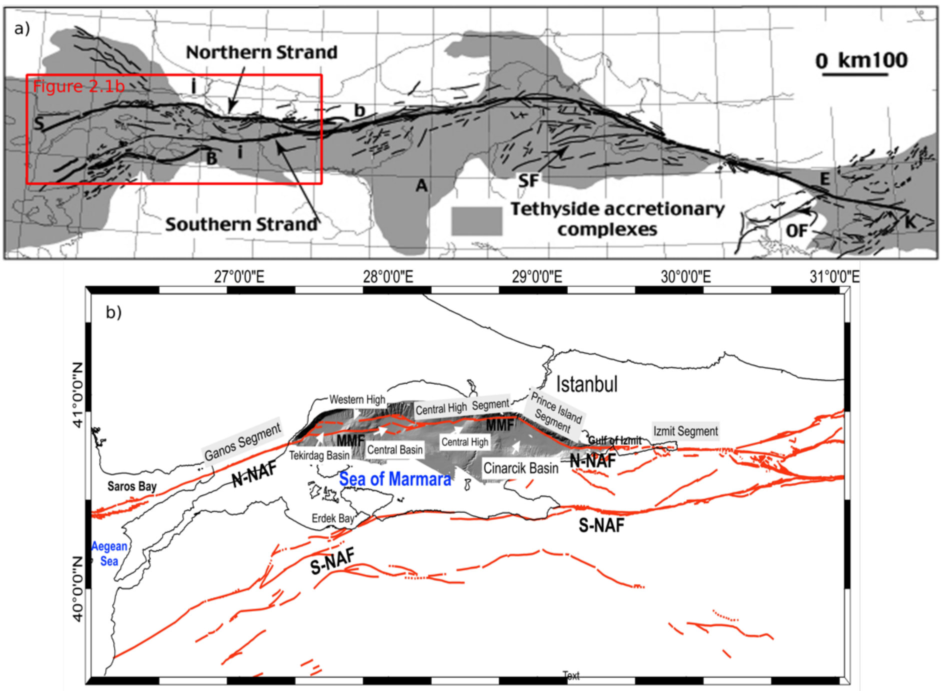

Figure 2-1 The location of the NAFZ. a) the location of the NAFZ (eastern NAFZ, central NAFZ and western NAFZ). The NAFZ is formed by a single main fault strand in most of eastern and central Anatolia, where it behaves mostly pure strike slip fault, but changes to a transtensional setting to the northwest where it becomes more complex and splits into two major splays within the Sea of Marmara. K: Karliova I: Pamukova strand, i:Istanbul. The map

is modified from Şengör et al., 2014 b) the NAF split in to two main branches in the Sea of Marmara. Fault modified from Grall et al., 2012, Le Pichon et al., 2011; bathymetry is from Le Pichon et al., 2011

2.1.1 The seismicity of the North Anatolian Fault

The 1200-km-long right-lateral North Anatolian Fault is seismically active. From 1939 to 1999 over 900 km of the fault has been broken by a sequence of eight large > M7 earthquakes that propagated from the east to the west (Toksöz et al., 1979; Barka, 1996; Stein et al., 1997). These earthquakes are the M 7.9 1939 Erzincan EQ., the M 7.1 1942 Erbaa-Niksar EQ., the M 7.6 1943 Tosya EQ., the M 7.3 1944 Bolu-Gerede EQ., the M 7 1957 Abant EQ., the M7.1 1967 Mudurnu Valley EQ., and the 1999 M 7.4 Izmit EQ. and M 7.2 Düzce EQ. (Fig. 2.2a). The 1999 M 7.4 Izmit and the M 7.2 Düzce earthquakes were the last of this series of catastrophic earthquakes; they localize along the eastern part of the northern branch of the NAFZ (Fig. 2.2) (Stein et al. 1997; Nalbant et al. 1998; Toksöz et al. 1999). Another destructive earthquake, the M∼7.3 1912 Ganos earthquake, preceded this sequence and occurred along the northern branch, west of the Sea of Marmara at the end of the NAFZ (Fig. 2.2a). This sequence leaves a ~150 km long seismic gap along the segment of the northern branch of the NAFZ that corresponds to the Sea of Marmara (Bohnhoff et al., 2013; Ergintav et al., 2014, Schmittbuhl et al., 2016)(Fig. 2.2a).

Along the northern branch of the NAF the MMF connects the 1912 Ganos EQ rupture zone with the 1999 İzmit EQ rupture zone. This in between segment has not been ruptured since 1766. The estimated recurrence time for events on the MMF is 200–250 years (Parsons 2004; Bohnhoff et al. 2016). This seismic gap has a potential for earthquakes up to M 7.4 and it is located only 40 km southeast of Istanbul (Parsons et al., 2000, 2004, Bohnhoof et al. 2013). According to time-dependent models the probability of the occurrence of an M ≥ 7 earthquake along the Sea of Marmara seismic gap is high, and it is currently increasing to about 70% within the 30 years after the 1999 Izmit earthquake (Parson, 2004). Depending on the geometrical model considered for the fault (this subject will be covered in the next paragraph 2.2) the elastic deformation accumulated over the Marmara segment could generate a single M ≥ 7.4 earthquake (Le Pichon et al., 1999; Hubert-Ferrari et al., 2000) or a number of smaller events (Armijo et al., 2002).

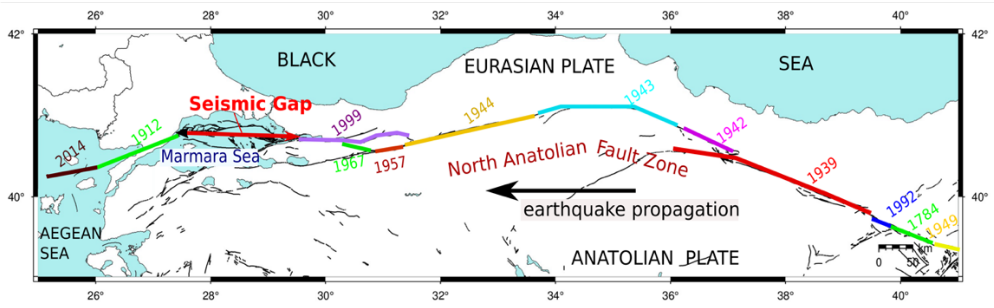

Figure 2-2 *Ruptures along the North Anatolian Fault due to large earthquakes (Mw ≥ 6.5) in the last 80 years. Large earthquakes on the NAF in the last century have followed a general westward trends in seismicity. Red line in the Sea of Marmara indicates the seismic gap.*

After the 1999 Izmit earthquake that broke the entire submarine portion of the Izmit segment (Gasperini et al., 2010; Uçarkus et al., 2011), scientists have been investigating the activity of the fault. Recent seismological and geodetic investigations reveal that the MMF currently has both locked and creeping fault sections (Ergintav et al., 2014; Bohnhoff et al., 2013). In particular, the MMF is subdivided in two segments: the Princes' Islands segment immediately to the west of the Izmit segment that reaches the area immediately south of Istanbul, where it joins the Central Marmara segment that proceeds to merge with the Ganos fault (Fig. 2.1b).

The onshore Ganos fault, where a M7.4 earthquake occurred in 1912, is positioned immediately to the west of the Sea of Marmara. According to GPS measurements, it is currently locked (Motagh et al. 2007; Ergintav et al. 2014; Klein et al. 2017).

Likewise, there are strong indications that the same is true for the Princes' Islands segment offshore Istanbul; the Princes' Islands segment accumulated slip deficit to a depth of ~10-km (Bohnhoff et al. 2013; Ergintav et al. 2014). Indeed several recent studies also support the hypothesis that the central segment of the MMF relaxes part of its tectonic loading continuously in a creeping mode without significant seismic activity (Karabacak et al., 2011; Çakir et al., 2012).

The historic record (Ambraseys, 2002; Guidoboni and Comastri, 2005) and the paleoseismologic data (Pondard et al., 2007; Drab et al., 2012) reveal that these segments of the MMF have been able to generate large earthquakes with M>7 (Fig. 2.3 and table 2.2).

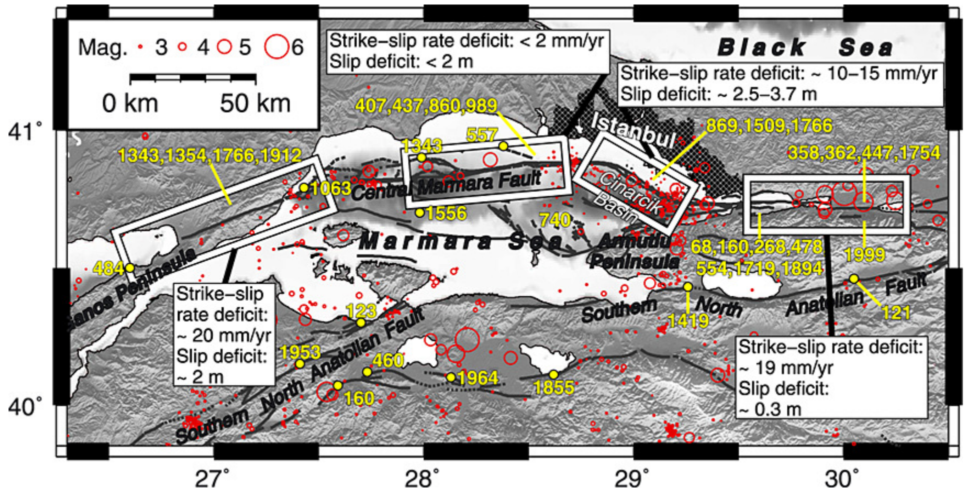

Figure 2-3 *The map of the seismicity with the historical earthquakes the northern branch of the NAF around the Sea of Marmara. Total slip rate deficit and total deficits were estimated by velocities obtained from GPS measurements, since the last major earthquakes are shown (taken from Ergintav et al., 2014). Historical earthquakes were referenced to Ambraseys (2002) and Pondard et al. (2007).*

Table 2-2 *Major historical seismic events (M > 6.8), corresponding the earthquake ruptures revealed from paleo-seismological studies of the Northern Branch of the NAF in Figure 2.1b (modified from Megrough et al., 2012)*

Date of Historical Earthquake AD (yr/m/d) [a,d]	Lat.	Lon.	M_s [a]	I_o	Earthquake ruptures from paleoseismologic studies	Localities with heavy damage [a,d]
477.08.25/484.09.00	40.8 [a]	29.	7.2	IX [a,b]	Guzelkoy (Ganos segment) [f],Gazikoy-Saros [h]	Çanakkale, Gelibolu, Saros
823 (824?).10	40.9	27.4	-	IX [a,b]	Guzelkoy(Ganos segment) [f], Gazikoy-Saros [h]	Panion (Barbaros), Marmara Ereğli
865	40.43	29.4	7.2	VIII	Izmit [i]	
1063.09.23	41.0	29.0	7.4	IX [c]	Guzelkoy(Ganos segment) [f], Saros [c] ,Tekirdag Basin [j]	Saros, Mürefte, Tekirdağ, İstanbul
1296	40.43	29.4	-	VII [c]	Izmit [i]	

1343.10.18	41.0	29.0	7	VIII[c]	Guzelkoy(Ganos segment) [f], Gazikoy-Saros [h] ,Tekirdag Basin[j], Central Basin[j]	İstanbul
1344.11.06	40.7	27.4	-	IX[c]	Guzelkoy(Ganos segment) [f], Gazikoy-Saros [h]	Tekirdağ, İstanbul
1354.03.01	40.6	26.9	7.4	X[c]	Guzelkoy(Ganos segment) [f], Gazikoy-Saros [h]	Çanakkale, Gelibolu, Saros, Tekirdağ
1509	40.43	29.4	7.2	IX	Izmit [i], Gazikoy-Saros [h] , Izmit Gulf[j]	Bolu, Gelibolu, Edirne
1659.02.17	40.5	26.4	7.2	-	Tekirdağ	Tekirdağ
1719.05.25 [h]			7.4	-	Izmit-Golcuk	Yalova, Sapanca, Düzce
1766.05.22 [g]	41.0	29.0	7.4	-		Istanbul, Bosphorus, Gulf of Mundaya, Bursa, Izmit, Tekirdağ
1766.08.05	40.6	27.0	7.4	-	Guzelkoy(Ganos segment) [f], Gazikoy-Saros[g],	Bozcaada, Çanakkale, Gelibolu, Saros, Tekirdağ,
1894.07.07			7.2			Istanbul, Gemlik, Mudanya
1912.08.09	40.7	27.2	7.3	X [d]	Guzelkoy(Ganos segment) [f], Gazikoy-Saros[g], Tekirdağ	Gelibolu, Saros, Tekirdağ
1912.09.13	40.7	27.0	6.9	VII[e]	Guzelkoy(Ganos segment) [f] , Gazikoy-Saros[g], Mürefte	Gelibolu, Saros, Mürefte

[a] Ambraseys (2002, 2009); [b] Guidoboni et al. [1994]; [c] Guidoboni and Comastri [2005]; [d] Ambraseys and Finkel [1987]; [e] Hecker [1920] ,[f] Meghraoui et., 2012; [g] Klinger et al., 2003; [h] Rockwell et al., 2001; [i] Cagatay et al., 2001,[j] et McHugh al., 2006

The southern branch of the NAFZ contains only 20% of Anatolia's westward motion (e.g. Ergintav et al. 2014). The southern branch lacks evidence of a compelling earthquake history. The only well-known event is the Mw 7.2 1953 Yenice-Gönen earthquake that generated a surface dislocation along ~70 km of the fault (Pınar, 1953; Kürcer et al., 2008) (Fig. 2.3).

2.2 North Anatolian Fault in the Sea of Marmara

The NAFZ regional seismotectonic setting has been extensively studied since it was first reported in the late 1940s by Ketin, who observed the fault traces at the surface for all major earthquakes since 1939. The surface breaks always had the character of east-west striking, right lateral fault (Şengör et al., 2005). Ketin (1957) also observed that the fault cuts across middle Miocene age sedimentary rocks and inferred that the fault was younger than these deposits. Using these cross-cutting relationships in the field he estimated that the fault initiated around 15-20 Ma ago (Ketin 1957).

More recent data depict an asynchronous onset of the NAF. At the NAF's eastern termination ^{40}Ar-^{39}Ar dating on volcanic deposits revealed that motion along the fault probably began around 12 Ma ago (Hubert-Ferrari et al., 2009).

The sediments involved in shear related deformation suggest that the NAF involved the Sea of Marmara region since about 200 ka (Le Pichon et al., 2001; Şengör et al., 2005). However, the oldest basins related to shear deformation suggest that the NAF propagated westward towards the Aegean already in the early Pliocene, ~4-5 Ma ago (Armijo et al., 1999; Hubert-Ferrari et al., 2003).

However, on the western end, Zattin et al. (2005) suggested that the Ganos segment of the NAF follows a pre-existing Oligocene structural discontinuity. Late Oligocene displacement along a NAF precursor is also supported by Uysal et al. (2006). They found that an early event of significant strike–slip was initiated at about 57 Ma, according to K–Ar dating of fault rocks.

These data reveal that despite the relatively young age of the NAF and of the modern tectonic setting of the Sea of Marmara, the NAF is partly taking advantage of older lithospheric deformation features that represent weak zones where the plate boundary was able to preferentially develop. These lithospheric deformation zones are inherited from the Oligocene collision of several different terrains following the closure of Tethys (Şengör, EPSL, 1987, Şengör and Yilmaz, Tectonophysics, 1981, Okay 1999). This collisional phase built in Anatolia a complex pattern of sutures highlighted by ophiolite belts (Fig. 2.4). Indeed, the NAF follows these pre-existing geological boundaries: it lies along part of the Ankara-Erzincan Suture in the east, while in the west it cuts through the intra-Pontide suture (IPS) zone (Fig. 2.4) between Eurasia and the Sakarya continental block (Fig. 2.5)(Şengör and Yilmaz, 1981, Okay and Gorur, 1995). These pre-existing geological boundaries are thought to continue vertically through the full thickness of the crust and the lithosphere, extending to a depth of ~100 km, thereby offering ideal weak zones for the determination of the NAF pattern rather than being ideally aligned with the modern stress field. (Frederiksen et al., 2005, Fichtner et al., 2013). Receiver functions and P/S velocity ratio also offer a view into the crustal structure (Frederiksen et al., 2015). North of the northern strand of the NAF, where it follows the IPS, the crust thickens sharply (from 35 km south of the NAF to 45 km to the north), the fault appears to be a nearly vertical feature, and the basement changes character. The IPS, in fact, represent the boundary between the accretionary Sakarya terrain and the continental late Proterozoic fragment of the Istanbul zone (Okay, 2008). Interestingly, despite its thicker crust, the region north of the northern strand of the NAF is characterised by low topographic variations, possibly related to mantle density variations (Frederiksen et al., 2015).

The pure strike-slip system along the NAFZ in the east of the Sea of Marmara goes into a transtensional setting in NW Turkey as a result of the rollback of the Hellenic subduction zone that formed ~15 Ma ago (Şengör et al., 2005; Le Pichon et al., 2015). This extensional component is responsible for the opening of the Sea of Marmara as a large pull-apart structure.

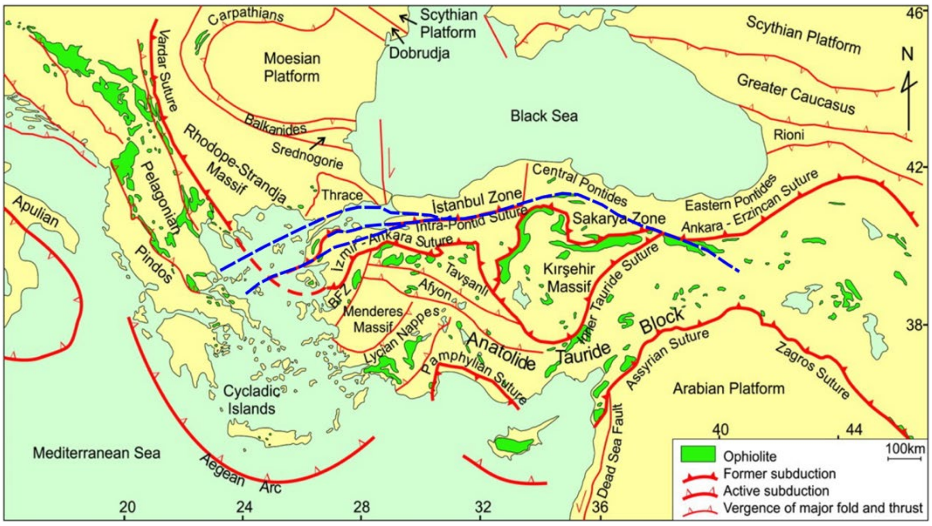

Figure 2-4 *Summary map showing continental blocks, major sutures and related ophiolite belts of the eastern Mediterranean. Dashed line in dark blue represents the NAFZ. BFZ, Bornova Flysch Zone. After Okay, A.I˙. 2008. Geology of Turkey: A synopsis. Anschnitt, 21, 19–42 and Tavlan et al., 2011, Journal of the Geological Society, London, 168 (4) 927–940.*

Figure 2-5 *(from Çağatay and Uçarkuş, 2019) shows the basement structures of the Sea of Marmara, the microcontinents (Sakarya Zone, Istanbul Zone, Strandja Massif), Tertiary Thrace Basin, Intra-Pontide suture zone. These zones were put together as a result of closure of the Neo-tethyan ocean during the early Eocene to Oligocene. NAFZ is now situated on these suture zones.*

2.3 Morphology of the Sea of Marmara

The structures and geomorphology within the Sea of Marmara have been a focus of recent offshore exploration. The Sea of Marmara is 170 km long and has a maximum water depth of 1300 m.

The deepest part of the basin is the North Marmara Through (NMT; Laigle et al., 2008; Bécel et al., 2009), which is characterised by three major sub-basins: the Çınarcık, the Central and the Tekirdağ basins (Fig. 2.6). These basins, reaching 1300 m below sea level, are separated by two NE-trending ridges where the seafloor rises to 450 and 600 m below sea level – respectively the Western High and the Central High (Le Pichon et al., 2001; Armijo et al., 2002; Sarı and Çağatay, 2006) (Fig. 2.6). A common trait of all sub-basins is the location of their depocenters towards their narrow terminations in the vicinity of fault bends (Fig. 2.6)(Okay et al., 2000).

Deep penetration seismic reflection and refraction data revealed that the basins are filled with up to 6 km of sediments (Laigle et al., 2008; Becel et al., 2010) and the sedimentation rate has varied between 1 to 3.5 mm/y (Cagatay et al., 2000, 2015;).

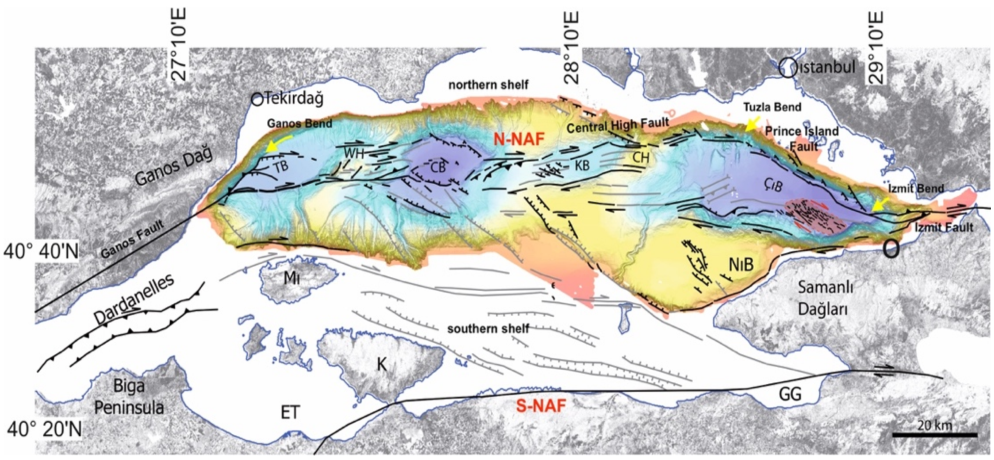

Figure 2-6 *Shaded elevation topography, bathymetric map and the fault map of the Sea of Marmara showing that main morphological elements (deep basins, highs, gulfs, bays, canyons;) modified from Le Pichon et al.,2014). Fault modified from Grall et al., 2012, Le Pichon et al., 2011; bathymetry is from Le Pichon et al., 2011. The location, where the bathymetry is located called as North Marmara Through (NMT; Laigle et al., 2008; Bécel et al., 2009). N-NAF: Northern Branch of the NAF; S-NAF: Southern branch of the NAF; Black fault lines indicate the active faults. Grey fault lines indicate the in-active faults. TB:Tekirdag Basin; WH:Western High; CB:Central Basin; KB:Kumburgaz Basin; CH:Central High; CiB: Cinarcik Basin; GG:Gemlik Gulf.*

The deep basins appear to be controlled by active faults (Okay et. al., 2000); their steep slopes (>18°) show scars of many paleo-landslides and submarine canyons (Gazioğlu et. al., 2002) (Fig. 2.6).
The Sea of Marmara starts in the east with the Gulf of İzmit and terminates sharply in the west where the Tekirdag basin abuts against the Ganos Mountain (Fig 2.6). The Ganos Mountain is a region that rises to ~1000 m high around the junction between the Ganos bend and the MMF. The Ganos Mountain trends parallel to the Ganos fault for ∼35 km and it has a uniform width between 8 and 11 km. The Ganos Mountain also terminates abruptly to the west in the Saros depression of the Aegean Sea (Fig 2.6).

The three major sub-basins of the Sea of Marmara are aligned along an east-west direction. From east to west they are: the Çınarcık Basin, the Central basin and the Tekirdağ Basin (Fig 2.6).

The Çınarcık Basin extends for about 50 km in a NW-SE direction and it is ∼18 km wide. It has a wedge shape in plan view. The basin floor of the Çınarcık Basin is relatively flat, and slightly inclines to the east where it reaches the maximum depth of 1270 m. (Gazioglu et al., 2002). The basin is bounded by steep slopes both in the north and in the south side. The northern slope is coincident with the master fault that has mainly normal displacements to the east and mainly strike-slip displacements to the west (Armijo et al., 2002). Reconstructions indicate that a significant amount of extension ~ 2 km has occurred at the northern border of the Cinarcik basin (Armijo et al., 2002). The bathymetry of the northern margin dips towards the south at approximately 17° over a 3 km wide slope. In contrast the bathymetry of the southern margin is more gentle with a 4-6 km wide slope dipping 7-10° towards the north (Okay et al., 2000). The maximum syn-kinematic sedimentary thickness in the Cinarcik basin is estimated to be 5-6 km (Carton et al., 2007) (Fig. 2.8). Sediment thickness maps reveal that the main depocentre has gradually migrated eastwards over time (Carton et al., 2007). The MMF runs to the north of the basin at the base of a steep escarpment, ∼1000 m high and ∼40 km long, and it takes the name of Princes' Island segment (See table 2.1).

The Central Basin also has an elongated shape with a length of ~25 km, and a width of ∼16 km. This E–W trending basin reaches 1268 m of water depth. The Central basin is separated from the Cinarcik basin at the east by the Central High, a ridge which reaches 400 m of water depth. In the west the Western High, that reaches ~600 m of water depth, separates the Central Basin from the Tekirdağ Basin. The basin's northern slope dips ~11°, while the south slope dips ~8° (Zitter et al., 2012). The Central Basin also has a very thick sediment infill of up to 5 km thick (Laigle et al., 2008)(Fig. 2.9)
Here the MMF is located in the middle of the basin. Unlike the Cinarcik Basin, the Central basin trends E-W: this is the consequence of a bend of the MMF (Istanbul bend) located between the Cinarcik Basin and the Central High (Laigle et al., 2008).

The Tekirdağ Basin, the westernmost basin of the Sea of Marmara (Imren et al., 2001; Okay et al., 1999, 2000), is ~40 km long and ~15 km wide.
It's a flat bottom that reaches ~ 1190 m below sea level and a rhomboidal form. This basin is bounded at the west by the Ganos mountain (with a summit of 924 m over sea level) and at the east by a submarine ridge (the Western High). The transition from the deep basin floor to the northern shelf is controlled by slopes that can locally reach inclinations between 11° and 23° (Okay et al., 2004). The southern slope of the basin is less steep than the northern slope with dips of 6-7° (Cagatay and Ucarkus, 2019). The Tekirdağ Basin appears as filled up to 6 km of sediments according to Laigle et al. (2008) and Becel et al. (2010). The depth of the basin increases eastward, but

the depocenter has progressively shifted westward (Seeber et al., 2006) (Fig. 2.10). The NAF is located to the south of the basin at the toe of the southern broad shelf. Here the NAF segment takes the name of Central High Fault Segment (Okay et al., 2004) (Fig. 2.6).

2.4 Proposed Fault Geometry for the Sea of Marmara

Following the Izmit EQ in 1999, the western portion of the NAF has been thoroughly mapped by several international surveys. Most of them focused on the northern strand of the NAF across the Sea of Marmara with the purpose to map the submarine fault and understand its tectonic characteristics. The results obtained from these surveys are presented by Le Pichon *et al.* (1999, 2000); Rangin *et al.* (2001, 2004); Imren *et al.* (2001); Le Pichon *et al.* (2001, 2003); Demirbağ (2003); Armijo *et al.* (2002); Sato *et al.* (2004); Armijo *et al.* (2005); Carton (2005); Carton *et al.* (2007); Laigle *et al.* (2008) and Becel *et al.* (2009). The current knowledge of the geometry of the NAF beneath the Sea of Marmara is based mainly on bathymetry and shallow onshore and offshore structural information.

Despite this intense international effort, the overall tectonic setting and the geometry of the fault in the Sea of Marmara is still controversial. This controversy has led to several distinct fault models being proposed that involve different kinematic and geometric constraints (see also discussion in Yaltirak, 2002). It is worth pointing that all the models discussed below were proposed in the aftermath of 1500 km of conventional reflection seismics that were acquired by the R/V Sismik-1 of the Mineral Research and Exploration Institute of Turkey (MTA) in 1997. Since then other projects collected additional geophysical data, but the basic controversy still remains. Here a summary of the proposed models:

1. Master Fault Models (Fig. 2.7a). Pinar (1943) was the first to propose a single strike-slip fault system for the Main Marmara Fault (MMF). This model was also proposed and expanded by LePichon et al. (2001,

2014) and Şengör et al. (2014). Here high-resolution bathymetry and shallow seismic reflection data were interpreted to demonstrate a thorough going strike-slip structure that cuts across pre-existing pull apart basins. This fault, the Great Marmara Fault, is a buried structure that extends the concept of the MMT by linking the southern boundary of the Cinarcik basin to the east, with the southern boundary of the Tekirdag basin to the west (LePichon et al., 2001) (See table 2.1).

2. En-Echelon models (Fig. 2.7b). These models involve different degrees of segmentation of the Great Marmara Fault to a point where the strike-slip NAFZ loses importance, while east-west normal faults are proposed to shape the Sea of Marmara (Parke et al., 1999). In the model by Okay (1999) the MMF bifurcates to the east as it enters the Sea of Marmara, with the main trace to the north that becomes a normal fault as it proceeds toward the east (Fig. 1.2a). In its more radical expression, the en-echelon model consists of east-west trending normal faults with no strike-slip fault in the central part of the Sea of Marmara (Parke et al., 1999).
3. Pull-apart models (Fig. 2.7c). In contrast to a single through-going fault, Armijo et al. (1999, 2002, 2005), Carton (2005) and Carton et al. (2007) proposed that the fault may be interrupted by a transtensional stepover in the center of the basin (Fig. 1.2b). This step-over would be responsible for significant subsidence and localized crustal stretching. In the Sea of Marmara, oblique slip to the west of the Tuzla bend (Fig. 2.6) is accommodated within the Cinarcik Basin by two E-W subparallel strike-slip surface faults and two SE-NW normal faults that bound the basin (Armijo et al., 2002; Flerit et al., 2003; Rangin et al., 2004), with a similar bounding fault geometry for the more westerly Central and Tekirdag Basins.

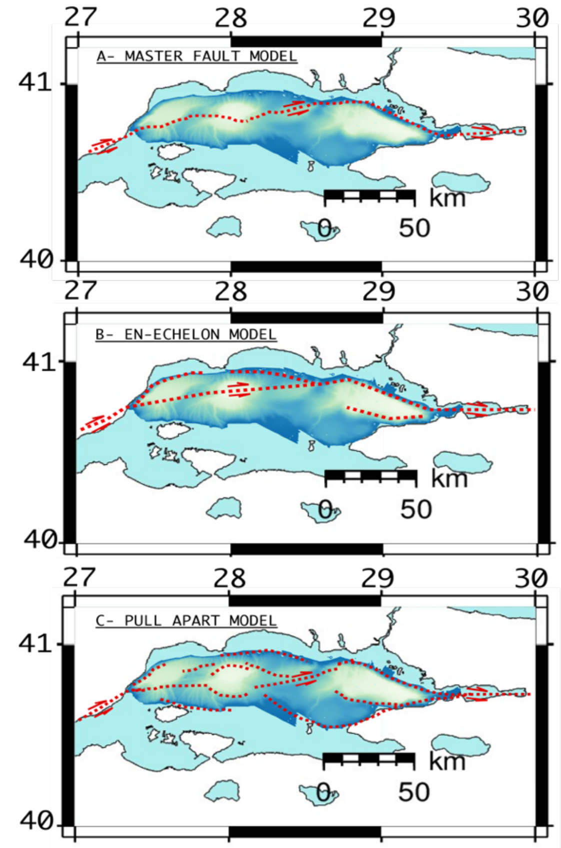

Figure 2-7 *The fault geometries for Sea of Marmara, proposed by different studies. A) Master Fault Model modified from Le Pichon et al., 2003 B) En-echelon Model modified from Okay et al., C) Pull Apart Model modified from Armijo et al., 2002.*

Within these three main categories of tectonic models, new versions have arisen as knowledge of Sea of Marmara structure has increased. Laigle et al., 2008 and Becel et al., 2009, for example, inferred that in the northern part of the Sea of Marmara the MMF changes its dip from sub-vertical to a proper detachment fault that drives tilting of fault-blocks and is responsible for crustal thinning beneath the basins (Fig. 2.11). A key observation supporting these models is the fanning of sedimentary sequences towards the boundary faults, which they considered to be normal faults.

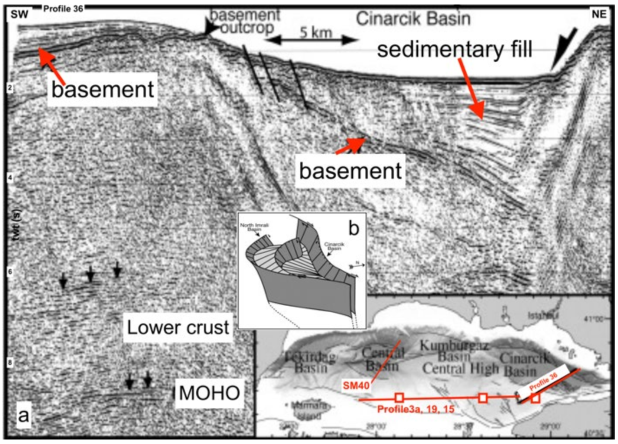

Figure 2-8 *The structures in Cinarcik Basin modified from Laigle et al., 2009. a) the multi-channel seismic profile SM36 from SEISMARMARA. The faults cut into the basement. The boundary faults are indicated thick black lines which show normal fault scarps. The top layers of the lower crust and the Moho are indicated by black arrows. Deep basin is filled with thick sedimentary and whole crust reached ~ 30 km depth. b) 3D block model of the basement topography between the basin-bounding faults interpreted as being a negative flower structure at the crustal scale. The right-bottom inset shows the location of profiles in Fig. 5.8a, Fig.2.9a.*

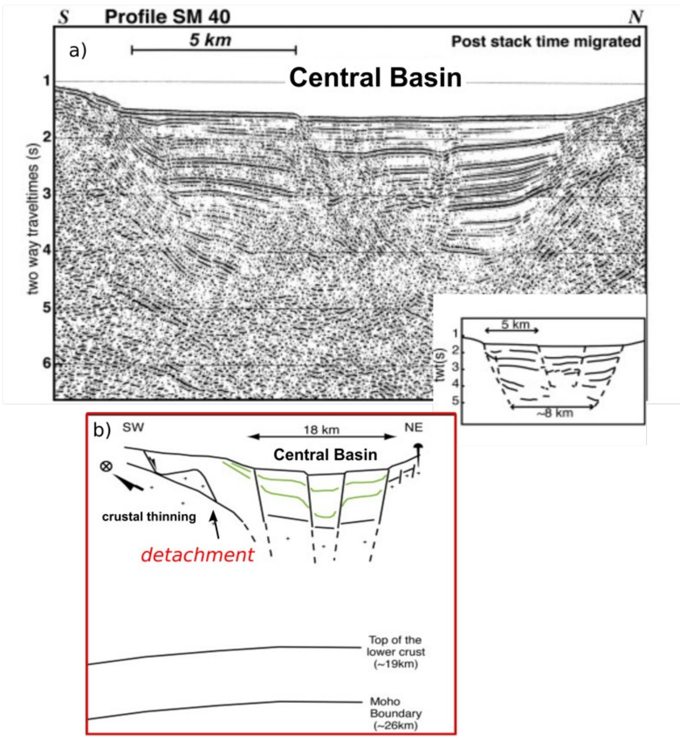

Figure 2-9 *The structures in Central Basin modified from Laigle et al., 2008. a) Multi-channel seismic profile SM40 from SEISMARMARA cruise. The inset shows the line drawing of the section and the location of the Central Basin b) The block model is from Becel et al., 2009. The*

model shows a detachment fault responsible for block tilting and crustal thinning in the Central Basin- Sea of Marmara. TB: Tekirdag Basin; CB:Central Basin; CiB: Cinarcik Basin.

In these interpretations, each of the splays of the NAF would be a negative flower structure that includes dipping detachments and divergent faults at the surface that experience both dip-slip and strike-slip displacements (Fig. 2.8b, 2.9b).

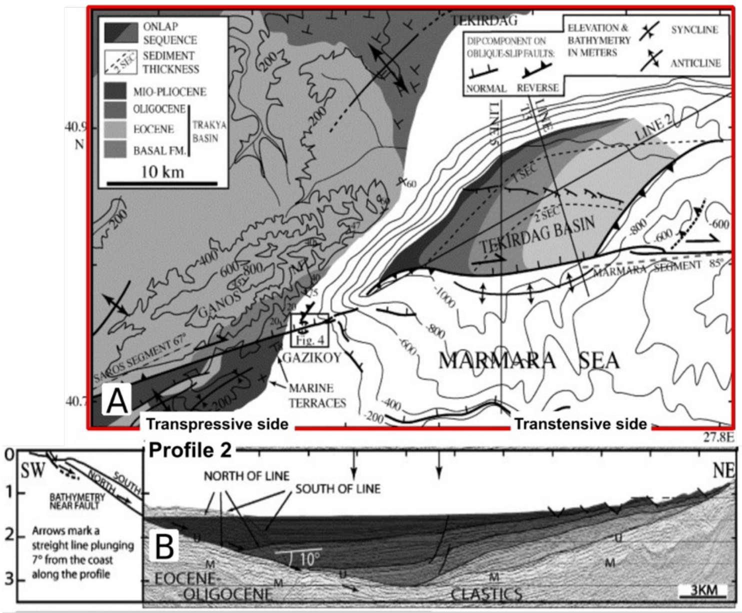

Figure 2-10 *The structures in Central Basin modified from Seeber et al., 2004. a) topography, bathymetry, and geology of the Ganos bend. The transpressive and transtensive deformation located around bend. b) seismic-reflection profile displays a nearly symmetric bowl-shaped basement surface, but, similarly to fault-normal profiles, the pattern of sedimentation and basin growth are remarkably asymmetric.*

Finally, Seeber et al., (2004) proposed that the basins and ridges within the Sea of Marmara are associated with the bends on strike slip segments of the western NAF, with the bends also linked to a vertical component of crustal motion in the west of the Sea of Marmara. This interpretation, for example, relates both the crustal shortening and uplift in the Ganos Mountain and crustal extension and subsidence in the Tekirdağ Basin to the Ganos bend (Fig. 2.10a). They suggest that the vertical deformation is controlled by oblique-slip on the non-vertical north dipping Ganos and Tekirdağ segments of the NAF.

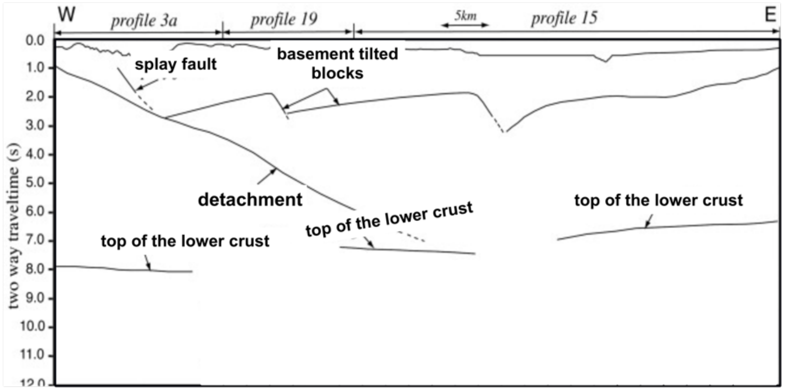

Figure 2-11 *The interaction between a reflector labeled "detachment" and tilted block above. The location map of the line is in Fig. 2.8. (from Laigle et al., 2008).*

The plethora of proposed structural models highlights the geological complexity of this strike-slip deformation zone.

Chapter 3: Methodology

This chapter details the methodologies employed in this thesis, categorised into analogue modelling and strain analysis. The description of analogue modelling also includes a discussion of the Particle Image Velocimetry (PIV) analysis that was performed to measure surface deformation in each experiment. These methodologies are used in Chapters 4, 5, and 6, which allows for holistic and novel analyses of the NAF in the Sea of Marmara.

Analogue models are explored in section 3.1 where they are applied to reproduce a releasing bend and restraining bend geometry analogous to the western part of the NAF. In this chapter I start in section 3.1.1 by reviewing the state of the art of analogue modelling for strike-slip tectonic system. In section 3.1.2 I present the materials used in the models performed during my study: dry sand and silicone putty, representing the rheological behaviour of the upper crust and the lower crust of the study area, respectively. In Section 3.2 and I review scaling theory and its application to the physical experiments. In Section 3.3 there is a detailed description of the deformation setups used in this thesis. The specifics of model setup are also explained in Chapter 4 and Chapter 5. Analogue models also carry some limitations regarding their application. In my study I favoured the approach of simple models that focussed on a single aspect, in this case geometry, to infer its influence on the characteristics of deformation and its evolution. A review of the limitations of analogue models is presented in Section 3.4. The PIV technique is presented in section 3.5. PIV is a rather novel technique and I have developed a MATLAB code to further elaborate its results. This code calculates the incremental displacement vector field between time-steps of the evolving model. In this thesis it is used to resolve shear/strain localisation on a master fault forming on releasing and restraining segments, as observed during the analogue experiments. The MATLAB code is explained in detail in this chapter and will be used in Chapter 4 and Chapter 5.

Strain analysis is the topic of section 3.6. This analysis is based on GPS (Global Positioning System) campaigns performed in Anatolia during the last decades. In this paragraph I review the datasets and their previous use by scientists working on the NAF. In section 3.6.2 I describe the analysis performed in this thesis. This technique and its results form the core of the analysis and results presented in Chapter 6.

3.1 Analogue Models

Analogue modelling is an experimental laboratory technique that uses scaled physical models to simulate geological settings to better understand their tectonic evolution. The great advantage of this technique is that it provides a three-dimensional visualization of the geological problem that we want to investigate. The experiments can evolve to show the entire tectonic process that is under investigation, or they can be stopped at any stage to examine its partial development in 3-D. Since it is easy to change parameters such as material thickness or geometries, analogue models are ideal to investigate the influence of these parameters in the whole process. Although the target of this technique usually is to accurately reproduce natural features, analogue models can also provide new ways of thinking about nature itself. This technique has known limitations such as: the short time of the laboratory experiments in comparison to the long timescale of geological processes; the lack of fluids and chemical reactions in the experiments; and systematic errors due to boundary conditions of the material used, such as the fixed length of the apparatus and its approximate initial setting.

Here we used scaled sandbox models of strike-slip faults to simulate in three dimensions the possible geometries responsible for subsidence along releasing segments and uplifts along restraining segments. The ultimate objective was to produce a model that could help to interpret the progressive development of topography and strain localization across the fault system that has developed in the western part of the NAF. To what extent this objective was fulfilled will be discussed in chapters 4 and 5.

3.1.1 Review of analogue experiments for strike-slip tectonics

Strike-slip fault systems, also known as “wrench” systems, are a key tectonic environment along with extensional and compressional settings. Strike-slip systems are characterised by faults on which displacement is mostly parallel to their surface intersection. Major strike-slip systems, like the NAFZ, are not formed by simple planar faults. Typically they have curved traces, can split in splays that can form braided branches, and, depending on the relative orientation of the fault trace and the displacement, can form areas of relative compression – transpression - or extension - transtension. The result of these geometries is usually a broad zone of shear characterised by a suite of deformation features. Thrust faults, folds and normal faults are therefore commonly associated with strike-slip faults. With these structures relative uplift or subsidence can also occur along the fault system. These structures, though, are usually developed at the upper crustal level, while at depth they merge into the main vertical plane. Cross-sections cut perpendicular to the fault trace reveal so called “flower” structures. Flower structures can be positive, if accompanied by compression and uplift, or negative, if accompanied by extension and subsidence (Fig. 3.1 a,b).

Strike slip faults are commonly segmented in the form of *en-echelon,* non-coplanar faults separated by offsets (or stepovers).

The strike- slip restraining bends that accommodate the shortening-type of deformation forms by pushing by the faults segments. Unlikely, the strike-slip releasing bends which accommodate the transtensional-type of deformation form by separating the faults segments (Cunningmann and Mann, 2007) (Fig. 3.1a).

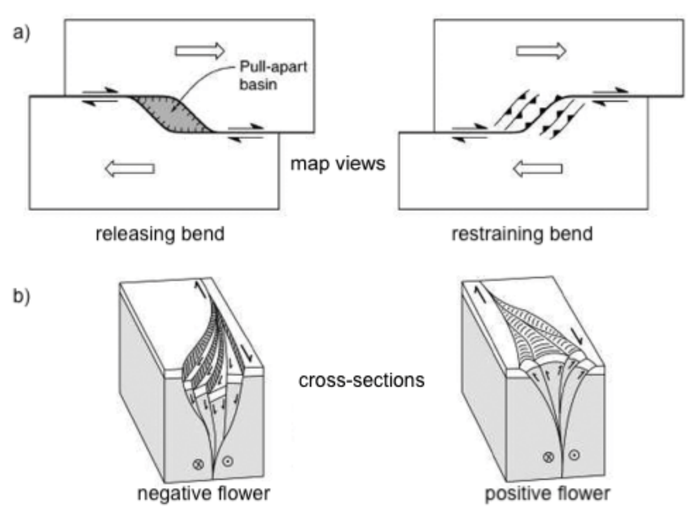

Figure 3-1 *The faults associated with bend in zones of strike slip deformation. a) the structural pattern of restraining and releasing bends along a strike-slip fault. b) the cross section views of a strike-slip fault (from Cunningmann and Mann, 2007).*

Analogue models performed in the strike-slip regime have focused on basic geometries, exploring the Riedel shares and kinematics responsible for the formation of pull-apart basins (Fig. 3.2). These models can be classified in those deforming only (a single layer) brittle layer (Richard et al., 1995; Dooley and McClay (1997); Rahe et al., 1998) or deforming (double layers) brittle-ductile layers (Sims et al., 1999; McClay and Bonora, 2001; Dooley et al., 2004; Wu et al., 2009). The category of Riedel experiments the deformation is reproduced by a single strike-slip fault in the base-plate and overlying sedimentary cover (sand packages). In these experiments, the single fault in the basement is simulated by two firm basement plates, can be moved parallel each other through the boundary in the approach of dextral or sinisterly. This setup was used by Richard in 1995 revealed that Riedel shears tends to be located at layer interfaces, either lithological boundaries or unconformities.

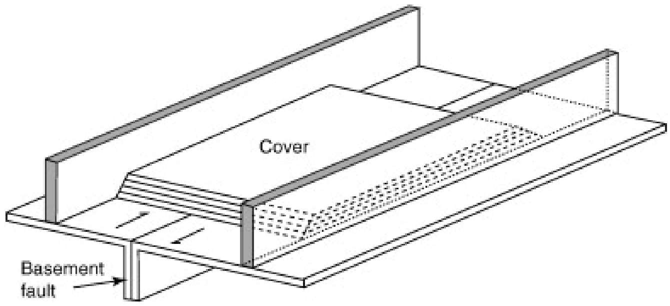

Figure 3-2 *The experiment setup designed for Riedel type structures (from Dooley and Schreurs, 2012)*

The geometries of pull-apart basins formed by changing the angle of releasing segments of a pure strike-slip master fault were investigated by Dooley and McClay (1997) (Fig. 3.3). They imposed sidestep angles of 30°,90°, and 150° from an underlapping to an overlapping array (Fig. 3.3). This simple baseplate geometry was able to produce pull-apart basins along the principal displacement zone (PDZ) (Fig. 3.4). This initial fault pattern produces releasing bend geometries similar to that described for nucleation of pull-apart basins by Mann et al. (1983). These models have been compared to several natural basins, Death Valley- California, Vienna Basin-Austria and the Dead Sea Basin and also shear zones, such as Las Vegas shear zone and Lake Mead fault system *etc.*

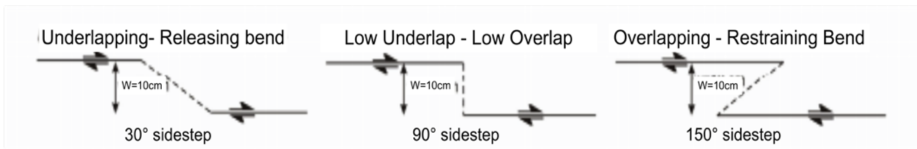

Figure 3-3 *(modified from Dooley and McClay, 1997) shows simple plan views of baseplate geometries produced from different angle of releasing steps; from underlapping to overlapping master fault geometries.*

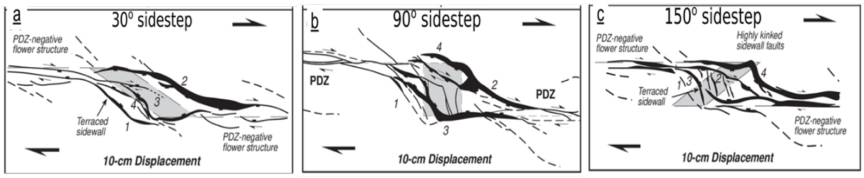

Figure 3-4 *Plan views of the experiments with 30°, 90° and 150° sidestep at the end of the deformation (from Dooley and McClay, 1997)*

Rahe et al. (1998) further progressed along the line of the simple models of the underlapping master fault geometries developed by Dooley and McClay (1997). These authors used a 40° angle on the releasing segment and experimented on relative displacements of base plates (Fig. 3.4). Rahe et al. (1998) also used a double brittle and ductile layer setting. They revealed that during the progressive evolution of pull-apart basin, the basin asymmetry and the geometry of the basin depend on the degree of decoupling between brittle and ductile crust underneath two crustal blocks moving in opposite directions (Fig. 3.5). The Figure 3.5 shows the study by Rahe in 1998.

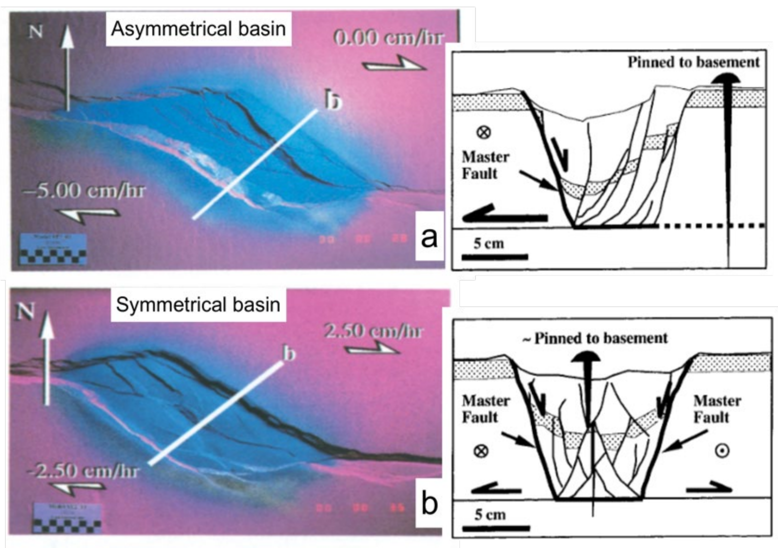

Figure 3-5 *Analogue model of asymmetrical pull-apart basin and symmetrical pull apart basin developed by Rahe et al., 1998. a) a plan view of the original asymmetrical basin with a cross section line-drawing. One plate is moving, indicating by the black arrow on left bottom. b) a plan view of the original symmetrical basin with a cross section line-drawing.*

The moving-direction of plates are indicated by the black arrow on the left and right side on bottom.

Most of the analogue models designed with a double layer systems (brittle-ductile) simulate long term deformation processes of pull-apart basins where Newtonian[2] behaviour is adequate (Dooley and Schreurs, 2012; McClay et al., 1998; Sims et al., 1999; Wu et al., 2009; Fig. 3.4 d,e,f). These models demonstrated how evolution and structural styles of pull-apart basins are significantly different depending on the sediment loads over a ductile layer, and the thickness of the ductile layer. Moreover, these models show how synthetic and antithetic strike-slip faults control basin geometries, while localized normal faulting and local oblique-slip on faults accommodate basin subsidence (Fig. 3.6).

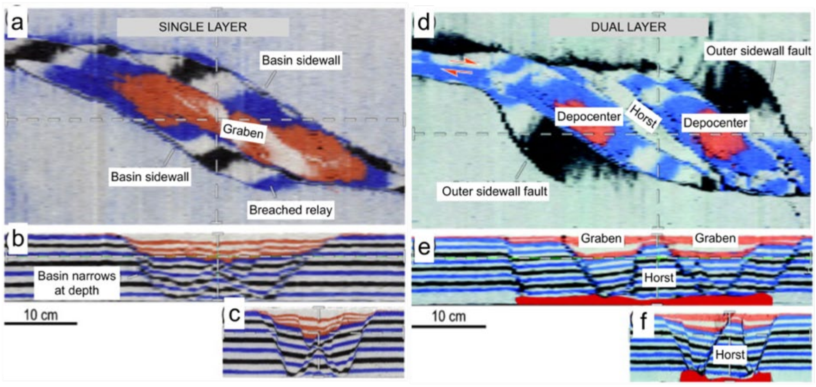

Figure 3-6 *shows a single layer model versus a dual layer model (modified from Dooley and Schreurs, 2012). a) single layer model developed pull-apart basin. b) displacement parallel; section c) displacement-normal section of the dual-layer model. d) dual-layer model developed pull-apart basin. e) displacement parallel; section f) displacement-normal section of the dual-layer model. Brittle-ductile deformation can be seen clearly in dual layer model.*

Sims et al. (1999) documented the evolutionary histories of dual-layer (two-layer setup; brittle upper crust, ductile lower crust) pull-apart basins using a classic underlapping initial fault geometry (Fig. 3.3a). Above a 1-cm-thick ductile layer, their 5-cm-thick model developed a spindle-shaped basin with a lower angle with respect to the PDZs, approximately 28°, than the basement offset. Similarly, Wu et al. (2009) used ductile decollement layer to investigate the brittle-ductile transition during the process of forming of the pull-apart basins. In this experimental setup the basement plates were cut with a 5° obliquity to the direction of plate motion for the purpose of creating transtensional deformation (Fig.3.7 a,b). Later, this transtensional geometry was used by Sugan et al. (2019) to compare to a natural example; with Cinarcik Basin, in the Sea of Marmara. However, these models have been mainly aimed at reproducing the pull-apart geometries of basins.

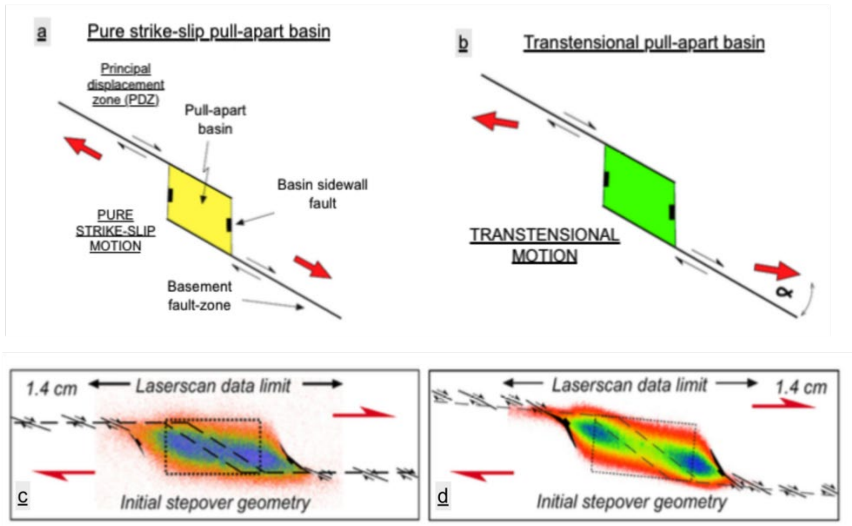

Figure 3-7 *Model setup after Wu et al., 2009: Strike-slip a) versus transtensional b) pull-apart basin c) plan view evolution of the pure strike-slip and the transtensional pull-apart basin model illustrated with fault interpretation and incremental basin subsidence calculated from differential laser scans. Baseplate geometry after 1.4 cm shown with dashed lines (from Wu et al., 2009).*

In recent years, simulations have also focused on fault propagation and strain localisation and accumulation (Adam et al., 2003; Adam et al., 2005; Dotare et al., 2016; Hatem et al., 2017). The techniques developed for these studies are revolutionising our understanding of fault evolution and facilitate the investigation of increasingly complex systems. Adam et al. (2005) studied fault propagation and strain localisation; as well as strain accumulation using the Digital Image Correlation (DIC) method (Fig. 3.8; also see the explanations in Section 3.5 ‘Particle Image Velocimetry (PIV) Analysis’) by taking successive overhead/side photographs as deformation progressed.

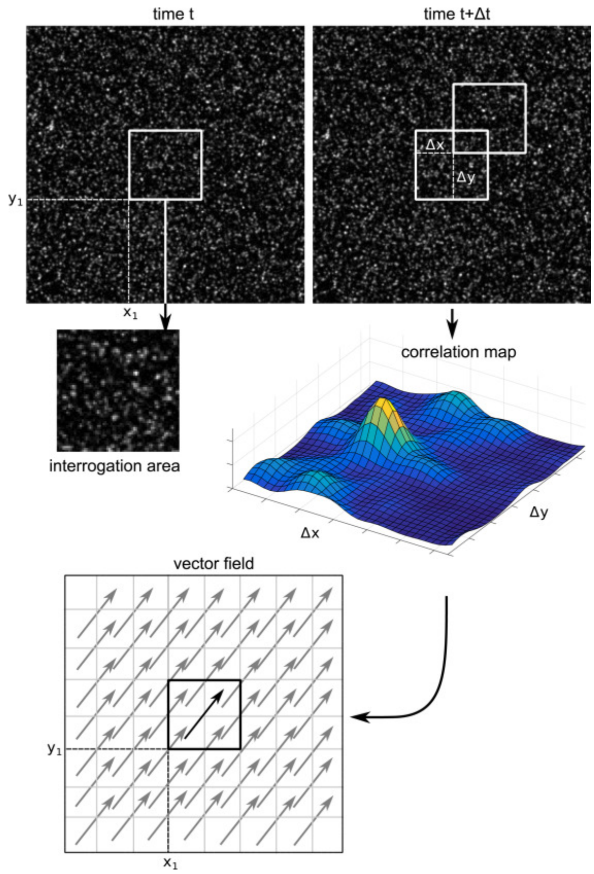

Figure 3-8 *The schematic view of the Particle Image Velocimetry Analysis. The displacement vector was calculated by cross-correlation method from successive raw images (from Boutelier, 2016).*

By applying the Digital Image Correlation technique to the compressional wedge model, Adam et al. (2005) revealed the complex deformation history along several transient shear zones (Fig. 3.9). Later, Dotare et al. (2016) used the PIV method to thrust initiation processes.

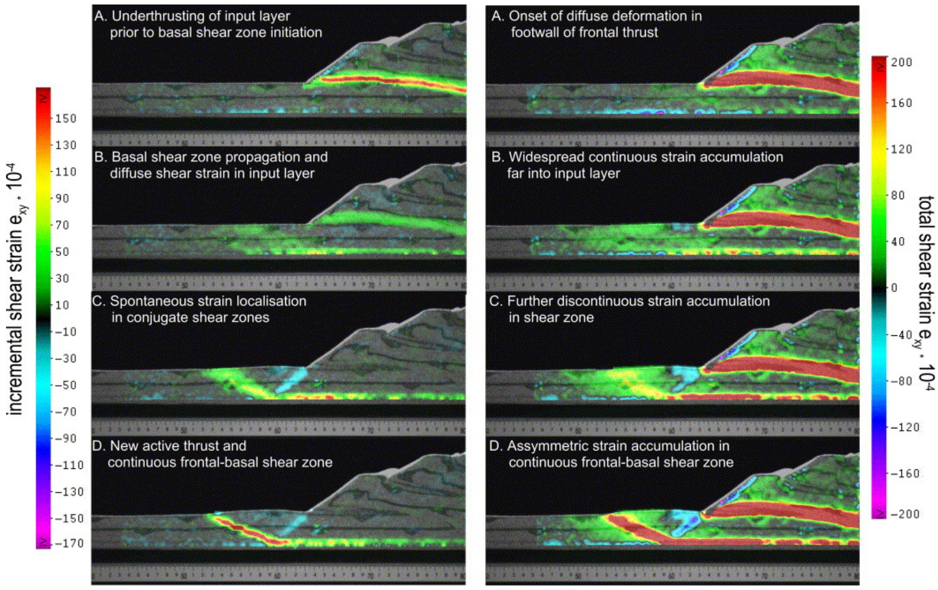

Figure 3-9 *Incremental shear strain (left) and total shear strain accumulation (right) patterns after digital image correlation (DIC) method referred to the classic experiment of Adam et al. (2005) depicted in figure 3.8. (A)–(D) Characteristic evolution stages during 2.2 cm of convergence. (A) Underthrusting of input layer and onset of distributed deformation beneath frontal wedge (dxZ10.8 mm). (B) Basal shear zone propagation and distributed strain accumulation in input layer (dxZ14.4 mm). (C) Spontaneous strain localisation in conjugate shear zones (dxZ18.0 mm). (D) Asymmetric strain accumulation on new active frontal thrust (dxZ21.6 mm) (from Adam et al., 2005)*

More, Hatem et al. (2015, 2017) demonstrated how PIV can produce two-dimensional deformation for crustal-scale experiment applied to strike-slip faults. Hatem et al. (2015) used sequential images obtained during deformation and processed them using the digital image correlation (DIC) method by particle image velocimetry (PIV) software, to provide high resolution displacement patterns. The analysis revealed that restraining bends along strike-slip fault systems evolve by both propagation of new faults and abandonment of fault segments.

Later, Hatem et al. (2017) improved their PIV analysis by adopting the different filter techniques of PIVLab. This technique allowed them to separate individual faults as localized features and map multiple, overlapping faults with confidence. The study revealed the PIV-documented strain localisation of strike-slip faulting as four stages by showing evolution of shear strain distribution: first, shear strain is accommodated as distributed shear (Stage 0), then by development of echelon faults (Stage I), then by interaction, lengthening and propagation of those echelon faults (Stage II) and, finally, by slip along through-going fault (Stage III) (i.e. Hatem et al.,2017).

All the model basins mentioned above were deformed over a classic initial basement cut. Therefore, we attempted to find a setup that best fits the North Anatolian Fault in its west sector. Our scaled-model is novel in the geometry of the basal plates (basement) cuts to reproduce the lithospheric fault, but the materials and the configuration of the model setup build from the findings of previous experiments.

3.1.2 Model Materials

The first essential step to perform an analogue model of a geological scenario is to properly identify the materials to use during the experiment. It is important to use materials that reproduce natural rock properties, as they constitute key model conditions that can influence the processes reproduced in the laboratory.

The experiments performed during this PhD project involve the whole crust, so the models include brittle-ductile layering to simulate the upper and lower crust. The mechanical and physical properties of the materials used in the experiments are shown in Table 3.1.

Table 3-1 *Physical Properties of Experiment Materials*

Material	Density (g/cm^3)	Mean grain size (mm)	Cohesion at peak (Pa)	Angle of internal friction	Dynamic shear viscosity h (Pas)
Sand	1.67	224[a]	102	33° [b]	- - - -
Silicone + barite	1.15	- - - -	- - - -	- - - -	1,4 x 10

Note. [a] (McClay, 1990a), [b] (Klinkmüller, et al. 2016).

Granular materials are commonly used in analogue models to simulate upper crustal rocks (Klinkmüller et al. 2016). An advantage of models consisting of granular materials, such as dry sand, is that the complex 3-D geometric evolution of strike-slip-related structures can be well imaged using X-ray-computed tomography (Richard et al., 1995, Schreurs, 1994, Schreurs, 2003, Schreurs and Colletta, 1998, Schreurs and Colletta, 2003, Ueta et al., 2000). Model materials must have the same coefficient of internal friction as the upper crust as well as a low cohesion (e.g. Abdelmalak et al. 2016). These criteria are met by many granular materials (quartz sand, corundum sand, sieved sand), which have a ϕ between 31° and 37° and negligible cohesion (Panien et al. 2006; Klinkmüller 2011). Quartz sand is a favourite in analogue modelling of low-cohesion-material (e.g. Montanari et al., 2017). It is widely used to reproduce sedimentary cover. However since quartz sand deforms in a brittle way following the Mohr-Coulomb criterion of failure (Hubbert, 1937, 1951; Mandl et al., 1977; Mandl, 1988; Schellart, 2000) it has also been widely used to reproduce the rheological behaviour of brittle crustal and upper crustal rocks or upper lithospheric mantle (e.g., Dooley and Schreurs, 2012; Rosas et al., 2017).

Brittle deformation of crustal rocks can be described with the Mohr-Coulomb law: (τ) shear stress; (C), cohesion; (μ), coefficient of internal friction; (σ) normal stress; (Φ) angle of internal friction.

Equation 3.1

$$\tau = C + \mu\sigma \text{, } with\, \mu = tan\, \Phi$$

We simulate the upper crust brittle layers with sieved sand, a Mohr-Coloumb material that is characterised by an internal friction angle of about 33° with a peak cohesion of 102 Pa (e.g. Klinkmüller et al., 2016; D'Adda et al., 2016; Table 3.1), and a density around 1.670 g/cm^3 (Klinkmüller et al., 2016; Table 3.1.). We also used a sand pack made of thin alternating coloured layers, which allows the identification of faults and folds on cross-sections, but maintains the same physical characteristics.

The ductile lower crust is generally simulated using silicone putty, which has a ductile Newtonian behaviour that can account for (lower viscous) crustal or upper lithospheric weak layers (e.g., Corti et al., 2005; Dooley and Schreurs, 2012; Koyi et al., 2008). In this study, the viscous lower crust was simulated as a layer of PDMS XIAMETER silicone putty mixed with barite powder that was placed at the base of the sand pack. The density of this layer was 1.15 g/cm^3. The dynamic shear viscosity for PDMS used for this study was 1.4 x 10^4 Pa-s. Klinkmüller (2011) determined the viscosities of samples of PDMS from five different analogue-modelling laboratories and obtained viscosities ranging between 2 × 10^4 Pa·s and 3.5 × 10^4 Pa·s. In our models, small quantities of barite were added to the silicone putty in order to slightly weaken it (after Cappelletti et al., 2013).

The comparison between natural and experimental main parameters in the upper and lower crust is shown in Table 3.2. These materials scaling, as well as an adaptable length ratio between model and nature of 1 x 10^{-6} to 2 x 10^{-6} have to be considered when choosing a suitable material for brittle models.

Table 3-2 *Comparison Between Natural and Experimental Main Parameters in the Upper and Lower Crust*

	Densities		Viscosities		
	Nature [a]	Model	Nature[b]	Model	
Brittle Upper Crust	1700 to 2300 kg m^{-3}	1670 kg m^{-3}		…	Sand
Ductile Lower Crust	2700 to 3000 kg m^{-3}	1150 kg m^{-3}	∼2 × 10^{20} Pa s	1,4 x 10^4 Pa s	Silicone + barite

[a] Hergert and Heidbach, (2010, 2011; Hergert et al., 2011)
[b] Yamasaki et al. (2014)
[c] Kende et al. (2018)

3.2 Model Scaling

According to the founding principles of analogue modelling, their applicability to nature requires appropriate scaling of geometric, dynamic, and kinematic pathways to be representative for natural examples (Hubbert, 1937). These scaling parameters have been more recently revised by Schellart (2000). Geometrical similarity are represented by all dimensions (length, width, depth, layer thickness) of setup in the analogue model which need to have the same ratios as its natural example. While the dynamic similarity is recognized by material's ratios of forces and stresses, which must be constant and represent the natural cases to scale. Material properties have given in section 3.1.2 Model Materials. Finally, the kinematic similarity is attained if with given geometrical and dynamical similarity, kinematical similarity can be ensured that the evolution of both model and natural item will be similar despite the different dimensions of size and time (similar change or shape or position). The model also needs to be rheologically similar, means that the strain or flow matter of the modelling materials should have the same form as its natural examples (see Corti, 2003; Weijermars and Schmeling, 1986).

The model performed for this thesis consisted of different thickness of the ductile silicon putty and sand pack layers, as well as different lengths of the fault segments (see Appendix I). Despite Kende et al. (2015) calculated ~30 km of brittle upper crust and ~ 15 km of ductile lower crust in the Sea of Marmara, this scaling was only maintained in experiment MAR-13 (Appendix I). Interestingly, MAR-13 did not produce faults and the deformation observed in the model was almost negligible. Thinner silicon putty layers were, instead, able to simulate the natural example much better – as presented in Chapter 4 and 5. Whether this circumstance implies heterogeneous crustal layering in the Sea of Marmara (beyond the resolution of free air gravity data used by Kende et al., 2017), or simply that the silicon putty in these experiments can be considered as a basal viscous layer to diffuse the deformation that would otherwise be far more localized by a very discrete velocity discontinuity at depth we have not explored. However, it is one of the interesting additional pathways that can be developed in the future.

3.3 Experimental Setup and Analysis Procedure

Analogue modelling was performed in the Analogue Modelling Laboratory "E. Costa" of the Department of Chemistry, Life Sciences and Environmental Sustainability, at the University of Parma, Italy (Fig. 3.10).

Figure 3-10 *The equipment's photograph of Analogue Modelling Laboratory "E. Costa" of the Department of Chemistry, Life Sciences and Environmental Sustainability, at the University of Parma, Italy*

The sandbox has unconstrained boundaries and dimensions of approximately 0.55×0.18×0.03 m. The dimensions of the whole experimental setup is sufficiently large to ensure that a large part of the model escapes boundary effects. The model apparatus consists of a table of 150.0x80.0x80.0 cm (height, length, width) equipped with two computer-controlled motors, with a structured light scanning laser and digital cameras. In our experiments, one camera, fixed at the top of the system, was dedicated to take top-view pictures at a regular time interval. The other camera was free to move and used to take pictures of cross sections of the model (Fig.3.10). The time-lapse photographing recorded the evolution of the surface topography of the model. This was a NIKON-D5200 digital camera which was capturing images every 5 minutes – constant distance of displacement – with 6000x4000 resolution. This resolution enabled us to visualize the progressive displacement and rotations during the physical experiments and the structured-light 3D scanning provided elevation data for every 5mm of fault displacement. The setup and dimensions of the model are shown in Fig. 3.11. The aim of the experiments was to investigate surface dynamics and kinematics of the western part of the NAF in brittle and ductile regimes. A set of thirteen experiments was performed to test different model configurations and observe how these variations were representing the natural case. Eleven of these thirteen experiments were successful. In this thesis, the results are presented from the two-most representative experiments, which are described in Chapter 4 MAR-02 and Chapter 5 MAR-12. Complete overview of models is presented in the Appendix I.

All experiments were performed with a basal geometry that consisted of a 1 mm-thick table free to move on top of the plexiglass table which was purposely cut to simulate the fault (Fig. 3.11a). Some experiments also were performed with a second overlaying 1 mm-thick plexiglass table to simulate multiple faults (such as the northern and southern strand). These moving plates were shaped with several segments characterised by different orientations following the models presented in Chapter 2. MAR-02 and MAR-12, the most successful experiments, simulate the geometry described in section 2.2: two segments at the right and left end parallel to each other, connected by two middle segments with different orientations (Fig. 3.12a). From right to left the first segment was 140 mm-long forming an angle of 22º from the longitudinal trace, followed by a 90 mm-long segment at 10º (Fig. 3.12a). A velocity discontinuity was imposed at the base of the model by moving the purposely cut plate so that a dextral displacement was applied to the base of the model. The movement applied to the purpose-cut table was parallel to the right and left end segments, while the two middle segments, because of their orientation, resulted in a releasing and adjacent, smaller, restraining segments that are separated by three fault bends.

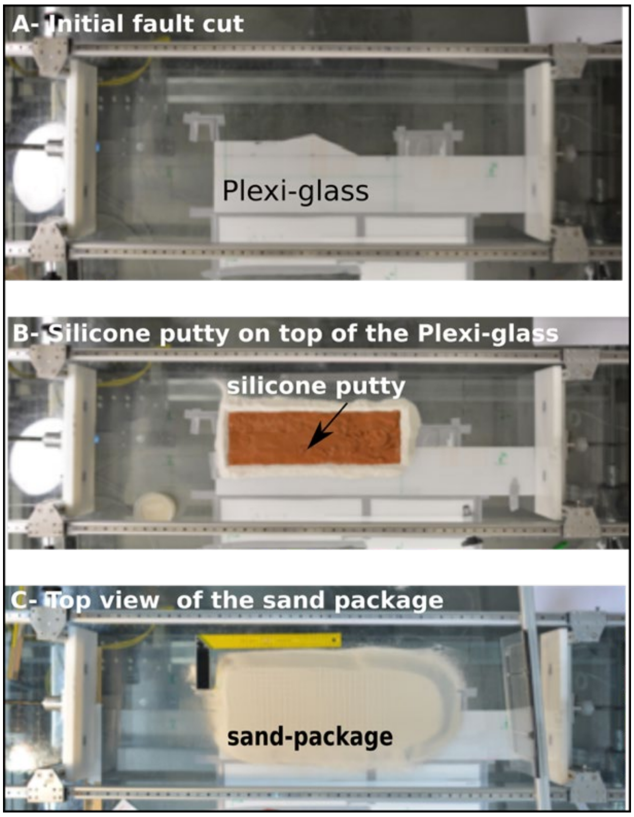

Figure 3-11 *The preparation of the experiemental setup before deformation a) the top view of the experimental setup before put the silicone. The plexiglass was cut regarding the fault geometry. B) the view of silicone putty on the plexiglass sheet. Silicone putty was put on the plexiglass and waited for 24 h to provide the equal thicknesses for the part area. c) The top view of the sand package.*

All models comprise an upper layer of sand and a lower layer of silicone with varying thicknesses (see in Table 1, Appendix I). In the most successful experiment MAR-02 and MAR-12 the viscous lower crust was simulated by a 2 mm-thick silicone layer, while the brittle upper crust was simulated with a 15 mm-thick sand pack consisting of both coloured and white sand layers to identify and quantify deformation in cross-section (Fig. 3.12b). They were deformed without the addition of syn-kinematic sediments in order to allow continuous monitoring of the surface deformation.

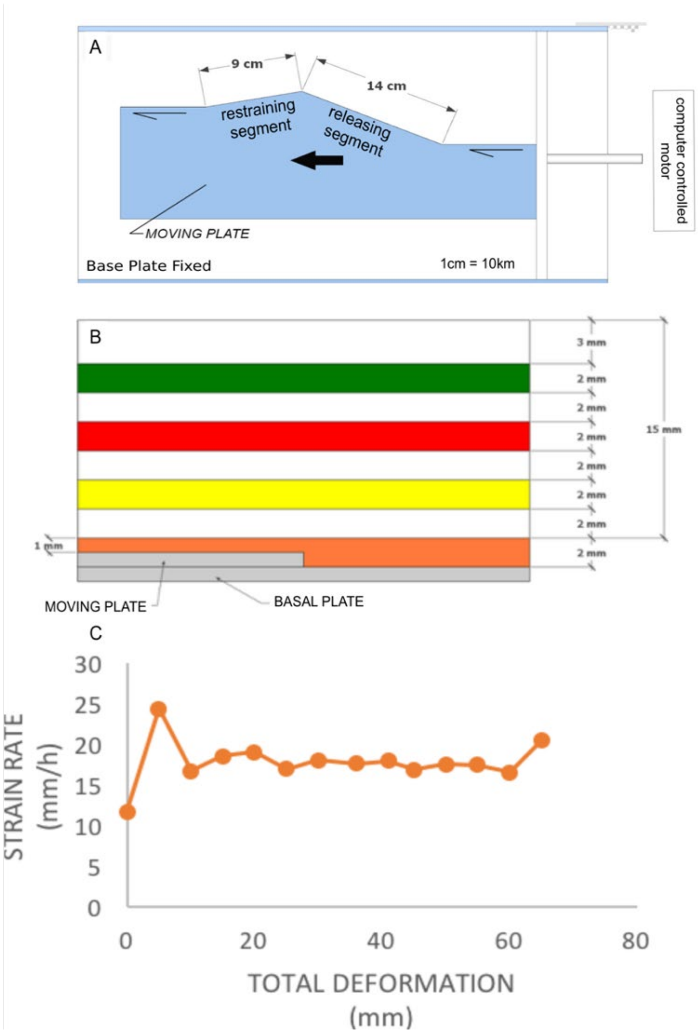

Figure 3-12 *The schematic view of the experimental setup of MAR-02 and MAR-11 and observed rates during the experiement a) the experimental setup plan; initial fault-cut plan of the moving plate. B) Stratigraphy of the model setup. Orange layer represents the silicone putty for lower crust, coloured layers represent the sand package for upper crust. Grey layers represent the base plate and moving plate. c) The strain rate during the deformation. Total deformation was 70-mm.*

MAR-02 and MAR-12 were deformed by applying a constant velocity to the mobile plate through a computer-controlled motor that generates dextral shearing. The velocity applied to the mobile plate consisted of horizontal translation at a constant displacement rate (v = 20 mm/h), for a total displacement of 70 mm for MAR-02 (Fig. 3.12c) and 6 mm for MAR-12. For the brittle–ductile ratio used in our rheological profile, this displacement rate is sufficiently fast so that deformation was concentrated above the velocity discontinuity and no deformation occurred near the walls of the models.

At the end of the experiments, the motor or motors were stopped, models were wetted, and after 24 h (necessary to create cohesion between sand particles) they were cut into cross-sections that expose the internal deformation structures of these models (e.g. Sokoutis et al., 2005).

3.4 Limitations of the analogue models

This method has several known limitations, despite their many advantages and the fascinating insights that laboratory experiments have useful tools over the years. Some of these were briefly mentioned above. Here we discuss these in more depth with specific references to our experiments.

Most experiments, ours included, consider a simplified rheology and geometry in comparison to more heterogeneous natural conditions. We use analogue materials containing two different, but homogeneous rheology, while in nature rocks show variable rheological properties at different depths and locations (e.g. Ranalli, 1997). The laboratory-scale of the models (our model was 55 cm long, 18 cm wide - the sandpackage size) also means that the models must be reasonably simple, i.e. it is tough to build the lithospheric heterogeneities, especially complex structures (Morley, 1999), especially without interference with model edge-effects. Various factors cannot be incorporated into the experiments. These include heat transfer and isostatic variations, effects of pore pressure, and mineral phase changes (Koyi 1997). One of the other limitations in analogue experiments is their boundary conditions. In spite of all efforts, it is difficult to avoid that boundary conditions at the base and sides of the model have some influence on deformation within sandboxes. It is needed to construct physical models with appropriate scale to make certain that the boundary conditions in the model actually imitate those in nature (i.e. McClay K.R., 1996).

It is worth mentioning that the aim of analogue modelling should not be to exactly replicate nature, but to provide better insights into the mechanics, kinematics, and geometry of natural tectonic processes. All input parameters must be carefully considered for their relation to natural processes since some input parameters may not have any similarity to natural conditions.

In our case we were interested in building models that could explore how the strike-slip fault geometry will shape the subsidence and uplift patterns in adjacent regions —we do not attempt to reproduce all details of the tectonic patterns observed in the Sea of Marmara.

3.5 Particle Image Velocimetry (PIV) Analysis

Particle Image Velocimetry (PIV) can be used to accurately measure the surface velocity/displacement fields of experimental deformation systems. It is applied in this thesis for high-resolution 2D strain monitoring in analogue sandbox experiments. PIV is an optical, non-intrusive method for visualisation of the non-linear flow and deformation by optical image correlation techniques. In granular-flow experiments, optical image correlation enables the spatial resolution of the displacement data in the particles of the sand material (White et al., 2001). These capabilities make PIV an ideal method for high-resolution 2-D and 3-D strain monitoring in sandbox experiments (Adam et al., 2004). The core of the PIV analysis is based on the following individual image elements (image patterns that consist of a specific arrangement of individual pixels) given the interval between the two images (Thielicke and Stamhuis, 2014) (Fig. 3.13a).

Our experiments were monitored using a camera (NIKON-D5200) above the model. This camera acquired a top view sequence of high-resolution images (with 6000x4000 resolution, 8 bits, 256 colour levels). These images were taken at an interval of 16 mm displacement during progressive deformation. Fine resolution of results requires small interrogation windows for the cross-correlation. We used interrogation areas (small sub-samples of the images) of pairs of images in 64x64 and 32x32 pixel subregions (see Fig. 3.13a, b). We derived the best-fit particle displacement in the interrogation areas with the cross-correlation method implemented in the free MATLAB-based PIV-Lab Software package (Thielicke and Stamhuis, 2014, Fig. 3.13 b, c, d, e; Fig. 3.14). This software lets us calculate the incremental displacement vector field, between the time-steps, through sequential photos, as well as the local displacement components or derived values such as the strain tensor components and the corresponding strain rates (Fig.3.14).

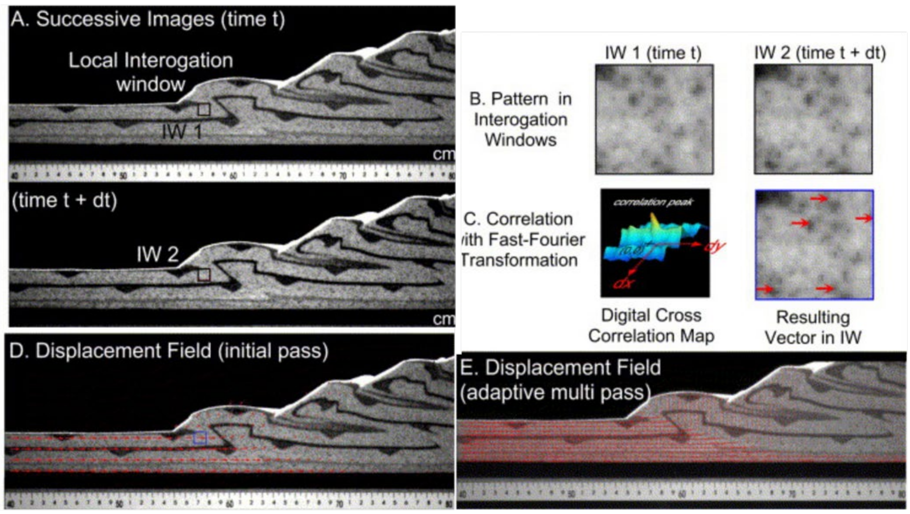

Figure 3-13 *The scheme of the Optical Image Correlation method principles by Adam et al. (2005). a) successive digital images with interrogation window, IW 1, IW 2 b) particle pattern in interrogation window with shift in time c) local displacement vector (dx, dy) by cross-correlation with Fast -Fourier Transformation d) complete displacement field from single pass correlation e) final displacement field from adaptive multi-pass cross-correlation*

From these, we use MATLAB (the MATLAB code we used is in Chapter 4, Supplementary Material II), to compute the incremental shear rates, angular velocity rates and areal strains (Fig. 3.15d). In particular, we determine the velocity gradient matrix by measuring the derivatives of the u and v velocity components in the x and y directions, respectively, namely $\partial u/\partial x, \partial u/$

∂y; $\partial v/\partial x$, and $\partial v/\partial y$, with the velocity gradient tensor being used to compute incremental strain tensors. The incremental horizontal shear rate is approximated as the velocity gradient perpendicular to the velocity discontinuity applied at the base of the model ($\partial u/\partial y$).

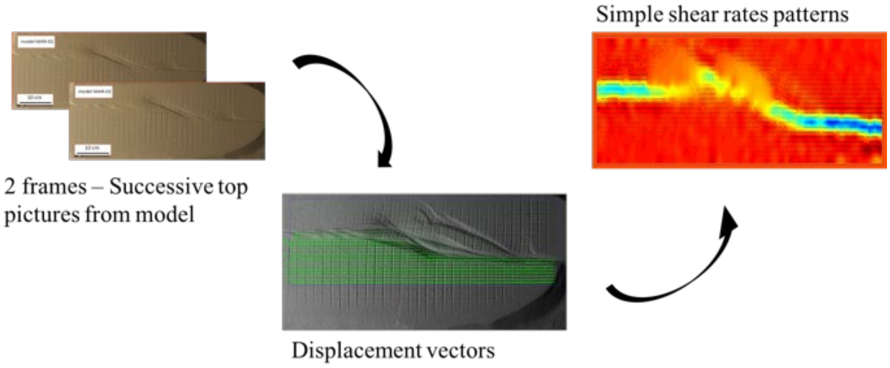

Figure 3-14 *The steps for PIV Analysis in MATLAB-based PIV-Lab Software, given in this thesis. Successive top pictures are given to the PIV-Lab Software package as input data. Displacement vectors are obtained as output data. The matlab code (see in Chapter 4, Supplementary material I) derives the strain patterns.*

The angular velocity was calculated from the curl of the velocity field; it shows the shear accommodated by faults in any orientation.

The incremental areal strain is the sum of the diagonal components of the strain tensor ($Exx + Eyy$):

Equation 3.2

$$Exx + Eyy = \partial u/\partial x + \partial v/\partial y$$

During the experiments, the structured-light 3D scanning provided elevation data for every 5mm of fault displacement.

The incremental rate of topographic change was calculated by subtracting the measured topography at time n-1 from the topography at time n, corrected for the surface advective displacement that occurred between times n-1 and n. Specifically, we determined the material derivative of topography, i.e. the change in topography over a time-step that follows surface motions. To do this, we measured the relief on the fine mesh of points available for each topographic measurement, and used an interpolation of the velocity field determined from the coarser mesh of PIV sampling subregions to backtrack each sample point on the fine mesh to where it started at the end of the previous time step. The difference between these measurements is the change in relief "felt" by this surface point over the time step. Computed rates of incremental topographic changes were then related to the incremental strain patterns in order to understand how relief is generated. Shear rate maps show how much shear deformation took place during each step of the model, while areal strain maps show the rates of extension and compression in each area. In general, areal strain maps display higher noise than shear strain maps.

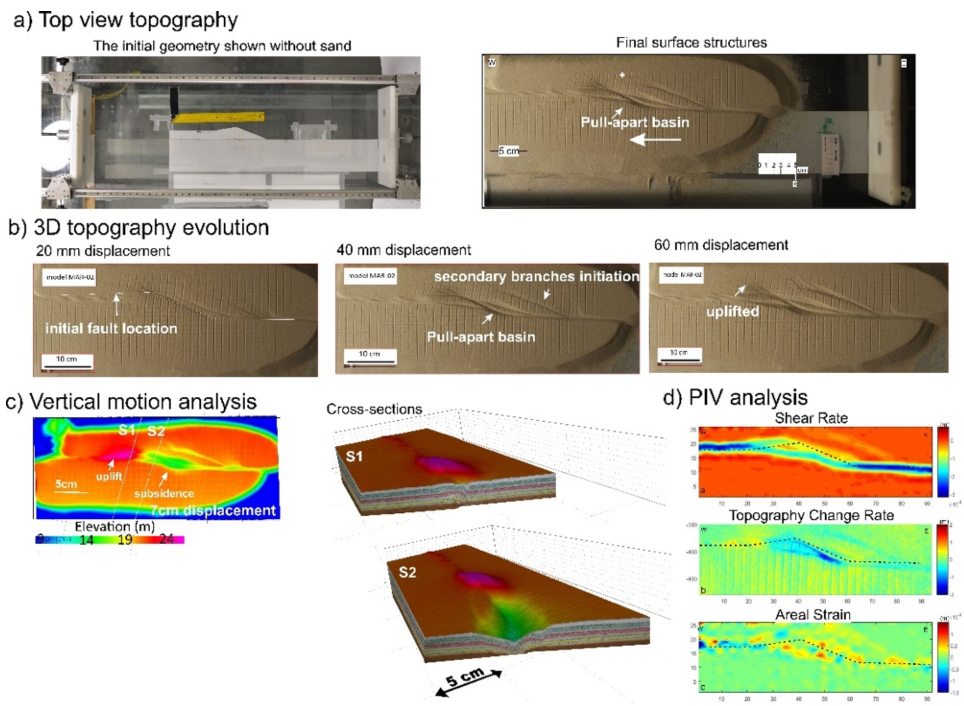

Figure 3-15 *Techniques, showing the analysis of releasing/restraining bend pairs of models (Model MAR2- in Appendix). (a) Top view of model setup, the view of initial fault geometry and final surface structures (b) Top view time-lapse photography in 20 mm, 40 mm, 60 mm (c) Vertical displacement derived from the Scan data and cross-sections (d) PIV analysis: Shear rate on the top, Topography change rate in the middle, areal strain in bottom, with initial state of fault*

3.6 Strain Analysis derived from GPS

"Tectonic geodesy uses measurements of changes in the position of a network of points on Earth's surface to study motion and deformation of the Earth. These motions mainly result from plate motions, slip on active faults (including earthquakes) …. " (J. Freymueller, Encyclopedia of Solid Earth Geophysics). In this thesis we used geodetic datasets, in particular Global Positioning System (GPS) measurements, to map variations in strain rate over the region of the Sea of Marmara in western Anatolia. We also calculated dilation and the second invariant rates of the major faults in the area.

GPS campaigns have been carried out in the Sea of Marmara region since 1988 (Barka and Kadinsky-Cade, 1988). They showed a complex system of restraining and releasing bends of structures in and around the Sea of Marmara.

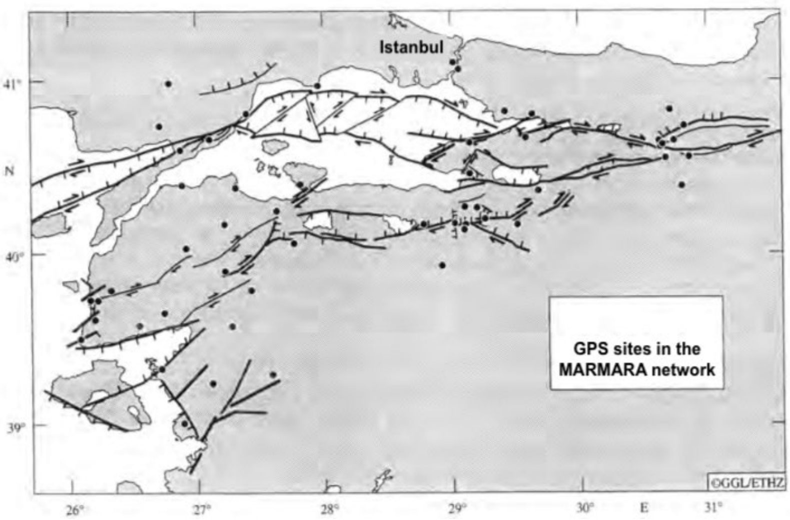

Figure 3-16 *Distribution of sites of the ETH GPS network. Major tectonic structures after Barka and Kadinsky-Cade (1988).*

Recent studies have focused on using the Global Positioning System (GPS) to monitor surface deformation (Straub et al., 1997, Kahle et al., 2000; McClusky et al., 2000, Flerit et al., 2003, 2004) in the Marmara region. The combined GPS-strain and seismicity data gives to present more reliable estimates of earthquake hazard (Straub et al., 1997; Kahle et al., 2000;

Westerhaus et al., 2002; Ayhan et al., 2002; Oncel and Wilson, 2004; Bulut et al., 2019).

Straub et al., 1997 used a dense network of 52 GPS stations to determine the velocity field and strain rate patterns for the western end of the NAF. They compared the results with the neo-tectonic data to reveal that most of the deformation occurs along a relatively narrow E-W oriented zone in the Sea of Marmara region. This E-W belt extends from the single fault trace of the NAFZ through the Gulf of lzmit, the Marmara Sea, the Sarkoy region, and the Gulf of Saros into the North Aegean Trough (NAT) (Fig. 3.17). Later, Kahle et al. (2000) determined the crustal strain rate field for the entire Eastern Mediterranean on a regional scale. Kahle pointed out that strain rates reach 50 nstrain/yr in Anatolia, whereas the rate is < 20 nstrain/yr in the Aegean and Marmara region. Moreover, they showed the NAFZ dextral strike-slip fault zone reaches rates of up to 170 nstrain/yr. This holds true also for the Izmit area where the August 17, 1999, earthquake occurred.

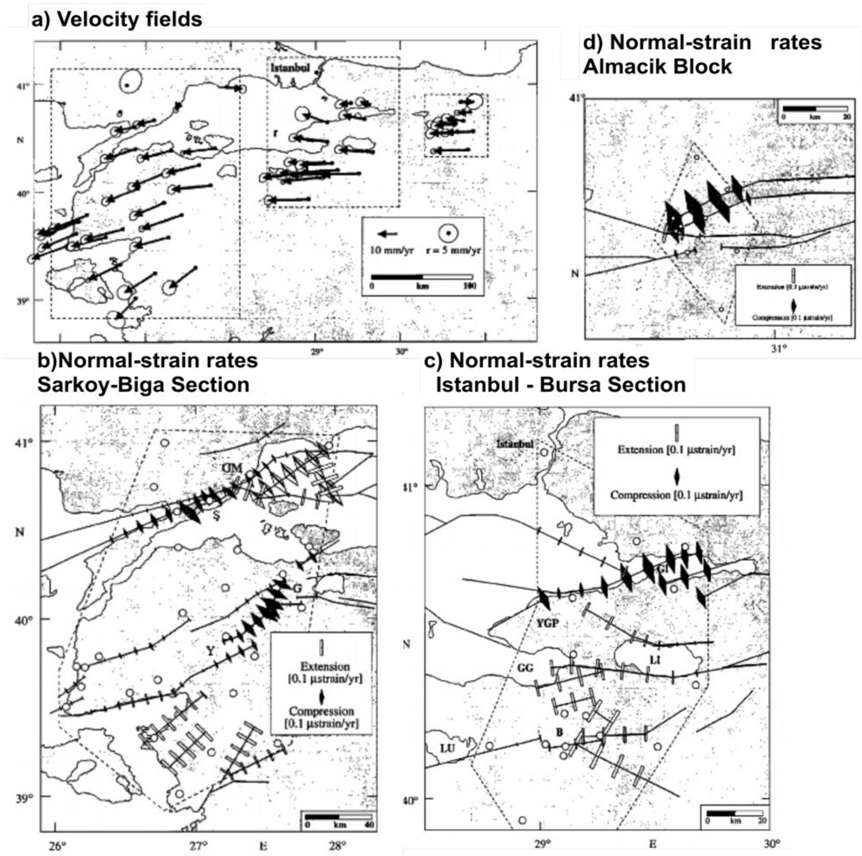

Figure 3-17 *Normal strain rates for western end of the NAF after Straub et al. (1997). A) Velocity field derived from the GPS campaigns (1990, 1992, 1994 and 1996). b) Normal strain rates projected onto major fault structures of the Sarkoy-Biga section. c) Normal strain rates projected onto major fault structures of the Istanbul-Bursa section. d) Normal strain rates projected onto major fault structures of the Mudurnu/Akyazi section. The thick black line represent the extension (0.1 nstrain/yr), while thin lines represent the compression (0.1 nstrain/yr).*

Most recently, McClusky et al. (2000) integrated GPS data from a number of campaigns to providing a basis for us to deduce a detailed strain rate field in terms of principal axes and values as well as components of the strain rate tensor along the major faults. McClusky et al. (2000) showed that the western NAF and North Aegean Trough (NAT) are dominantly strike-slip and extensional, while west of Turkey, the SE Aegean zone has dominent N-S extension (Fig. 3.18).

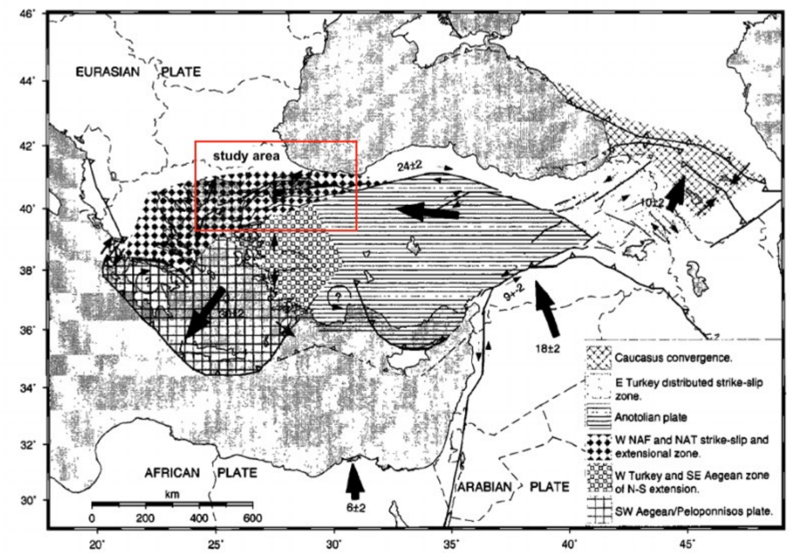

Figure 3-18 *shows the principal result of the study by McClusky et al., 2002. The rectangular in red shows the study area of this thesis. The western NAF and NAT are under the deformation of strike slip and extensional zone.*

According to Ayhan et al. (2002), the maximum shear-strain rate reaches 220 nstrain/yr in the Sea of Marmara where the deformation zone extends for 110 km. The largest shear-strain rate accumulation is along the northern branch of the NAF (Fig. 3.19). GPS measurements were also used to investigate the interseismic strain accumulation pattern in the Sea of Marmara region (Ayhan et al. 2002). This strain field analysis showed that the Sea of Marmara region is influenced by two forcing factors — the westward extrusion of the Anatolian plate and the north-south extension of the Aegean block (Fig. 3.20). Although these studies showed the substantial Aegean extension responsible for the finite deformation of the region of the Sea of Marmara, there is no overall extension perpendicular to the slip direction between the north of the Sea of Marmara and about 100 km to the south of it (Flerit et al. 2003). Faulting in the region can still have been influenced by the Aegean stress field. The extension is enhanced to the south of the Sea of Marmara, while slip partitioning is responsible of the decreasing amount of extension to the north (Flerit et al., 2003).

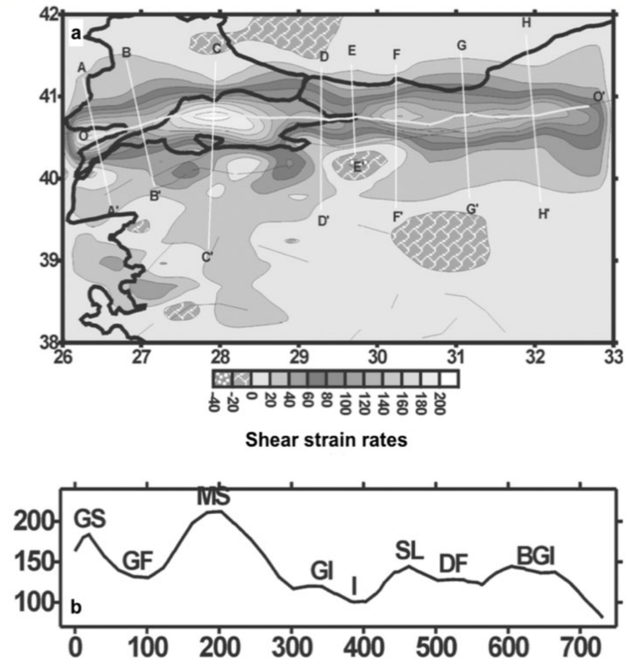

Figure 3-19 *Strain field analysis by Ayhan et al., 2002. Shear strain rates are in strain/year (1.0x 10^9 rad/yr) from Ayhan et al., 2002. Positive and negative shear-strain rates correspond to dextral strike slip and sinistral strike slip for transform faulting, respectively. The maximum shear rates seem to be in Sea of Marmara region.*

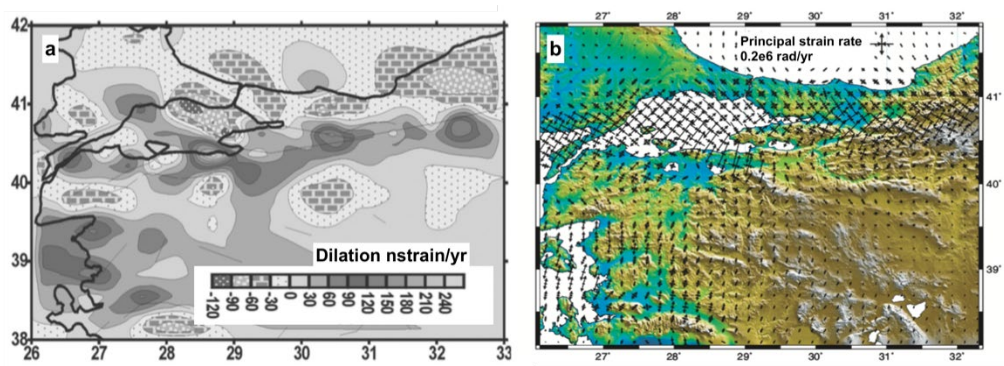

Figure 3-20 *The interaction between Anatolian block and the Aegean system, principal strain analysis by Ayhan et al., 2002. A) Dilation rates in nstrain/yr. Complexity of the NAF is indicated by local extensional and compressional dilatation areas along strike of the northern branch in the Sea of Marmara. The effect of north–south extension of the Aegean Block is recognized clearly. B) Principal strain rates. Arrows directed outside indicate the extension, inside directed arrows show to compression.*

Studies of earthquakes and active deformation have also shown the kinematic relations between dextral shear along the North Anatolian Fault and the back-arc extension in the Aegean (McClusky et al., 2000; Flerit et al., 2004). Flerit et al. (2004) suggests that the back-arc extension associated with the Hellenic arc-pull has been responsible by the development of the stretching in Aegean lithosphere. This results in the propagation of the NAF into the elastically strained Anatolian lithosphere.

Bulut et al. (2019) combined GPS measurements from 16 different published catalogues to determine a slip-deficit model for the Sea of Marmara. England et al. (2016) introduced a study that revealed the relationship between strain rates and the mean viscosity of the lithosphere. They pointed out a litospheric weaker zone than rest of the area which follows the NAF and its extension in the Aegean Sea where the strain rates are very high.

3.6.1 GPS Velocity Measurements in Western Anatolia used in this Thesis

In this thesis, we used GPS data to calculate specific strain rate fields in terms of principal axes, values, and components of the strain rate tensor. Several studies have computed strain rates from GPS data acquired in the area between 1988 and 1997, using a network that had a relatively poor density of stations (Straub et al., 1997; Kahle et al., 1998, 1999, 2000).

Our reference data sets were compiled from Bulut et al. (2019) and Ayhan et al. (2002) (Figure 3.21; Table 1 in Appendix II). We combined these two data sets that were compiled for different regions (Fig. 21). Ayhan compiled a catalogue from local and national networks within Turkey from 1988 to 1999 until the event of Izmit 1999 EQ. Bulut compiled a catalogue from previous measurements of TUSAGA, TUSAGA-Aktif, TUTGA, Ayhan et al. (2002), Reilinger et al. (2006), Aktuğ et al. (2009), Reilinger and McClusky (2011), Aktuğ et al. (2013), Ergintav et al. (2014) and Özdemir (2016). Bulut's study is the most recent study that has been made in the region of interest for this thesis. Therefore, we used Bulut's (denser) catalogue for the region of the Sea of Marmara and used Ayhan's study for Aegean stations.

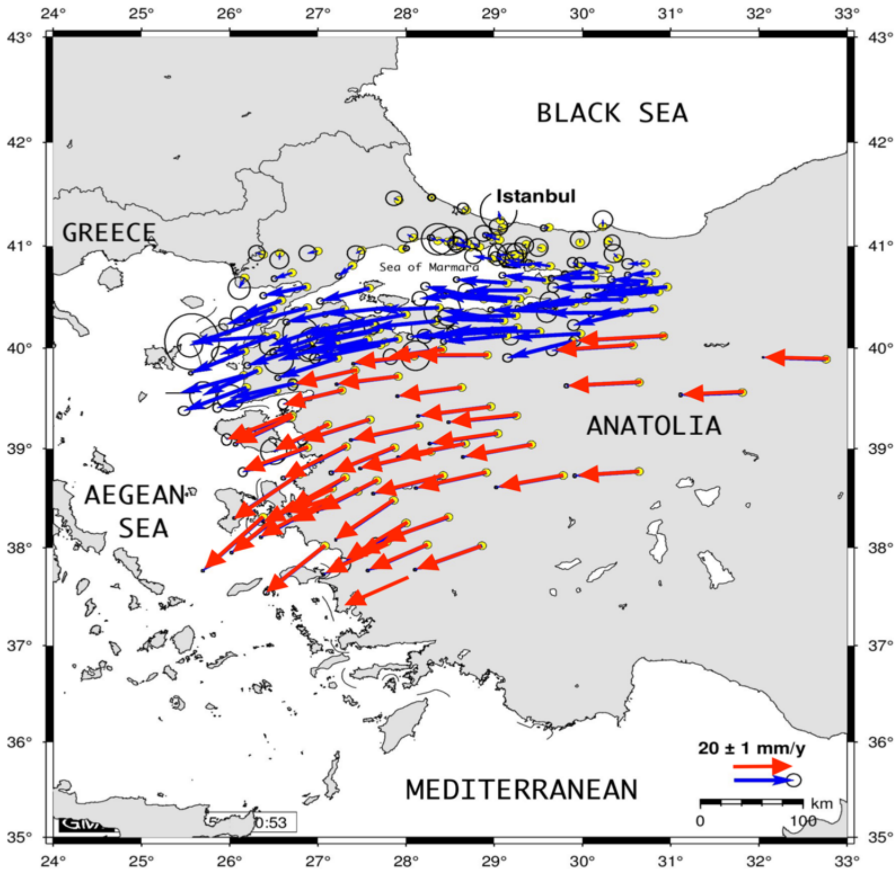

Figure 3-21 *Combined velocity field in the north western Turkey relative to a Europe-fixed reference frame, used in this thesis. They based on GPS results from Bulut et al. (2019) in blue arrows and Ayhan et al. (2002) in red arrows. Yellow dots represent the stations of the study area.*

GPS velocities are determined for total 156 stations in the study area (Fig.3.21). These velocities are given in Table 1 in Appendix II.

3.6.2 Method for Strain Rate Determination

We derived the strain rate field using the open-source software StrainTool: A software package to estimate strain tensor parameters; Dimitros et al. (2019) (Version v1.0; http://doi.org/10.5281/zenodo.3266398). This program applies the algorithm VISR (Velocity Interpolation for Strain Rate; Shen et al., 2015). This is a standard method to calculate strain rates that is based on the discretization of the area to be investigated into triangles (e.g. Delauney triangulation), followed by the computation of the internal strain rate for each triangle (see e.g. Frank, 1966; Shen et al.,1996 ; Cai and Grafarend,2007; Wdowinski et al.,2007).

The steps of this procedure are:

1. Delauney triangulation is used to divide the network into a set of triangles.
2. The average strain rate in each triangle is then determined from the three stations at the vertices of that triangle (see figure below).

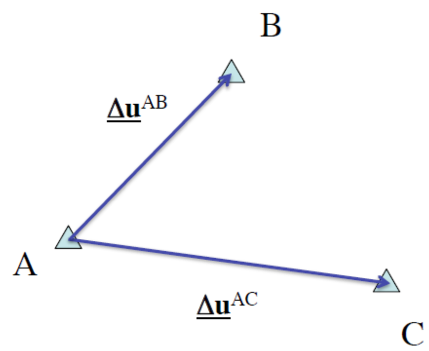

With $\underline{\Delta u}$ being the angular velocity vectors

3. Strain rates are then smoothed over several triangles using a continuous interpolation function with a degree of smoothing that depends on the size of each triangle.

This method requires no assumption on the stationarity of the deformation field and does not assume that all data must have the same errors (Shen et al., 2015). The technique solves for horizontal strain rate components with the assumption that all rotations are about a vertical axis.

3.6.3 Idealised Tests for Edge Effects

We tested the StrainTool code to learn how its smoothing assumptions would affect the solution near the boundaries of the dataset where edge artefacts

are likely to form. Our tests created an idealized velocity distribution with linearly increasing velocities in a single direction and no velocity in the other horizontal direction. The test was done for both E-W and N-S directions (Fig. 3.22). These tests (see in Chapter 6 Supplementary Material I) showed that stretching and shearing occurred uniformly near the edges of the idealized region, and also showed that the method did not return strain rates to the edges of the region where observations were present. This indicates that there is an attempt in this algorithm to minimize its edge effects (Fig. 3.22).
In the test the code was used to determine strain tensor components for the region between 24°E-33°E and 35°N-43°N. Velocity components were specified on a regular grid with 0.1°-spacing. The program was then asked to smooth the measurements over cells of size 0.5° and to estimate one strain rate tensor at each cell centre.

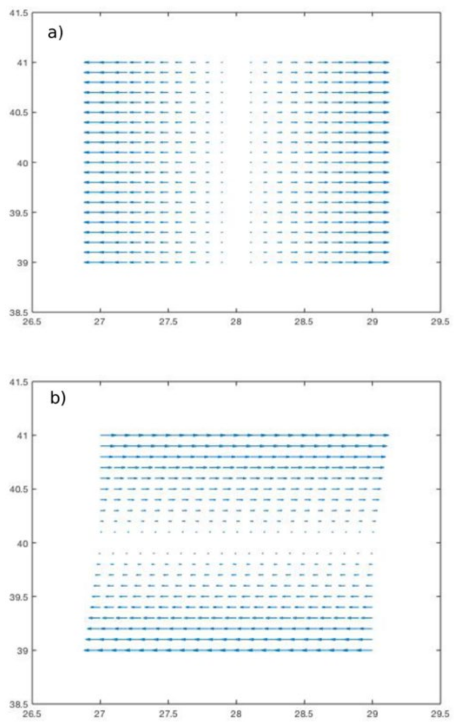

Figure 3-22 *The results for the testing of edge effects which the STRAINTOOL (https://github.com/DSOlab/StrainTool) results in. a) the uniform stretching b)uniform shearing.*

Chapter 4: The evolution of restraining and releasing bend pairs: analogue modelling investigation and application to the Sea of Marmara

S. Bulkan[1], P. Henry[2], P. Vannucchi[1,3], F. Storti[4], C. Cavozzi[4], J. P Morgan[1,5].

[1] Royal Holloway, University of London, Earth Sciences Department, Egham, UK.

[2] CEREGE, CNRS-Aix Marseille Université, Marseille, France

[3] Dipartimento di Scienze della Terra, Universita' degli Studi di Firenze, Via La Pira, 4, Firenze, Italy

[4] NEXT – Natural and EXperimental Tectonics research group, Department of Chemistry, Life Sciences and Environmental Sustainability, University of Parma, Italy

[5] Department of Ocean Science and Engineering, SUSTech, Shenzhen, China

The following chapter is a co-authored manuscript submitted to the Journal of Tectonics.

Key Points:

- Reproduces and explores, by analogue modelling, the effect of a releasing-restraining bend pair geometry for the western part of the NAF.
- Presents crustal strain patterns and associated topographic changes obtained from analogue model PIV Analysis.
- Experimental results are compared with the actual structural/topographic evolution of the Sea of Marmara region.

In spite of many specific studies focussing on the Sea of Marmara segment of the North Anatolian Fault (NAF), its deformation and stress accumulation pattern remain difficult to understand. In part this is due to the complexity of the transform fault system which here combines a releasing and restraining bend. In this study, we use analogue modelling to reproduce and monitor the strain patterns across a releasing and restraining bend pair. We also compare the strain evolution with the evolution of topographic changes.
The experiments reveal how the master right-lateral strike-slip fault system and newly formed fault zones change their geometry as displacement accumulates across a releasing and restraining bend pair. We find that the master shear zone develops from a single to a multi-branch fault system, with different branches active and dominant at different times. Comparison with the tectonic setting of the Sea of Marmara suggests that the western portion of the basin may be characterized by a fault shortcut associated with both a compressional regime and uplift of the Ganos Mountain.

4.1 Introduction

Continental transform faults can vary from single, pure strike-slip shear zones to complex domains with branching, bending or oversteps that partition and diffuse tectonic deformation (LePichon et al., 2001), while often creating adjacent releasing and restraining bends. In these complex systems current debate focuses on: i) the evolution of strain localization in different fault segments over time; ii) which fault segments tend to remain active over long periods of time; iii) to what extent fault localization controls the development of subsidence or uplift.

Here we use scaled sandbox analogue modelling to address the problem of how strain and surface relief develop during the evolution of a major fault system that contains adjacent restraining and releasing bends. We also apply this model to explore the potential evolution of the North Anatolian Fault (NAF) in the Sea of Marmara. In the simplified view taken here, we idealise the geometry of the Sea of Marmara as a releasing bend adjacent to the Ganos segment to the west, which is considered to be a restraining bend (Mann, 2007) (Fig. 4.1). We use a crustal master strike-slip fault system geometry derived from onshore and offshore tectonic maps (e.g. Armijo et al., 2002; Le Pichon et al., 2003; 2015; Becel et al., 2010; Grall et al., 2012, 2013).

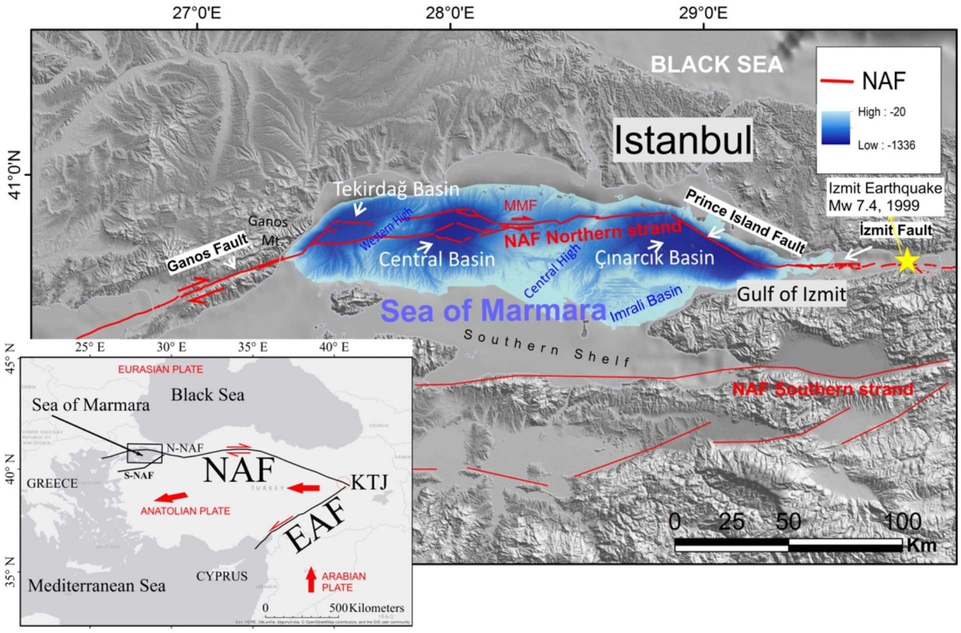

Figure 4-1 *Tectonic map of the North Anatolian Fault in the Sea of Marmara region (simplified from Grall et al., 2013 et al., Gasperini et al., 2011). The inset shows the tectonic setting of the Anatolian plate. Plate motions are with respect to the Eurasian plate. KTJ is the Karliova triple Junction. EAF is the East Anatolian Fault.This natural system motivates the geometry chosen for the analogue experiments in this study. NAF Northern strand represents the NAF-N in the text. NAF Southern strand represents the NAF-S in the text.*

Numerous studies have focused on the geology of the Sea of Marmara, the geometry of its basin-boundary faults from the Izmit to the Ganos segments (Fig. 4.1) (Armijo et al., 1999, 2005; LePichon et al., 2001; Imren et al., 2001; Seeber et al.,2004, 2006; Okay et al., 2004; Carton et al., 2007; Laigle et al., 2008; Becel et al., 2010; Gasperini et al., 2011; Sorlien, et al.,2012; Kurt et al., 2013; Grall et al., 2012), and on slip rates over different time scales across different fault segments (Armijo et al., 2002; Flerit et al., 2003; Ergintav et al., 2009; Gasperini et al., 2011; Reilinger and McClusky, 2011; Grall et al., 2013; Akbayram et al., 2016; Hussain et al., 2016). Although faults in the Sea of Marmara have been thoroughly mapped, their overall tectonic setting is still controversial. Three model scenarios have been proposed (Fig. 4.2): 1) the pull-apart model (Armijo, et al., 1999, 2002), 2) the en-echelon fault segment model (Okay et al., 2000, 2004), and 3) the single throughgoing fault (LePichon et al., 2001, 2014; Sengor et al., 2014; Seeber et al., 2004, 2006, 2010; Kurt et al., 2013). A previous numerical model used to test these three scenarios found that a series of pull-apart basins along with a master strike-slip fault system could best reproduce the observed morphology of the region (Muller and Aydin, 2005; Hergert and Heidbach, 2011), including the reproduction of vertical structural offsets within the Sea of Marmara.

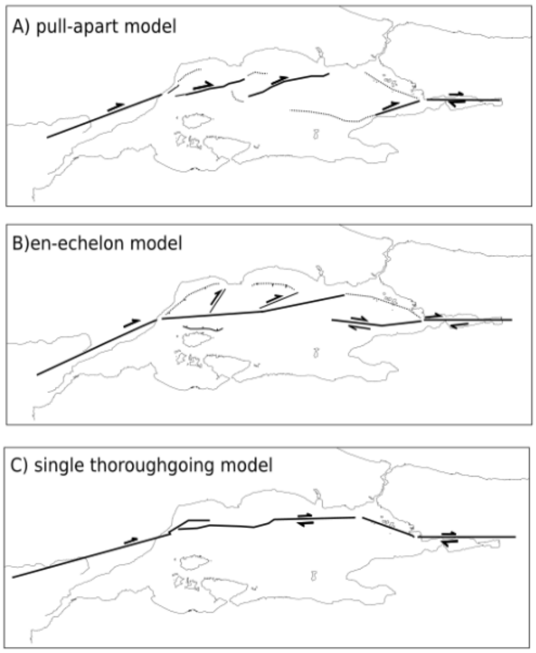

Figure 4-2 *Simplified, tectonic models proposed for the tectonic evolution of the Sea of Marmara. a) the pull-apart model (Armijo, et al., 1999, 2002), b) the en-echelon fault segment model (Okay et al., 2000, 2004. c) the single thoroughgoing fault (LePichon et al., 2001, 2003; Seeber et al., 2004).*

Previous scaled sandbox models have investigated the evolution of strike-slip fault systems in different kinematic environments, with and without crustal heterogeneities, with their main goal being to reproduce local pull-apart basin or pop-up geometries (McClay and Dooley, 1995; Dooley and McClay, 1997; Rahe el al., 1998; Sims et al., 1999; McClay and Bonora, 2001; Dooley et al., 2004; Wu et al., 2009; Dooley et al., 2012; Sugan et al., 2014), or specific evolutionary pathways (e.g. D'Adda et al., 2016). Analogue models have been used to study fault propagation and strain localization and accumulation (Adam et al., 2002; Adam et al., 2005; Dotare et al., 2016; Hatem et al., 2017).

The formation of strike-slip bends from stepovers and their topographic evolution has also been previously investigated with analogue models (Cooke et al., 2013; McClay and Bonora, 2001; Wu et al., 2009, Toeneboehn et al., 2018).

4.2 Methods

Here we combine scaled analogue modelling with Particle Image Velocimetry (PIV) analysis (Adam et al., 2005) to explore the geometry, topography, and shear strain patterns associated with the propagation and distribution of deformation along a major fault strand with adjacent releasing and restraining bends. A set of ten experiments was performed with varied model configurations. Here we present results from the most representative ones.

4.2.1 Model Setup

The experimental apparatus consisted of a sandbox with a 250 x 100 cm glass basal plate, equipped with two computer-controlled motors, and a "structured light scanner" to monitor the topographic surface of the model with a resolution of 0.71 mm in the x and y directions. Structured light scanning is also known as "point cloud" mapping. In structured light scanning a pattern, e.g. a regular grid of dots, is projected onto the surface to be scanned. The distortion of this grid is then used to determine surface relief. This provides an effective tool to comprehensively describe the vertical evolution of the model, i.e the uplift and subsidence of the system. It allows quantitative measurements to be easily made with relatively high precision (e.g. Nestola et al., 2013; D'Adda et al., 2016). We use an overhead NIKON-D5200 digital camera to record the model evolution at 6000x4000 pixel resolution. In this experimental setup, overhead camera captured images and structured light scanning provided elevation data for every 5 minutes of model deformation, i.e. for every 1.6 mm of displacement along the basal fault. Experiments were performed using a 1 mm-thick Plexiglas mobile plate that was cut to simulate a releasing-restraining band pair. This geometry approximates the geometry of the northern strand of the NAF at the Sea of Marmara (Fig 4.3). Dextral shear was imposed to the mobile plate by translating it at a constant displacement rate of 2 cm/h, with a total displacement of 5 cm in each experiment. The scale factor of the models was 1×10^{-6} (1cm ⇔ 10km), which models the 15 km-thick upper crust in the Sea of Marmara region (Kende et al., 2017) as a 1.5 cm-thick sandpack. A grid with 1x1 cm squares was pressed on the surface of the sandpack to better monitor surface fault locations and the progression of surface displacement.

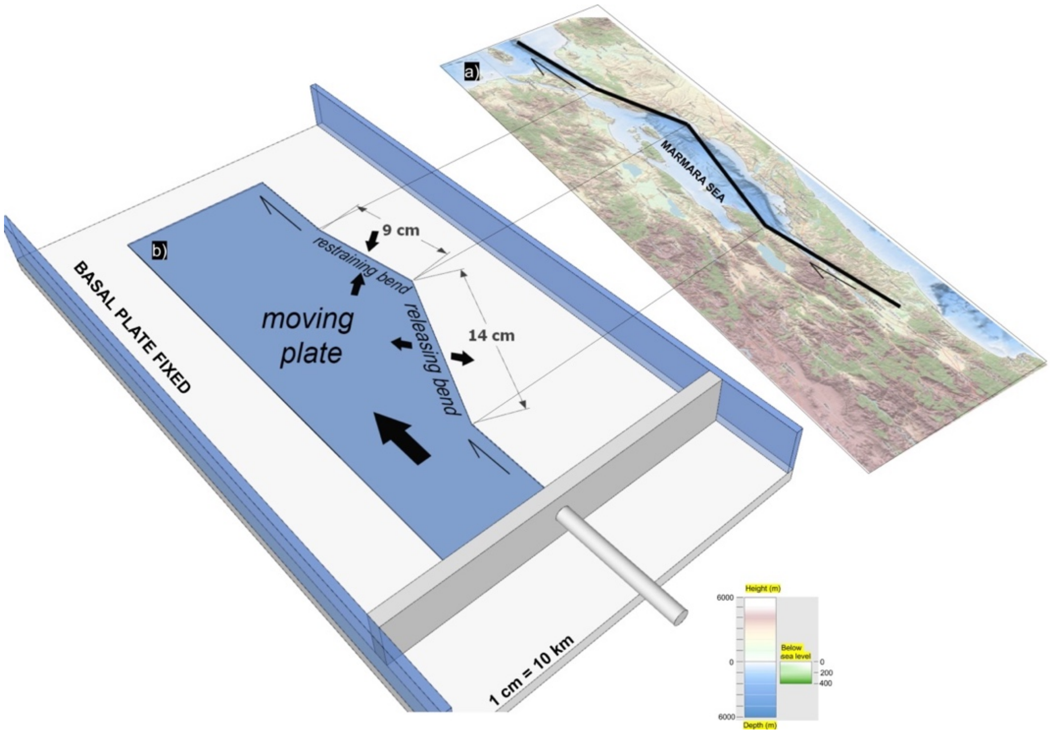

Figure 4-3 *a) Simplified fault map trace used to produce the Plexiglas basal plate. Bathymetric metadata and Digital Terrain Model data products are derived from the EMODnet Bathymetry portal - http://www.emodnet-bathymetry.eu. (b) Setup of sand boxexperiments, initial pre-cut fault setup with its analogue scaled lengths in 3d perspective. Model scale is 1cm per 10 km. The moving plate was placed on a fixed basal plate.*

4.2.2 Materials

In the undeformed experimental multilayer, the brittle upper crust was simulated with a 1.5 cm-thick sandpack consisting of six 2 mm-thick alternating white and coloured quartz sand layers overlain by a 3 mm-thick white sand layer (Fig. 4.4). The density of the sieved sand was 1.670 g/cm^3 and the mean size of quartz grains was 224 μm (from Klinkmüller et al., 2016). The angle of internal friction was 33° with a peak cohesion of 102 Pa (e.g. D'Adda et al., 2016). To simulate the mechanical role of the viscous lower crust, a 2 mm-thick basal layer of PDMS XIAMETER silicone putty mixed with barite powder was placed at the base of the sandpack. The density of this layer was 1.15 g/cm^3 and its dynamic shear viscosity was 1.4 x 10^4 Pa-s (after Cappelletti et al., 2013). The mechanical and physical properties of the materials used in the experiments are shown in Table 4.1.

***Table 4-1** Mechanical and physical properties of the materials used in the model*

Materials	Density (g/cm^3)	Mean grain size (μm)	Peak Cohesion (Pa)	Angle of internal friction φ	Dynamic shear viscosity η (Pa s)
Sand[1]	1.670	224	102	33°	- - - -
Silicone + barite [2]	1.150	- - - -	- - - -	- - - -	$1,4 \times 10^4$

[1] Upper crust (from Klinkmüller et al., 2016)

[2] Weak lower crust (from Cappelletti et al., 2013)

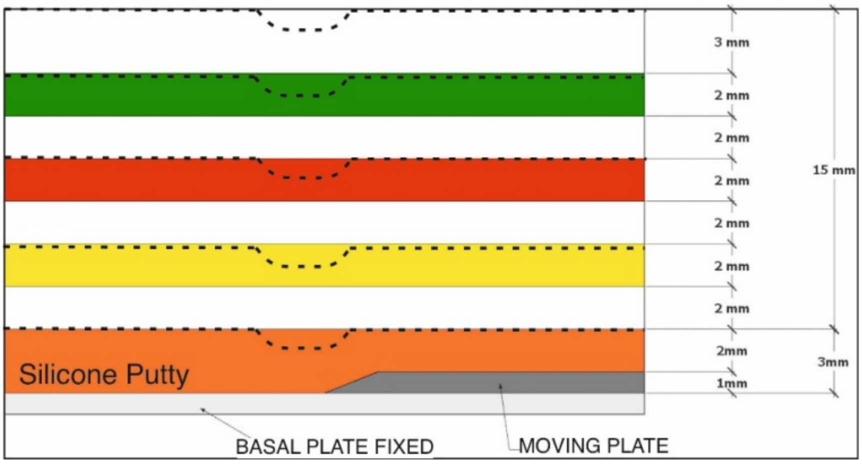

***Figure 4-4** Undeformed experimental stratigraphy of the experiments. Dashed line represents the anticipated basin subsidence after deformation of the model.*

4.2.3 Particle Image Velocimetry (PIV)

Particle Image Velocimetry is an optical image correlation method that is often used to monitor displacement/velocity fields in laboratory flow and deformation systems. This technique is commonly used for dynamic flow analyses, heat transfer, and soil mechanics (White et al., 2001; Adam et al., 2002; Adam et al., 2005; Wolf et al., 2003), and has also been applied to structural geology modelling (Adam et al., 2005; Funiciello et al., 2006; Hatem et al., 2017). Here we use interrogation areas of pairs of images in 64x64 and 32x32 pixel subregions, and derive the best-fit particle displacement in the interrogation areas with the cross-correlation method implemented in the free MATLAB-based PIV-Lab Software package (Thielicke and Stamhuis, 2014). This lets us obtain velocity fields from incremental particle displacements throughout the experiments. PIV-Lab provides incremental displacement fields from 76 images. From these we calculate incremental shear rates and shear strains. In particular, we determine the velocity gradient matrix by measuring the derivatives of the u and v velocity components in the x and y directions, respectively, namely $\partial u/\partial x$, $\partial u/\partial y$; $\partial v/\partial x$, and $\partial v/\partial y$, with the velocity gradient matrix being used to compute incremental strain tensors. The incremental horizontal shear rate is approximated as the velocity gradient perpendicular to the velocity discontinuity applied at the base of the model ($\partial u/\partial y$).

Angular velocity is calculated from the curl of the velocity field, and shows the shear accommodated by faults in any orientation.

The incremental areal strain is the sum of the diagonal components of the strain tensor ($E_{xx} + E_{yy}$):

Equation 4.1

$$E_{xx} + E_{yy} = \partial u/\partial x + \partial v/\partial y$$

The incremental rate of topographic change is calculated by subtracting the measured topography at time *n-1* from the topography at time *n*, corrected for any displacement that occurred between times *n-1* and *n*. Specifically, we determine the material derivative of topography, i.e. the change in topography over a time-step that follows surface motions. To do this, we measure relief on the fine mesh of points available for each topographic measurement, and use an interpolation of the velocity field determined from the coarser mesh of PIV sampling subregions to backtrack each sample point on the fine mesh to where it started at the end of the previous time step. The difference between these measurements is the change in relief felt by this surface point over the time step. Computed rates of incremental topographic changes are then related to the incremental strain patterns in order to understand how relief is generated. Shear rate maps show how much shear deformation takes place during each step of the model, while areal strain maps show the rates of extension and compression in each area. In general, areal strain maps display higher noise than shear strain maps. However, the resulting strain patterns correlate well with the results obtained from the topographic changes.

4.3 Experimental Results

4.3.1 Strain and Topographic Evolution

In early stages of deformation, as the basal plate is activated by dextral relative displacement, a principal shear zone develops that mimics the geometry of the underlying basal master fault (Fig. 4.5a). Incremental shear rate analysis shows that this initial principal shear zone is discontinuous, with a left-stepping offset coincident with the location of the restraining bend (Fig. 4.7a). This offset also corresponds to a zone of topographic build up that is expressed as a pop-up structure. Uplift is fastest over the eastern half of the restraining bend, where strain patterns show that compression, indicated as negative areal strain, is localized along the edges of the topographic high, while its top experiences a little spreading as indicated by slightly positive areal strain (Figs. 7b, c). In contrast, subsidence above the releasing bend is accommodated by a major linear depression (Fig. 4.5b). The extension rate is higher along the releasing bend, which leads to subsidence and graben development (Fig. 4.7c). A subsidiary fault zone parallel to the main graben splays from the eastern portion of the right-lateral strike-slip master fault system. This produces subsidence around the branching point and develops as a shallower basin. East of the releasing bend, the master fault system generates a narrow zone of shear localization without developing any striking topographic features (Fig. 4.7b).

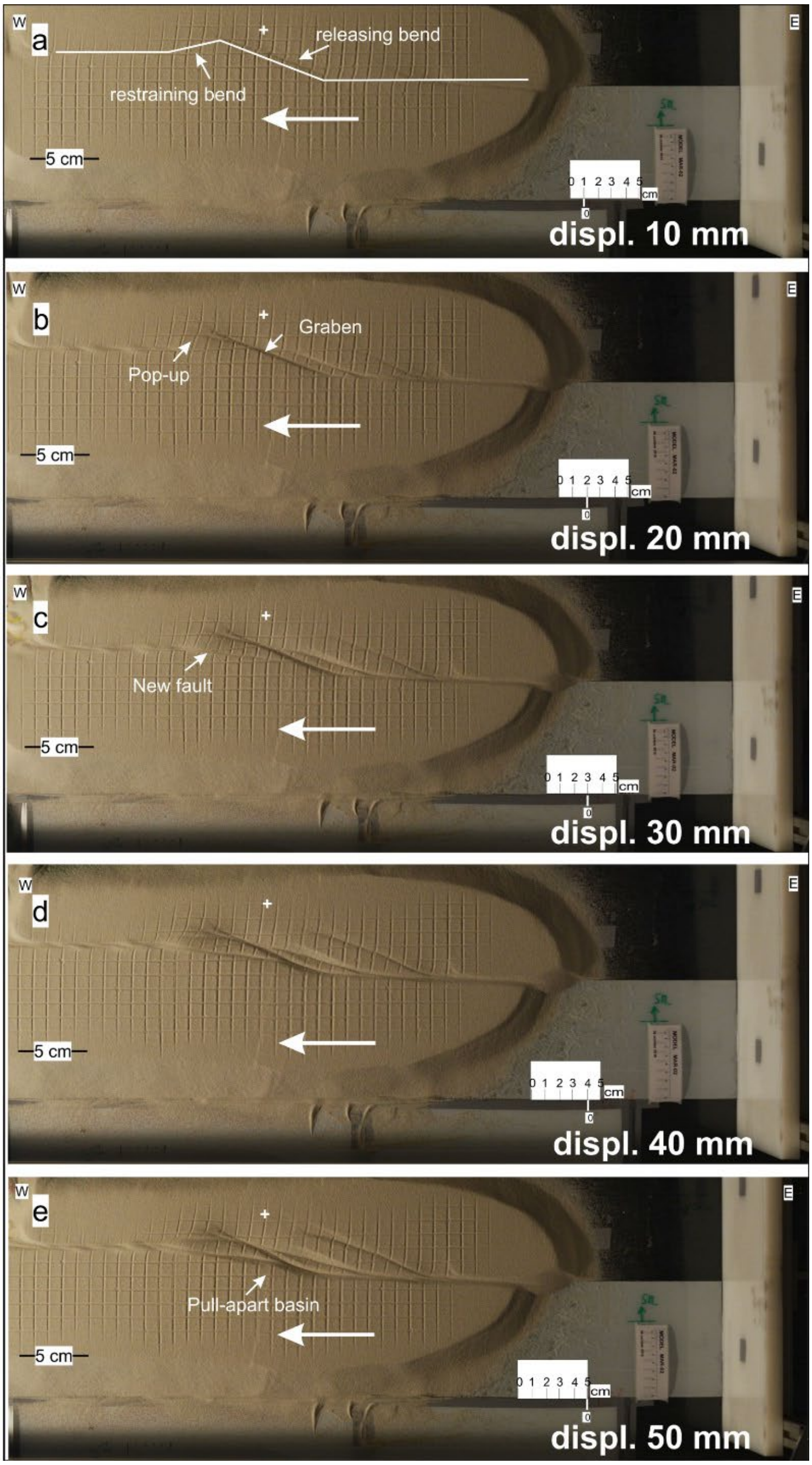

Figure 4-5 *Overhead photographs illustrating the evolution of the experiment at 10 mm displacement steps. See text for details. + indicates the region north of the NAF, which is fixed in the experiment. The white arrow shows the direction of translation of the mobile Plexiglas basal plate. The ruler on the right-bottom represents the 5 cm displacement on the basal plate that was applied over each entire experiment.*

Between the 25 mm and 30 mm of displacement, a new fault zone develops in the releasing bend, and branches out to the south of the principal shear zone. The incremental shear map allows us to observe how this new shear zone breaches the left-step that previously developed. Shear is partitioned between this new fault zone and the older fault system that more closely mimics the basal discontinuity (Fig. 4.7d). The new fault zone is located southward of the previously developed pop-up structure, which leads to cessation of major compression and de-activated of its eastern sector (Fig. 4.7e). In this western sector of the fault system, alternating compression and extension occurs to the north of the basal master fault system, while to the south, less intense opposite-alternating strain areas are present (Fig. 4.7f). This strain pattern of compression and extension only partially corresponds to model uplift and subsidence, with uplift being less prominent than in the earlier phase, but more widespread, while subsidence occurs at the intersection of the releasing and restraining bends, and along part of the latter. Within the releasing bend, subsidence is fastest around the branching point of the new shear zone (Fig. 4.7e). Although some digital noise (a PIV processing artefact) is present, Figure 4.7f shows three domains of areal extension, corresponding to the main graben, the eastern graben and the new fault zone.

With increasing displacement to between 45 mm and 50 mm of horizontal translation of the mobile basal plate, the new southern fault accommodates most of the shear strain deformation in that region of the model, and a strongly compartmentalized pull-apart basin eventually develops (Fig. 4.5e). Development of a doubly-branched fault results in: a) the basin becoming asymmetric, b) the depocenter becoming localized near the branching point, after having migrated to the east, and c) subsidence propagating north, eastward of the releasing bend (Figs. 4.7g-i). To the west, minor uplift characterises the region of the restraining bend, with persistent alternating extensional and compressional areas.

4.3.2 Shear zone development and migration

The maps of the angular velocity rate or vorticity (1/sec) show how fast the reference points on the surface of the experiment are rotating (Fig. 4.6), with horizontal velocity vectors also superimposed. In general, the vorticity patterns highlight regions of active strike-slip deformation.
Shear rate and vorticity have very similar spatial patterns (compare Figs. 4.7a, 4.7c, 4.7e). The major shear zone is characterized by dextral shear. A common feature in figure 6 is a reduction in vorticity at the intersection between the releasing bend and the strike-slip fault segment to the east.

Between the 15-20 mm displacement steps (Fig. 4.6a), vorticity is concentrated in the western portion of the releasing bend where displacement vectors rotate clockwise. In the restraining bend, clockwise rotation is present in an area of low vorticity (Fig. 4.6a).

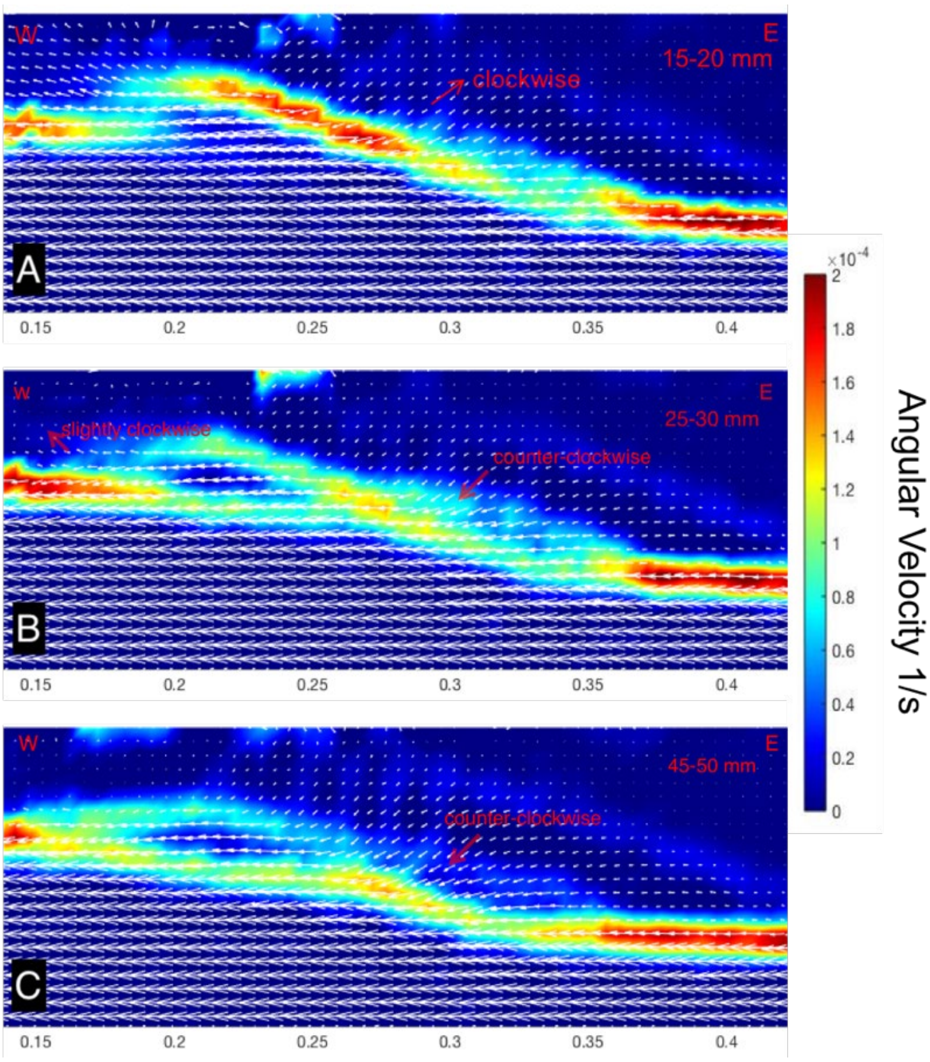

Figure 4-6 *shows the vorticity patterns and velocity vectors during each 5mm step of displacement. A colorblind-friendly version of this image is available in the Supplementary Material I.*

Between 25-30 mm of overall displacement (Fig. 4.6b), the vorticity decreases in the releasing bend, as deformation is partitioned into a newly formed shear zone that intersects the releasing bend. In contrast vorticity increases at the restraining bend. Between 45-50 mm of overall displacement (Fig. 4.6c), the vorticity remains lower along the western part of the releasing bend. However, vorticity increases in the southern newly formed shear zone, while decreasing in the northern part of the releasing bend. The restraining bend also experiences decreasing vorticity. In this interval, the northern region moves SW toward the migrating shear zone.

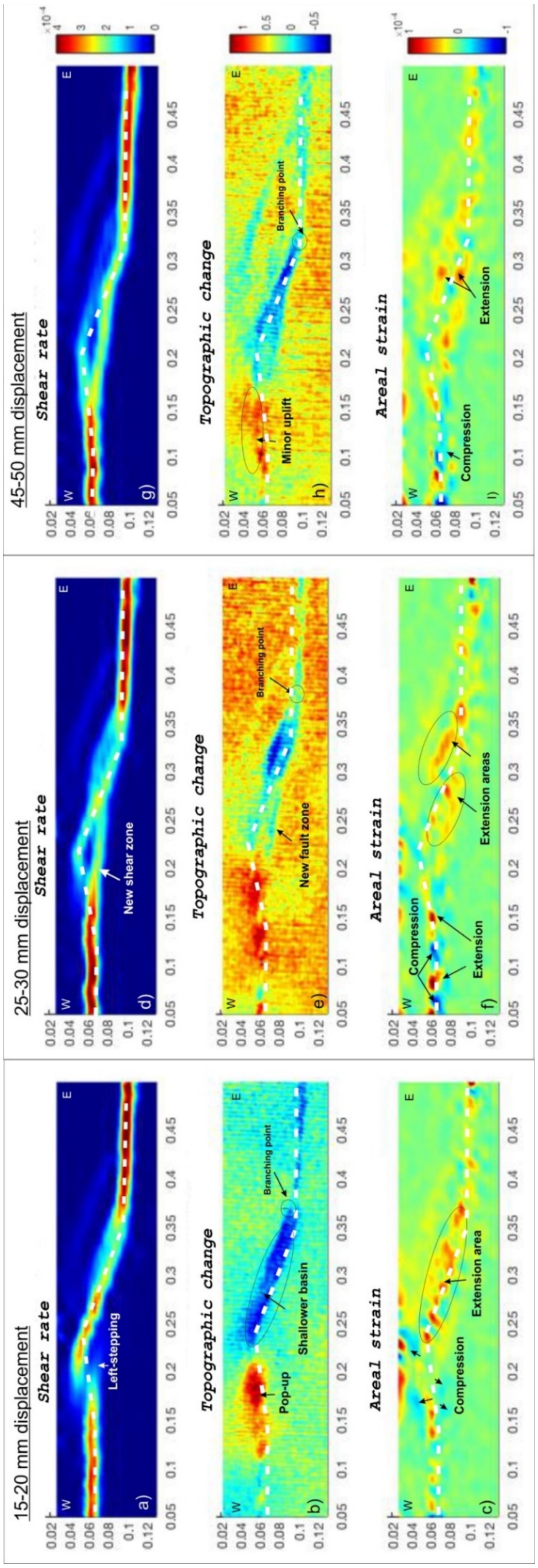
15-20 mm displacement
Shear rate
Left-stepping
Topographic change
Pop-up
Shallower basin
Branching point
Areal strain
Compression
Extension area
25-30 mm displacement
Shear rate
New shear zone
Topographic change
New fault zone
Branching point
Areal strain
Compression
Extension
Extension areas
45-50 mm displacement
Shear rate
Topographic change
Minor uplift
Branching point
Areal strain
Compression
Extension

Figure 4-7 *Comparison the shear rate, topographic changes, and areal strain at prominent times, between 15 mm-20 mm(a,b,c) , 25 mm -30 mm(d,e,f) and 45 mm-50 mm(g,h,i) of displacement. The unit ot he shear rate is 1/m, the unit of areal strain is dimensionless (m/m). See text for details. Colour-blind friendly version is available in the Supplementary Material 1.*

4.4 Tectonic Setting of the Sea of Marmara

Before discussing the potential implications of the above modelling for the evolution of the Sea of Marmara region of the NAF, we briefly review its tectonic setting. The Sea of Marmara is a basin controlled by strike-slip tectonics (LePichon et al., 2014). Strike-slip deformation along the eastern part of the NAF has been constrained by several techniques. Geodetic measurements indicate ≈25 mm/yr of slip (Reilinger et al., 2006), while geologically-inferred motions are inferred to be ≈18 mm/yr in the last 10k years (Hubert-Ferrari et al., 2002; Kozacı et al., 2009), which suggests that some plate deformation is also being accommodated away from the main fault. Total slip on the eastern branch of the NAF has been estimated to be between 30-75 km (Barka and Gülen, 1989; Herece and Akay, 2003; Hubert-Ferrari et al., 2002; Şengör et al., 2005). In the west of Anatolia, plate motion is partitioned between the different NAF fault strands, with the NAF-N strand accommodating ~80% of total slip (Reilinger and McClusky, 2011). Geological estimates in general support this determination, with a minimum of 52±1 km cumulative dextral displacement in the Sea of Marmara region and additional ~15 km displacement across the Duzce fault (Akbayram et al., 2016). However, this displacement might record only post-Oligocene activity within the NAF (Sengor et al., 2005). West of the Sea of Marmara, displacement has been estimated to be between 40-80 km across the Ganos Fault (Armijo et al., 1999, Okay et al., 2004).

Slip rates on the order of 15-20 mm/yr have been inferred for different segments of the NAF-N (Kurt et al., 2013; Grall et al., 2013; Aksoy et al., 2010; Meghraoui et al., 2013). Most of these estimates imply that slip on the NAF-N at the eastern end of the Sea of Marmara is transferred to the

Ganos Fault to the west of the basin and, ultimately, to the Aegean Sea (LePichon et al., 2014). However, data from the Gulf of Izmit imply much lower average slip rates: ~9 mm/yr over the past 10ky (Gasperini et al., 2011). Short-term GPS-based models that combine strike slip and normal faults in the Sea of Marmara predict a right-lateral slip rate of about 18–20 mm/yr and extension of 8 mm/yr across the northern Marmara basin (Armijo et al., 2002; Flerit et al., 2003).

Measurements along the NAF-S are less abundant. These suggest 16-26 km of displacement (Koçyiğit, 1988; Özalp et al., 2013; Şengör et al., 2005), with slip rates of ≈4 mm/year over the past 10-15 ka. (Gasperini et al., 2011).

The Sea of Marmara is characterised by three tectonic depressions: the Çınarcık, Central, and Tekirdağ basins (Fig. 4.1). They are controlled by active fault zones, which link up in the so-called Main Marmara Fault (MMF) (Okay et. al., 2000; Le Pichon, 2001). These basins are separated by two NE-trending transpressional ridges, the Western High and the Central High, where the seafloor shallows to 570 and 380 m below sea level, respectively (Fig. 4.1). The position and migration through time of the depocenters appears to be related to the evolution of a releasing bend and to slip along the MMF (Grall et al. 2012). In the Çınarcık Basin, the active fault is located toward the north of the basins, while in the Central and Tekirdag Basins the deformation is active in the south (Armijo et al., 1999; LePichon et al., 2001, 2014; Okay et al. 2004; Carton et al., 2007; Grall et al. 2012; Kurt et al., 2013). However, some ambiguity still persists. For example, there are uncertainties regarding the kinematic importance of a fault system that intersect the Çınarcık Basin in the central part and join the Izmit fault (Carton et al., 2007; Grall et al., 2012). To the south of this fault system in the Çınarcık Basin, Becel et al. (2010) observed low angle normal faults connecting to a south transtensional zone that seems to have accommodated early Pliocene stretching.

The Çınarcık Basin reaches a depth of 1270 m and contains 4-6 km of sediments (Carton et al., 2007). The Central Basin is 1250 m deep, with up to 6 km of syn-kinematic sediments, and the Tekirdağ Basin is 1130 m deep with >3 km of sediments (Bayrakci et al., 2013; Kende et al., 2017). Due to the lack of direct sampling, age-estimates for these sub-basins are inferred from models built from geophysical imaging of their geometry, estimates of the rates of sediment supply, and thermal modeling (Seeber et al., 2004, 2006; Carton et al., 2007; Sorlien et al., 2012; Grall et al., 2012; Kurt et al., 2013). Seismic imaging in deep basins has been proven successful, as evident in the deep Marmara Sea. The main active faults within the sedimentary basin of Sea of Marmara have been seismically imaged, in depths down to 6 km below the sea floor (Becel et al., 2010). According to age estimates, the onset of basin formation occurred between 5 to 3.5 Ma in the southern part of the Sea of Marmara, in an area encompassing all the three deep sub-basins and also the Imrali basin (Sorlien et al., 2012, Grall et al., 2012). Starting at about 2.5-1.5 Ma, subsidence accelerated along the currently active master fault system and progressively migrated towards the west, in the Tekirdağ basin, and towards the east in the Çınarcık Basin. The Tekirdağ basin's growth was associated with 25-30 km of strike-slip displacement on the master fault system, located in the southern edge; this occurred over the past 1.4 to 1 Ma (Seeber et al., 2004; Okay et al., 2004; LePichon, 2014). In the Tekirdağ basin, subsidence has migrated to the west and sediments are thicker in the east (Seeber et al., 2004). The Çınarcık Basin, with the master fault system located at its north, started to grow from the west around 2.5-1.5 Ma. Later on, the depocenter migrated to an intermediate area at about 1.4 Ma and, eventually, to its present location at about 1 Ma (Carton, 2007; Sorlien et al., 2012; Kurt, 2013).

The Sea of Marmara terminates westward against the Ganos Mountain. This is a region of about 1000 m of elevation around the junction between the Ganos bend and the MMF (Fig. 4.1). Ganos Mountain lies north of and trends parallel to the Ganos fault for about 35 km, with an almost uniform width of 8-11 km. Geological evidence indicates that the northern slope of the Tekirdağ basin represents the direct submarine continuation of the Ganos Mountain's southern slope, which implies there has been about 1100m of subsidence of the eastern flank of the mountain (Okay et al., 2004). Subsidence and uplift seem to be controlled by the Ganos bend, working as a buttress that concentrates compression (Seeber et al., 2004). Armijo et al. (1999) interpret the Ganos mountain uplift to be related to early Pliocene compression that was responsible for fold growth and then deactivated at ≈5 Ma by the Ganos Fault, which offsets these folds of about 80 km. Okay et al. (1999), instead, consider the uplift to be still active and linked to thrusting on a limb of a negative flower structure.

4.5 Discussion

4.5.1 Experimental limitations

Before analysing differences and similarities between models and nature, some major experimental limitations need to be pointed out. First of all, a typical limiting factor in sandbox modelling is the lack of fluids to permeate the experimental crust, both in host rock pores and localized within shear zones. Pore fluid pressure is undoubtedly a major factor that can shape deformation patterns and fault activity in nature (e.g. Chester et al., 1993). Other significant oversimplifications in the sandbox experiments are their lack of a geothermal gradient, lack of mineral reactions constraining rock rheology variations, and lack of an isostatic and flexural response to tectonic deformation. A specific feature of most experiments that simulate strike-slip faulting is the localization of the master shear zone by a sharp boundary between nondeformable, mobile basal plates. This is not anticipated to be the most appropriate analogue to shear localization in nature at the scale of the entire crust (e.g. Schreurs, 2003). In our model, we used a 2 mm-thick silicone layer, scaled to the relative thickness of the viscous lower crust in the study of Kende et al. (2017), to better approximate the natural situation. Differences in the viscosity or thickness of this layer will shape how efficiently basal displacements are transferred to the shallower crust.

Additional oversimplifications affect these model results. The experimental crust is assumed to be mechanically homogeneous, without any heterogeneity or inheritance that might influence the deformation pattern. For example, heterogeneities in the crust deformed by the NAF system have been proposed to play an important role in strain localization (LePichon et al., 2014). Moreover, the shape of the master strike-slip right-lateral fault system in the experiments is simplified with respect to nature (Fig. 4.7). Since the purpose of our experiments is to obtain insights on the role of the strike-slip fault geometry in controlling subsidence and uplift patterns in adjacent regions, we do not attempt to reproduce all details of the tectonic pattern of the Sea of Marmara. In spite of its limitations, analogue modelling has been widely proved to provide a useful tool for investigating tectonic processes (e.g. Koyi, 1997; Schreurs et al., 2006, 2016; Corti, 2012; Dooley and Schreurs, 2012; Gravelau et al., 2012).

4.5.2 Correction for Earth sphericity

To better compare analogue modelling results with the major tectonic features associated with the Sea of Marmara fault system, it is helpful to correct the “flat geometry” of model experiments for Earth sphericity and the overall small-circle geometry of the plate boundary fault system (Fig. 4.8). For this purpose, we use a Hotine-Oblique Mercator projection along the pole of rotation that represents the relative motion between blocks on either sides of the transform fault (e.g. Le Pichon et al., 2003). Unlike the WGS84 projection, the Hotine-Oblique Mercator projection customizes the map for a particular location and linear unit of measure (Engels and Grafarend, 1994). The rotation poles assumed for the Anatolia/Eurasian rigid plate motion and between Eurasia and a hypothetical "Marmara block" located between the northern and southern NAF branches are given in Reilinger et al., (2006).

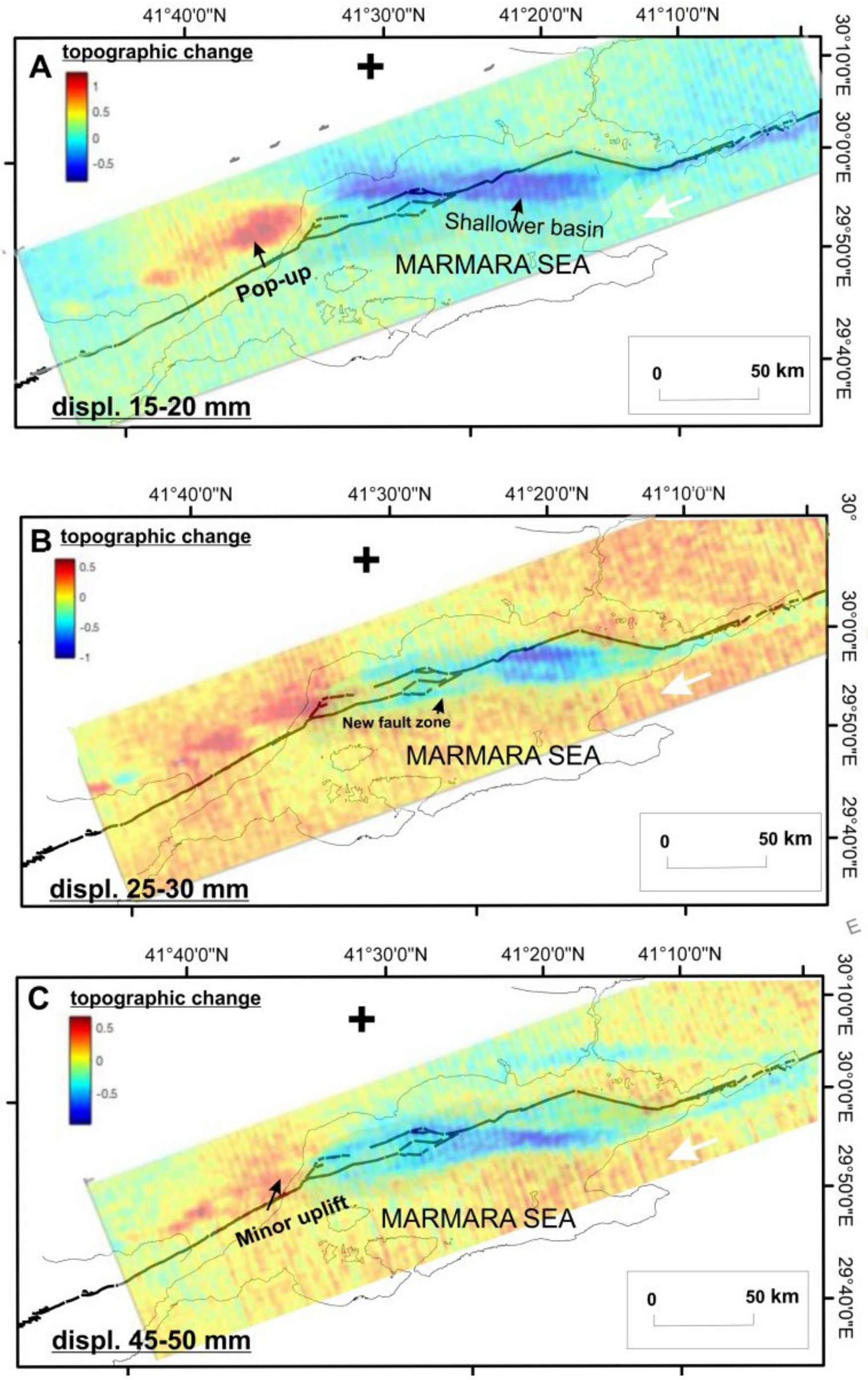

Figure 4-8 *Model topography changes superimposed onto the map of the Sea of Marmara, including the traces of major fault zones pertaining to the northern North Anatolian Fault. The projection system was converted from WGS 84 to Oblique Mercator in order to correct for the flat model of the Sea of Marmara fault system. White arrows represent the direction*

of motion of the base of the analogue model; the black cross is on the fixed plate. A colorblind-friendly version of this image is available in the Supplementary Metarial I.

4.5.3 Strike-slip fault system evolution and strain localization in the model and in the natural case

The experimental deformation pattern produced by a fault geometry with adjacent releasing and restraining bends shows the development of an asymmetric pull-apart basin with associated development of sub-basins and relative topographic highs. The pull-apart basin morphology is caused by increasing offset along the master strike-slip fault system. This simple geometric model can reproduce the first-order morphology of the Marmara Sea, without need for other external factors such as extension linked to the Aegean Sea. This finding is in line with the results of numerical models tested by Muller and Aydin (2005). However, our model is more effective at capturing the potential evolution of this fault system, since it has the capacity for new faults to form with progressive deformation, and can also model the topographic responses to these changes. In our model, for example, the fault system's evolution includes the progressive smoothing of the restraining bend buttress, accompanied by a transition from a single to a multi-branch fault system, with different branches active and dominant at different times. Overall, subsidence in basins is driven by the activation of different dominant strike-slip fault zones that locally generate extension and compression. Although these characteristics of these model experiments also typify tectonic features described for the Sea of Marmara, specific similarities and differences are present. Model experiments develop an asymmetry of faulting that is generally more localised in the fixed northern part of the model. In the Sea of Marmara, however, most NAF branching occurs at the expense of the Anatolian block, different than the observed model behaviour, in particular in its initial phases. This difference in fault branching may arise from the (known) heterogeneous crustal thickness observed in the Eurasian and Anatolian plates adjacent to the Sea of Marmara (Kende et al., 2017), while our models start with a homogeneous crustal thickness. We will see that predicted and observed surface relief are more consistent between model and nature.

Starting from the east, the releasing bend in the model is controlled by a shear zone that maintains a quasi-steady state position throughout the experimental evolution, while concentrated subsidence to the north or to the south of the shear zone creates major asymmetries in the basins. In the Çınarcık Basin and Central Basin, strain seems to have migrated northward and localized near the northern edge of a broader deformation zone (Armijo et al., 2002; Le Pichon et al., 2014, 2016; Kende et al., 2017; Sengor et al., 2005, 2014). There, the MMF has been nearly at steady state for at least 400 kyrs (e.g. Sorlein et al., 2012; Grall et al., 2012). In spite of this difference, the model successfully reproduces both the modern boundary fault location on the northern side of the basin, and the asymmetric shape of the Cinarcik Basin with its steep northern slope and a gentler slope in the south (Fig. 4.8c). In fact, geological, seismological and geodetic evidence all indicate that the main active fault in the Cinarcik Basin is currently the Prince Island fault along the northern edge of this basin (Seeber et al., 2006; Bohnhoff et al., 2013; Ergintav et al., 2014), and also indicate that sediment thickness has increased towards the north (Seeber et al., 2006; Kurt et al., 2013; Grall et al. 2012; Le Pichon et al., 2014, 2016; Kende et al., 2017). The model also is consistent with the reduction in slip rates – from 15-20 to 9 mm/yr – in the Gulf of Izmit, as a persistent ≈50% reduction in vorticity is associated with the intersection of the releasing bend and the strike-slip segment to the east (Fig. 4.6).

In the western region of the model, the master shear zone migrated to the south by development of a “short-cut fault”. Westward of the Sea of Marmara, localization of strain to the south seems to occur in the region of the Western High and Tekirdag Basin (Okay et al. 1999; Seeber et al., 2004; Şengör et al. 2014; Henry et al., 2018). According to Seeber et al. (2004), the Tekirdag Basin is controlled by the interaction of the restraining bend and the master transform fault at depth. The result is oblique slip on a non-vertical master fault which has caused the migration of shear from north to south. In our experiment, instead, the concentration of shear to the south is related to the development of a new fault zone that cuts across the restraining bend. This deformation style is not clearly visible in the Sea of Marmara. However, the kinematic importance of the Central Fault System in the Central Basin is at the moment poorly constrained. The Central Fault System and the MMF have been described as two distinct fault systems, but uncertainty exists regarding the relative roles of these two fault systems (LePichon et al., 2015), which could in fact be more interconnected than previously supposed. Another difference between the experiments and the Sea of Marmara is that the experiments have an asymmetry of faulting that generally seems opposite to that observed in nature. The experiments generate fault systems that splay towards the fixed 'northern' plate of the experiment. In contrast, in the Sea of Marmara, most NAF branching takes place within the southern Anatolian block. This difference may be a consequence of heterogeneous crustal thicknesses within the northern Eurasian and southern Anatolian Plates [Kende et al., 2017], while in our model each plate has a constant crustal layer thickness. In the following section, we will see that the topographic evolution is more consistent between experiments and nature.

4.5.4 Subsidence and uplift patterns in the model and in the natural case

The topographic evolution of the model shows that subsidence progressively concentrates towards the east, in a position that would correspond to the Çınarcık Basin. In the experiment, this corresponds to the longest-living portion of the initial graben, while further west the growth of a short-cut fault has transferred subsidence to the southward region of the strike-slip tectonic system. According to multichannel seismic, tomography, and heat flow data, the basement depth of the Çınarcık Basin reaches a maximum of >6 km, comparable to what occurs in the Central Basin and in the eastern part of the Tekirdag Basin. Sediment thickness maps for the

Çınarcık Basin also imply that the main depocenter has gradually migrated eastwards over time (Carton et al., 2007). This may also be a consequence of slip obliquity at a fault bend (Seeber et al., 2004). Failure of the model to reproduce the eastward migration of subsidence that appears to have occurred in nature may indicate that this feature does not directly relate to the geometry of the master strike-slip shear zone, but to other factors, e.g. that there is asymmetric lower crustal flow underneath the extending region. In addition, the Cinarcik basin depocentre moved with the Anatolian plate but was fixed relative to the opposing Eurasian plate. This may have generated its characteristic shingled, asymmetric wedge of syn-kinematic strata (Seeber et al., 2010). In the western region of the model, the transition from one to two active fault branches caused the formation of an asymmetric basin similar to the present setting of the Tekirdag Basin.

Experimental topographic evolution shows that uplift in the restraining bend is more prominent when the southern fault zone has yet to fully form (Fig. 4.7b). This uplifted area correlates with the location of Ganos Mountain, which is indeed located to the north of the NAF. In the model, activation of the southern fault branch leads to a partial bypass of the restraining bend, and induces uplift to be replaced by subsidence in the eastern part of the previously formed pop-up. After this transition, uplift continues at a lower rate and progressively migrates westward. Geological and morphological observations of Armijo et al., (2002) show that in the Ganos Mountain uplift has stopped. Okay et al. (2004) propose that uplift in the Ganos area started at about 2 Ma. In the last few hundred thousand years the eastern end of the Ganos Mountain has collapsed by >1100 m. Seeber et al. (2004) proposed there has been progressive westward migration of subsidence in the area where the Ganos Fault crosses the shelf of the western Tekirdag Basin, while uplift has continued in the western part of the mountains throughout the Quaternary (Yaltirak, 2002). Moreover, tectonic inactivity of the fault bounding the northern side of Tekirdag Basin (Grall et al., 2018) may be understood if the main active fault, which follows the southern side of the Basin, is considered to be a partial short-cut of adjacent releasing and restraining bends.

4.6 Conclusions

Our experimental results suggest that a strike-slip system with a releasing-restraining bend geometry does not favour the persistence of a single thoroughgoing fault system at shallow crustal levels. Instead it should evolve into a multi-branch fault system, with different branches active and dominant at different times. Comparing the model evolution with the geological record in the northern strand of the NAF within the Sea of Marmara provides insights that help us to better understand the natural system.

I. In the eastern region of the analogue model, location of the main active fault zone northward of the main subsiding domain appears to simulate the development of the Prince Island Fault, i.e. the northern boundary fault of the Çınarcık basin and Central high. Both the analogue and the Çınarcık basins develop an asymmetric shape, with a shared steep northern slope and a gentler slope to the south.

II. In the western region of the Sea of Marmara as well as in the analogue model, strain localizes to the south of the deformation zone/major fault. In the model, a major short-cut fault cuts through the restraining bend. This may also be the case in the Sea of Marmara, although definitive evidence is lacking and the formation of the Western High and Tekirdag Basin may instead be controlled by the interaction of the restraining bend with the master transform fault at depth (Seeber et al., 2004).

III. Locations of the tectonic depressions developed in the model correspond with those of sub-basins in the Sea of Marmara. In particular, in the model the principal depocenter is located in the eastern part, similar to what happens in nature regarding the location of the currently active depocenter in the Çınarcık Basin.

IV. In the model, uplift associated with the restraining bend is located north of the major fault system and occurs early, when the southern fault zone is yet to be active. This evolution correlates extremely well with the occurrence of Ganos Mountain, which is indeed located to the north of the NAF. In the model, uplift ceases and migrates to the west when the southern fault zone forms. In nature, the main Marmara Fault can be interpreted as an incomplete short-cut that still allows for some compression and uplift of Ganos Mountain, although this short-cut was apparently successful in deactivating the presumed fault scarp along the edge of the northern shelf in the Western Sea of Marmara.

Acknowledgments. This work was fostered by visits funded by the FLOWS-COST Action ES1301 "FLOWS". Analogue models were produced in the Analogue Modelling Laboratory "E. Costa" of the Department of Chemistry, Life Sciences and Environmental Sustainability, University of Parma, Italy. The paper benefitted by conversations with I. Watkinson and N. Scarselli at RHUL.

4.7 References

Adam, J., Lohrmann, J., Hoth, S., Kukowski, N., & Oncken, O. (2002). Strain variation and partitioning in thrust wedges: High-resolution data from scaled sandbox experiments by 2D–3D PIV analysis. *Bollettino di Geofisica teorica ed applicata, 42,* 123-125.

Adam, J., Urai, J. L., Wieneke, B., Oncken, O., Pfeiffer, K., Kukowski, N., & Schmatz, J. (2005). Shear localisation and strain distribution during tectonic faulting—New insights from granular-flow experiments and high-resolution optical image correlation techniques. *Journal of Structural Geology, 27(2),* 283-301.

Adam, J., Klinkmüller, M., Schreurs, G., & Wienecke, B. (2013). Quantitative 3D strain analysis in analogue experiments: Integration of X-ray computed tomography and digital volume correlation techniques. *Journal of structural geology, 55,* 127-14.

Akbayram, K., Sorlien, C. C., & Okay, A. I. (2016). Evidence for a minimum 52±1 km of total offset along the northern branch of the North Anatolian Fault in northwest Turkey. *Tectonophysics, 668,* 35-41.

Aksoy, M. E., Meghraoui, M., Vallée, M., & Çakır, Z. (2010). Rupture characteristics of the AD 1912 Mürefte (Ganos) earthquake segment of the North Anatolian fault (western Turkey). *Geology, 38(11),* 991-994.

Armijo, R., B. Meyer, A. Hubert, and A. Barka, 1999. Westward propagation of the North Anatolian fault into the northern Aegean: Timing and kinematics, *Geology, 27*, 267–270.

Armijo, R., Meyer, B., Navarro, S., King, G., & Barka, A. 2002. Asymmetric slip partitioning in the Sea of Marmara pull apart: A clue to propogation processes of the North Anatolian Fault. *Terra Nova, 14,* 80–86. 10.1046/j.1365-3121.2002. 00397.x

Armijo, R., et al., 2005. Submarine fault scarps in the Sea of Marmara pull-apart (North Anatolian Fault): implications for seismic hazard in Istanbul, *Geochem. Geophys. Geosyst, 6,* Q06009, doi:10.1029/2004GC000896.

Barka, A. A., & Gülen, L. (1989). Complex evolution of the Erzincan Basin (eastern Turkey). *Journal of Structural Geology, 11*(3), 275-283.

Bayrakci, G., Laigle, M., Bécel, A., Hirn, A., Taymaz, T., Yolsal-Çevikbilen, S., &Team, S. (2013). 3-D sediment-basement tomography of the Northern Marmara trough by a dense OBS network at the nodes of a grid of controlled source profiles along the North Anatolian fault. *Geophysical Journal International, 194*(3), 1335-1357

Bécel, A., Laigle, M., De Voogd, B., Hirn, A., Taymaz, T., Yolsal-Cevikbilen, S.,& Shimamura, H. (2010). North Marmara Trough architecture of basin infill, basement and faults, from PSDM reflection and OBS refraction seismics. *Tectonophysics, 490*(1-2), 1-14

Bohnhoff, M., Bulut, F., Dresen, G., Malin, P. E., Eken, T., & Aktar, M. (2013). An earthquake gap south of Istanbul. *Nature communications, 4,* 1999

Cappelletti, A., Tsikalas, F., Nestola, Y., Cavozzi, C., Argnani, A., Meda, M., & Salvi, F. (2013). Impact of lithospheric heterogeneities on continental rifting evolution: constraints from analogue modelling on South Atlantic margins. *Tectonophysics, 608, 30-50.*

Carton, H., Singh, S. C., Hirn, A., Bazin, S., De Voogd, B., Vigner, A., ... & Sevilgen, V. (2007). Seismic imaging of the three-dimensional architecture of the Çınarcık basin along the North Anatolian fault. *Journal of Geophysical Research: Solid Earth, 112*(B6).

Chester, F. M., Evans, J. P., and Biegel, R. L. (1993), Internal structure and weakening mechanisms of the San Andreas Fault, *J. Geophys. Res., 98*(B1), 771– 786, doi:10.1029/92JB01866.

Corti, G. (2012). Evolution and characteristics of continental rifting: Analog modeling-inspired view and comparison with examples from the East African Rift System. *Tectonophysics, 522*, 1-33.

Cooke, M. L., Schottenfeld, M. T., & Buchanan, S. W. (2013). Evolution of fault efficiency at restraining bends within wet kaolin analog experiments. *Journal of Structural Geology, 51,* 180-192

D'ADDA P., LONGONI R., MAGISTRONI C., MEDA M., RIGHETTI F., CAVOZZI C., NESTOLA Y. & STORTI F. (2016) – Extensional reactivation of a deep transpressional architecture: insights from sandbox analogue modeling applied to the Val d'Agri basin (Southern Apennines, Italy). *Interpretation, 5,* 55-66.

Dooley, T., Monastero, F., Hall, B., McClay, K., & Whitehouse, P. (2004). Scaled sandbox modeling of transtensional pull-apart basins: Applications to the Coso geothermal system. *Geothermal Research Council Transactions, 28*, 637-641.

Dooley, T., McClay, K., Analog modeling of pull-apart Basins, (1997*) AAPG Bulletin, 81 (11*), pp. 1804-1826.

Dooley, T. P., & Schreurs, G. (2012). Analogue modelling of intraplate strike-slip tectonics: A review and new experimental results. *Tectonophysics, 574*, 1-71.

Dotare, T., Yamada, Y., Adam, J., Hori, T., & Sakaguchi, H. (2016). Initiation of a thrust fault revealed by analog experiments. *Tectonophysics, 684*, 148-156.

Hatem, A. E., Cooke, M. L., & Toeneboehn, K. (2017). Strain localization and evolving kinematic efficiency of initiating strike-slip faults within wet kaolin experiments. *Journal of Structural Geology, 101,* 96-108.

Henry, P., Grall, C., Kende, J., Viseur, S., Özeren, M. S., Şengör, A. M. C., ... & Géli, L. (2018). A statistical approach to relationships between fluid emissions and faults: The Sea of Marmara case. Deep Sea Research Part II: *Topical Studies in Oceanography, 153*, 131-143.

Engels, J., & Grafarend, E. (1995). The oblique Mercator projection of the ellipsoid of revolution IE a 2, b. *Journal of Geodesy, 70(1-2*), 38-50.

Ergintav, S., McClusky, S., Hearn, E., Reilinger, R., Cakmak, R., Herring, T., &Tari, E. (2009). Seven years of postseismic deformation following the 1999, M= 7.4 and M= 7.2, Izmit-Düzce, Turkey earthquake sequence. *Journal of Geophysical Research: Solid Earth, 114*(B7).

Ergintav, S., R. E. Reilinger, R. Çakmak, M. Floyd, Z. Cakir, U. Doğan, R. W. King, S. McClusky, and H. Özener (2014). Istanbul's earthquake hot spots: Geodetic constraints on strain accumulation along faults in the Marmara seismic gap, *Geophys. Res. Lett., 41*, 5783–5788, doi:10.1002/2014GL060985.

Flerit, F., Armijo, R., King, G. C. P., Meyer, B., & Barka, A. (2003). Slip partitioning in the Sea of Marmara pull-apart determined from GPS velocity vectors. *Geophysical Journal International, 154(1),* 1-7.

Flerit, F., Armijo, R., King, G., & Meyer, B. (2004). The mechanical interaction between the propagating North Anatolian Fault and the back-arc extension in the Aegean. Earth and Planetary Science Letters, 224(3-4), 347-362.

Funiciello, F., Moroni, M., Piromallo, C., Faccenna, C., Cenedese, A., & Bui,H. A. (2006). Mapping mantle flow during retreating subduction: Laboratory models analyzed by feature tracking. *Journal of Geophysical Research: Solid Earth, 111*(B3),doi:10.1029/2005JB003792

Gasperini, L., Polonia, A., Çağatay, M. N., Bortoluzzi, G., & Ferrante, V. (2011). Geological slip rates along the North Anatolian Fault in the Marmara region. *Tectonics, 30*(6).

Grall, C., Henry, P., Tezcan, D., Mercier de Lepinay, B., Bécel, A., Géli, L., & Harmegnies, F. (2012). Heat flow in the Sea of Marmara Central Basin: Possible implications for the tectonic evolution of the North Anatolian fault. *Geology, 40(1*), 3-6

Grall, C., Henry, P., Thomas, Y., Westbrook, G.K., Çağatay, M.N., Marsset, B., Saritas, H., Çifçi, G., Géli, L., (2013). Slip rate estimation along the western segment of the Main Marmara Fault over the last 405–490 ka by correlating mass transport deposits. *Tectonics 32,* 1–15

Grall, C., Henry, P., Dupré, S., Geli, L., Scalabrin, C., Zitter, T. A., ... & Cifci, G. (2018). Upward migration of gas in an active tectonic basin: An example from the sea of Marmara. *Deep Sea Research Part II: Topical Studies in Oceanography, 153,* 17-35.

Graveleau, F., Malavieille, J., & Dominguez, S. (2012). Experimental modelling of orogenic wedges: A review. *Tectonophysics, 538*, 1-66.

Hergert, T., & Heidbach, O. (2011). Geomechanical model of the Marmara Sea region—II. 3-D contemporary background stress field. *Geophysical Journal International, 185*(3), 1090-1102.

Herece, E., and E. Akay (2003), Kuzey Anadolu Fayı (KAF) Atlası / Atlas of North Anatolian Fault (NAF), Maden Tetk. Arama Genel. Müdürlügü, Özel Yayın. Ser. 2/General Directorate of Mineral Research and Exploration, Special Publications Series 2, Ankara, 61 pp. + 13 appendices as separate maps.

Hubert-Ferrari, A., Armijo, R., King, G., Meyer, B., & Barka, A. (2002). Morphology, displacement, and slip rates along the North Anatolian Fault, Turkey. *Journal of Geophysical Research: Solid Earth, 107*(B10), ETG-9.

Hussain, E., Wright, T. J., Walters, R. J., Bekaert, D., Hooper, A., & Houseman, G. A. (2016). Geodetic observations of post seismic creep in the decade after the 1999 Izmit earthquake, Turkey: Implications for a shallow slip deficit. *Journal of Geophysical Research: Solid Earth, 121(4),* 2980-3001.

Imren, C., Le Pichon, X., Rangin, C., Demirbağ, E., Ecevitoğlu, B., & Görür, N. (2001). The North Anatolian Fault within the Sea of Marmara: a new interpretation based on multi-channel seismic and multi-beam bathymetry data. *Earth and Planetary Science Letters, 186(2),* 143-158.

Kende, J., Henry, P., Bayrakci, G., Özeren, M. S., & Grall, C. (2017). Moho depth and crustal thinning in the Marmara Sea region from gravity data inversion. *Journal of Geophysical Research: Solid Earth, 122(2),* 1381-1401.

Klinkmüller, M., Schreurs, G., Rosenau, M., & Kemnitz, H. (2016). Properties of granular analogue model materials: A community wide survey. *Tectonophysics, 684*, 23-38.

Koçyiğit, A. (1988). Tectonic setting of the Geyve Basin: Age and total displacement of the Geyve Fault Zone. *METU Journal of Pure and Applied Sciences, 21*, 81-104.

Kozacı, Ö., Dolan, J. F., & Finkel, R. C. (2009). A late Holocene slip rate for the central North Anatolian fault, at Tahtaköprü, Turkey, from cosmogenic 10Be geochronology: Implications for fault loading and strain release rates. *Journal of Geophysical Research: Solid Earth, 114*(B1).

Kurt, H., et al. (2013), Steady late quaternary slip rate on the Cinarcik section of the North Anatolian fault near Istanbul, Turkey, *Geophys. Res. Lett., 40,* 4555–4559, doi:10.1002/grl.50882.

Laigle, M., Becel, A., de Voogd, B., Hirn, A., Taymaz, T., & Ozalaybey, S. (2008). A first deep seismic survey in the Sea of Marmara: Deep basins and whole crust architecture and evolution. *Earth and Planetary Science Letters, 270*(3-4), 168-179.

Le Pichon, X., Şengör, A. M. C., Demirbağ, E., Rangin, C., Imren, C., Armijo, R., ... & Saatçılar, R. (2001). *The active main Marmara fault. Earth and Planetary Science Letters, 192(4)*, 595-61.

Le Pichon, X., N. Rangin, C. Chamot-Rooke, and A. M. C. Sengör, 2003. The North Anatolian Fault in the Sea of Marmara, *J. Geophys. Res., 108(B4),* 2179.

Le Pichon, X., Imren, C., Rangin, C., Şengör, A. C., & Siyako, M. (2014). The South Marmara Fault. *International Journal of Earth Sciences, 103(1),* 219-231.

Mann, P. (2007). Global catalogue, classification, and tectonic origins of restraining-and releasing bends on active and ancient strike-slip fault systems. *Geological Society, London, Special Publications, 290*(1), 13-142.

Meghraoui, M., & Pondrelli, S. (2013). Active faulting and transpression tectonics along the plate boundary in North Africa. *Annals of Geophysics, 55*(5).

Nestola, Y., Storti, F., Bedogni, E., & Cavozzi, C. (2013). Shape evolution and finite deformation pattern in analog experiments of lithosphere necking. *Geophysical Research Letters, 40*(19), 5052-5057.

McClay, K., & Dooley, T. (1995). Analogue models of pull-apart basins. *Geology, 23*(8), 711-714.

McClay, K. R., & White, M. J. (1995). Analogue modelling of orthogonal and oblique rifting. Marine and Petroleum *Geology, 12*(2), 137-151.

McClay, K., & Bonora, M. (2001). Analog models of restraining stepovers in strike-slip fault systems. *AAPG bulletin, 85*(2), 233-260.

Muller, J. R., & Aydin, A. (2005). Using mechanical modeling to constrain fault geometries proposed for the northern Marmara Sea. *Journal of Geophysical Research: Solid Earth, 110*(B3).

Okay, A. I., Demirbağ, E., Kurt, H., Okay, N., & Kuşçu, İ. (1999). An active, deep marine strike-slip basin along the North Anatolian fault in Turkey. *Tectonics, 18*(1), 129-147.

Okay, A. I., A. Kaslilar-Ozcan, C. Imren, A. Boztepe-Guney, E. Demirbag, and I. Kuscu (2000), Active faults and evolving strike-slip basins in the Marmara Sea, Northwest Turkey: A multichannel seismic reflection study, *Tectonophysics*, ***321***, 189–218.

Okay, A. I., Tüysüz, O., & Kaya, Ş. (2004). From transpression to transtension: changes in morphology and structure around a bend on the North Anatolian Fault in the Marmara region. *Tectonophysics, 391*(1-4), 259-282.

Özalp, S., Emre, Ö., & Doğan, A. (2013). The segment structure of southern branch of the North Anatolian Fault and paleoseismological behaviour of the Gemlik Fault, NW Anatolia. *General Directorate of Mineral Research and Exploration (MTA) Bulletin, 147*, 1-17.

Rahe, B., Ferrill, D. A., & Morris, A. P. (1998). Physical analog modeling of pull-apart basin evolution. *Tectonophysics, 285*(1-2), 21-40

Reilinger, R., & McClusky, S. (2011). Nubia–Arabia–Eurasia plate motions and the dynamics of Mediterranean and Middle East tectonics.*Geophysical Journal International, 186*(3), 971-979.

Reilinger, R., McClusky, S., Vernant, P., Lawrence, S., Ergintav, S., Cakmak, R.,& Nadariya, M. (2006). GPS constraints on continental deformation in the Africa-Arabia-Eurasia continental collision zone and implications for the dynamics of plate interactions. *Journal of Geophysical Research: Solid Earth, 111*(B5).

Schreurs, G., Hänni, R., Panien, M., & Vock, P. (2003). Analysis of analogue models by helical X-ray computed tomography. *Geological Society, London, Special Publications, 215*(1), 213-223.

Schreurs, G., Buiter, S. J., Boutelier, D., Corti, G., Costa, E., Cruden, A. R., ... & Lohrmann, J. (2006). Analogue benchmarks of shortening and extension experiments. *Special Publication-Geological Society of London, 253*, 1.

Schreurs, G., Buiter, S. J., Boutelier, J., Burberry, C., Callot, J. P., Cavozzi, C., & Cruz, L. (2016). Benchmarking analogue models of brittle thrust wedges. *Journal of structural geology*, 92, 116-139.

Seeber, L., O. Emre, M.-H. Cormier, C. C. Sorlien, C. M. G. McHugh, A.Polonia, N. Ozer, and N. Cagatay (2004), Uplift and subsidence from oblique slip: The

Ganos-Marmara bend and the North Anatolian Transform, western Turkey, *Tectonophysics, 391*, 239–258.

Seeber, L., Cormier, M. H., McHugh, C., Emre, O., Polonia, A., & Sorlien, C. (2006). Rapid subsidence and sedimentation from oblique slip near a bend on the North Anatolian transform fault in the Marmara Sea, Turkey. *Geology, 34*(11), 933-936.

Seeber, L., Sorlien, C., Steckler, M., & Cormier, M. H. (2010). Continental transform basins: Why are they asymmetric? *Eos, Transactions American Geophysical Union, 91*(4), 29-30.

Sims, D., Ferrill, D. A., & Stamatakos, J. A. (1999). Role of a ductile decollement in the development of pull-apart basins: Experimental results and natural examples. *Journal of Structural Geology, 21*(5), 533-554.

Sorlien, C. C., Akhun, S. D., Seeber, L., Steckler, M. S., Shillington, D. J., Kurt,H., ... & İmren, C. (2012). Uniform basin growth over the last 500 ka, North Anatolian Fault, Marmara Sea, Turkey. *Tectonophysics, 518*, 1-16.

Sugan, M., Wu, J. E. L., & McClay, K. (2014). 3D analogue modelling of transtensional pull-apart basins: comparison with the Cinarcik basin, Sea of Marmara, Turkey. *Bollettino di Geofisica Teorica ed Applicata, 55*(4).

Şengör, A. M. C., Tüysüz, O., Imren, C., Sakınç, M., Eyidoğan, H., Görür, N., & Rangin, C. (2005). The North Anatolian fault: A new look. *Annu. Rev. Earth Planet. Sci., 33*, 37-112.

Şengör, A. C., Grall, C., İmren, C., Le Pichon, X., Görür, N., Henry, P., ... & Siyako, M. (2014). The geometry of the North Anatolian transform fault in the Sea of Marmara and its temporal evolution: implications for the development of intracontinental transform faults. *Canadian Journal of Earth Sciences*, *51*(3), 222-242.

Thielicke, W and Stamhuis, E J 2014 PIVlab – Towards User-friendly, A ordable and Accurate Digital Particle Image Velocimetry in MATLAB. *Journal of Open Research Software, 2*: e30, DOI: http://dx.doi.org/10.5334/jors.bl.

Toeneboehn, K. (2017). Exploring Long-term Fault Evolution in Obliquely Loaded Systems Using Tabletop Experiments and Digital Image Correlation Techniques.

Yaltırak, C. (2002). Tectonic evolution of the Marmara Sea and its surroundings. *Marine Geology, 190*(1-2), 493-529.

White, D. J., Take, W. A., & Bolton, M. D. (2001, September). Measuring soil deformation in geotechnical models using digital images and PIV analysis. In 10th international conference on computer methods and advances in geomechanics (No. 1, pp. 997-1002).

Wolf, H., König, D., & Triantafyllidis, T. (2003). Experimental investigation of shear band patterns in granular material. *Journal of Structural Geology, 25*(8), 1229-1240.

Wu, J. E., McClay, K., Whitehouse, P., & Dooley, T. (2009). 4D analogue modelling of transtensional pull-apart basins. *Marine and Petroleum Geology, 26*(8), 1608-1623.

4.8 Supplementary Material I

The images presented the colormap colorblind friendly as suggested by the reviewer of the Tectonics' journal.

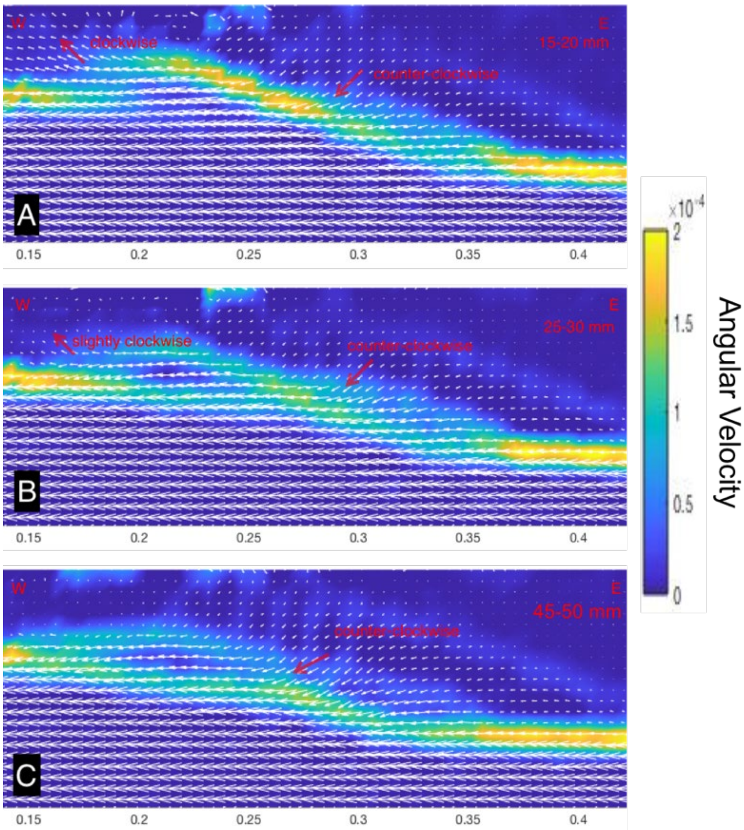

Figure S 1 *shows the angular velocity rate patterns with velocity displacement vectors at during 5mm changes. The rotations marked on the map with red arrows. The image presented by the color map colorblind friendly representing the Fig. 4.6.*

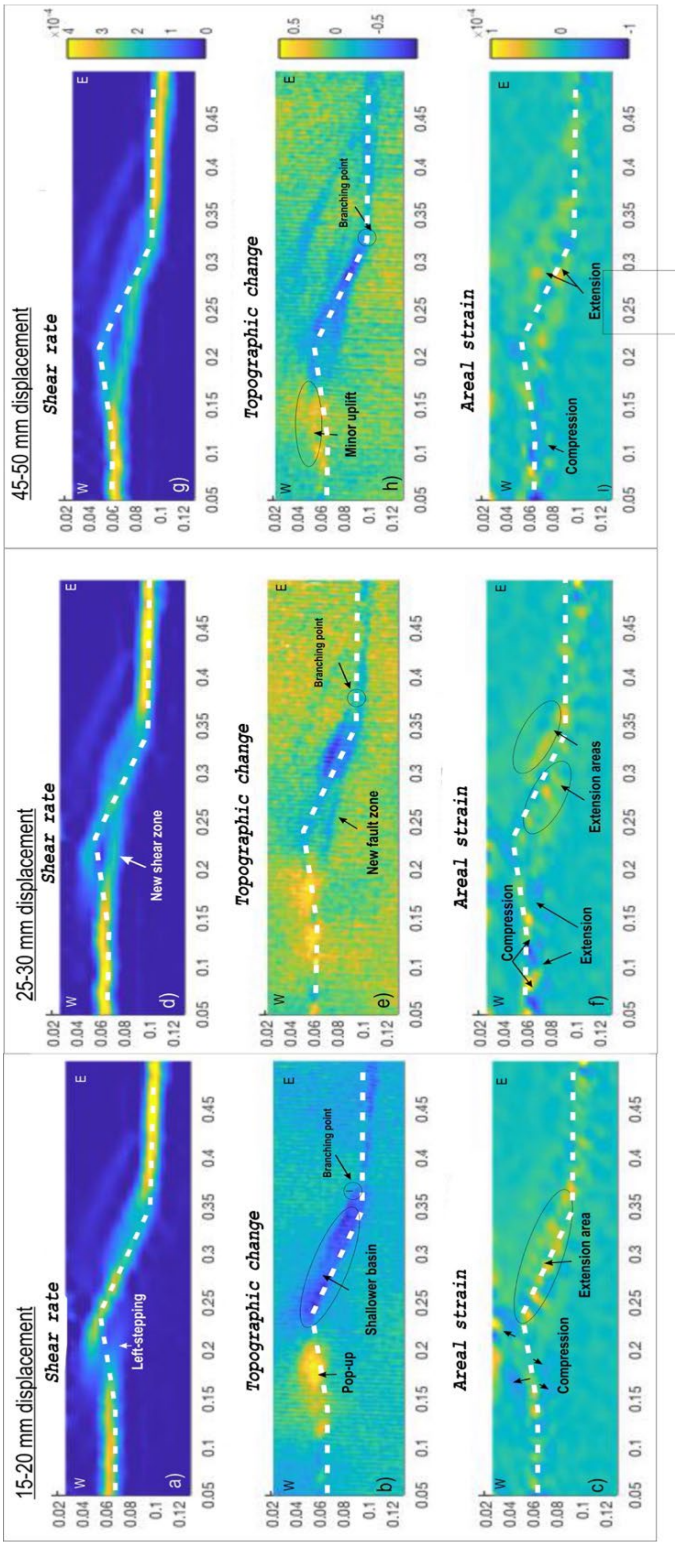

Figure S 2 *Comparison the shear rate, topographic changes and areal strain at prominent times ; between 15 mm-20 mm(a,b,c), 25mm-30mm(d,e,f) and 45mm-50mm(g,h,I) of displacement. The unit of the shear rate is 1/m, the unit of areal strain is dimensionless (m/m). The image presented by the colormap colorblind friendly representing the Fig. 4.7.*

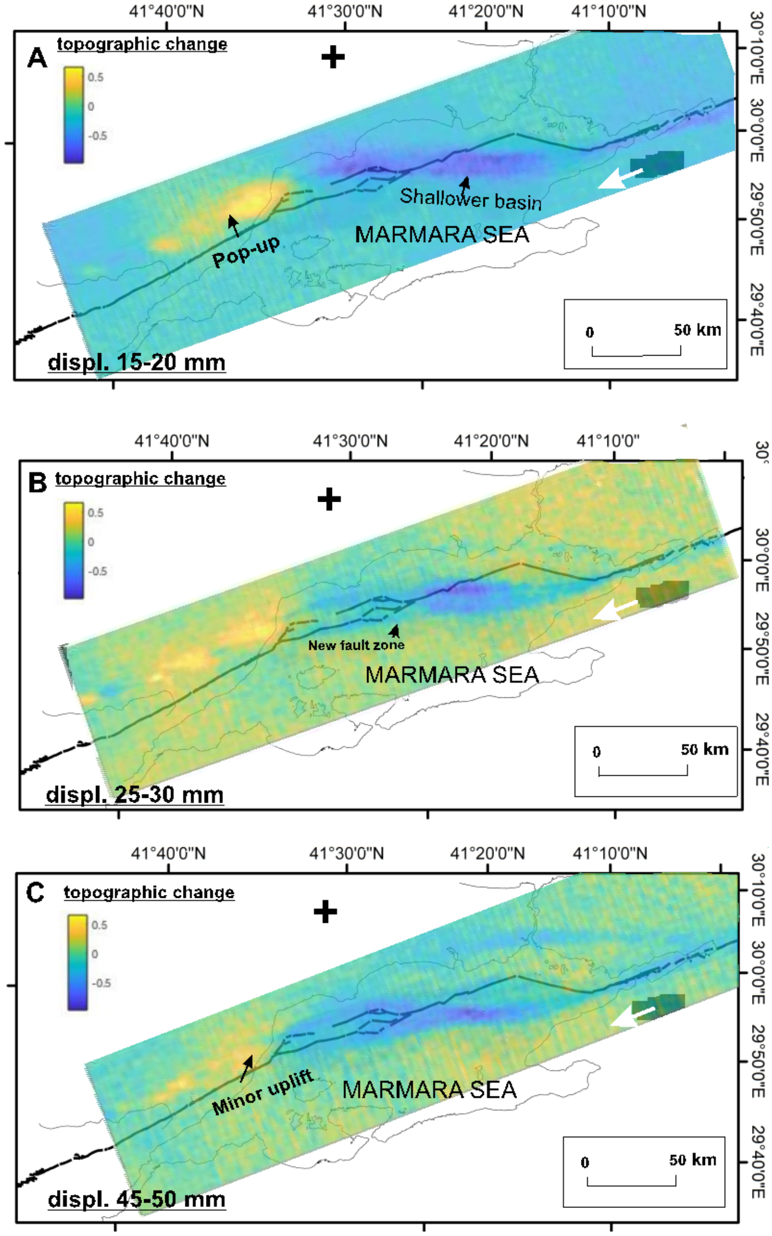

Figure S 3 *Model topography changes superimposed onto the map of the Sea of Marmara, including the traces of major fault zones pertaining to the northern North Anatolian Fault. The projection system was converted from WGS 84 to Oblique Mercator in order to correct for the flat model of the Sea of Marmara fault system. White arrows represent the direction of motion of the base of the analogue model; the black cross is on the fixed plate. The image presented by the colormap colorblind friendly representing the Fig.4.8.*

4.9 Supplementary Material II

This code was programmed by Pierre Henry & Sibel Bulkan in Oct 2019 and modified by Jason Phips Morgan to sample material derivative. The MATLAB code is available on the Zenodo, open-access repository web-site (https://doi.org/10.5281/zenodo.3597335).

```
% at the resolution of the 'finer' topographic grid -- although still
% interpolating from velocities calculated on the coarser grid. 2 Nov 2019
clear all
close all
load('/Users/sibel/Desktop/France_STSM/Matlab-France/gridded_calc/gridded_data.mat');
x0=515;
y0=-325;
xlims=[0.05 0.5];
ylims=[0.015 0.13];
itopo=4;
defstep=[num2str(5*(itopo-1)) '-' num2str(5*itopo) ' mm']
if itopo>1 & itopo<=14
i0=3*(itopo-1)+1
icount=0
for i = i0:3*itopo
  filename2=['modelraw_00' num2str(i,'%02i') '.txt'];
  ModelMatrix=importdata(filename2,',',3);
  ModelMatrix_3Row=ModelMatrix.data(:,3);
  ModelMatrix_4Row=ModelMatrix.data(:,4);
  if icount==0
    ModelMatrix_1Row=ModelMatrix.data(:,1);
    ModelMatrix_2Row=ModelMatrix.data(:,2);
    xaxisvalues = unique(ModelMatrix_1Row);
    yaxisvalues = unique(ModelMatrix_2Row);
    nxaxis = length(xaxisvalues);
    nyaxis = length(yaxisvalues);
    xx=repmat(xaxisvalues',nyaxis,1);
    yy=repmat(yaxisvalues,1,nxaxis);
    Dx=[ 0 0 0 0 0;
```

```
    1 1 0 -1 -1;
    0 0 0 0 0]
    Dy=[0 1/2 1 1/2 0;
    0 0 0 0 0;
    0 -1/2 -1 -1/2 0]
    dx=conv2(xx,Dx,'valid');
    dy=conv2(yy,Dy,'valid');
    ucM = reshape((ModelMatrix_3Row),[nyaxis nxaxis]);
    vcM = reshape((ModelMatrix_4Row),[nyaxis nxaxis]);

else

end

  icount=icount+1

end

ucM=ucM/icount;
vcM=vcM/icount;
gradux=conv2(ucM,Dx,'valid')./dx;
gradvx=conv2(vcM,Dx,'valid')./dx;
graduy=conv2(ucM,Dy,'valid')./dy;
gradvy=conv2(vcM,Dy,'valid')./dy;

%set dimension
ucM = ucM + reshape((ModelMatrix_3Row),[nyaxis nxaxis]);
vcM = vcM + reshape((ModelMatrix_4Row),[nyaxis nxaxis]);
```

02/01/20 22:44 /Users/sibel/Desktop.../rewind_results2.m 2 of 5

```
[nrows,ncols] = size(gradux);
xn=xx(2:1+nrows,3:2+ncols);
yn=yy(2:1+nrows,3:2+ncols);
exy = 0.5*(graduy+gradvx);
eyx = exy;
exx = gradux;
```

```
eyy = gradvy;
%Angular velocity
cav = curl(xx,yy,ucM,vcM);
Arealchange = eyy+exx;
ShearI = exx - eyy;
Invariant2 = ((exx .* eyy)-(exy.*eyx));
Jnvariant2 = (0.5*ShearI).^2 + 0.5*exy.^2;
Shearrate = graduy;
Angvel = (cav);
dt=15*60 % 15 minutes between topographic scans
% xb=1000*(xx-ucM*dt/2)+x0;
% yb=-1000*(yy-vcM*dt/2)+y0;
% xf=1000*(xx+ucM*dt/2)+x0;
% yf=-1000*(yy+vcM*dt/2)+y0;
% find backtrack points on coarse grid
xb=  1000*(xx-ucM*dt)+x0;
yb= -1000*(yy-vcM*dt)+y0;
xf=  1000*(xx)+x0;
yf= -1000*(yy)+y0;
zf=interp2(xgrid,ygrid,zgrid(:,:,itopo),xf,yf);
zb=interp2(xgrid,ygrid,zgrid(:,:,itopo-1),xb,yb);
% write output (Shear)
filenameout=['Shear' num2str(i) '.txt'];
dlmwrite(filenameout, Shearrate);
% backtrack on fine grid
% find grid points of fine grid inside the region of the coarse grid
% (remember they are offset by x0,y0)
min_xf = min(min(xf));
max_xf = max(max(xf));
min_yf = min(min(yf));
max_yf = max(max(yf));
xgrid_allpts = unique(xgrid); % list of all xgrid points
ygrid_allpts = unique(ygrid); % list of all ygrid points
% extract list of all xgrid points between min_xf and max_xf
xgrid_axis = ...
  xgrid_allpts((xgrid_allpts >= min_xf) & (xgrid_allpts <= max_xf));
% extract list of all ygrid points between min_yf and max_yf
ygrid_axis = ...
```

02/01/20 22:44 /Users/sibel/Desktop.../rewind_results2.m 3 of 5

```
 ygrid_allpts((ygrid_allpts >= min_yf) & (ygrid_allpts <= max_yf));
% now make a list of all points in the mesh made up of xgrid_pts and
% ygrid_pts
xgrid_pts = repmat(xgrid_axis',length(ygrid_axis),1);
ygrid_pts = repmat(ygrid_axis,1,length(xgrid_axis));
zfgrid_pts = interp2(xgrid,ygrid,zgrid(:,:,itopo),xgrid_pts,ygrid_pts);
% redefine (xgrid_pts,ygrid_pts) to be in 'original' coordinate system for plots
xx_pts =  (xgrid_pts - x0)/1000;
yy_pts = -(ygrid_pts - y0)/1000;
% xf=1000*(xx)+x0;
% yf=-1000*(yy)+y0;
ucM_pts = interp2(xx,yy,ucM,xx_pts,yy_pts);
vcM_pts = interp2(xx,yy,vcM,xx_pts,yy_pts);
% xb_pts=  1000*(xx_pts+ucM_pts*dt)+x0;
% yb_pts= -1000*(yy_pts+vcM_pts*dt)+y0;
xb_pts=  1000*(xx_pts-ucM_pts*dt)+x0;
yb_pts= -1000*(yy_pts-vcM_pts*dt)+y0;
zbgrid_pts = interp2(xgrid,ygrid,zgrid(:,:,itopo-1),xb_pts,yb_pts);
zf=interp2(xgrid,ygrid,zgrid(:,:,itopo),xf,yf);
zb=interp2(xgrid,ygrid,zgrid(:,:,itopo-1),xb,yb);
%
% % CHECK PLOT comparing velocity components sampled on coarse and fine grids
%
% % 1st subplot
% figure(itopo+102);
% subplot(2,1,1);
% %surface(xgrid/1000,ygrid/1000,zgrid(:,:,itopo),'edgecolor','none');
% %surface(xx,yy,ucM,'edgecolor','none');
% surface(xx,yy,vcM,'edgecolor','none');
% shading(gca,'interp');
% %caxis([-1.5 1.5]);
% axis('equal');
% view(0,-90);
% colorbar;
```

```
% %title(['ucM (coarse mesh) ' defstep],'FontSize',14 )
% title(['vcM (coarse mesh) ' defstep],'FontSize',14 )
% xlim(xlims)
% ylim(ylims)
%
%
% % 2nd subplot
% figure(itopo+102);
% subplot(2,1,2);
% %surface(xgrid/1000,ygrid/1000,zgrid(:,:,itopo),'edgecolor','none');
% %surface(xx_pts,yy_pts,ucM_pts,'edgecolor','none');
% surface(xx_pts,yy_pts,vcM_pts,'edgecolor','none');
% shading(gca,'interp');
% %caxis([-1.5 1.5]);
% axis('equal');
% view(0,-90);
% colorbar;
% %title(['ucM (fine mesh) ' defstep],'FontSize',14 )
% title(['vcM (fine mesh) ' defstep],'FontSize',14 )
```

02/01/20 22:44 /Users/sibel/Desktop.../rewind_results2.m 4 of 5

```
% xlim(xlims)
% ylim(ylims)
% CHECK PLOT comparing topography sampled on coarse and fine grids

% 1st subplot


figure(itopo+101);
subplot(2,1,1);
%surface(xgrid/1000,ygrid/1000,zgrid(:,:,itopo),'edgecolor','none');
%surface(xx,yy,zf,'edgecolor','none');
%surface(xx,yy,zb,'edgecolor','none');
surface(xx,yy,(zf-zb),'edgecolor','none');
shading(gca,'interp');
%caxis([-1.5 1.5]);
axis('equal');
```

```
view(0,-90);
colorbar;
colormap parula
title(['Material Derivative of Topography (coarse mesh) ' defstep],'FontSize',14 )
xlim(xlims)
ylim(ylims)

% 2nd subplot

figure(itopo+101);
subplot(2,1,2);
%surface(xgrid/1000,ygrid/1000,zgrid(:,:,itopo),'edgecolor','none');
%surface(xx_pts,yy_pts,zfgrid_pts,'edgecolor','none');
%surface(xx_pts,yy_pts,zbgrid_pts,'edgecolor','none');
surface(xx_pts,yy_pts,(zfgrid_pts-zbgrid_pts),'edgecolor','none');
shading(gca,'interp');
%caxis([-1.5 1.5]);
axis('equal');
view(0,-90);
colorbar;
colormap parula
title(['Material Derivative of Topography (fine mesh) ' defstep],'FontSize',14 )
xlim(xlims)
ylim(ylims)
cl = caxis;  % save caxis for check
%-----------
% Make Plots
%-----------
% 1st subplot
figure(itopo+100);
subplot(4,1,1);
surface(xn,yn,-Shearrate,'edgecolor','none');
shading(gca,'interp');
colormap(jet);
axis('equal');
caxis([0 4e-4]);
view(0,-90);
colorbar;
```

```
colormap parula;
title(['Shear Rate ' defstep,],'FontSize',14 );
xlim(xlims)
ylim(ylims)
```

```
% 2nd subplot

figure(itopo+100);
subplot(4,1,2);
surface(xx,yy,Angvel,'edgecolor','none');
shading(gca,'interp');
caxis([0 2e-4]);
axis('equal');
view(0,-90);
colorbar;
colormap parula;
title(['Angular velocity ' defstep],'FontSize',14);
xlim(xlims)
ylim(ylims)

% 3rd subplot

figure(itopo+100);
subplot(4,1,3);
surface(xn,yn,Arealchange,'edgecolor','none');
shading(gca,'interp');
caxis([-1e-4 1e-4]);
axis('equal');
view(0,-90);
colorbar;
colormap parula;
title(['Areal Strain ' defstep],'FontSize',14 )
xlim(xlims)
ylim(ylims)
```

```
% 4th subplot (hi-res)
figure(itopo+100);
subplot(4,1,4);
%surface(xgrid/1000,ygrid/1000,zgrid(:,:,itopo),'edgecolor','none');
%surface(xx,yy,(zf-zb),'edgecolor','none'); % mat. der. on low-res mesh
surface(xx_pts,yy_pts,(zfgrid_pts-zbgrid_pts),'edgecolor','none');% mat. der. on hi-
res mesh
shading(gca,'interp');
%caxis([-1.5 1.5]);
%caxis('auto')
caxis(cl)
colormap parula;
axis('equal');
view(0,-90);
colorbar;
title(['Topographic change ' defstep],'FontSize',14 ); % material derivative plot
xlim(xlims)
ylim(ylims)

end
```

Chapter 5: Modelling tectonic deformation along the North-Anatolian Fault in the Sea of Marmara

S. Bulkan[1], P. Vannucchi[2], L. Gasperini[3], A. Polonia[3], C. Cavozzi[4]

[1] Royal Holloway, University of London, Earth Sciences Department, Egham, UK.
[2] Dipartimento di Scienze della Terra, Università degli Studi di Firenze, Via La Pira, 4, Firenze, Italy
[3] Istituto di Scienze Marine-Consiglio Nazionale delle Ricerche (ISMAR), IT-40129 Bologna, Italy
[4] NEXT – Natural and Experimental Tectonics research group, Department of Chemistry, Life Sciences and Environmental Sustainability, University of Parma, Italy

The following chapter is a co-authored manuscript has published in the Journal of Tectonophysics.

Key Points:

1. We successfully reproduced the tectonic deformations associated with the northern branch of the North Anatolian Fault in the Cinarcik Basin of the Sea of Marmara using analogue modelling.
2. We show how the differently oriented segments of the northern branch of the North Anatolian Fault in the Cinarcik Basin of the Sea of Marmara are accumulating strain at different rates with potential consequences for their earthquake cycles.

Keywords: analogue modelling, pull-apart basins, stress transfer, fault orientation, Cinarcik basin, Sea of Marmara

Using analogue techniques, we attempted to model the complex tectonic deformation pattern observed along the North-Anatolian Fault in the Sea of Marmara from morpho-bathymetry and seismic reflection images. In particular this paper focuses on the so-called Cinarcik segment of the fault connecting the eastern Izmit segment, which entirely ruptured during the Mw 7.4, 1999 earthquake, to the western segment of the Central High. The Çınarcık segment, potentially loaded after the Izmit earthquake, is expected to rupture during an earthquake occurring in the near future, possibly the next decades, with a high potential to affect the Istanbul metropolitan area. Our analysis suggests that the development of the observed structures accommodating strike-slip, transtensional and transpressional deformations, could be explained by changes in the geometry of fault segments within a right-lateral strike-slip tectonic regime. Tectonic deformations were reproduced in the analogue model by imposing a small (about 10°) and sharp difference in the relative orientations of the strike-slip segments at the edges of a major releasing bend. In the model slower strain accumulation occurs along the analogue of the Çınarcık segment than along the analogue of the Izmit segment of the fault. This would predict a delay for earthquakes triggered by stress transfer between the Izmit and Çınarcık segments. The model further predicts that most of the deformation in the Çınarcık basin is controlled by the sharp changes in the geometry of the fault itself.

5.1 Introduction

The North Anatolian Fault (NAF) is a right-lateral, >1200 km-long continental transform fault that separates the Eurasian and Anatolian plates (Fig. 5.1) (Şengör et al., 2005). In its eastern part, the NAF is constituted by a single fault strand that experiences almost pure strike-slip deformation. To the west, it separates into two major branches, the Northern branch (N-NAF) and the Southern branch (S-NAF) (Fig. 5.1) that accommodate predominantly transtensive deformation. According to GPS modelling, the northernmost of these branches (NAF-N in Fig. 5.1) takes up most Eurasian-Anatolian relative motion, about 24±1 mm/yr (McClusky et al., 2003). Geodynamic models explain the transtension pattern observed in the Marmara basin as a consequence of Anatolia escaping towards the west, with its rate of counterclockwise rotation progressively increasing westward in response to the Hellenic subduction (McClusky et al., 2000). The NAF-N pull-apart system of the Sea of Marmara creates deep tectonic depressions that reach over 1200 m below sea level, separated by structural highs (Fig. 5.1). Despite the formation of the Sea of Marmara being elegantly explained as a consequence of major oversteps along the westward propagating NAF (Barka et al., 1988; Armijo et al., 1999; Şengör et al., 2005), there remain unsolved issues regarding its recent tectonic evolution and present activity, issues that are particularly critical for reliable earthquake scenarios in a region of high seismic hazard. According to historical catalogues (Ambraseys, 2002) the Sea of Marmara and other adjacent regions along the NAF are sites of major earthquakes (Mw>= 7) with a rather regular periodicity of about 250-300 years along specific fault segments. The delimitation of these segments and analysis of their mutual interaction through time is particularly complex in the Sea of Marmara due the presence of releasing and restraining bends. This structural complexity has led to contrasting interpretations. Existing models assume: (1) the presence of a single through-going fault (Le Pichon et al., 2001); (2) a sequence of pull-apart basins with northwest-trending normal faults and ENE-trending strike-slip faults (Armijo et al., 2002); or (3) a major negative flower structure (Laigle et al., 2008). Models of seismic hazard depend strongly on the assumed tectonic model because the length of potentially rupturing seismogenic segments differs significantly between the different model reconstructions.

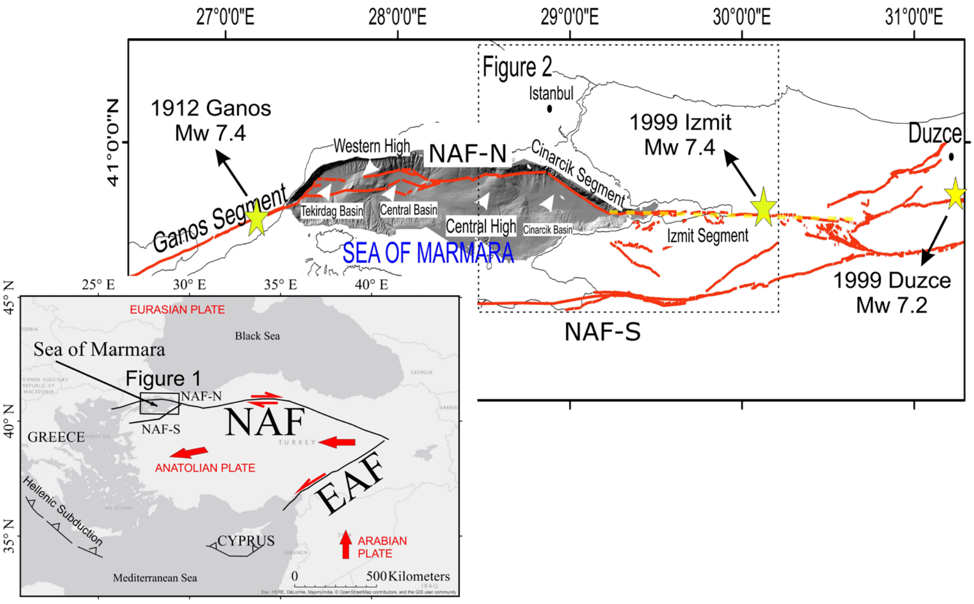

Figure 5-1 *Tectonic map of the Sea of Marmara region (modified from Le Pichon et al., 2003; Gasperini et al., 2011a; Grall et al., 2012, 2013). Stars show locations of earthquake epicentres. Dotted line in yellow shows the surface rupture of the 1999 Izmit earthquake as estimated from its aftershock locations. Black dotted box shows the area of the map displayed in Fig. 5.2. The lower inset highlights the main regional tectonic elements in this area.*

Here we focus on structural analysis of the Cinarcik Basin, the easternmost deep basin (about 1200 m) in the Sea of Marmara. The basin is bounded to the north by the so called Cinarcik segment of the NAF-N that connects the Izmit segment to the east with the Central High to the west (Fig. 5.2). This segment is inferred to have been tectonically loaded by the 1999 Mw=7.4 Izmit earthquake which ruptured the fault through the entire Gulf of Izmit (Gasperini et al., 2011). For this reason, describing the position and geometry of active faults and reconstructing their recent deformation history can provide key information for reliable seismic risk scenarios in the Istanbul metropolitan area.

In particular, our work will address the following topics:

1) Can restraining and releasing bends along a transcurrent-type fault act as barriers to stress transfer and earthquake slip? Or do they help earthquake propagation, as suggested by Cunningham and Mann, (2007)?

2) Does co-seismic strain release on the Izmit segment directly affect strain accumulation on the Cinarcik segment?
3) Since the Izmit segment is (and has been) oriented at an angle relative to the Central High segment towards the west (about 10°), could this difference be responsible for the compressive deformation observed at the NW edge of the Cinarcik basin?

To analyse these problems, we used a 3D scaled sandbox model which reproduced the NAF-N segmentation as imaged by geophysical data, i.e., by morphobathymetry and seismic reflection profiles across the Cinarcik Basin. Our model experiment was successful in reproducing observed deformation patterns along the basin, and therefore the eastern part of the NAF-N, and gives us insights on possible stress transfer mechanisms between fault segments near the Istanbul metropolitan area.

5.2 Tectonic Setting

The Cinarcik basin is the easternmost sub-basin of the Sea of Marmara, located ∼20 km to the southeast of Istanbul (Fig. 5.1). It is about 50 km long, 18 km wide, and reaches a maximum depth of 1270 m. The basin is positioned on the extensional side of the prominent Tuzla fault bend (Fig. 5.2). A second major bend, the Istanbul bend, connects the Cinarcik basin with the Central High segment to the west (Fig. 5.2).

Seismic reflection profiles indicate that the southern and the northern margins of the Cinarcik basin accommodate a large amount of extension, and that the master fault creating the asymmetric basin-forming depression is located along its northern edge (Okay et al., 2004; Seeber et al., 2004, 2006; Carton et al., 2007; Sorlien et al., 2012). These studies also show that the main basin depocenter gradually migrated to the east following the development of the master fault, which coincides with the NAF-N principal displacement zone and it is known as the Cinarcik Segment (Le Pichon et al., 2001). Tectonic reconstructions assume that the basin depocenter grew by propagating from the west ≈2.5-1.5 Ma, and reached its present location at ≈1 Ma (Carton, 2007; Sorlien et al., 2012; Kurt, 2013) (Fig. 5.2). This evolution is recorded in the 4-6 km-thick sediment fill (Carton et al., 2007) which shows a marked asymmetry toward the Gulf of Izmit, where the basin narrows (Okay et al., 2004).

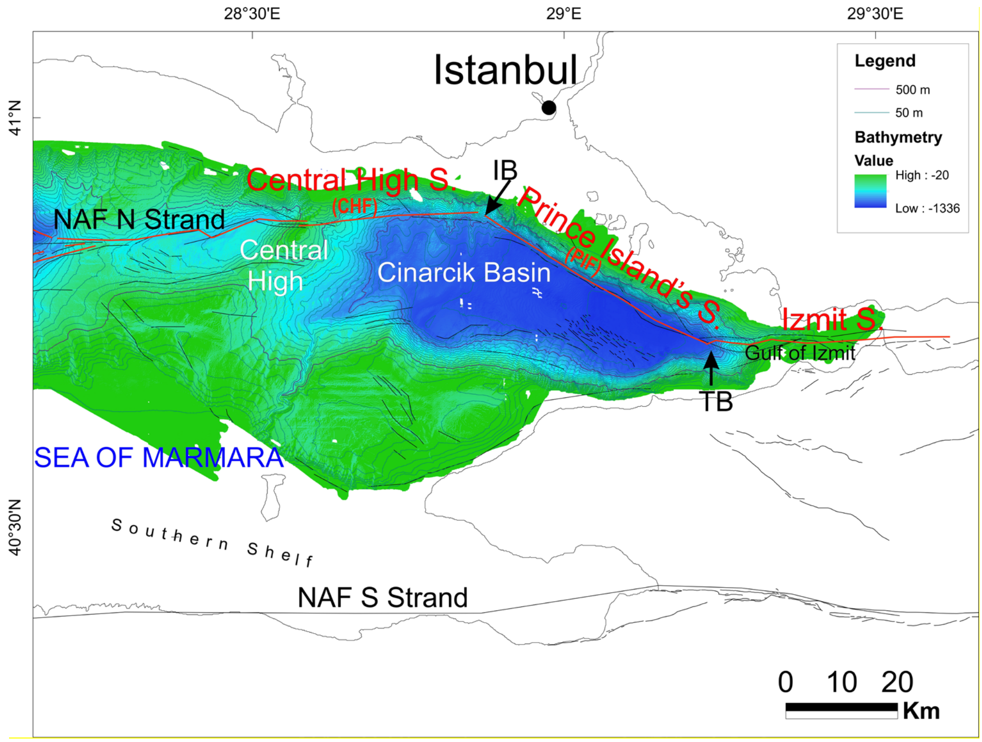

Figure 5-2 *Tectonic setting of the Cinarcik Basin. Faults modified from Le Pichon et al., 2003; Gasperini et al., 2011a; Grall et al., 2012, 2013. The major fault (Northern Strand of NAF) is highlighted in red. Thin lines represent the isobath lines for every 50 m and 500 m. IB and TB represent the Istanbul Bend and Tuzla Bend, respectively.*

The active NW-SE trending fault bordering the basin to the north corresponds to a steep scarp cut by canyons that can reach 12 km in length, affected by scars of submarine landslides up to 2.5 to 4 km wide. A major landslide affecting the NE edge of the basin, activated in the upper Pleistocene, was interpreted as being triggered by one or more earthquakes along the NAF (Görür and Çağatay, 2010; Özeren et al., 2010). To the south, the Cinarcik basin is bounded by an antithetic set of *en-echelon* normal faults that trend subparallel to the NAF-N (Fig. 5.2) (Smith et al., 1995; Le Pichon et al., 2001;

Armijo et al., 2002). Bécel et al. (2010) observed that this low angle normal fault system connects to a transtensional zone towards the south which seems to have accommodated early Pliocene stretching. In the central part of the basin another fault system joins the Izmit segment (Carton et al., 2007; Grall et al., 2012).

The tectonics of the Cinarcik basin has been interpreted in the frame of the overall Sea of Marmara geologic setting, following several models. Armijo et al. (2002) considered the basin to be a wedge-shaped transtensional basin that formed across a large releasing step-over of the main strike-slip fault zone. Other models (e.g., Laigle et al., 2008) assume that the general architecture and lateral heterogeneities below the Cinarcik basin are caused by inherited basement structures with numerous faulted and tilted upper crustal blocks. These bounding block faults seem to penetrate to a maximum depth of 6 km below the seafloor (Bécel et al., 2009, 2010). In all these models, the Cinarcik basin formed at a bend in the NAF and basin subsidence was due to oblique slip on a steeply-dipping, non-vertical transform fault (Seeber et al., 2006, 2010). Thus, fault geometry, potentially inherited from pre-existing sutures, controls the kinematics of the faults in the basin, and is critical for modelling their seismogenic behavior (Seeber et al., 2006).

Seismically, the Cinarcik basin is located in a key area. Since 1939, the NAF has been site of seven M>7 earthquakes, following a sequence which originated in eastern Anatolia and propagated to the west towards Istanbul. The most recent earthquake, the 1999 Mw7.4 Izmit event, ruptured a segment of the NAF-N at the eastern end of the Sea of Marmara (Gasperini et al., 2011b). The Ganos segment, at the opposite western end of the Sea of Marmara, was the site of a Mw 7.4 earthquake in 1912 (Fig. 5.1). The most recent event occurring along the Cinarcik segment and affecting the Istanbul metropolitan area is a Ms=6.4 event in 1963 - recently re-evaluated by Baştürk et al., 2020. This seismic sequence leaves a seismic gap along the 150 km-long NAF-N segment cutting through the Cinarcik basin between the

Prince Islands Fault (PIF) and the Central High Fault (CHF) (Bohnhoff et al., 2013; Ergintav et al., 2014). This gap is located only 40 km southeast of Istanbul, with a potential for earthquakes estimated to be M=7 or higher (Parsons et al., 2000, 2004, Bohnhoff et al. 2013). The earthquake fault slip in the 1999 Izmit earthquake is assumed to have increased the elastic strain accumulation on the adjacent segment towards the west (Parsons, 2000; H. Ferrari et al., 2000; Uçarkuş et al., 2011; Gasperini et al., 2011b, Bohnhoff et al., 2013) which is considered locked to a depth of ~10 km accumulating the slip deficit (Bohnhoff et al., 2013). At the surface of the 1999 Izmit rupture zone, however, the observed current maximum creep rate is 8 mm/yr (Çakir et al., 2012; Aslan et al., 2019).

5.2.1 Cross-Sectional Geometries of the Cinarcik Basin

We used a set of seismic reflection profiles collected in the Cinarcik basin during the SEISMARMARA cruise (Hirn et al. 2001) to characterize tectonic deformation along the NAF in this region, and to compare to results from analogue modelling. The SEISMARMARA seismic lines were collected onboard of the R/V Nadir using a 4.5 km long streamer and an airgun source. These dataset has been used by Carton et al. (2007) to reconstruct the three-dimensional structure and seismostratigraphy of the Cinarcik basin, and to infer its geological evolution. Most of the seismic lines cut orthogonally across the northern shelf of the Cinarcik basin from 28.4°E to 29.3°E, crossing the principal deformation zone of the NAF-N (Fig. 5.3). Geophysical data presented here consists of time-migrated sections that were filtered and plotted using SeisPrho (Gasperini and Stanghellini, 2009) to produce geo-referenced bitmaps that were used for data interpretation and line-drawings. In this study we focus on three seismic sections: 1) Line 101, in the eastern part of the basin, to the east of the Tuzla Bend; 2) Line 122, in the central part of the Cinarcik basin; 3) Line 184, which cuts across the NAF-N immediately to the west of the Istanbul Bend.

Line 101 (section A-A', Fig. 5.3a) to the west of the Izmit Gulf highlights the presence of a narrow sub-vertical deformation zone that corresponds to the main strand of the NAF-N. We interpret this pattern as diagnostic of almost pure strike-slip deformation. The minor features that 'deform' the seafloor are probably related to gravity failures caused by co-seismic shaking during large magnitude earthquakes.

Moving to the centre of the basin, seismic Line 122 (section B-B', Fig. 5.3b) shows the presence of growth structures and fanning of the sediment packages towards the NNE, suggesting the presence of extensional/transtensional syn-depositional deformation. The main fault trace extends across the continental shelf and slope which constitute the footwall of an extensional/transtensional fault, that vertically displaces the seafloor by more than 1 km (Fig. 5.3b). This deformation pattern characterizes the Cinarcik segment of the NAF-N from 29.10°to 28.8°E, where the morphobathymetric data show a sharp change in the NAF-N's orientation from 300°N to 270°N.

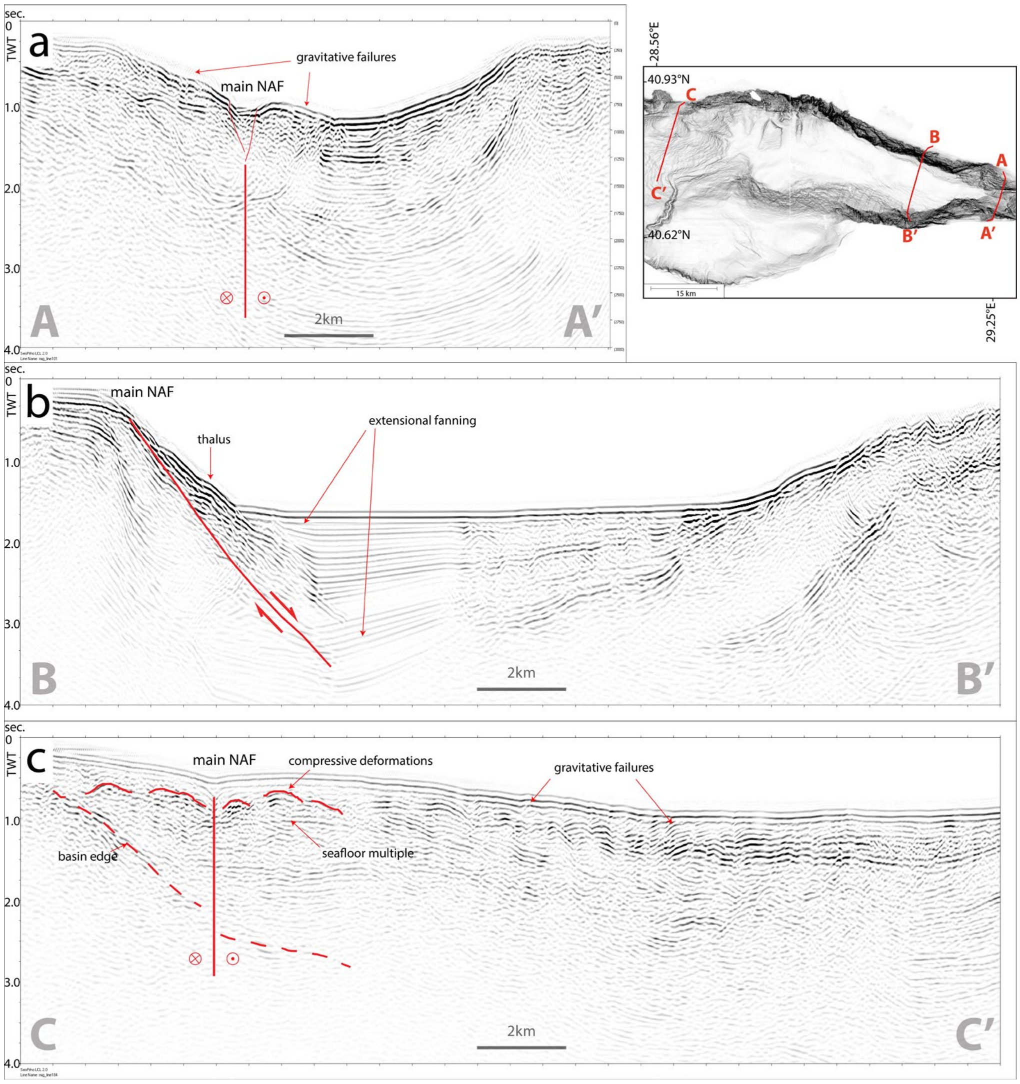

Figure 5-3 *Seismic profiles across the Cinarcik Basin. a) Line 101 (section A-A') located immediately E of the Tuzla Bend; b) Line 122 (section B-B'), crossing the central part of the Cinarcik basin; c) Line 184 (section C-C') cutting across the NAF trace to the west the Istanbul Bend. All seismic reflection profiles were collected during the SEISMARMARA cruise (Hirn et al. 2001; Carton et al., 2007).*

At the western end of the basin, the shelf margin bends again towards 255°N and shows a rectilinear shape clearly controlled by tectonic deformation (Fig. 5.3b). Line 184 (section C-C' in Fig. 5.3c) shows a composite deformation pattern. To the north, a high-amplitude reflector, probably marking the acoustic basement's top (basin edge in Fig. 5.6), is displaced by a sub-vertical fault showing a clear topographic expression. This structure, characterized by strike-slip kinematics, coincides with the present-day principal displacement zone of the NAF-N, (Fig. 5.3c). Between the high-amplitude reflector and the vertical fault, reflectors are folded and pervasively deformed by compressive deformation. This pattern is probably the effect of transpressive stresses, active in the past and subsequently replaced by almost pure strike-slip displacement along the sub-vertical NAF-N trace. This interpretation seems to be confirmed by the presence of more recent gravitative/extensional failures along the slope that mark the slumping and dismantling of the topographic high through mass-wasting towards the basin depocenter.

5.3 Analogue Models: setup and material

The analogue model experiments described in this paper were designed to simulate the eastern portion of the NAF-N in the Sea of Marmara, and to obtain further insights on the relationships between the present segmentation and the evolution of the major fault (Fig. 5.2). In particular we focussed on how the different orientations of the fault segments can influence the kinematics of the pull-apart basin and the propagation of strain in a dextral transtensional regime. Model results were compared with marine geophysical data that includes a multibeam echosounder morpho-bathymetric map collected by IFREMER in 2000 (Le Pichon et al., 2001) and a set of multichannel seismic reflection profiles collected during the SEISMARMARA cruise (Hirn et al., 2001) described in the previous section.

The experimental apparatus consisted of a sandbox with a 250 x 100 cm glass basal plate, equipped with one computer-controlled motor, and a “structured” light scanner to monitor the topographic surface of the model with a resolution of 0.71 mm in the x and y directions. In structured light scanning, also known as “point cloud ”, mapping, a pattern (e.g., a grid of dots) is projected onto the surface to be scanned. The distortion of this grid is then used to reconstruct the surface’s relief. This provides an effective tool to comprehensively measure model uplift and subsidence. This method allows for high precision quantitative measurements of deformation (e.g., Nestola et al., 2013; D'Adda et al., 2017). The evolution of the model was recorded using an overhead NIKON-D5200 digital with 6000x4000 pixel resolution, while a free to move secondary camera was dedicated to photograph cross sections. In this experimental programme, the overhead camera captured images and the structured light scanning provided elevation data every 20 minutes, corresponding to 5 mm increments of basal plate displacement. Experiments were performed using a 1 mm-thick Plexiglas mobile plate that was properly cut to reproduce a simplified geometry of the NAF-N in the study area (Fig. 4).

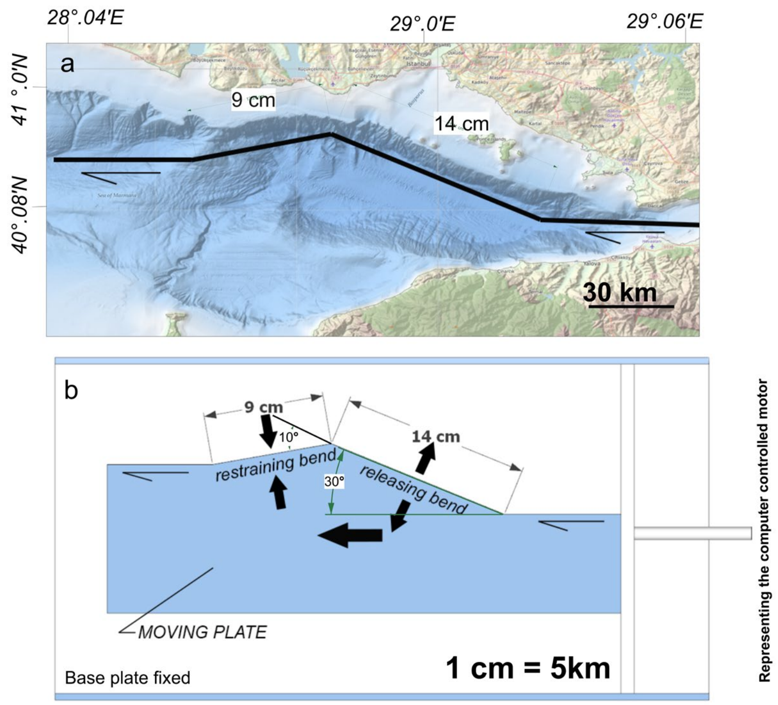

Figure 5-4 *a) Geometrical setting of the plate boundary in the study area reproduced using a plexiglas-moving plate. b) Plan view of the setup a the initial pre-cut step including analogue scaled lengths. The piston on the right represents the computer-controlled motor within the system.*

The base plate was cut with a 14 cm length releasing bend adjacent to a 9 cm restraining bend which form an angle of 10° (Fig. 5.4). This cut constitutes the "basal fault" of the model. Dextral shear was imposed onto the mobile plate by translating it at a constant displacement rate of 2 cm/h, for a total displacement of 7 cm. The scaling factor of the models was 2 x 10^{-6} (1 cm per 5 km): the 15 km-thick upper crust (Kende et al., 2017) was reproduced by a 1.5 cm-thick sand pack, while 0.2 cm of silicone represented the ductile lower crust. Serial cross sections with 0.5 cm spacing were cut at the end of the experiments after wetting the models with tap water and waiting 24 h to ensure complete imbibition. The brittle upper crust was simulated with a 1.5 cm-thick sand pack consisting of six 0.2 cm-thick alternating white and coloured quartz sand layers. Density of the sieved sand was 1.670 g/cm^3 and the mean quartz grain size was 224 ηm. The angle of internal friction was 33° and cohesion at peak was 102 Pa (see Table 1) (e.g., D'Adda et al., 2017). To simulate the mechanical displacement of the viscous lower crust, a basal layer of PDMS XIAMETER silicone putty mixed with barite powder was placed at the base of the sand pack, resulting in a thickness of 0.1 cm on the moving plate and 0.2 cm on the basal plate (orange layer in Fig. 5.5). The density of this layer was 1.15 g/cm^3 and the dynamic shear viscosity was 1.4 x 10^4 Pa-s.

Table 5-1 **Mechanical and physical properties of the materials used in the model**

Materials	Density (g/cm^3)	Mean grain size (ηm)	Cohesion at peak (Pa)	Angle of internal friction (φ)	Dynamic shear viscosity η (Pas)
Sand[1]	1.670	224	102	33°	- - - -
Silicone + barite [2]	1.150	- - - -	- - - -	- - - -	1,4 x 10^4

[1] Upper crust (from Klinkmüller et al., 2016)
[2] Weak lower crust (from Cappelletti et al., 2013)

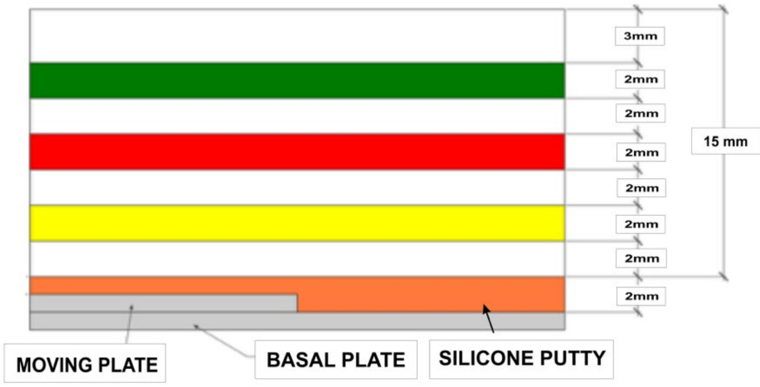

Figure 5-5 *Initial stratigraphy chosen for the experiment. The multilayer is formed by a basal plate topped by a purposely cut, 1 mm-thick plexiglass plate able to move, overlaid by silicon putty reaching a maximum thickness of 2 mm. Six 2 mm-thick sand layers topped by a 3 mm-thick layer complete the setup.*

5.3.1 Particle Image Velocimetry (PIV)

Particle Image Velocimetry allows for compilation of displacement/velocity map through measurements of particle displacements across the sand surface between successive photographs (White et al., 2001; Adam et al., 2002; Adam et al., 2005; Wolf et al., 2003), here taken every 4 mins during the experiment. It reveals where, how and when deformation occurs in the model.

Here we use interrogation areas of pairs of images in 64x64 and 32x32 pixel subregions gathered from 146 images to derive the best-fit particle displacement in the interrogation areas through use of the cross-correlation method implemented in the free MATLAB-based PIV-Lab Software package (Thielicke and Stamhuis, 2014). This led us to obtain a velocity field from incremental particle displacements at any the time frame. Incremental shear rates, shear strains and rates of topographic change were calculated using an open source code;

(see Bulkan, 2020; https://doi.org/10.5281/zenodo.3597335) to sample the material derivative of the finer topographic grid. It uses the velocity gradient matrix created by measuring the derivatives of the u and v velocity components in the x and y directions (Eq.1) ΔV represents the velocity gradient matrix:

$$\Delta V = \begin{bmatrix} \partial u/\partial x & \partial u/\partial y & \partial u/\partial z \\ \partial v/\partial x & \partial v/\partial y & \partial v/\partial z \end{bmatrix} \quad (1)$$

The incremental horizontal shear rate is approximated to be a velocity gradient perpendicular to the velocity discontinuity applied at the base of the model ($\partial u/\partial y$).

The areal strain is the sum of the diagonal components of ΔV ($E_{xx} + E_{yy}$):

$$E_{xx} + E_{yy} = \partial u/\partial x + \partial v/\partial y \quad (2)$$

The code calculates incremental rates of topographic changes by subtracting the measured topography at time *n-1* from topography at time *n*, corrected for any displacement between times *n-1* and *n*. Specifically, the material derivative of topography is determined, i.e., the change in topography over a time-step that follows the motion at the surface. To do this, the software measures the relief on the finer mesh of points at each model step, and uses an interpolation of the velocity field determined from the coarser mesh of PIV sampling subregions to backtrack each sample point on the fine mesh to where it started from at the end of the previous time step. The difference between these measurements is the change in relief of this surface point over the time step. Rates of incremental topographic changes are then related to the incremental strain patterns in order to understand how relief is generated. Shear rate maps estimate the amount of shear deformation during each step of the model, while areal strain maps show the rates of extension and compression in each area.

5.4 Experimental Results

5.4.1 Cross-sections

The setup geometry imposed to the model fault generated through transtensional and transpressional deformation with distributed and focused patterns that follow the along-strike segmentation of the fault. This is visible in the 3D perspective view of the final model step, after 7 cm of cumulative displacement (Fig. 5.6). Overall, the basin topography shows a graben corresponding to the Cinarcik basin depocenter, and the development of a topographic high at the western end of the basin, in correspondence with the Istanbul Bend. The graben forms as an asymmetric pull-apart basin narrowing towards the eastern (right) side, with the deepest area localised in the centre of the basin (Fig. 5.6). From east to west, the deformation pattern shows the along-strike development of three systems with different fault characters and associated relief: 1) almost pure strike-slip with neutral relief; 2) transtension and negative topography; 3) transpression and high positive relief.

The final model state was cut along eighteen profiles to provide vertical cross- sections displaying the internal geometry within the block. Variability in the deformation patterns is represented by three profiles including pure strike-slip deformation, transtension, and transpression (Figs. 5.6 and 5.7).

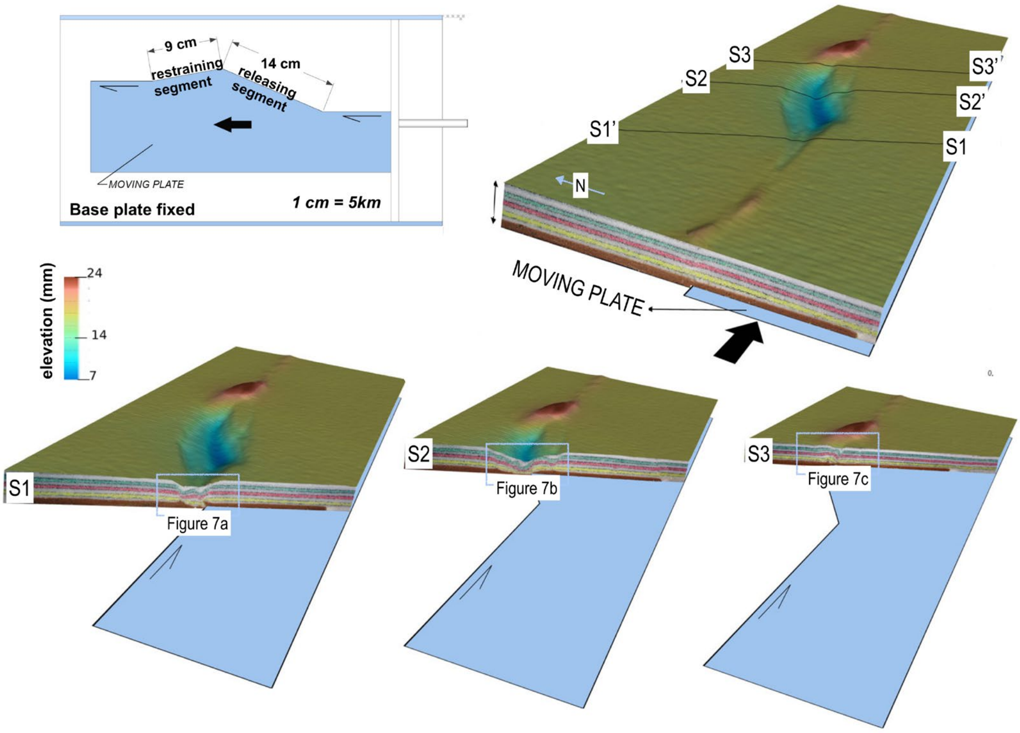

Figure 5-6 *Results of the analogue modelling experiment. 3D view of the last deformation step after 7 cm of total deformation with areas of uplift and subsidence highlighted by a colour pattern (red= uplift; blue=subsidence; green=neutral). Key sections chosen as representative of the overall deformation pattern are also indicated (see close up views in Fig. 5.7). Photographs are complemented by laser scan images of the model surfaces observe the total subsidence and interpreted faults. Blue arrow points north. The left top image shows the initial model setup.*

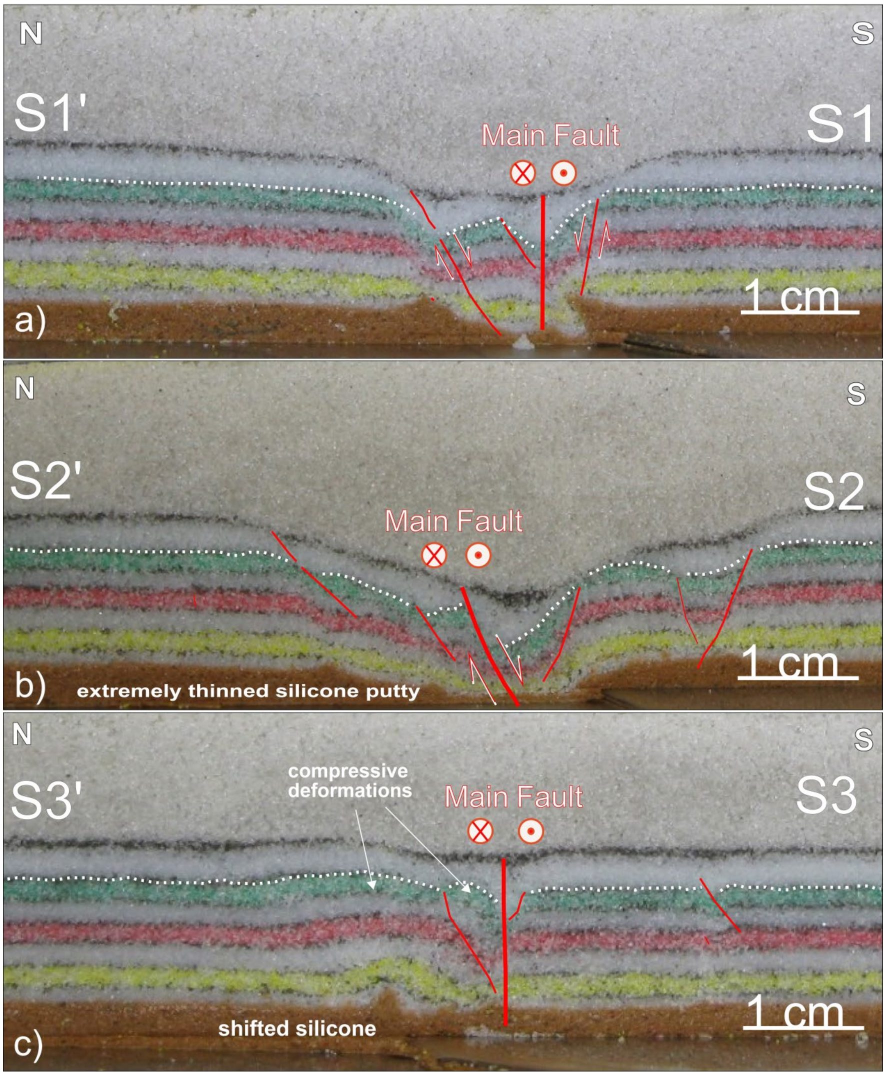

Figure 5-7 *Close-up views of the fault trace in the cross sections presented in Fig.6. The coloured sand packages represent sediments layers in the upper crust, each layer is 2 mm thick. The upper 3 mm-thick white layer was applied after the experiment was run to preserve the developed structures. The orange silicone putty represents the lower crust.*

Section 1 represents modelled deformations in the easternmost region. The close-up view of Fig. 5.7a shows that deformation in this region is accommodated by a main sub vertical strike-slip fault that cuts through the lower crust (silicon putty), with this fault being bounded by a series of secondary faults that accommodate transtensive deformation. The normal component of displacement taken up by secondary faults is responsible for the development of a narrow asymmetric depression.

Proceeding towards the basin centre, Section 2 (Fig. 5.7b) highlights the presence of extensional deformation (with a minor strike-slip component) that creates a topographic depression cutting through the entire lower crust putty. The extensional stress generates a wide graben controlled by a series of domino faults and rollover anticlines. Deformation is mainly controlled by a main fault located to the north of the basin and dipping towards the south, corresponding to the NAF-N principal displacement zone. This fault that follows the weak zone with the thinned silicone putty is bounded by synthetic and antithetic secondary faults (Fig. 5.7b).

To the west of the model, Section 3 (Fig. 5.7c) shows folding of the layers to form a gentle transpressional pop-up structure in the north that is cut by a master fault and by secondary faults. Here the master fault is almost vertical, and the dextral strike-slip motion appears localised, analogous to the behaviour of the NAF main track in this region. The lower crust silicone putty was mobilized by deformation, resulting in a shift and protrusion at the base of the folded layers. Despite compression and uplift of the layers, the secondary faults show a normal component. These secondary faults are present only to the south of the master faults and show decreasing dip angles and increasing displacements as they approach the master fault (Fig. 5.7c).

To summarize, the simple initial geometry imposed to the model was able to reproduce a deformation pattern similar to that observed in the Cinarcik basin, both in term of basin geometries and the fault deformation patterns observed in the seismic reflection profiles.

5.4.2 *Tectonic Strain and Topography*

Segmentation of the NAF-N is responsible for oversteps and changes in fault orientation at both ends of the Cinarcik basin. To understand how these geometries can influence strain accumulation and propagation during and after major earthquakes, we analysed the evolution of the incremental shear rate over the course of our experiment. Fig. 5.8 shows three phases of deformation corresponding to increasing displacement along the basal fault.

Shear rate, topographic change and areal strain portray how intensity and velocity of deformation is distributed and how they are translated into permanent deformation. Elastic strain accumulation is not directly calculated. Initially, between 15 and 20 mm of basal displacement, the imposed shear is transferred from the E-W segments of the fault to the releasing-restraining pair, but deformation there seems much slower (Fig. 5.8a). The eastern and the western fault bends are nodal points where the strain rate dramatically changes. Model topography shows that the releasing-restraining sectors accumulate most of the permanent deformation, both transtensive and transpressive. The apparent slower deformation possibly implies a diffuse *vs.* concentrated shear distribution. However, to the east of the eastern bend (corresponding to the Tuzla Bend) and to the west of the western bend (corresponding to the Istanbul Bend) the presence of high relief coincident with shear maxima suggest that shear stress is not completely transferred, and permanent deformation is a direct effect of fault segmentation (Fig. 5.8b). Interestingly, the restraining bend is characterised by compressional strain at the edge of the uplifted area, while extension is present along the central fault trace within the compressional region (Fig. 5.8b, c). The same pattern is visible between 25 and 30 mm of displacement, when the high shear rate of the eastern east-west segment drops at the releasing bend more than it did earlier, while the shear rate increases more strongly across the restraining bend (Fig. 5.8d). Associated with these changes in shear rate, the topographic change seems to slowly migrate towards the west (Fig. 5.8e). The strain pattern of compression and extension only partially corresponds to the observed uplift and subsidence. In fact, the extensional deformation on the releasing bend becomes wider and is distributed into three separate zones (Fig. 5.8f). Between 45 and 50 mm of displacement, more deformation is concentrated throughout the restraining bend. The maximum shear rate in the releasing bend shifts toward the south and, most interestingly, is dissipated in the central part (Fig. 5.8g).

In general, through its evolution, the model shows that most of the shear strain was concentrated along the two edges of the model Cinarcik segment, with strong drops at its centre. Moreover, it suggests that maximum topographic changes, i.e., the stronger permanent deformations, are the result of strain concentrations at the bending points, while the reduction of the shear rate along the releasing and restraining bends might be the result of strain diffusion (Fig. 5.8a). The equivalent of the Cinarcik segment shows that slow deformation corresponds to topographic uplift, but compression only marks the edge of the uplifted area. In contrast, extension and subsidence above the releasing bend is accommodated by a narrow asymmetric depression (Fig. 5.8b, e, h).

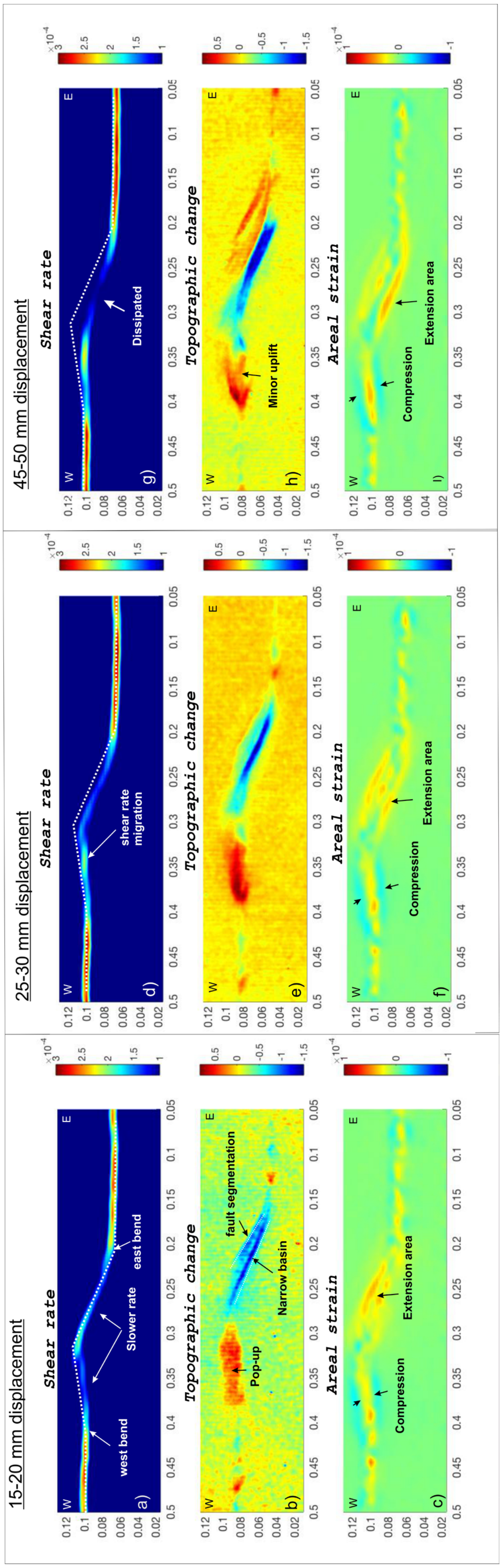
15-20 mm displacement
25-30 mm displacement
45-50 mm displacement
Shear rate
Topographic change
Areal strain
west bend
Slower rate
east bend
fault segmentation
Narrow basin
Pop-up
Compression
Extension area
shear rate migration
Dissipated
Minor uplift
W
E
a)
b)
c)
d)
e)
f)
g)
h)
i)

Figure 5-8 *Comparison of shear rate, topographic change, and areal strain during three phases of the progressive deformation: between 15-20 mm (a,b,c); 25-30 mm (d,e,f); and 45-50 mm (g,h,i), of displacement. Shear rate unit is 1/m, areal strain is dimensionless (m/m). In the figure panels, blue refers to low shear rates, negative topographic changes and compression, while red refers to high shear rates, positive topographic changes and extension, respectively. See text for details.*

5.5 Discussion

5.5.1 Experimental limitations

Before exploring how the analogue models correlate with marine geological/geophysical data, we should underline their possible limitations. First of all, a typical limiting factor in sandbox modelling is the lack of fluids permeating the "experimental" crust, both in host rock pores and localized within shear zones. It is known that pore fluid pressure is a major factor that shapes deformation patterns and fault activity in nature (e.g., Chester et al., 1993). In our case, being the Cinarcik fault segment below sea water, fluid percolation could play a key role in reducing the effective stress along the fault. Other significant oversimplifications in the sandbox experiments are also their lack of a geothermal gradient, of mineral reactions constraining rock rheology variations, and of an isostatic and flexural response to tectonic deformation. A specific feature of most experiments that simulate strike-slip faulting is localization of the master shear zone at a sharp boundary between nondeformable and mobile basal plates. In our model, we used a 2 mm-thick silicone layer, scaled to the relative thickness of the viscous lower crust as suggested by Kende et al. (2017). The thickness and viscosity of this layer controls how efficiently basal displacement is transferred to the shallower crust. Crustal heterogeneities were also not incorporated into the model, and this should be considered when comparing the experiments to nature. The experimental crust is, in fact, assumed to be mechanically homogeneous, without heterogeneities or inheritances that might influence deformation patterns. For example, heterogeneities in the crust deformed by the NAF system have been proposed to play an important role in strain localization

(LePichon et al., 2016). Moreover, our model does not include the effects of sedimentation, while in nature the Cinarcik Basin has 4-6 km of sedimentary infill that is likely to consist of Pliocene-Quaternary syn-kinematic sediments (Carton et al., 2007). Finally, the shape of the master strike-slip right-lateral fault system in the experiments is simplified with respect to nature (Fig. 5.4a).

In this study, where the strain accumulation was directly linked along different segments of the fault, another limitation is the lack of distinction between elastic and anelastic deformation. Since we are dealing with restraining and releasing bends, topographic changes are able to record permanent deformations, as well as their intensity and nature, while this would not be possible in a pure strike-slip kinematic environment. Given the above, the purpose of our modelling was not to exactly reproduce the geometries of the real world, but rather to verify whether a simple geometry imposed as an initial condition in the model was able to account for the strain distribution observed along this complex tectonic system.

5.5.2 Bending points as stress barriers: comparison between the model and the natural case

The analogue experiment, with a releasing and restraining bend pair along a segmented transform fault, shows that the bending points represent indeed a “transition” in terms of the strain rate and character of the observed deformation pattern. The model shows relatively “slow” shear along the releasing and restraining bend pair. In contrast, the eastern and western east-west parallel segments, with “pure” strike-slip displacements, are characterised by relatively high shear rates. Despite their slower shear rate, the topographic response on the releasing and restraining pairs is significant, with the generation of subsidence and uplift over wide areas, and with the generation of high morphological gradients (Fig. 5.8h). In the model counterpart to the extending Cinarcik segment, for example, strain partitioning results in the formation of a basin, i.e., a permanent topographic depression. So, since strain is able to be transferred from the eastern pure strike-slip segment to the depocenter of the basin, the bending point cannot be considered a stress barrier, but rather a point where strain spreads out and diffuses. This characteristic seems to increase with the amount of displacement up to the centre of the extending Cinarcik segment, where differences across surrounding structures are not measurable (Fig. 5.8g). Nevertheless, the total strain in this region may still be constant. In fact, the areal strain pattern in our model shows that deformation involves a wider region compared to the pure strike-slip segment to the east of Tuzla Bend, and that deformation increases in the area characterised by negligible strain rate (Fig. 5.8i). Interestingly, this area in the model corresponds to one of the most debated areas of the Sea of Marmara, where both fault kinematic and strain accumulation along the faults is discussed, as it is considered the next segment that will rupture after the Izmit 1999 event, in the assumed westward-migrating earthquake sequence (Parsons, 2000; H. Ferrari et al., 2001; Uçarkuş et al., 2011; Bohnhoff et al., 2013). Most studies agree that the strike-slip motion characterising the eastern part of the NAF before entering the Gulf of Izmit, changes into transtension as it reaches the Cinarcik basin (Armijo et al., 2002; Le Pichon et al., 2003; Carton et al., 2007). This interpretation is also confirmed by the analysis of seismic reflection profiles presented in this paper, clearly showing the transition from a focused, mostly strike-slip shear east to the eastern bending point (Section A-A’ in Fig. 5.3), to the wider mostly normal shear in the centre of the basin (Section B-B’ in Figure 3). This observation is supported by the experimental results that indicate a transition from concentrated to diffuse shear, but not to the presence of a barrier to the westward propagation of strain.

Further extrapolation of our results would suggest that seismic slip occurring to the east of the bend would increase elastic strain accumulation on the adjacent segment to the west, but this strain might be partitioned over a wide area. Our experiments are not able to discriminate whether strain could be dissipated through aseismic creep or small seismic events. Subsidence might be facilitated because complete elastic rebound in normal faults is inhibited by gravity, so that permanent deformation accumulates with time (Carton 2003; Hirn 2003; Seeber et al., 2004; Pondard et al., 2007). The experiments suggest that if elastic strain is involved, it accumulates at a slower rate in transtensional faults than in strike-slip segments. Therefore, the normal faulting at the edges of the Cinarcik basin might involve several seismic cycles of the adjacent strike-slip fault segment to reach a critical stress state. This would imply significative differences in seismic cycles between the Izmit and Cinarcik segments of the NAF. Thus, if the Tuzla Bend is able to transfer shear stress towards the west, it appears that it would be distributed into several fault strands, affecting the earthquake magnitudes and recurrence time intervals along the Cinarcik segment, that would be less effective in accumulating and releasing tectonic loads in comparison to the Izmit segment.

Many geological and geodetic observations document evidence of the impact of fault bends and associated folding on earthquake cycles (Suppe, 1983; Shaw et al., 2005; Sathiakumar et al., 2020). In the case of San Andreas Fault, slip partitioning because of the restraining Big Bend and the loading of buried faults below the Los Angeles metropolitan area might have an impact on earthquake cycles (Li & Liu, 2007; Li et al., 2009; Daout et al., 2016). Similarly, the Lebanese restraining bend along the Dead Sea Fault Zone seems to be responsible for partitioned crustal deformation into NNE-SSW strike slip faults and regional WNW-ESE crustal shortening that involves distinct sets of earthquakes in different striking faults (Gomez et al., 2007).

5.5.3 The compressive deformations of the NW edge of the Cinarcik Basin

The NW edge of the Cinarcik basin is the site of a topographic high characterized by evidence of folding and compressive deformation. To highlight this pattern, we combined the morphobathymetric map of the Cinarcik basin area (slope map in the background) with the elevation map resulting from the analogue model at the end of the experiment (Fig. 5.9). Scaling between the two representations was carried out by using as a reference the position and length of the NAF-N principal deformation zone. The transtensional deformation pattern of the model, characterized by negative topography (the blue colour in the topographic change panel in Fig. 5.8), overlaps with the deepest portion of the Cinarcik basin, while the red pattern, highlighting the generation of positive relief in a region of overall compressive deformation in Fig. 5.8, is concentrated immediately to the west of the Istanbul Bend. We note that the geometrical conditions imposed to the model, although very simple, account surprisingly well for the observed regional deformation pattern, both in its nature and scaled magnitudes. However, since bathymetry can be affected by surficial processes (gravitative instability, erosion, currents, sediment deposition, etc.) rather than deformation caused by deep-seated faults, the comparison between the model and the nature of deformation should consider the subsurface images, such as seismic reflection profiles described in paragraph 2.1.

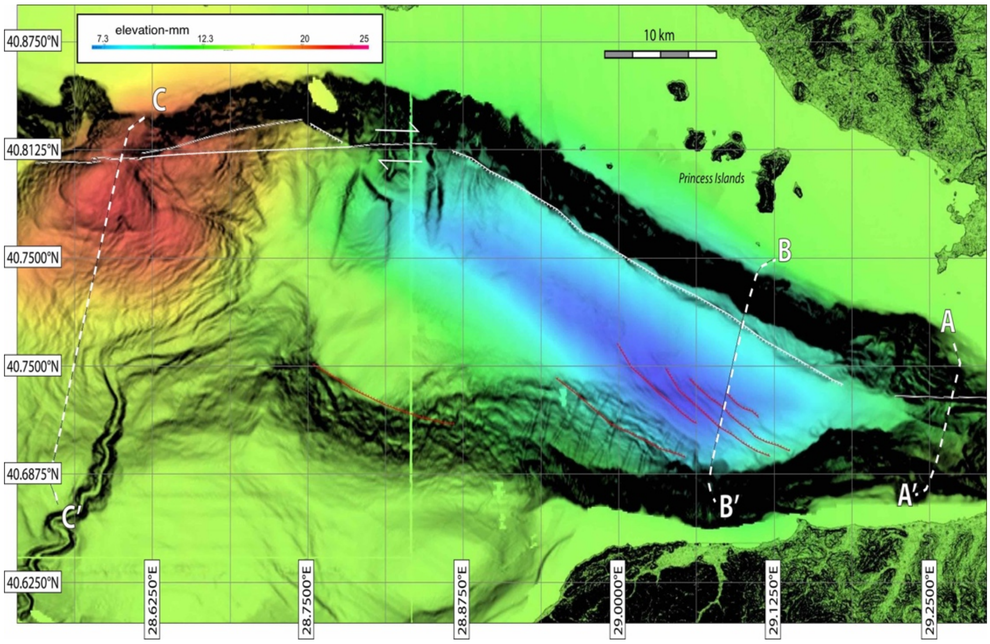

Figure 5-9 *Superposition of morphobathymetry (slope map in background) and elevation map resulting from analogue modelling (red=uplift; blue=subsidence; green= neutral). Morphobathymetric data are from Le Pichon et al., (2001). White solid lines mark fault segments constituting the principal deformation zone of the NAF, while red lines indicate secondary normal faults. Position of seismic sections shown in Fig. 5.3 is also indicated (white dashed lines).*

Starting from the east, both the model and geophysical data show a narrow through resulting from a sub-vertical trace of the fault (Figs. 2, 7a). In the model, in fact, the northern boundary fault of the basin is steeply dipping, which correlated well with the geometry of the fault at the margin of (Carton et al., 2007). Moving to the west, in the centre of the Cinarcik Basin, the features imaged along the seismic profiles and the model show similar deformation patterns (Fig. 5.3b and Fig. 5.7b), with an important component of extension being the characteristic of this segment of the fault (Fig. 5.9). The seismic profile shows that the change in dip orientation of the major fault plays a key role in the morphology of the basin, that becomes wide and deep, but with asymmetric slope angles. The model shows that this change is compatible with a small – 30° - diversion of the trace of the main fault. The resulting morphology of the basin is also well matched, with the northern side of the basin steeper and therefore more prone to gravitational instability of sediments than the opposite side.

Finally, compressional deformation characterizes the western half of the Cinarcik basin to the west of the so-called Istanbul Bend (Fig. 5.2). In both the model and real world, the western half of the depression becomes narrower and shallower towards the west. The model also correlates well with the NE-SW trending morphobathymetric uplift of the Central High. The orientation of the main fault changes again to a vertical trace in both the model and the Cinarcik basin (Fig. 5.7c). The comparison between experimental results and seismic interpretations carried out on available seismic lines strengthens the idea that a restraining bend adjacent to a releasing bend with a difference of ~10° in orientation might produce a change in width of the basin, a topographic high with the characteristics observed in the NW Cinarcik basin, and changes in fault orientations as observed along the tectonic boundary (Fig. 5.7c). This would support the idea that the formation of the Central High with its ~400m relief may be controlled by the interaction of the restraining bend and the master fault at depth. The model also suggests that this relief may be related to the characteristics of the fault at depth, where the lower crust appears to be deformed and mobilized by the fault and by flower style branching faults cut the entire crust.

5.6 Conclusions

The Cinarcik basin, a tectonic depression along the North Anatolian Fault in the Sea of Marmara, is bounded in its northern edge by a seismogenic fault that connects the Istanbul metropolitan area to the Izmit fault segment which ruptured in 1999 during a Mw 7.4 earthquake. We successfully reproduced tectonic deformations in this area with a simple analogue model characterised by a velocity discontinuity imposed at its base by a moving basal plate that has an edge profile which reproduces the shape of the principal displacement zone of the North-Anatolian Fault in this sector. As displacements are slowly applied at the base of the model, a first principal shear zone forms along the velocity discontinuity, with associated growth of horst and graben deformation patterns above the restraining and releasing bend segments, respectively. The model layout is able to reproduce the main characteristics of the Cinarcik basin, both in terms of its fault kinematics and morphology. This led us to analyze the transfer of stress between the different fault segments. We propose that the Izmit segment can transfer strain to the Cinarcik segment, as most probably happened after the 1999 earthquake. However, the partitioning of deformation from strike-slip to transtension, moving from the Izmit to the Cinarcik segment, may induce slower strain accumulation in this latter, resulting in a longer seismic-cycle for earthquakes of similar magnitude. This conclusion might suggest a general delay for earthquakes occurring on the Cinarcik segment that will be eventually triggered by tectonic loading from the east. Our results also suggest that most of deformation observed along the North-Anatolian Fault between the rupture termination of the Izmit 1999 earthquake and the Istanbul metropolitan area is controlled by the change in geometry of the fault segments. In particular, compressive deformation observed at the connection between the Cinarcik and the Central High segments was reproduced in the model by imposing a small - 10° - sharp change in the relative orientations of the segments. We suggest that this change in orientation could reflect the presence of inherited geological heterogeneities cut by the NAF along the complex suture that constitutes this margin, particularly in the Sea of Marmara region.

Acknowledgments

We thank Associate Editor Ramon Carbonell, and anonymous reviewers for their constructive feedback that helped improve the quality of the manuscript. This work was fostered by visits funded by the FLOWS-COST Action ES1301 “FLOWS”. Analogue models were produced in the Analogue Modelling Laboratory “E. Costa” of the Department of Chemistry, Life Sciences and Environmental Sustainability, University of Parma, Italy. We thank J. P. Morgan for his help with the science and writing.

The seismic reflection profiles are part of the SEISMARMARA cruise dataset and are downloaded from the IFREMER web site (https://campagnes.flotteoceanographique.fr). The MATLAB code for geological models is available on the Zenodo, open-access repository web-site (https://doi.org/10.5281/zenodo.3597335). We would like to thank Pierre Henry for contributing in our code to analyse our dataset.

All other sources used to build to geological models are published and referenced in the manuscript. Input files necessary to reproduce the model are available from the authors upon request (Sibel.Bulkan.2015@live.rhul.ac.uk).

5.7 References

Adam, J., Lohrmann, J., Hoth, S., Kukowski, N., & Oncken, O. (2002). Strain variation and partitioning in thrust wedges: High-resolution data from scaled sandbox experiments by 2D–3D PIV analysis. Bollettino di Geofisica teorica ed applicata, 42, 123-125.

Adam, J., Urai, J. L., Wieneke, B., Oncken, O., Pfeiffer, K., Kukowski, N., & Schmatz, J. (2005).Shear localisation and strain distribution during tectonic faulting—New insights from granular-flow experiments and high-resolution optical image correlation techniques. Journal of Structural Geology, 27(2), 283-301.

Ambraseys, N. 2002. The seismic activity of the Marmara Sea region over the last 2000 years Bull. Seismol. Soc. Am., 92, 1–18.

Armijo, R., B. Meyer, A. Hubert, and A. Barka, 1999. Westward propagation of the North Anatolian fault into the northern Aegean: Timing and kinematics, Geology, 27, 267–270.

Armijo, R., B. Meyer, S. Navarro, G. King, and A. A. Barka (2002). Asymmetric slip partitioning in the Sea of Marmara pull-apart: A clue to propagation processes of the North Anatolian Fault? Terra Nova,14,80–86, doi:10.1046/j.1365-3121.2002.00397.x.

Armijo, R., Pondard, N., Meyer, B., Mercier de Lapinay, B., & Ucarkus, G. the MARMARASCARPS Cruise Party (2005). Submarine fault scarps in the Sea of Marmara pull-apart (North Anatolian Fault): implications for seismic hazard in Istanbul. Geochem. Geophys. Geosyst, 6(6), 453-468.

Baştürk, N. B., Özel, N. M., & Caciagli, M. (2016). Seismic parameters re-determined from historical seismograms of 1935-Erdek–Marmara Island and 1963-Çınarcık Earthquakes. Earth, Planets and Space, 68(1), 158.

Başarır Baştürk, Nilay & Meral Ozel, Nurcan. (2020). Seismic parameters re-determined from Historical Seismograms of 1935-Erdek– Marmara Island and 1963-Çınarcık Earthquakes.

Barka, A. A. (1992), The North Anatolian fault zone, Ann. Tectonicae,6,164–195.

Barka, A. A., and K. Kadinsky-Cade (1988), Strike-slip fault geometry in Turkey and its influence on earthquake activity, Tectonics,7, 663–684,doi:10.1029/TC007i003p00663.

Barka, A. A., and I. Kuscu (1996), Extents of the North Anatolian Fault inthe Izmit, Gemlik and Bandirma Bays,Turkish J. Mar. Sci.,2,93–106.

Bécel, A., Laigle, M., de Voogd, B., Hirn, A., Taymaz, T., Galvé, A., ... & Özalaybey, S. (2009). Moho, crustal architecture and deep deformation under the North Marmara Trough, from the SEISMARMARA Leg 1 offshore–onshore reflection–refraction survey. *Tectonophysics*, *467*(1-4), 1-21.

Bécel, A., Laigle, M., De Voogd, B., Hirn, A., Taymaz, T., Yolsal-Cevikbilen, S., & Shimamura, H. (2010). North Marmara Trough architecture of basin infill, basement and faults, from PSDM reflection and OBS refraction seismics. Tectonophysics, 490(1-2), 1-14.

Bohnhoff, M., Bulut, F., Dresen, G., Malin, P. E., Eken, T., & Aktar, M. (2013). An earthquake gap south of Istanbul. Nature communications, 4, 1999.

Bulkan, S., (2020). Geological and kinematic evolution of the western part of the North Anatolian Fault system: an analogue modelling investigation. Thesis. Royal Holloway, University of London. Available at: https://pure.royalholloway.ac.uk/portal/en/publications/

Cappelletti, A., Tsikalas, F., Nestola, Y., Cavozzi, C., Argnani, A., Meda, M., & Salvi, F. (2013). Impact of lithospheric heterogeneities on continental rifting evolution: Constraints from analogue modelling on South Atlantic margins. *Tectonophysics*, *608*, 30-50.

Carton, H., Singh, S. C., Hirn, A., Bazin, S., De Voogd, B., Vigner, A., ... & Sevilgen, V. (2007). Seismic imaging of the three-dimensional architecture of the Çınarcık basin along the North Anatolian fault. Journal of Geophysical Research: Solid Earth, 112(B6).

Chester, F. M., Evans, J. P., and Biegel, R. L. (1993), Internal structure and weakening mechanisms of the San Andreas Fault, J. Geophys. Res., 98(B1), 771– 786, doi:10.1029/92JB01866.

Cunningham, W. D., & Mann, P. (2007). Tectonics of strike-slip restraining and releasing bends. *Geological Society, London, Special Publications*, *290*(1), 1-12.

Çakir, Z., Ergintav, S., Özener, H., Dogan, U., Akoglu, A. M., Meghraoui, M., & Reilinger, R. (2012). Onset of aseismic creep on major strike-slip faults. Geology, 40(12), 1115-1118.

D'ADDA P., LONGONI R., MAGISTRONI C., MEDA M., RIGHETTI F., CAVOZZI C., NESTOLA Y. & STORTI F. (2016) – Extensional reactivation of a deep transpressional architecture: insights from sandbox analogue modeling applied to the Val d'Agri basin (Southern Apennines, Italy). Interpretation, 5, 55-66.

Daout, S., Barbot, S., Peltzer, G., Doin, M. P., Liu, Z., & Jolivet, R. (2016). Constraining the kinematics of metropolitan Los Angeles faults with a slip-partitioning model. Geophysical research letters, 43(21), 11-192.

Ergintav, S., R. E. Reilinger, R. Çakmak, M. Floyd, Z. Cakir, U. Doğan, R. W. King, S. McClusky, and H. Özener (2014). Istanbul's earthquake hot spots: Geodetic constraints on strain accumulation along faults in the Marmara seismic gap, Geophys. Res. Lett., 41, 5783–5788, doi:10.1002/2014GL060985.

Gasperini, L., Stanghellini, G. (2009). SeisPrho: an interactive computer program for processing and interpretation of high-resolution seismic reflection profiles. *Computers & Geosciences*, 35, 1497-1507.

Gasperini, L., Polonia, A., M Çağatay, N., Bortoluzzi, G., Ferrante, V. (2011a). Geological slip rates along the North Anatolian Fault in the Marmara region. Tectonics, 30, C6001, doi:10.1029/2011TC002906.

Gasperini, L., A. Polonia, G. Bortoluzzi, P. Henry, X. Le Pichon, M. Tryon, M. N. Çağatay, and L. Geli (2011b), How far did the surface rupture of the1999 Izmit earthquake reach in Sea of Marmara Tectonics, 30, TC1010,doi:10.1029/2010TC002726.

Grall, C., Henry, P., Tezcan, D., Mercier de Lepinay, B., Bécel, A., Géli, L., & Harmegnies, F. (2012). Heat flow in the Sea of Marmara Central Basin: Possible implications for the tectonic evolution of the North Anatolian fault. *Geology, 40(1*), 3-6.

Grall, C., Henry, P., Thomas, Y., Westbrook, G.K., Çağatay, M.N., Marsset, B., Saritas, H., Çifçi, G., Géli, L., (2013). Slip rate estimation along the western segment of the Main Marmara Fault over the last 405–490 ka by correlating mass transport deposits. *Tectonics 32,* 1–15.

Gomez, F., Karam, G., Khawlie, M., McClusky, S., Vernant, P., Reilinger, R., ... & Barazangi, M. (2007). Global Positioning System measurements of strain accumulation and slip transfer through the restraining bend along the Dead Sea fault system in Lebanon. Geophysical Journal International, 168(3), 1021-1028.

Görür, N., & Çağatay, M. N. (2010). Geohazards rooted from the northern margin of the Sea of Marmara since the late Pleistocene: a review of recent results. *Natural Hazards*, *54*(2), 583-603.

HIRN Alfred, SINGH Satish (2001) SEISMARMARA cruise, RV Le Nadir, https://doi.org/10.17600/1080050

Hubert-Ferrari, A., Barka, A., Jacques, E., Nalbant, S. S., Meyer, B., Armijo, R., ... & King, G. C. (2000). Seismic hazard in the Marmara Sea region following the 17 August 1999 Izmit earthquake. Nature, 404(6775), 269-273.

Kende, J., Henry, P., Bayrakci, G., Özeren, M. S., & Grall, C. (2017). Moho depth and crustal thinning in the Marmara Sea region from gravity data inversion. Journal of Geophysical Research: Solid Earth, 122(2), 1381-1401.

Klinkmüller, M., Schreurs, G., Rosenau, M., & Kemnitz, H. (2016). Properties of granular analogue model materials: A community wide survey. *Tectonophysics*, *684*, 23-38.

Kurt, H., et al. (2013), Steady late quaternary slip rate on the Cinarcik section of the North Anatolian fault near Istanbul, Turkey, Geophys. Res. Lett., 40, 4555–4559, doi:10.1002/grl.50882.

Laigle, M., Becel, A., de Voogd, B., Hirn, A., Taymaz, T., & Ozalaybey, S. (2008). A first deep seismic survey in the Sea of Marmara: Deep basins and whole crust architecture and evolution. *Earth and Planetary Science Letters*, *270*(3-4), 168-179.

Le Pichon, X., Şengör, A. M. C., Demirbağ, E., Rangin, C., Imren, C., Armijo, R., ... & Saatçılar, R. (2001). The active main Marmara fault. Earth and Planetary Science Letters, 192(4), 595-616.

Le Pichon, X., N. Rangin, C. Chamot-Rooke, and A. M. C. Sengör, 2003. The North Anatolian Fault in the Sea of Marmara, J. Geophys. Res., 108(B4), 2179.

Le Pichon, X., Şengör, A. C., Kende, J., İmren, C., Henry, P., Grall, C., & Karabulut, H. (2016). Propagation of a strike-slip plate boundary within an extensional environment: the westward propagation of the North Anatolian Fault. *Canadian Journal of Earth Sciences*, *53*(11), 1416-1439.

Li, Q., Liu, M., & Zhang, H. (2009). A 3-D viscoelastoplastic model for simulating long-term slip on non-planar faults. Geophysical Journal International, 176(1), 293-306.

Li, Q., & Liu, M. (2007). Initiation of the San Jacinto fault and its interaction with the San Andreas fault: insights from geodynamic modeling. Pure and Applied Geophysics, 164(10), 1937-1945.

McClusky, S., Balassanian, S., Barka, A., Demir, C., Ergintav, S., Georgiev, I., ... & Kastens, K. (2000). Global Positioning System constraints on plate kinematics and dynamics in the eastern Mediterranean and Caucasus. Journal of Geophysical Research: Solid Earth, 105(B3), 5695-5719.

McClusky, S., Reilinger, R., Mahmoud, S., Ben Sari, D., & Tealeb, A. (2003). GPS constraints on Africa (Nubia) and Arabia plate motions. Geophysical Journal International, 155(1), 126-138.

Nestola, Y., Storti, F., Bedogni, E., & Cavozzi, C. (2013). Shape evolution and finite deformation pattern in analog experiments of lithosphere necking. *Geophysical Research Letters*, *40*(19), 5052-5057.

Okay, A. I., Tüysüz, O., & Kaya, Ş. (2004). From transpression to transtension: changes in morphology and structure around a bend on the North Anatolian Fault in the Marmara region. Tectonophysics, 391(1-4), 259-282.

Özeren, M. S., Çağatay, M. N., Postacıoğlu, N., Şengör, A. C., Görür, N., & Eriş, K. (2010). Mathematical modelling of a potential tsunami associated with a late glacial submarine landslide in the Sea of Marmara. *Geo-Marine Letters*, *30*(5), 523-539.

Parsons, T., Toda, S., Stein, R. S., Barka, A., & Dieterich, J. H. (2000). Heightened odds of large earthquakes near Istanbul: An interaction-based probability calculation. *Science*, *288*(5466), 661-665.

Parsons, T. (2004). Recalculated probability of M≥ 7 earthquakes beneath the Sea of Marmara, Turkey. Journal of Geophysical Research: Solid Earth, 109(B5).

Pondard, N., Armijo, R., King, G. C., Meyer, B., & Flerit, F. (2007). Fault interactions in the Sea of Marmara pull-apart (North Anatolian Fault): earthquake clustering and propagating earthquake sequences. Geophysical Journal International, 171(3), 1185-1197.

Sathiakumar, S., Barbot, S., & Hubbard, J. (2020). Earthquake cycles in fault-bend folds. Journal of Geophysical Research: Solid Earth, e2019JB018557.

Seeber, L., O. Emre, M.-H. Cormier, C. C. Sorlien, C. M. G. McHugh, A. Polonia, N. Ozer, and N. Cagatay (2004), Uplift and subsidence from oblique slip: The Ganos-Marmara bend and the North Anatolian Transform, western Turkey, Tectonophysics, 391, 239–258.

Seeber, L., Cormier, M. H., McHugh, C., Emre, O., Polonia, A., & Sorlien, C. (2006). Rapid subsidence and sedimentation from oblique slip near a bend on the North Anatolian transform fault in the Marmara Sea, Turkey. Geology, 34(11), 933-936.

Seeber, L., Sorlien, C., Steckler, M., & Cormier, M. H. (2010). Continental transform basins: Why are they asymmetric?. Eos, Transactions American Geophysical Union, 91(4), 29-30.

Shaw, J. H., Connors, C. D., & Suppe, J. (Eds.). (2005). Seismic interpretation of contractional fault-related folds: An AAPG seismic atlas (Vol. 53). Tulsa: American Association of Petroleum Geologists.

Smith, A. D., Taymaz, T., Oktay, F., Yuce, H., Alpar, B., Basaran, H., ... & Simsek, M. (1995). High-resolution seismic profiling in the Sea of Marmara (northwest Turkey): Late Quaternary sedimentation and sea-level changes. *Geological Society of America Bulletin*, *107*(8), 923-936.

Sorlien, C. C., Akhun, S. D., Seeber, L., Steckler, M. S., Shillington, D. J., Kurt, H., ... & İmren, C. (2012). Uniform basin growth over the last 500 ka, North Anatolian Fault, Marmara Sea, Turkey. Tectonophysics, 518, 1-16.

Suppe, J. (1983). Geometry and kinematics of fault-bend folding. American Journal of science, 283(7), 684-721.

Şengör, A. M. C., O. Tuysuz, C. Imren, M. Sakınc, H. Eyidogan, N. Gorur, X. Le Pichon, and C.Rangin (2005), The North Anatolian fault: A new look, Annu. Rev. Earth Plan Sci., 33, 37–112.

Thielicke, W and Stamhuis, E J 2014 PIVlab – Towards User-friendly, A ordable and Accurate Digital Particle Image Velocimetry in MATLAB. Journal of Open Research Software, 2: e30, DOI: http://dx.doi.org/10.5334/jors.bl

UÇARKUŞ, G., Cakir, Z., & Armijo, R. (2011). Western termination of the Mw 7.4, 1999 İzmit Earthquake rupture: Implications for the expected large earthquake in the Sea of Marmara. *Turkish Journal of Earth Sciences*, *20*(4), 379-394.

White, D. J., Take, W. A., Bolton, M. D., & Munachen, S. E. (2001). A deformation measurement system for geotechnical testing based on digital imaging, close-range photogrammetry, and PIV image analysis. In *Proceedings of the International Conference on Soil Mechanics and Geotechnical Engineering* (Vol. 1, pp. 539-542). AA Balkema Publishers.

Wolf, H., König, D., & Triantafyllidis, T. (2003). Experimental investigation of shear ban patterns in granular material. Journal of Structural Geology, 25(8), 1229-1240.

Chapter 6: Strain variation along western part of the North Anatolian Fault based on GPS data

S. Bulkan[1], P. Vannucchi[2]

[1]Royal Holloway, University of London, Earth Sciences Department, Egham, UK.
[2]Dipartimento di Scienze della Terra, Universita' degli Studi di Firenze, Via La Pira, 4, Firenze, Italy

This chapter is a manuscript that is currently in preparation to be submitted for publication in a peer-reviewed journal.

A dense network of Global Positioning System (GPS) sites is used to determine the velocity field and two-dimensional strain rate tensors. We mapped the dilatation and maximum shear strain rates for the western end of the North Anatolian Fault (NAF) in the Marmara Sea region, NW Anatolia. The results show that deformation around the northwest Anatolia and the Sea of Marmara region does not appear to capture the regional strain buildup or release that would be linked to the westward stepping seismic activity on the NAF sections. The GPS-inferred pattern of regional strain also implies that Anatolia is tending to deform by dilation as well as strike-slip in the region closest to the Aegean Sea. A prominent zone of dilation is present SW of Izmit in a region with an increased number of surface faults with multiple fault strikes, which may be linked to its 'weaker' tectonic behaviour than its surrounding regions. Any dilation south of the NAF will also accommodate some of the extension prompted by the Nubian slab rollback in the Aegean.

6.1 Introduction

The North Anatolian Fault (NAF) accommodates the overall strike-slip motion between the Eurasian plate and the Anatolian block in the northwest region of Turkey. In this region, motion is linked to the westward extrusion of the Anatolian block (Armijo et al., 1999, 2003, Sengor et al., 1985) induced by the northward motion of the Arabian plate with respect to Eurasia (McClusky et al., 2000, Reilinger et al., 2006). A further component of extension is present in the Aegean Sea to the SW, which has been linked to rollback of the Nubian slab beneath the Hellenic Arc (McKenzie, 1972, 1978; Dewey and Sengor, 1979; Royden, 1993)(Fig. 6.1). The Sea of Marmara region is located at the transition between the E-W strike slip Anatolian regime and the N-S extension of the Aegean region. Here, widespread large shallow earthquakes show focal mechanisms that vary from strike-slip faulting to the east to normal-plus-strike-slip faulting to the west (Jackson and McKenzie, 1988, Ekström et al., 2012). Also in this region, the NAF splays with a northern branch that cuts through Izmit, the Sea of Marmara and the Gulf of Saros, and a southern branch that goes into the Lake of Iznit, Bursa and the Gulf of Edremit. Considerable uncertainty still exists regarding strain variations across the Sea of Marmara region and how the Anatolian and Aegean tectonic regimes influence lateral variations in deformation within it. To help better understand spatial variations in strain accumulation, the correlation of these variations with E-W stress changes, and the extent to which strain rates are linked to recent earthquakes, we examine the present-day deformation field inferred from recent GPS observations.

Several studies have integrated GPS data from different campaigns that provide a dataset to deduce detailed horizontal strain rate fields in western Anatolia, and their relationship to seismotectonic processes. (Straub et al., 1997; Kahle et al., 1998, 1999; McClusky et al. 2000; Reilinger et al., 2006; England et al., 2016). In this paper, we use data gathered in the Marmara GPS networks described in Bulut et al. (2019) and Ayhan et al. (2002) to reassess the regional strain rate pattern around this section of the NAF. We determine the strain rate field, and discuss its implications for the state and evolution of this section of the NAF. In particular, we wish to reassess: (1) How does the spatial pattern of strain rate change going from the east to the west of this transitional zone of the NAF?; (2) Do these changes correlate with regional changes in stress orientations?; (3) To what extent are these variations in strain rate linked to recent earthquake patterns?

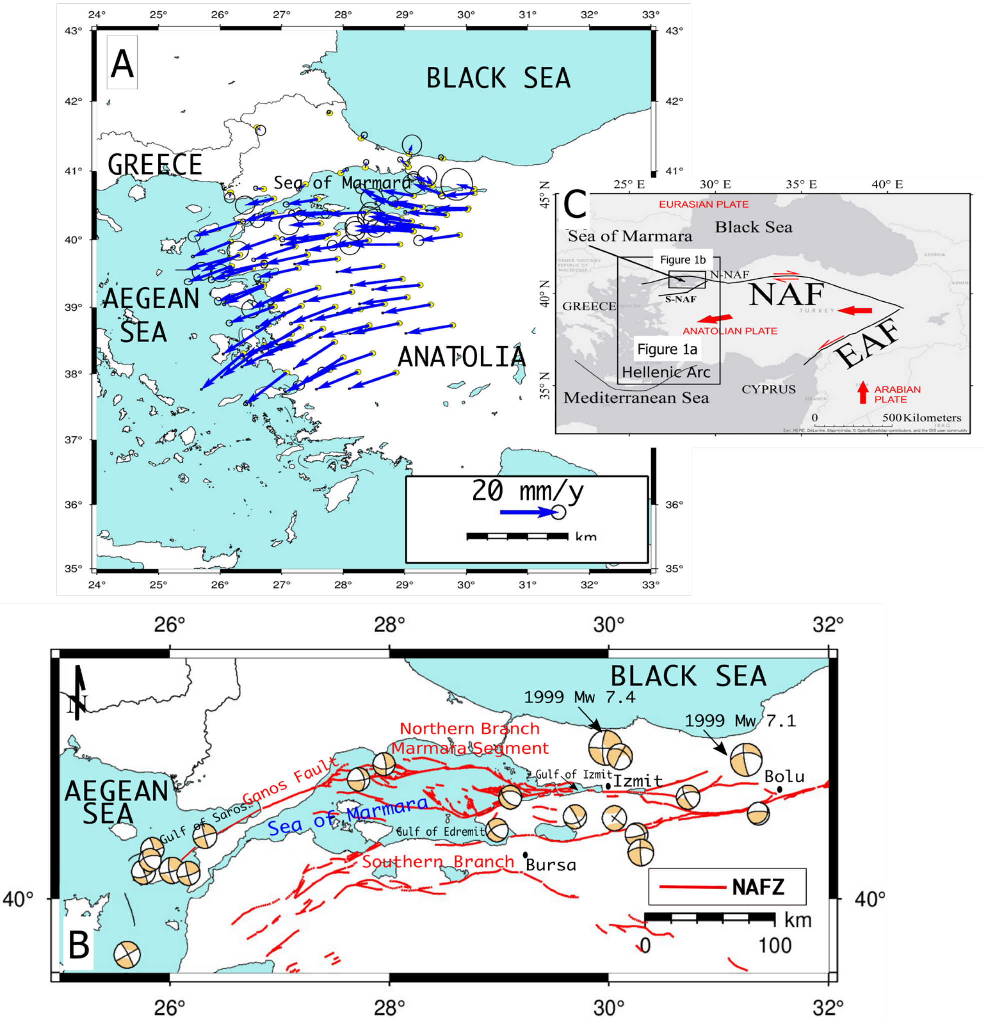

Figure 6-1 *A) Combined velocity field in the north western Turkey relative to a Europe-fixed reference frame, based on GPS results from Bulut et al. (2019) and Ayhan et al. (2002) B) Tectonic frames of Anatolia.C) The falt map of Marmara. Focal mechanisms from the GCMT catalog (the e.q's between the years 1976-2020) (Dziewonski et al., 1981; Ekström et al., 2012). The fault map re-drawn from (Armijo et al., 2005) and MTA, Turkey. Yellow circles are GPS stations.*

6.2 Methods and Data

6.2.1 GPS Derived strain rate field

Our analysis is constrained by measurements of crustal velocities made using the Global Positioning System (GPS) at 153 stations distributed over northwest Anatolia (Fig. 6.1B). We use the data set of England et al. (2016) and Bulut et al. (2019) as our reference data sets, which were compiled from previous measurements of TUSAGA, TUSAGA-Aktif, TUTGA (Ayhan et al., 2002; Reilinger et al., 2006; Aktuğ et al., 2009; Reilinger and McClusky, 2011; Aktuğ et al., 2013; Ergintav et al., 2014; Özdemir, 2016). The velocity estimates are calculated in the Eurasian plate fixed frame (1σ error ellipses are shown in Figure 6.2 for clarity; shows 95% confidence ellipses), given in Table 1 in Appendix II and shown in Fig. 6.1, as input to strain analysis.

We calculated the principal axes of the strain rate tensor and the principal values of compressional and extensional strain rates from the GPS deformation using the open-source software STRAINTOOL (https://github.com/DSOlab/StrainTool) (Anastasiou et al., 2019) which uses the algorithm VISR (Velocity Interpolation for Strain Rate - Shen et al., 2015).This method is based on a discretization of the investigated area into triangles (e.g. Delauney triangulation) and computation of internal strain rate for each triangle (see e.g. Shen et al.,1996 ; Cai and Grafarend,2007; Wdowinski et al.,2007). The method uses a least squares inversion procedure in which the horizontal velocity gradients are estimated at a set of regularly spaced grid points from the weighted GPS velocities. The problem was considered as two-dimensional, because the GPS surveys can provide deformation rates on the Earth's surface directions x(E) and y(N), but not on deformation rates in the radial direction z(U) (e.g. Erdogan et al., 2009). The accuracy within the study area is appropriate for comparisons with our strain models, with its cell size of 0.5 degree. Basically, we are separating the region into cells of size 0.5 degrees and estimating one strain tensor in each cell centre. All figures created with GMT (Wessel and Smith, 1995) within the StrainTool.

6.3 Results & Discussion

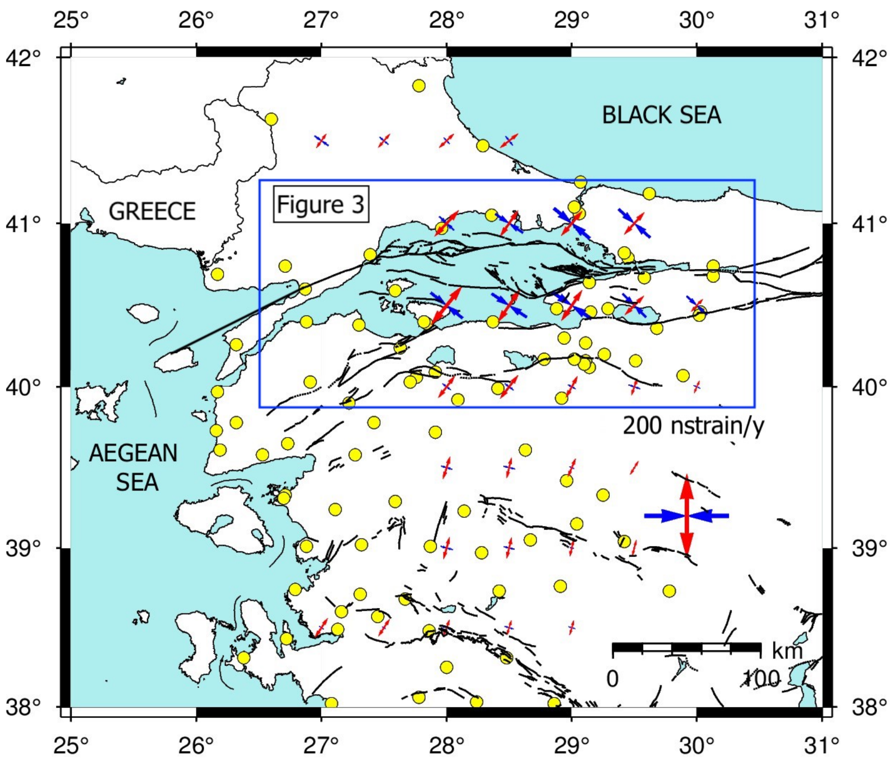

Figure 6-2 *Principal axes of strain rates for north-western and western Anatolia . Red arrows indicate extension, while blue arrows indicate compression. Yellow dots are stations. The rectangale represent the area in Figure 6.3.*

Figures 6.2 and 6.3 show the GPS-inferred strain-rate pattern around the northern branch of the NAF. The overall pattern is NE–SW extension and NW–SE compression, consistent with the pervasive dextral strike-slip faulting in this region (Wollin et al., 2019). Extensional and compressional strain rate components have approximately the same magnitude; toward the west they progressively rotate counterclockwise by ~15°. South of the northern branch of the NAF this counterclockwise rotation is more evident, except at the western end of Anatolia (Fig. 6.2). This extension is seen by the red extensional principle strain rate component in this region being several times larger than the blue compressional strain rate component. We interpret this rotation as the influence of the Aegean extension (Flerit et al., 2004). The recent GPS strain field also implies that the region to the south of the northern branch of the NAF is currently experiencing broad regional deformation, but at rates less than those around the northern NAF fault branch (Fig. 6.3B). The regional stress pattern inferred from earthquake focal mechanisms in this region (Heidbach, Oliver; Rajabi, Mojtaba; Reiter, Karsten; Ziegler, Moritz; WSM Team (2016): World Stress Map Database Release 2016. V. 1.1. GFZ Data Services. http://doi.org/10.5880/WSM.2016.001) shows a small ~15°-20° counterclockwise rotation of the principle stress field from the E -eastern Marmara - to W – Ganos Fault - along the northern NAF branch (Ozturk et al., 2019; Wollin et al., 2019). Ozturk et al., 2019 proposed that this rotation in stress regime might be responsible for the opening of the Sea of Marmara as a pull-apart structure.

Figure 6.3 compares the spatial pattern of the second invariant of the strain rate (a measure of the local magnitude of the strain rate) with the principle horizontal strain directions derived from the GPS data. Here we will not discuss the behavior at the edges of the analysed area as the second invariant in these regions is likely to be less accurately determined. The second invariant shows a narrow band of high strain rate that runs through the Sea of Marmara from the east to west along the NAF. This trend highlights the E-W direction of the fault zone, with the highest values in the middle of the Sea of Marmara and lower values to the east and west of this region of the NAF (Fig 6.3a).

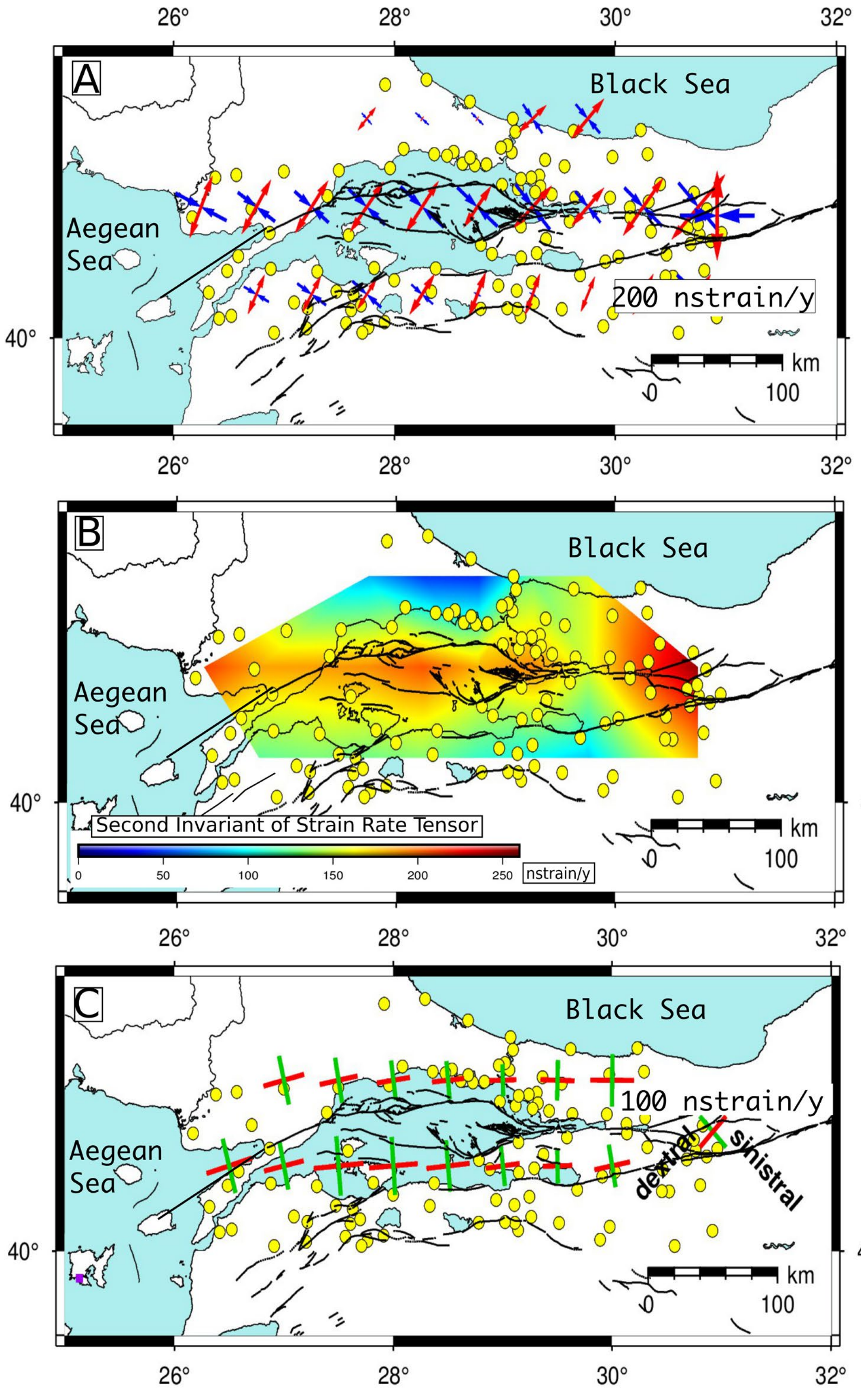

Figure 6-3 *a) Second invariant of strain-rates in units ofnanostrain/yr. b) Principal axes of strain rates. Red arrows indicate extension, and blue arrows indicate compression. C)Conjugate line segments show the magnitude and direction of the maximum dextral(red) and sinistral(green) local shear strain rate*

Figure 6.4 shows the regional patterns of compression and dilation along the fault zone. In general, there are overall compressional strain rates to the north of the NAF and extensional strain rates, almost two times larger, to the south. This area is located at the western tip of the 60 km long NAF segment that slipped during the 1999 M7.4 Izmit earthquake (Tibi et al., 2001). The strain rate pattern in Figure 6.4 is opposite to the stress perturbation near the fault tip induced by slip along a dextral strike-slip fault like the NAF (Segall and Pollard, 1980; Pollard and Segall, 1987). This implies that we are not seeing a transient stress perturbation liked to the Izmit earthquake. In addition, the difference in magnitude between the opposing extensional and compressional dilations is inconsistent with a fault-slip-induced effect. Interestingly, the extensional horizontal dilation is concentrated in the region to the SW of Izmit, which is also the region south of the NW-ward bend in the NAF at the Sea of Marmara. This area appears to be currently stretching more than the Sea of Marmara (Flerit et al., 2004). Instead the Sea of Marmara is characterized by moderate dilation on its Anatolian plate side, while compression is concentrated on the Eurasian plate side (Fig. 6.4). Any dilation south of the NAF will also accommodate some of the extension prompted by the Nubian slab rollback in the Aegean.

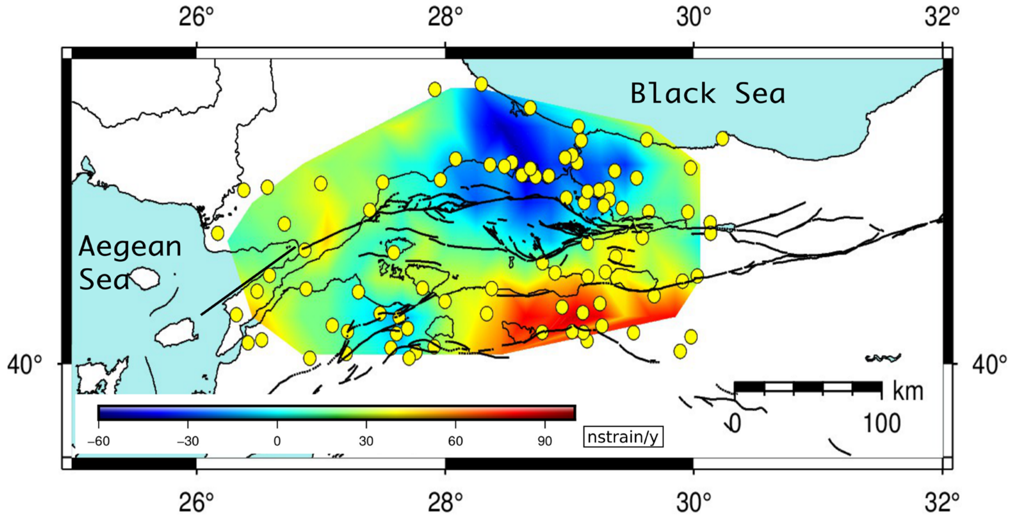

Figure 6-4 *Dilational regional strain-rates around the NAF. Note that maximum extensional horizontal strainrates reach ~120 nstrain/yr in the region SE of the Sea of Marmara, while maximum compressional horizontal strainrates only reach ~-40 nstrain/yr, in the region to the NE of the Sea of Marmara. Multiple non-parallel sets of surface faults are seen in the region of maximum extensional dilation, suggesting that at least some of this dilational deformation is being accommodated by distributed brittle strike-slip in this region.*

6.4 Conclusions: Links between regional deformation around the NAF in the Sea of Marmara and the local Earthquake Cycle

GPS measurements of deformation around the northwest Anatolia and the Sea of Marmara region does not appear to capture the regional strain buildup or release that would be linked to the westward stepping seismic activity on the NAF sections. Historic strike-slip earthquake epicenters clearly show a westward stepping migration along the NAF in the 20th century (Armijo et al., 1999), while the GPS data do not clearly show that an EQ-slip-driven precursor has built up within the Marmara Sea strand of this fault.

The GPS-inferred pattern of regional strain also implies that Anatolia is tending to deform by dilation as well as strike-slip in the region closest to the Aegean Sea. The concentrated region of dilation SW of Izmit is in a region with an increased number of surface faults with multiple fault strikes, which may be linked to its 'weaker' tectonic behavior than its surrounding regions. However, it is not spatially connected to regions of coastal dilation, and its only apparent tectonic feature is that this is the region where the NAF splays into multiple sub-parallel strands. In the western region the NAF has subparallel arcuate northern, middle, and southern strands. Here, the GPS-inferred pattern of regional strain is consistent with all of these faults being simultaneously active, as implied by geological observations.

6.5 References

Aktug, B., Nocquet, J. M., Cingöz, A., Parsons, B., Erkan, Y., England, P., ... &Tekgül, A. (2009). Deformation of western Turkey from a combination of permanent and campaign GPS data: Limits to block-like behavior. *Journal of Geophysical Research: Solid Earth*, *114*(B10).

Aktuğ, B., Meherremov, E., Kurt, M., Özdemir, S., Esedov, N., & Lenk, O. (2013). GPS constraints on the deformation of Azerbaijan and surrounding regions. *Journal of Geodynamics*, *67*, 40-45.

Anastasiou D., Ganas A., Legrand J., Bruyninx C., Papanikolaou X., Tsironi V. and Kapetanidis V. (2019). Tectonic strain distribution over Europe from EPN data. EGU General Assembly 2019, Geophysical Research Abstracts, Vol. 21, EGU2019-17744-1

Armijo, R., B. Meyer, A. Hubert, and A. Barka, 1999. Westward propagation of the North Anatolian fault into the northern Aegean: Timing and kinematics, Geology, 27, 267– 270.

Armijo, R., Pondard, N., Meyer, B., Uçarkus, G., de Lépinay, B. M., Malavieille, J., ... & Cagatay, N. (2005). Submarine fault scarps in the Sea of Marmara pull-apart (North Anatolian Fault): Implications for seismic hazard in Istanbul. *Geochemistry, Geophysics, Geosystems*, *6*(6).

Bulut, F., Aktuğ, B., Yaltırak, C., Doğru, A., & Özener, H. (2019). Magnitudes of future large earthquakes near Istanbul quantified from 1500 years of historical earthquakes, present-day microseismicity and GPS slip rates. *Tectonophysics*, *764*, 77-87.

Cai, J., & Grafarend, E. W. (2007). Statistical analysis of the eigenspace components of the two-dimensional, symmetric rank-two strain rate tensor derived from the space geodetic measurements (ITRF92-ITRF2000 data sets) in central Mediterranean and Western Europe. *Geophysical Journal International*, *168*(2), 449-472.

Dewey, J. F., & ŞENGÖR, A. C. (1979). Aegean and surrounding regions: complex multiplate and continuum tectonics in a convergent zone. *Geological Society of America Bulletin*, *90*(1), 84-92.

Ergintav, S. E. M. I. H., Reilinger, R. E., Çakmak, R., Floyd, M., Cakir, Z. I. Y. A.D. I. N., Doğan, U., ... & Özener, H. (2014). Istanbul's earthquake hot spots: Geodetic constraints on strain accumulation along faults in the Marmara seismic gap. *Geophysical Research Letters*, *41*(16), 5783-5788.

Dziewonski, A. M., Chou, T. A., & Woodhouse, J. H. (1981). Determination of earthquake source parameters from waveform data for studies of global and regional seismicity. *Journal of Geophysical Research: Solid Earth*, *86*(B4), 2825-2852.

Ekström, G., Nettles, M., & Dziewoński, A. M. (2012). The global CMT project 2004–2010: Centroid-moment tensors for 13,017 earthquakes. *Physics of the Earth and Planetary Interiors*, *200*, 1-9.

Erdoğan, S., Şahin, M., Tiryakioğlu, İ., Gülal, E., & Telli, A. K. (2009). GPS velocity and strain rate fields in Southwest Anatolia from repeated GPS measurements. *Sensors*, *9*(3), 2017-2034.

Heidbach, O., Rajabi, M., Reiter, K., Ziegler, M., & Wsm Team. (2016). World stress map database release 2016. *GFZ Data Services*, *10*.

Flerit, F., Armijo, R., King, G. C. P., Meyer, B., & Barka, A. (2003). Slip partitioning in the Sea of Marmara pull-apart determined from GPS velocity vectors. *Geophysical Journal International*, *154*(1), 1-7.

Flerit, F., Armijo, R., King, G., & Meyer, B. (2004). The mechanical interaction between the propagating North Anatolian Fault and the back-arc extension in the Aegean. Earth and Planetary Science Letters, 224(3-4), 347-362.

Jackson, J., & McKenzie, D. (1988). The relationship between plate motions and seismic moment tensors, and the rates of active deformation in the Mediterranean and Middle East. *Geophysical Journal International*, *93*(1), 45-73.

Kahle, H. G., Straub, C., Reilinger, R., McClusky, S., King, R., Hurst, K., ... & Cross, P. (1998). The strain rate field in the eastern Mediterranean region, estimated by repeated GPS measurements. *Tectonophysics*, *294*(3-4), 237-252.

Kahle, H. G., Cocard, M., Peter, Y., Geiger, A., Reilinger, R., McClusky, S., ... & Veis, G. (1999). The GPS strain rate field in the Aegean Sea and western Anatolia. *Geophysical research letters*, *26*(16), 2513-2516.

McKenzie, D. (1972). Active tectonics of the Mediterranean region. *Geophysical Journal International*, *30*(2), 109-185.

McClusky, S., Balassanian, S., Barka, A., Demir, C., Ergintav, S., Georgiev, I., ... & Kastens, K. (2000). Global Positioning System constraints on plate kinematics and dynamics in the eastern Mediterranean and Caucasus. *Journal of Geophysical Research: Solid Earth*, *105*(B3), 5695-5719.

Reilinger, R., McClusky, S., Vernant, P., Lawrence, S., Ergintav, S., Cakmak, R., ... & Nadariya, M. (2006). GPS constraints on continental deformation in the Africa-Arabia-Eurasia continental collision zone and implications for the dynamics of plate interactions. *Journal of Geophysical Research: Solid Earth*, *111*(B5).

Özdemir, S. (2016). On the estimation of precise coordinates and velocities of TNPGN and TNPGN-active stations. *Journal of Mapping*, *155*, 53-81.

Öztürk, Y. K., Özel, N. M., & Özbakir, A. D. (2015). States of local stresses in the Sea of Marmara through the analysis of large numbers of small earthquakes. Tectonophysics, 665, 37-57.

Pollard, D. D., & Segall, P. (1987). Theoretical displacements and stresses near fractures in rock: with applications to faults, joints, veins, dikes, and solution surfaces. In *Fracture mechanics of rock* (pp. 277-347).

Royden, L. H. (1993). Evolution of retreating subduction boundaries formed during continental collision. *Tectonics*, *12*(3), 629-638.

Straub, C., Kahle, H. G., & Schindler, C. (1997). GPS and geologic estimates of the tectonic activity in the Marmara Sea region, NW Anatolia. *Journal of Geophysical Research: Solid Earth*, *102*(B12), 27587-27601.

Segall, P., & Pollard, D. D. (1980). Mechanics of discontinuous faults. *Journal of Geophysical Research: Solid Earth*, *85*(B8), 4337-4350.

Shen, Z.-K., M. Wang, Y. Zeng, and F. Wang, (2015), Strain determination using spatially discrete geodetic data, Bull. Seismol. Soc. Am., 105(4), 2117-2127, doi: 10.1785/0120140247

Şengör, A. M. C., Görür, N., & Şaroğlu, F. (1985). Strike-slip faulting and related basin formation in zones of tectonic escape: Turkey as a case study.

Tibi, R., Bock, G., Xia, Y., Baumbach, M., Grosser, H., Milkereit, C., ... & Zschau, J. (2001). Rupture processes of the 1999 August 17 Izmit and November 12 Düzce (Turkey) earthquakes. *Geophysical Journal International*, *144*(2), F1-F7.

Wessel, P., & Smith, W. H. (1998). New, improved version of Generic Mapping Tools released. Eos, Transactions American Geophysical Union, 79(47), 579-579.

Wdowinski, S., Smith-Konter, B., Bock, Y., & Sandwell, D. (2007). Diffuse interseismic deformation across the Pacific–North America plate boundary. *Geology*, *35*(4), 311-314.

Wollin, C., Bohnhoff, M., Vavryčuk, V., & Martínez-Garzón, P. (2019). Stress inversion of regional seismicity in the Sea of Marmara Region, Turkey. Pure and Applied Geophysics, 176(3), 1269-1291.

6.6 Supplementary Material I

We wrote a basic MATLAB code for testing the possible edge effects by StrainTool programme described in Chapter 3 Section 3.6.2.

The description for the code below were presented in Chapter 3, Section 3.6.3.

```
load('//Users/sibel/Desktop/PhD/3rdpaper/GPS/data_newl.txt');

% Get longitude and latitude vectors
   x = unique(data_newl(:,1)) ;
   y = unique(data_newl(:,2)) ;
   vx = unique(data_newl(:,3)) ;
   vy = unique(data_newl(:,4)) ;


      xaxisvalues = unique(data_newl(:,1)) ;
      yaxisvalues =unique(data_newl(:,2));

       nxaxis = length(xaxisvalues);
       nyaxis = length(yaxisvalues);

%Grid the data
 n=1
xmin = min(data_newl(:,1))
xmax = max(data_newl(:,1))

ymin = min(data_newl(:,2))
ymax = max(data_newl(:,2))

zmin = min(data_newl(:,3))
zmax = max(data_newl(:,3))

  % dimensions of the data
   nx = length(x) ;
   ny = length(y) ;

xgrid = repmat(linspace(xmin,xmax,nx),ny,1);
ygrid = repmat(linspace(ymin,ymax,ny)',1,nx);

size(xgrid)
size(ygrid)

zq = griddata(data_newl(:,1),data_newl(:,2),data_newl(:,3),xgrid,ygrid);
zgrid(:,:,n)=zq;
figure(n);

surface(xgrid,ygrid,zq,'edgecolor','none');
hold on;
colormap 'jet'
```

Chapter 7: Discussion

Continental transform faults have been intensely studied by geologist because they are fundamental tectonic features which are hardly confined to simple faults. They, instead, form broad zones of extensive fracturing commonly containing more than one major strike-slip fault surface, thus forming major shear zones (Sengor et al., 2019). This fault type can play a significant role in accommodating lithospheric plate movements and may be the site of major earthquakes (e.g., North Anatolian Faults, San Andreas, Dead Sea) thereby representing a major geo-hazard (Maia, 2019). Analogue modelling is one of the useful tools of displaying the large lithospheric strike-slip zones which are associated not only with horizontal displacements, but with secondary vertical movements along these faults as well. Rhomb-shaped depressions such as pull-apart basins, elongated depressions (e.g., transform valleys), pressure ridges, uplifted and faulted flower structures, and drag folds (Sylvester, 1988) are typical structural expressions of these vertical displacements along strike-slip faults. In this thesis, I address questions that are still open in the complex strike-slip faulting processes. The studied parameters have general applicability, nevertheless in this thesis, I focus on the western part of the NAF around the Sea of Marmara. In detail, I investigated the complex NAF strike-slip system, which is characterised by a complex geometry with several sub-parallel splays, structural expressions involving depressions such as the Sea of Marmara, and uplifted regions such as the Ganos Mountain. I performed this study by using analogue modelling and GPS-derived strain rate field and I compared my results coming from modelling with geomorphological observations in nature and high resolution shallow seismic images.

Summarising, this thesis seeks to make two major contributions: (1) a contribution to modelling of strike-slip faulting (2) a contribution to the understanding of the evolution of the NAF- Sea of Marmara more-in depth.

In the present chapter I first discuss the parameters that shaped the overall modelling approach - section 7.1 and section 7.2 -, and then I summarise the contributions analysed in Chapter 4, Chapter 5, and Chapter 6 - section 7.3.

7.1 Discussion of Setup Choosing

The defining factor in analogue modelling is the model set-up. Throughout this thesis, a brittle-ductile configuration is applied on plexiglass basement to localize deformation in the brittle top layer. The first and most important factor is the control on the initial geometry of the setup. In our models, we used one type of fault geometry to simulate the western part of the North Anatolian Fault. The design of these models presented a challenge when considering the analogue laboratory experimental techniques. It is difficult to directly interpret modelling results of the actual fault system with the complexities in its geometry. Therefore, the adjacent restraining and releasing bend was designed to reproduce the transition at the western end of the Sea of Marmara between the compressive Ganos segment onland and the Sea of Marmara, which may, in a simplified view, be considered as a whole as a transtensive system (Mann, 2007, Le Pichon et al., 2016, Rangin et al., 2004) that confines the first-order geometrical features of the Sea of Marmara (Chapter 4 and Chapter 5).

This thesis showed how the initial geometry and the placement of each layer in the sandbox controled the output. Our focus was to limit unwanted additional deformations on the lower layer of the experiment as well as in the surface.

7.2 Discussion of Silicone Thickness Effect

The viscous lower layer in the model facilitates fault localization because it distributes deformation, and reduces coupling, allowing the brittle cover to behave as a rigid block. The decoupling effect of the silicone layer was observed, for example, during the deformation of the model presented in

Chapter 4, where we observed the development of a new shear zone south of the initial somewhat forced shear zone and the initial pop-up structure (Chapter 4; Fig.4.7d-g). This new shear zone takes up most of the strike-slip motion, causing the pop up to become inactive. This is an example that shows how decoupling in the lower ductile silicone layer allows a simplification of the shear zone geometry in the brittle layer. We suggest that the viscosity of the lower crust and its possible variations may play an important role in the amount of decoupling.

Thickness and viscosity of this lower/ductile layer controlled how efficiently the basal displacement is transferred to the shallower crust. In our models, we showed that the low silicone thickness built a minor and progressive readjustment of the shear localization, while a thick silicone layer diminished the localization of shear.

The results confirm that the initial geometry and the strain accommodation by a viscous silicone layer can be considered as a factor controlling the characteristics of the modelled pull-apart basins.

7.3 The contribution to the modelling of strike slip faulting

Chapter 4 and Chapter 5 approached the problems related to the interaction of restraining/releasing bend (double-bend) structures in strike-slip faults system. There we describe how the same initial “fault” geometry, but with different model two set-ups, can produce different results. In general, the experiments show how the releasing bend seconds the development of an asymmetric pull-apart basin while the restraining bend develops topographic highs. The vertical deformations of both the brittle and the ductile layers vary inside the deformed layer defining the master fault. These deformations are more significant in places where they form deep depressions with distinct thinning of viscous lower layer. The most common result of our models is that the master fault system generates a narrow zone of shear localization without developing any striking topographic features in the edges of the bend pairs (Fig. 4.7b).

7.4 The contribution to the evolution of the NAF- Sea of Marmara

As discussed in Chapter 4, the evolution of the major fault in the Sea of Marmara is similar to those observed and described in the analogue models. In general, the fault evolution matches that of the transition from a single to a multi-branch fault system, with branches active at different time. In a simplified picture, this transition may be considered as a whole as a transtensive system in the Sea of Marmara (e.g. Rangin et al., 2004; Mann, 2007; LePichon et al., 2014). The architecture of the Sea of Marmara and its segmentation in sub-basins is controlled by the presence of restraining bends and releasing bends and their progressive offsets.

One of the results of a "short-cut fault" development in our model described in Chapter 4 concluded that the Main Marmara Fault (MMF) - from Ganos Fault to the Cinarcik Basin - may be interpreted as a shortcut. The Cinarcik Basin is comparable to the basin formed in the model in terms of the existence boundary fault on the north side of the basin. The model provides the evidence to demonstrate that the main active fault in Cinarcik Basin is currently the Prince Island fault along the northern edge of the basin (Seeber et al., 2006; Bohnhoff et al., 2013; Kurt et al., 2013 Grall et al. 2012; Ergintav et al., 2014; Le Pichon et al., 2014, 2016; Kende et al., 2017). The model generates the uplift above the restraining bends and a graben system formed in relation to the releasing bend. The uplift correlates with the occurrence and evolution of the Ganos Mountain. When the activity of the younger southern fault system started, in fact, the restraining bend was bypassed causing the end of uplift in the Ganos region and the beginning of the subsidence according to the observations by Okay et al. (2004)

In Chapter 5, the strain patterns support the ideas that partitioning of the deformation on Cinarcik segment may cause slower accumulation of stress, resulting in a longer seismic-cycle. This result supports the delay of an earthquake triggered on that part of fault.

Most of the observed deformation is controlled by the changes of geometry of the fault segments in a 90°-striking dextral wrench tectonic regime. In particular, the compressive deformations observed at the connection between the Cinarcik and the Central High segments were reproduced by the model. Imposing a small, but sharp, change in relative orientations of the segments was enough to gently build uplift, and this is in good agreement with the location of the Central High.

In Chapter 6, the strain patterns derived from GPS propose that the tectonic activity in Anatolia and the Aegean can be explained by the dilatation and associated weak lithospheric zones influenced by the extensional Aegean system. Comparison the pre and post seismic deformation patterns (see in Appendix III) contributes by showing that the partitioning between normal and strike-slip faulting, are explained by the stress regimes within the Sea of Marmara region.

Chapter 8: Conclusions

This thesis focuses on strike slip faulting, and specifically on the effects that a fault geometry with realising and restraining bends has on surface topography and strain distribution. The general consensus is that subsidence would develop in response to a releasing bends, while uplift would build on a restraining bend. Here we join these two elements and study the progressive development of deformation related to a releasing-restraining bend pair within a transform fault zone system.

The deformation has been studied through analogue experiments. The direct display of progressive deformation typical of analogue modelling has been improved in this thesis with the application of Particle Image Velocimetry (PIV) analysis. PIV allowed to trace single particles of the surface of the model, and therefore the positions on the master fault, of the fault tips and associated structures, such as folds, over time. This precise tracing also allowed to calculate strain gradients.

The results of the analogue models were then compared with the deformation patterns observed in the western part of the NAF, trying to address how the geometry of each segment influence the overall geodynamic evolution of the area of the Sea of Marmara. We also compared the strain rate values derived from the PIV analysis to those calculated from GPS measurement for the north western Anatolia. This last analysis allowed us to gain an overall perspective on the deformation trend of the Sea of Marmara resulting from the interaction of Anatolia with the Nubian slab rollback in the Aegean Sea.

In this conclusive chapter, the results of the thesis are briefly summarised and followed by a discussion of aspects that could be investigated in the future.

8.1 Reflections on the key questions

This section compiles the interpretations from Chapters 4, 5 and 6 with relevant existing literature (detailed in Chapter 2) to answer the specific questions which are addressed in the Introduction.

1 Can a releasing-restraining bend pair along the strike-slip fault reproduce the structures observed in the Sea of Marmara?

As discussed in Chapter 4, we simplify the geometry of the whole Sea of Marmara and consider it as a releasing bend. Moving to the west, the adjacent Ganos segment is considered to be a restraining bend (Mann, 2007). This simple geometry used as input in an analogue model can reproduce the first-order morphological characteristics developed within and around the northern strand of the NAF, without the need for other external factors such as extension linked to the Aegean Sea.

Specifically, the geometry of the releasing bend in the east of the model successfully reproduced the shape of the Cinarcik Basin in the eastern part of the N-NAF. Likewise, the transition to the restraining bend in the western portion of the model reproduced the progressive migration of the depocenter. Finally the restraining bend to the west is accompanied by a depression, which could be associated to the Tekirdag Basin, and related uplift, which could be represented by the Ganos Mountains - which are forming around the Ganos bend (Okay et al., 2004).

2 How is the evolution of the strain localisation in different fault segments? And which fault segments tend to remain active over long period of time?

The experiments described in Chapter 4 show that the geometry used in this study for the Sea of Marmara does not produce a single thoroughgoing fault system at shallow crustal levels. The prominent result of this chapter is that the evolution of the fault has led to the development of a multi-segment fault system, with different segments active and dominant at different times. We proposed that the model evolves in a left stepping fault system, with older faults following the geometry of the basal discontinuity, while the more mature system progressively partitions the deformation into new forming faults which are short-cutting the releasing-restraining bends transition.

Moreover, we noticed that the deformation is more localized toward the "fixed" northern part of the model. In the natural N-NAF system, the main active fault runs along the northern edge of the Cinarcik Basin – the so called "Prince Island" fault - (Seeber et al., 2006; Bohnhoff et al., 2013; Ergintav et al., 2014). The development of the short-cut in the western portion of the Sea of Marmara basin has been associated by both a compressional regime and uplift of the Ganos Mountain. Here, strain localized in the region of the Western High and Tekirdag Basin (Okay et al. 1999; Seeber et al., 2004; Şengör et al. 2014; Henry et al., 2018).

3 To what extent fault localization controls the development of subsidence or uplift?

According to the Chapter 4, our strain patterns show that the releasing bend subsidence is controlled by a shear zone which corresponds to the major faults at the edge of the basin to the north. Also, the experimental topographic evolution shows that uplift in the restraining bend is more prominent when the southern fault zone has yet to fully form as shown in Fig. 4.7b. This uplifted area correlates with the location of Ganos Mountain, which is indeed located to the north of the NAF.

4 Restraining and releasing bends along transform type faulting can work as barriers or help earthquake propagation (Cunningham and Mann, 2007). Does the co-seismic strain release on the Izmit segment directly affect the strain accumulation on Prince Island's segment?

In Chapter 5, we reproduced the eastern part of the fault geometry of the Sea of Marmara. Using analogue modelling techniques, we attempted to link the tectonic deformation observed in morpho-bathymetric maps with seismic reflection profiles, with the final aim to reconstruct the recent evolution and neotectonic deformation pattern in the Çınarcık basin. We proposed that the Izmit segment might be able to transfer strain to the Prince Island's segment. However, in the model the segment corresponding to the Prince Island faults seems to accumulate strain slower than the segment corresponding to the Izmit fault. This difference followed strain partitioning from strike-slip to extensional fault displacement. We interpreted this difference as responsible for a longer recurrence interval along the Prince Island's fault than the Izmit fault for earthquakes of magnitude similar to the 1999 Izmit earthquake. This conclusion correlates with a general "delay" of earthquakes expected to occur along the Prince Island's segment.

Similarly, in the case of San Andreas Fault slip partitioning across the restraining Big Bend and the loading of buried faults below the Los Angeles metropolitan area might have an impact on the earthquake cycles (Li & Liu, 2007; Li et al., 2009; Daout et al., 2016).

5 The Izmit segment is oriented at an angle relative to the Central High segment, that we quantified in 10°. Could this difference in orientation be responsible for the compressive deformation observed at the NW edge of the Çınarcık basin?

Regarding this question, in Chapter-5 we successfully reproduced with our model (realising/restraining bends pairs) the compressive deformations observed at the connection between the Çınarcık and Central High Segments.

In nature, the western half of the Cinarcik basin distinguishes the Istanbul Bend from the Central part of the basin (Fig. 5.2). The model is a good fit with the NE-SW trending morphobathymetric uplift of the Central High.

In particular the orientation of the main fault changes to a vertical trace in both the model and the Cinarcik basin (Fig. 5.7c). The comparison between experimental results and interpretation carried out on available seismic lines strengthens the idea that a restraining bend adjacent to a releasing bend with a difference of ~10° in orientation might produce a change in width of the basin, a topographic high with the characteristics observed in the NW Cinarcik basin, and changes in fault as observed along the tectonic boundary (Fig. 5.7c). This would support the hypothesis that the formation of the Central High with its ~400m relief may be controlled by the interaction of the restraining bend with the master fault at depth. The model also suggests that this relief may be related to the characteristics of the fault at depth, where the lower crust appears deformed and mobilized by the fault while flower style branching faults cut the entire crust.

Common examples can be seen around the world. In the case of San Andreas Fault, for example, the complex system of faults due to bends (e.g. Big Bend) might have an impact on the overall compression on the area and the loading of buried faults (Li & Liu, 2007; Li et al., 2009; Daout et al., 2016). Similarly, the uplift is an expected manifestation of crustal shortening and thickening within the Lebanese restraining bend along the Dead Sea Fault Zone (Gomez et al., 2007).

6 How does the spatial pattern of strain rate change going from the east to the west of the Sea of Marmara, which is located at the transition between a pure strike-slip region and the extensional regime of the Aegean Sea?

As presented in Chapter 6, from the GPS deformation we calculated the principal axes of the strain rate tensor and the principal values of compressional and extensional strain rates. We used crustal velocities measured by GPS at 153 stations distributed over NW Anatolia. This calculation confirmed the high strain focused around the Sea of Marmara from the east to west along the NAF. On the contrary, the dilation patterns tend to change in the N-S direction, showing more extension on the south of the northern branch of the NAF where extension due to the Nubian slab rollback in the Aegean is accommodated. It is suggested that the dilation does not correlate with the strike slip faulting, but it is likely with deformation of Anatolia relative to fixed Eurasia.

a. How is this correlated to the change in stress?

In Chapter 6, we showed that the regional stress pattern inferred from earthquake focal mechanisms in this region (Heidbach, Oliver; Rajabi, Mojtaba; Reiter, Karsten; Ziegler, Moritz; WSM Team (2016): World Stress Map Database Release 2016. V. 1.1. GFZ Data Services. http://doi.org/10.5880/WSM.2016.001) correlates with the extensional and compressional strain rate components; toward the west they progressively rotate counterclockwise by ~15°-20°.

7 To what extent the strain rate is linked to recent earthquakes?

The analysis presented in Chapter 6 show that GPS measurement does not capture the regional stress buildup – or release - that would be linked to the westward propagation of earthquakes along the NAF during the 20th century.

In fact, the strain analysis conducted with GPS measurement show that compressional strain rate to the north of the 60 km long Izmit segment of the NAF slipped during the 1999 M7.4 Izmit earthquake (Tibi et al., 2001) and extensional strain rates to the south of it. The strain rate pattern is opposite to the stress perturbation expected near the fault tip induced by slip along a dextral strike-slip fault like the NAF (Segall and Pollard, 1980; Pollard and Segall, 1987). This implies that we are not seeing a transient stress perturbation liked to the Izmit earthquake.

8.2 Recommendations for future works

The Sea of Marmara is a structural complex area, and future work will increase the knowledge and the understanding of the fault network. Recommended future work for the topics in this thesis can be summarized in the following points.

1. The models presented in this thesis describe the master fault propagation which formed in releasing and adjacent restraining bends pairs. We used one type of fault geometry to simulate the western part of the North

Anatolian Fault. The design of these models presents a challenge when considering the analogue laboratory experimental techniques. This thesis showed how the initial geometry and the placement of each layer in the sandbox control the output. Our focus was to limit unwanted additional deformations on the lower layer of the experiment as well as in the surface. Further investigation with analogue models should experiment with different fault geometry - i.e. basal plate cut – and different rheology and thickness of layers.

2. In our models, we used a 2 mm-thick silicone layer, scaled to the relative thickness of the viscous lower crust, the latter inferred by the study of Kende et al. (2017), to better approximate the natural situation in the Sea of Marmara. Differences in the viscosity or thickness of this layer will shape how efficiently the basal displacements are transferred to the shallower crust.
3. In this thesis we just touched on a numerical approach. But numerical models could greatly complement the analogue modelling technique, as the geometry can be easily defined and reproduced.

References

Abdelmalak, M. M., Bulois, C., Mourgues, R., Galland, O., Legland, J. B., & Gruber, C. (2016). Description of new dry granular materials of variable cohesion and friction coefficient: Implications for laboratory modeling of the brittle crust. Tectonophysics, 684, 39-51.

Adam, J., Lohrmann, J., Hoth, S., Kukowski, N., & Oncken, O. (2002). Strain variation and partitioning in thrust wedges: High-resolution data from scaled sandbox experiments by 2D–3D PIV analysis. Bollettino di Geofisica teorica ed applicata, 42, 123-125.

Adam, J., Urai, J. L., Wieneke, B., Oncken, O., Pfeiffer, K., Kukowski, N., & Schmatz, J. (2005). Shear localisation and strain distribution during tectonic faulting—New insights from granular-flow experiments and high-resolution optical image correlation techniques. Journal of Structural Geology, 27(2), 283-301.

A.Polonia, L. Gasperini, A. Amorosi, E. Bonatti, G. Bortoluzzi, N. Çagatay, L. Capotondi, M.-H. Cormier, N. Gorur, C. McHugh, L. Seeber, Holocene slip rate of the North Anatolian Fault beneath the Sea of Marmara, Earth and Planetary Science Letters, Volume 227, Issues 3–4, 15 November 2004, Pages 411-426, ISSN 0012-821X.

Aktug, B., Nocquet, J. M., Cingöz, A., Parsons, B., Erkan, Y., England, P., ... &Tekgül, A. (2009). Deformation of western Turkey from a combination of permanent and campaign GPS data: Limits to block-like behavior. *Journal of Geophysical Research: Solid Earth*, *114*(B10).

Aktuğ, B., Meherremov, E., Kurt, M., Özdemir, S., Esedov, N., & Lenk, O. (2013). GPS constraints on the deformation of Azerbaijan and surrounding regions. *Journal of Geodynamics*, *67*, 40-45.

Ambraseys, N. N., & Finkel, C. F. (1987). Seismicity of Turkey and neighbouring regions, 1899-1915. In Annales geophysicae. Series B. Terrestrial and planetary physics (Vol. 5, No. 6, pp. 701-725).

Ambraseys, N. 2002. The seismic activity of the Marmara Sea region over the last 2000years, Bull. Seismol. Soc. Am., 92, 1–18.

Anastasiou D., Ganas A., Legrand J., Bruyninx C., Papanikolaou X., Tsironi V.and Kapetanidis V. (2019). Tectonic strain distribution over Europe from EPN data. EGU General Assembly 2019, Geophysical Research Abstracts, Vol. 21, EGU2019-17744-1

Armijo, R., B. Meyer, A. Hubert, and A. Barka, 1999. Westward propagation of the North Anatolian fault into the northern Aegean: Timing and kinematics, Geology, 27, 267–270.

Armijo, R., Meyer, B., Navarro, S., King, G., & Barka, A. 2002. Asymmetric slip partitioning in the Sea of Marmara pull apart: A clue to propagation processes of the North Anatolian Fault. Terra Nova, 14, 80–86. 10.1046/j.1365-3121.2002. 00397.x

Armijo, R., et al., 2005. Submarine fault scarps in the Sea of Marmara pull-apart (North Anatolian Fault): implications for seismic hazard in Istanbul, Geochem. Geophys. Geosyst, 6, Q06009, doi:10.1029/2004GC000896.

Ayhan, M. E., Demir, C., Lenk, O., Kiliçoglu, A., Altiner, Y., Barka, A. A., ... & Özener, H. (2002). Interseismic strain accumulation in the Marmara Sea region. Bulletin of the Seismological Society of America, 92(1), 216-229.

B. Alpar, C. Yaltirak, 2002. Characteristic features of the North Anatolian Fault in the eastern Marmara region and its tectonic evolution, Marine Geology, 190 (2002), pp. 329–350

Barka, A., Kuscu I., 1996. Extent of the North Anatolian Fault in the Izmit, Gemlik and Bandırma Bays. Turkish Journal Marine Science 2, 93– 106.

Barka, A. A., & Kadinsky-Cade, K. (1988). Strike-slip fault geometry in Turkey and its influence on earthquake activity. Tectonics, 7(3), 663-684.

Barka, A.A., Gülen, L., 1989. Complex evolution of the Erzincan Basin (Eastern Turkey). J. Struct. Geol. 11 (3), 275–283.

Bécel, A., Laigle, M., de Voogd, B., Hirn, A., Taymaz, T., Galvé, A., ... &

Özalaybey, S. (2009). Moho, crustal architecture and deep deformation under the North Marmara Trough, from the SEISMARMARA Leg 1 offshore–onshore reflection–refraction survey. *Tectonophysics*, *467*(1-4), 1-21.

Bohnhoff, M., F. Bulut, G. Dresen, P. E. Malin, T. Eken, and M. Aktar 2013. An earthquake gap south of Istanbul, Nature, doi:10.1038/ncomms2999.

Bulut, F., Aktuğ, B., Yaltırak, C., Doğru, A., & Özener, H. (2019). Magnitudes of future large earthquakes near Istanbul quantified from 1500 years of historical earthquakes, present-day microseismicity and GPS slip rates. *Tectonophysics*, *764*, 77-87.

Cai, J., & Grafarend, E. W. (2007). Statistical analysis of the eigenspace components of the two-dimensional, symmetric rank-two strain rate tensor derived from the space geodetic measurements (ITRF92-ITRF2000 data sets) in central Mediterranean and Western Europe. *Geophysical Journal International*, *168*(2), 449-472.

Cappelletti, A., Tsikalas, F., Nestola, Y., Cavozzi, C., Argnani, A., Meda, M., & Salvi, F. (2013). Impact of lithospheric heterogeneities on continental rifting evolution: Constraints from analogue modelling on South Atlantic margins. Tectonophysics, 608, 30-50.

Carton, H. (2005). *Etudes tectonics en Mediterranee orientale par analyse dedonnées de sismique reflexion: Mer de Marmara Bassin de Çınarcık et merge du Liban* (Doctoral dissertation, PhD thesis, Institute De Physique Du Globe De Paris).

Carton, H., Singh, S. C., Hirn, A., Bazin, S., De Voogd, B., Vigner, A., ... & Sevilgen, V. (2007). Seismic imaging of the three-dimensional architecture of the Çınarcık basin along the North Anatolian fault. Journal of Geophysical Research: Solid Earth, 112(B6).

C. Straub, H.G. Kahle, C. Schindler 1997. GPS and geologic estimates of the tectonic activity in the Marmara Sea region, NW Anatolia, J. Geophys. Res., 102 (B12) (1997), pp. 27587–27601

Corti, G., Moratti, G., & Sani, F. (2005). Relations between surface faulting and granite intrusions in analogue models of strike-slip deformation. *Journal of Structural Geology*, *27*(9), 1547-1562

Cunningham, W. D., & Mann, P. (2007). Tectonics of strike-slip restraining and releasing bends. Geological Society, London, Special Publications, 290(1), 1-12.

Çağatay, M. N., Görür, N., Algan, O., Eastoe, C., Tchapalyga, A., Ongan, D., ... & Kuşcu, I. (2000). Late Glacial–Holocene palaeoceanography of the Sea of Marmara: timing of connections with the Mediterranean and the Black Seas. Marine Geology, 167(3-4), 191-206.

Çağatay, M. N., Wulf, S., Sancar, Ü., Özmaral, A., Vidal, L., Henry, P., ... & Gasperini, L. (2015). The tephra record from the Sea of Marmara for the last ca. 70 ka and its palaeoceanographic implications. Marine Geology, 361, 96-110.

Çağatay, M. N., & Uçarkuş, G. (2019). Morphotectonics of the Sea of Marmara: basins and highs on the North Anatolian continental transform plate boundary. In Transform plate boundaries and fracture zones (pp. 397-416). Elsevier.

Çakir, Z., Ergintav, S., Özener, H., Dogan, U., Akoglu, A. M., Meghraoui, M., & Reilinger, R. (2012). Onset of aseismic creep on major strike-slip faults. Geology, 40(12), 1115-1118.

D'ADDA P., LONGONI R., MAGISTRONI C., MEDA M., RIGHETTI F., CAVOZZI C., NESTOLA Y. & STORTI F. (2016) – Extensional reactivation of a deep transpressional architecture: insights from sandbox analogue modeling applied to the Val d'Agri basin (Southern Apennines, Italy). *Interpretation, 5,* 55-66.

Demirbag, E., C. Rangin, X. Le Pichon, and A. M. Celal Sengor, 2003. Investigation of the tectonics of the Main Marmara fault by means of deep towed seismic data, Tectonophysics, 361, 1–19.

Drab, L., Hubert, A., Schmidt, S., & Martinez, P. (2012). The earthquake sedimentary record in the western part of the Sea of Marmara, Turkey. Natural Hazards and Earth System Sciences.

D.P., McKenzie, 1972. Active tectonics of the Mediterranean region, Geophys. J. R. Astron.Soc., 30 pp. 109–185

Dooley, T., Monastero, F., Hall, B., McClay, K., & Whitehouse, P. (2004). Scaled sandbox modeling of transtensional pull-apart basins: Applications to the Coso geothermal system. *Geothermal Research Council Transactions, 28*, 637-641.

Dooley, T., & McClay, K. (1997). Analog modeling of pull-apart basins. *AAPG bulletin*, *81*(11), 1804-1826.

Dooley, T. P., & Schreurs, G. (2012). Analogue modelling of intraplate strike-slip tectonics: A review and new experimental results. Tectonophysics, 574, 1-71.

Dotare, T., Yamada, Y., Adam, J., Hori, T., & Sakaguchi, H. (2016). Initiation of a thrust fault revealed by analog experiments. *Tectonophysics, 684*, 148-156.

Ergintav, S., R. E. Reilinger, R. Çakmak, M. Floyd, Z. Cakir, U. Doğan, R. W. King, S. McClusky, and H. Özener, 2014. Istanbul's earthquake hot spots: Geodetic constraints on strain accumulation along faults in the Marmara seismic gap, Geophys. Res. Lett., 41, 5783–5788, doi:10.1002/2014GL060985.

England, P., Houseman, G., & Nocquet, J. M. (2016). Constraints from GPS measurements on the dynamics of deformation in Anatolia and the Aegean. Journal of Geophysical Research: Solid Earth, 121(12), 8888-8916.

F. Flerit, R. Armijo, G.C.P. King, B. Meyer 2004. The mechanical interaction between the propagating North Anatolian Fault and the back-arc extension in the Aegean, Earth Planet. Sci. Lett., 224, pp. 347–362

Frederiksen, A. W., Thompson, D. A., Rost, S., Cornwell, D. G., Gülen, L., Houseman, G. A., ... & Utkucu, M. (2015). Crustal thickness variations and isostatic disequilibrium across the North Anatolian Fault, western Turkey. Geophysical Research Letters, 42(3), 751-757.

Freymueller, J. T. (2011). GPS—Tectonic geodesy. Encyclopedia of Solid Earth Geophysics, 431-449.

Gasperini, L., Polonia, A., Cagatay, M.N., Bortoluzzi, G., Ferrante, V., 2011. Geological slip rates along the North Anatolian Fault in the Marmara region. Tectonics 30, TC6001.

Gasperini, L., Polonia, A., Çağatay, M. N., Bortoluzzi, G., & Ferrante, V. (2011). Geological slip rates along the North Anatolian Fault in the Marmara region. Tectonics, 30(6).

Gazioğlu, C., Gökaşan, E., Algan, O., Yücel, Z., Tok, B., & Doğan, E. (2002). Morphologic features of the Marmara Sea from multi-beam data. Marine Geology, 190(1-2), 397-420.

Gholamrezaie, E., Scheck-Wenderoth, M., Heidbach, O., & Strecker, M.R. (2019). 3-D crustal density model of the Sea of Marmara. *Solid Earth*, *10*(3), 785-807.

Gonca Örgülü; 2011. Seismicity and source parameters for small-scale earthquakes along the splays of the North Anatolian Fault (NAF) in the Marmara Sea. *Geophys J Int*; 184 (1): 385-404. doi: 10.1111/j.1365-246X.2010.04844.x

Grall, C., Henry, P., Tezcan, D., Mercier de Lepinay, B., Bécel, A., Géli, L.,& Harmegnies, F. (2012). Heat flow in the Sea of Marmara Central Basin: Possible implications for the tectonic evolution of the North Anatolian fault. *Geology, 40(1*), 3-6.

Grall, C., Henry, P., Thomas, Y., Westbrook, G.K., Çağatay, M.N., Marsset, B., Saritas, H., Çifçi, G., Géli, L., (2013). Slip rate estimation along the western segment of the Main Marmara Fault over the last 405–490 ka by correlating mass transport deposits. *Tectonics 32,* 1–15.

Guidoboni, E., Comastri, A., Traina, G., & Rom Istituto Nazionale di Geofisica. (1994). Catalogue of Ancient Earthquakes in the Mediterranean Area up to the 10th Century (p. 504). Rome: Istituto nazionale di geofisica.

Guidoboni, E., & Comastri, A. (2005). Catalogue of Earthquakes and Tsunamis in the Mediterranean Area from the 11th to the 15th Century (p. 1037). Rome, Italy: Istituto nazionale di geofisica e vulcanologia.

Gurbuz, C., Aktar, M., Eyidogan, H., Cisternas, A., Haessler, H., Barka, A., ... & Kuleli, S. (2000). The seismotectonics of the Marmara region (Turkey): results from a microseismic experiment. *Tectonophysics*, *316*(1-2), 1-17.

Hatem, A. E., Cooke, M. L., & Toeneboehn, K. (2017). Strain localization and evolving kinematic efficiency of initiating strike-slip faults within wet kaolin experiments. *Journal of Structural Geology, 101,* 96-108.

Hecker, O., 1920, Mitteilungen über Erdbeben im Jahre 1912: Jena, A. Sieberg, Hauptstation für Erdbebenforschung, 26 p.

Herece, E., Akay, E., 2003. Atlas of North Anatolian Fault, Serial Number 2. General Directorate of Mineral Research and Exploration (MTA), Ankara, Turkey.

Hubbert, M. K. (1937). Theory of scale models as applied to the study of geologic structures. Bulletin of the Geological Society of America, 48(10), 1459-1520.

Hubert-Ferrari, A., Barka, A., Jacques, E., Nalbant, S. S., Meyer, B., Armijo, R., ... & King, G. C. (2000). Seismic hazard in the Marmara Sea region following the 17 August 1999 Izmit earthquake. Nature, 404(6775), 269-273.

Hubert-Ferrari, A., Armijo, R., King,G., Meyer,B., Barka, A., 2002. Morphology, displacement, and slip rates along the North Anatolian Fault, Turkey. Journal of Geophysical Research - Solid Earth 107 B10, 2235.

Hergert, T., and Heidbach, O., 2010. Slip-rate variability and distributed deformation in the Marmara Sea fault system, Nature Geoscience, 3, 132-135, doi: 10.1038/NGEO739.

Imren, C., Le Pichon, X., Rangin, C., Demirbağ, E., Ecevitoğlu, B., & Görür, N. (2001). The North Anatolian Fault within the Sea of Marmara: a new interpretation based on multi-channel seismic and multi-beam bathymetry data. *Earth and Planetary Science Letters, 186(2),* 143-158.

Kahle, H. G., Straub, C., Reilinger, R., McClusky, S., King, R., Hurst, K., ... & Cross, P. (1998). The strain rate field in the eastern Mediterranean region, estimated by repeated GPS measurements. *Tectonophysics*, *294*(3-4), 237-252.

Kahle, H. G., Cocard, M., Peter, Y., Geiger, A., Reilinger, R., McClusky, S., ... & Veis, G. (1999). The GPS strain rate field in the Aegean Sea and western Anatolia. *Geophysical research letters*, *26*(16), 2513-2516.

Karabacak, V., Altunel, E., & Cakir, Z. (2011). Monitoring aseismic surface creep along the North Anatolian Fault (Turkey) using ground-based LIDAR. Earth and Planetary Science Letters, 304(1-2), 64-70.

Kaşlılar-Özcan A., İmren C., Boztepe-Güney A., Demirbağ E., Kuşçu İ. 2000. Active faults and evolving strike-slip basins in the Marmara Sea, northwest Turkey: a multichannel seismic reflection study, Tectonophysics, 321, 189-218.

Kenan Akbayram, Christopher C. Sorlien, Aral I. Okay, Evidence for a minimum 52 ± 1 km of total offset along the northern branch of the North Anatolian Fault in northwest Turkey, Tectonophysics, Volumes 668–669, 8 February 2016, Pages 35-41, ISSN 0040-1951, http://dx.doi.org/10.1016/j.tecto.2015.11.026.

Kende, J., Henry, P., Bayrakci, G., Özeren, M. S., & Grall, C. (2017). Moho depth and crustal thinning in the Marmara Sea region from gravity data inversion. Journal of Geophysical Research: Solid Earth, 122(2), 1381-1401.

Klein, E., Vigny, C., Fleitout, L., Grandin, R., Jolivet, R., Rivera, E., & Métois, M. (2017). A comprehensive analysis of the Illapel 2015 Mw8. 3 earthquake from GPS and InSAR data. Earth and Planetary Science Letters, 469, 123-134.

Klinger, Y., Sieh, K., Altunel, E., Akoglu, A., Barka, A., Dawson, T., ... & Rockwell, T. (2003). Paleoseismic evidence of characteristic slip on the western segment of the North Anatolian fault, Turkey. Bulletin of the Seismological Society of America, 93(6), 2317-2332.

Klinkmüller, M., Schreurs, G., Rosenau, M., & Kemnitz, H. (2016). Properties of granular analogue model materials: A community wide survey. *Tectonophysics, 684*, 23-38.

Kurt, H., Sorlien, C.C., Seeber, L., Steckler, M.S., Shillington, D.J., Cifci, G., Cormier, M.H., Dessa,J.X., Atgin, O., Dondurur, D., Demirbag, E., Okay, S., İmren, C., Gurcay, S., Carton, H., 2013. Steady late quaternary slip rate on the Çınarcık section of the North Anatolian fault near Istanbul, Turkey. Geophys. Res. Lett. 40 (17), 4555–4559.

Ketin, İ. (1948). Son on yılda Türkiye'de vukua gelen büyük depremlerin tektonik ve mekanik neticeleri hakkında. Türkiye Jeoloji Bülteni, 2(1), 1-13.

Kurtuluş, C., & Canbay, M. M. (2007). Tracing the middle strand of the North Anatolian Fault zone through the southern Sea of Marmara based on seismic reflection studies. Geo-Marine Letters, 27, 2740. 10.1007/s00367-006-0050-2

Kuşçu İ. 2009. Cross-basin faulting and extinction of pull-apart basins in the Sea of Marmara,NW Turkey. Turkish Journal of Earth Sciences 18: 331-349.

Kürçer, A., Chatzipetros, A., Tutkun, S. Z., Pavlides, S., Ateş, Ö., & Valkaniotis, S. (2008). The Yenice–Gönen active fault (NW Turkey): Active tectonics and palaeoseismology. *Tectonophysics*, *453*(1-4), 263-275.

Koyi, H. A., Ghasemi, A., Hessami, K., & Dietl, C. (2008). The mechanical relationship between strike-slip faults and salt diapirs in the Zagros fold–thrust belt. Journal of the Geological Society, 165(6), 1031-1044.

Kozacı, Ö., Dolan, J. F., & Finkel, R. C. (2009). A late Holocene slip rate for the central North Anatolian fault, at Tahtaköprü, Turkey, from cosmogenic 10Be geochronology: Implications for fault loading and strain release rates. *Journal of Geophysical Research: Solid Earth, 114*(B1).

Laigle, M., Becel, A., de Voogd, B., Hirn, A., Taymaz, T., & Ozalaybey, S. (2008). A first deep seismic survey in the Sea of Marmara: Deep basins and whole crust architecture and evolution. *Earth and Planetary Science Letters*, *270*(3-4), 168-179.

LePichon, X., Şengör, A.C., Demirbağ, E., Rangin, C., İmren, C., Armijo, R., … T ok, B., 2001. The active main Marmara fault. Earth and Planetary Science Letters, 192, 595–616. 10.1016/S0012-821X(01)00449-6

Le Pichon, X., N. Rangin, C. Chamot-Rooke, and A. M. C. Sengör, 2003. The North Anatolian Fault in the Sea of Marmara, J. Geophys. Res., 108(B4), 2179.

Le Pichon, X., Imren, C., Rangin, C., Şengör, A. C., & Siyako, M. (2014). The South Marmara Fault. *International Journal of Earth Sciences, 103(1),* 219-231.

Le Pichon, X., & Kreemer, C. (2010). The Miocene-to-present kinematic evolution of the Eastern Mediterranean and Middle East and its implications for dynamics. Annual Review of Earth and Planetary Sciences, 38, 323-351.

Mandl, G. (1988). Mechanics of tectonic faulting (p. 407). Amsterdam: Elsevier.

Mann, P., Hempton, M. R., Bradley, D. C., & Burke, K. (1983). Development of pull-apart basins. The Journal of Geology, 91(5), 529-554.

McClay, K. R. (1990). Extensional fault systems in sedimentary basins: a review of analogue model studies. Marine and petroleum Geology, 7(3), 206-233.

McClay, K., & Dooley, T. (1995). Analogue models of pull-apart basins. *Geology, 23*(8), 711-714.

McClay, K. R., & White, M. J. (1995). Analogue modelling of orthogonal and oblique rifting. Marine and Petroleum *Geology, 12*(2), 137-151.

McClay, K. R. (1996). Recent advances in analogue modelling: uses in section interpretation and validation. Geological Society, London, Special Publications, 99(1), 201-225.

McClay, K., & Bonora, M. (2001). Analog models of restraining stepovers in strike-slip fault systems. *AAPG bulletin, 85*(2), 233-260.

McClusky, S*., et al.,* 2000. Global Positioning System constraints on plate kinematics and dynamics in the eastern Mediterranean and Caucasus*,* J. Geophys. Res.*,* 105*,* 5695– 5719*.*

McHugh, C. M., Seeber, L., Cormier, M. H., Dutton, J., Cagatay, N., Polonia, A., ... & Gorur, N. (2006). Submarine earthquake geology along the North Anatolia Fault in the Marmara Sea, Turkey: A model for transform basin sedimentation. Earth and Planetary Science Letters, 248(3-4), 661-684.

Meghraoui, M., and Pondrelli, S., 2012. Active faulting and transpression tectonics along the plate boundary in North Africa, Annals of Geophysics v. 55, pp. 5; doi: 10.4 401/ag4970.

Montanari, D., Agostini, A., Bonini, M., Corti, G., & Ventisette, C. D. (2017). The use of empirical methods for testing granular materials in analogue modelling. Materials, 10(6), 635.

Morley, C. K. (1999). How successful are analogue models in addressing the influence of pre-existing fabrics on rift structure?. Journal of Structural Geology, 21(8-9), 1267-1274.

Motagh, M., Djamour, Y., Walter, T. R., Wetzel, H. U., Zschau, J., & Arabi, S. (2007). Land subsidence in Mashhad Valley, northeast Iran: results from InSAR, levelling and GPS. Geophysical Journal International, 168(2), 518-526.

N. N. Ambraseys, J. A. Jackson; 2000. Seismicity of the Sea of Marmara (Turkey) since 1500*. Geophys J Int;* 141 (3): F1-F6. doi: 10.1046/j.1365-246x.2000.00137.x

Nalbant, S.S., Hubert, A. & King, G.C.P., 1998. Stress coupling between earthquakes in northwest Turkey and the North Aegean Sea, J. geophys. Res., 103, 24 469–24 486.

Nocquet, J. M. (2012). Present-day kinematics of the Mediterranean: A comprehensive overview of GPS results. Tectonophysics, 579, 220-242.

Okay, A. I., & Görür, N. (1995). Time and space relations in the formation of the West Black Sea and Thrace Basins. In Proc Symp on the Geology of the Thrace Basin (pp. 9-10).

Okay, A. I., Demirbağ, E., Kurt, H., Okay, N., & Kuşçu, İ. (1999). An active, deep marine strike-slip basin along the North Anatolian fault in Turkey. *Tectonics, 18*(1), 129-147.

Okay, A. I., A. Kaslilar-Ozcan, C. Imren, A. Boztepe-Guney, E. Demirbag, and I. Kuscu (2000), Active faults and evolving strike-slip basins in the Marmara Sea, Northwest Turkey: A multichannel seismic reflection study, *Tectonophysics*, ***321***, 189–218.

Okay, A. I. (2008). Geology of Turkey: a synopsis. Anschnitt, 21, 19-42.

Özdemir, S. (2016). On the estimation of precise coordinates and velocities of TNPGN and TNPGN-active stations. *Journal of Mapping*, *155*, 53-81.

Parke, J. R., T. A. Minshull, G. Anderson, R. S. White, D. McKenzie, I. Kuscu, J. M.Bull, N.Gorur, and C. Sengor (1999), Active faults in the Sea of Marmara, western Turkey, imaged by seismic reflection profiles, Terra Nova, 11, 223–227.

Panien, M., Schreurs, G., & Pfiffner, A. (2006). Mechanical behaviour of granular materials used in analogue modelling: insights from grain characterisation, ring-shear tests and analogue experiments. Journal of Structural Geology, 28(9), 1710-1724.

Parsons, T., Toda, S., Stein, R. S., Barka, A., & Dieterich, J. H. (2000). Heightened odds of large earthquakes near Istanbul: An interaction-based probability calculation. *Science*, *288*(5466), 661-665.

Parsons, T. (2004). Recalculated probability of M≥ 7 earthquakes beneath the Sea of Marmara, Turkey. Journal of Geophysical Research: Solid Earth, 109(B5).

Pinar, N. (1953). Preliminary note on the earthquake of Yenice-Gönen, Turkey, March 18, 1953. Bulletin of the Seismological Society of America, 43(4), 307-310.

Pondard, N., Armijo, R., King, G. C., Meyer, B., & Flerit, F. (2007). Fault interactions in the Sea of Marmara pull-apart (North Anatolian Fault): earthquake clustering and propagating earthquake sequences. Geophysical Journal International, 171(3), 1185-1197.

Rahe, B., Ferrill, D. A., & Morris, A. P. (1998). Physical analog modeling of pull-apart basin evolution. *Tectonophysics, 285*(1-2), 21-40.

Rangin, C., Le Pichon, X., Demirbag, E., & Imren, C. (2004). Strain localization in the Sea of Marmara: Propagation of the North Anatolian Fault in a now inactive pull-apart. *Tectonics*, *23*(2).

Ranalli, G. (1995). Rheology of the Earth. Springer Science & Business Media.

Ranalli, G. (1997). Rheology and deep tectonics. Annals of Geophysics, 40(3).

Reilinger, R. E.*,* S. C. McCLusky*,* M. B. Oral*,* R. W. King*, and* M. N. Toksoz*,* 1997. Global Positioning System measurements of present-day crustal movements in the Arabia-Africa-Eurasia plate collision zone*,* J. Geophys. Res.*,* 102*,* 9983–9999*.*

Reilinger, R., McClusky, S., Vernant, P., Lawrence, S., Ergintav, S., Cakmak, R.... & Nadariya, M. (2006). GPS constraints on continental deformation in the Africa-Arabia-Eurasia continental collision zone and implications for the dynamics of plate interactions. Journal of Geophysical Research: Solid Earth, 111(B5).

Reilinger, R., S. McClusky, D. Paradissis, S. Ergintav, and P. Vernant, 2010. Geodetic constraints on the tectonic evolution of the Aegean region and strain accumulation along the Hellenic subduction zone, Tectonophysics, 488, 22–30.

Reilinger, R., & McClusky, S. (2011). Nubia–Arabia–Eurasia plate motions and the dynamics of Mediterranean and Middle East tectonics. *Geophysical Journal International, 186*(3), 971-979.

Richard, P. D., Naylor, M. A., & Koopman, A. (1995). Experimental models of strike-slip tectonics. Petroleum Geoscience, 1(1), 71-80.

ROCKWELL, T., BARKA, A., SEITZ, G., RAGONA, D., AKSOY, E., KLINGER, Y., ... & UKARCUS, G.(2001, March). PALEOSEISMOLOGY OF THE NORTH ANATOLIAN FAULT EAST AND WEST OF THE MARMARA SEA: IMPLICATIONS FOR SEISMIC HAZARD TO ISTANBUL. In *Geological Society of America Abstracts with Programs,* (Vol. 33, No. 3, p. 78).

Royden, L. H. (1993). Evolution of retreating subduction boundaries formed during continental collision. Tectonics, 12(3), 629-638.

Sarı, E., & Çağatay, M. N. (2006). Turbidites and their association with past earthquakes in the deep Çınarcık Basin of the Marmara Sea. *Geo-Marine Letters*, *26*(2), 69

Schellart, W. P. (2000). Shear test results for cohesion and friction coefficients for different granular materials: scaling implications for their usage in analogue modelling. Tectonophysics, 324(1-2), 1-16.

Schmittbuhl, J., Karabulut, H., Lengliné, O., & Bouchon, M. (2016). Long-lasting seismic repeaters in the Central basin of the Main Marmara fault. *Geophysical Research Letters*, *43*(18), 9527-9534.

Schreurs, G. (1994). Experiments on strike-slip faulting and block rotation. Geology, 22(6), 567-570.

Schreurs, G., & Colletta, B. (1998). Analogue modelling of faulting in zones of continental transpression and transtension. Geological Society, London, Special Publications, 135(1), 59-79.

Schreurs, G. (2003). Fault development and interaction in distributed strike-slip shear zones:an experimental approach. Geological Society, London, Special Publications, 210(1), 35-52.

Seeber, L., et al., Emre, Ö. Cormier, M.-H., Sorlien, C.C., McHugh, C.M.G., Polonia, A., Özer, N., Cagatay, N., 2004. Uplift and subsidence from oblique slip: the Ganos–Marmara bend of the North Anatolian Transform, Western Turkey. Tectonophysics 391 (1-4), 239–258.

Seeber, L., Cormier, M. H., McHugh, C., Emre, O., Polonia, A., & Sorlien, C. (2006). Rapid subsidence and sedimentation from oblique slip near a bend on the North Anatolian transform fault in the Marmara Sea, Turkey. Geology, 34(11), 933-936.

Selim, H.H. and Tüysüz, O., 2013. The Bursa-Gönen Depression, NW Turkey: a complex basin developed on the North Anatolian Fault (NAF).

Shen, Z.-K., M. Wang, Y. Zeng, and F. Wang, (2015), Strain determination using spatially discrete geodetic data, Bull. Seismol. Soc. Am., 105(4), 2117-2127, doi: 10.1785/0120140247

Straub, C., Kahle, H. G., & Schindler, C. (1997). GPS and geologic estimates of the tectonic activity in the Marmara Sea region, NW Anatolia. *Journal of Geophysical Research: Solid Earth*, *102*(B12), 27587-27601.

Sylvester, A. G. (1988). Strike-slip faults. Geological Society of America Bulletin, 100(11), 1666-1703.

S. Pucci, P.M. De Martini, D. Pantosti, 2008. Preliminary slip rate estimates for the Düzce segment of the North Anatolian Fault Zone from offset geomorphic markers,Geomorphology,Volume 97, Issues 3–4, 15 May, Pages 538-55 ISSN 0169-555X.

Stein, R.S., Barka, A.A. & Dieterich, J.H., 1997. Progressive failure on the North Anatolian fault since 1939 by earthquake stress triggering, Geophys. J. Int., 128, 594–604

Sims, D., Ferrill, D. A., & Stamatakos, J. A. (1999). Role of a ductile decollement in the development of pull-apart basins: Experimental results and natural examples. Journal of Structural Geology, 21(5), 533-554.

Sugan, M., Wu, J. E. L., & McClay, K. (2014). 3D analogue modelling of transtensional pull-apart basins: comparison with the Cinarcik basin, Sea of Marmara, Turkey. *Bollettino di Geofisica Teorica ed Applicata, 55*(4).

Sengör, A. M. C. (1979). The North Anatolian transform fault: its age, offset and tectonic significance. Journal of the Geological Society, 136(3), 269-282.

Şengör, A. C., & Yilmaz, Y. (1981). Tethyan evolution of Turkey: a plate tectonic approach. Tectonophysics, 75(3-4), 181-241.

Şengör, A. M. C., Görür, N., & Şaroğlu, F. (1985). Strike-slip faulting and related basin formation in zones of tectonic escape: Turkey as a case study.

Şengör, A. M. C., O. Tuysuz, C. Imren, M. Sakınc, H. Eyidogan, N. Gorur, X. Le Pichon, and C.Rangin (2005), The North Anatolian fault: A new look, Annu. Rev. Earth Plan Sci., 33, 37–112.

Tavlan, M., Thorne, R., & Herrington, R. J. (2011). Uplift and lateritization history of the Çaldağ ophiolite in the context of Neo-Tethyan ophiolite obduction and uplift: implications for the Cenozoic weathering history of western Anatolia. Journal of the Geological Society, 168(4), 927-940.

Thielicke, W and Stamhuis, E J 2014 PIVlab – Towards User-friendly, A ordable and Accurate Digital Particle Image Velocimetry in MATLAB. Journal of Open Research Software, 2: e30, DOI: http://dx.doi.org/10.5334/jors.bl

Toksöz, M.N., Shakal, A.F. & Michael, A.J 1979. PAGEOPH, 117: 1258. Y.Yilmaz, S.C. Genç, Z. Karacik, S. Altunkaynak, 2001. Two contrasting magmatic associations of NW Anatolia and their tectonic significance, J. Geodyn., 3, pp. 243–271

UÇARKUŞ, G., Cakir, Z., & Armijo, R. (2011). Western termination of the Mw7.4, 1999 İzmit Earthquake rupture: Implications for the expected large earthquake in the Sea of Marmara. *Turkish Journal of Earth Sciences*, *20*(4), 379-394.

Ueta, K., Tani, K., & Kato, T. (2000). Computerized X-ray tomography analysis of three-dimensional fault geometries in basement-induced wrench faulting. Engineering Geology, 56(1-2), 197-210.

Yaltırak, C. (2002). Tectonic evolution of the Marmara Sea and its surroundings. *Marine Geology, 190*(1-2), 493-529.

Yamasaki, T., Wright, T. J., & Houseman, G. A. (2014). Weak ductile shear zone beneath a major strike-slip fault: Inferences from earthquake cycle model constrained by geodetic observations of the western North Anatolian Fault Zone. Journal of Geophysical Research: Solid Earth, 119(4), 3678-3699.

Zattin, M., Okay, A. I., & Cavazza, W. (2005). Fission-track evidence for late Oligocene and mid-Miocene activity along the North Anatolian Fault in south-western Thrace. Terra Nova, 17(2), 95-101.

Zitter, T. A. C., Grall, C., Henry, P., Özeren, M. S., Çağatay, M. N., Şengör, A.M. C., ... & Géli, L. (2012). Distribution, morphology and triggers of submarine mass wasting in the Sea of Marmara. *Marine Geology*, *329*, 58-74.

Wdowinski, S., Smith-Konter, B., Bock, Y., & Sandwell, D. (2007). Diffuse interseismic deformation across the Pacific–North America plate boundary. *Geology*, *35*(4), 311-314.

Weijermars, R., & Schmeling, H. (1986). Scaling of Newtonian and non-Newtonian fluid dynamics without inertia for quantitative modelling of rock flow due to gravity (including the concept of rheological similarity). Physics of the Earth and Planetary Interiors, 43(4), 316-330.

White, D.J., Take, W.A., Bolton, M.D., 2001. Measuring soil deformation in geotechnical models using digital images and PIV analysis. In: 10th International Conference on Computer Methods and Advances in Geomechanics, Tucson, Arizona.

Wu, J. E., McClay, K., Whitehouse, P., & Dooley, T. (2009). 4D analogue modelling of transtensional pull-apart basins. Marine and Petroleum Geology, 26(8), 1608-16

Appendix I: Complete Overview Models

Models MAR-03, 05, 06, 07, 08, 09, 10 and 13 have not been used in papers and therefore, not described in the thesis's chapters. Table 1 summarize all the experiments performed for this thesis and their parameters. The models differ in the thickness of the silicon putty, the sand pack, the velocity of the plates, and the total displacement.

Table 1 Summary of the parameters used in the experiments run for the purpose of this thesis. In red those described only in this appendix.

Model number	Silicone Thickness (mm)	Dry sand Thickness (mm)	Plates' Velocity mm/hr	Total Displacement (mm)	Upper Plate Displacement (mm)	Total Time hh.mm
MAR-01	Failed					
MAR-02 1 plate	2	15	V:20	70	…	
MAR-03 2 plates	2	15	V_L: 20 V_U: 4 (@20 mm V_U: 6)	70	5.4	4.06
MAR-04 2 plates	2	15	V_L: 20; V_U:6 (@55 mm V_U:2)	70	10	4.11
MAR-05 2 plates	1	15	V_L: 20 (@30 mm V_U:6)	70	10	4.15
MAR-06 2 plates	1	15	V_L: 20 V_U:12	70	37	3.58
MAR-07 1 plate	5	10	V_L: 20;	70	..	3.50
MAR-08 2 plates	5	10	V_L: 20(@70 mm V_L: 1) V_U:12	110	40	11.35+3.49
MAR-09 1 plate	2	15	..	40	…	1.02
MAR-10	2	15	..	55	..	1.31
MAR-11	Failed					
MAR-12 1 plate	2	15	V:10	70	…	6.50
MAR-13 1 plate	5	30	V:5	100	….	

Note. In two-plates experiments V_L and V_U represent the velocity of lower plate and velocity of upper plate, respectively.

Table 2 presents the inventory of the material related to the analogue experiments.

Table 2 All plus marked represent the materials presented in this thesis, both in Chapters and in Appendix I.

Models	Top Images of the model	Scan Data (3D Topographic Evolution of the Model)	Cross- sections
MAR-01	-	-	-
MAR-02	+	+	+
MAR-03	+	+	+
MAR-04	+	+	-
MAR-05	+	+	+
MAR-06	+	+	+
MAR-07	+	+	+
MAR-08	+	+ xyz.file Not processed	+
MAR-09	+partly	+	-
MAR-10	+partly	+ xyz.file Not processed	-
MAR-11	-	-	-
MAR-12	+	+	+
MAR-13	+	+	+

Note. Mar-01 and MAR-11 failed. In the experiments MAR-04, MAR-06, MAR-07, MAR-08, MAR-09, MAR-10 we observed high boundary effect. So, we suspended the experiment.

MAR-02

MAR-02 is the model which I described in Chapter 4. Here I present the results of MAR-02 that are not mentioned before in this thesis.

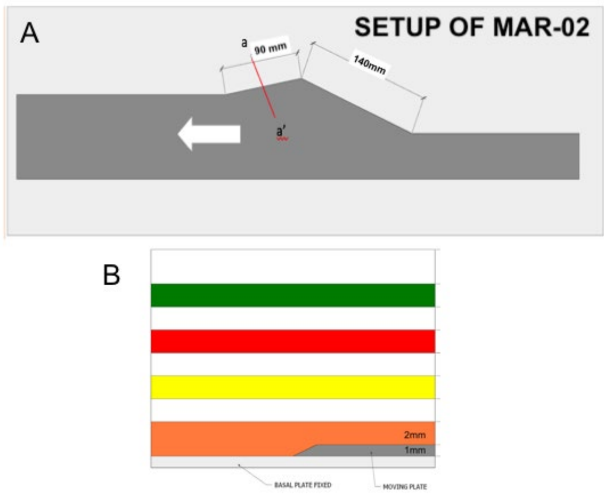

Figure 1 *a) the experimental setup for the models of MAR-02. The white arrows represent the direction of the plate movement. b) The stratigraphic view (a-a' section) of the model setups.*

The basal plate which we used for the model MAR-02 is the same basal plate that was used as lower plate in MAR-03 (compare with Fig. 3). The layering of MAR-02 started with 2 mm-thick silicone putty resting on the composite base made of two plexiglass sheets. On the silicone putty layer, we put 15 mm-thick sand pack. The plate velocity was 20 mm/h; and the total displacement was 70 mm (see in Table 1).

Figure 2 shows the cross sections cut at the end of the experiment.

Figure 2: CROSS-SECTIONS OF MAR-02

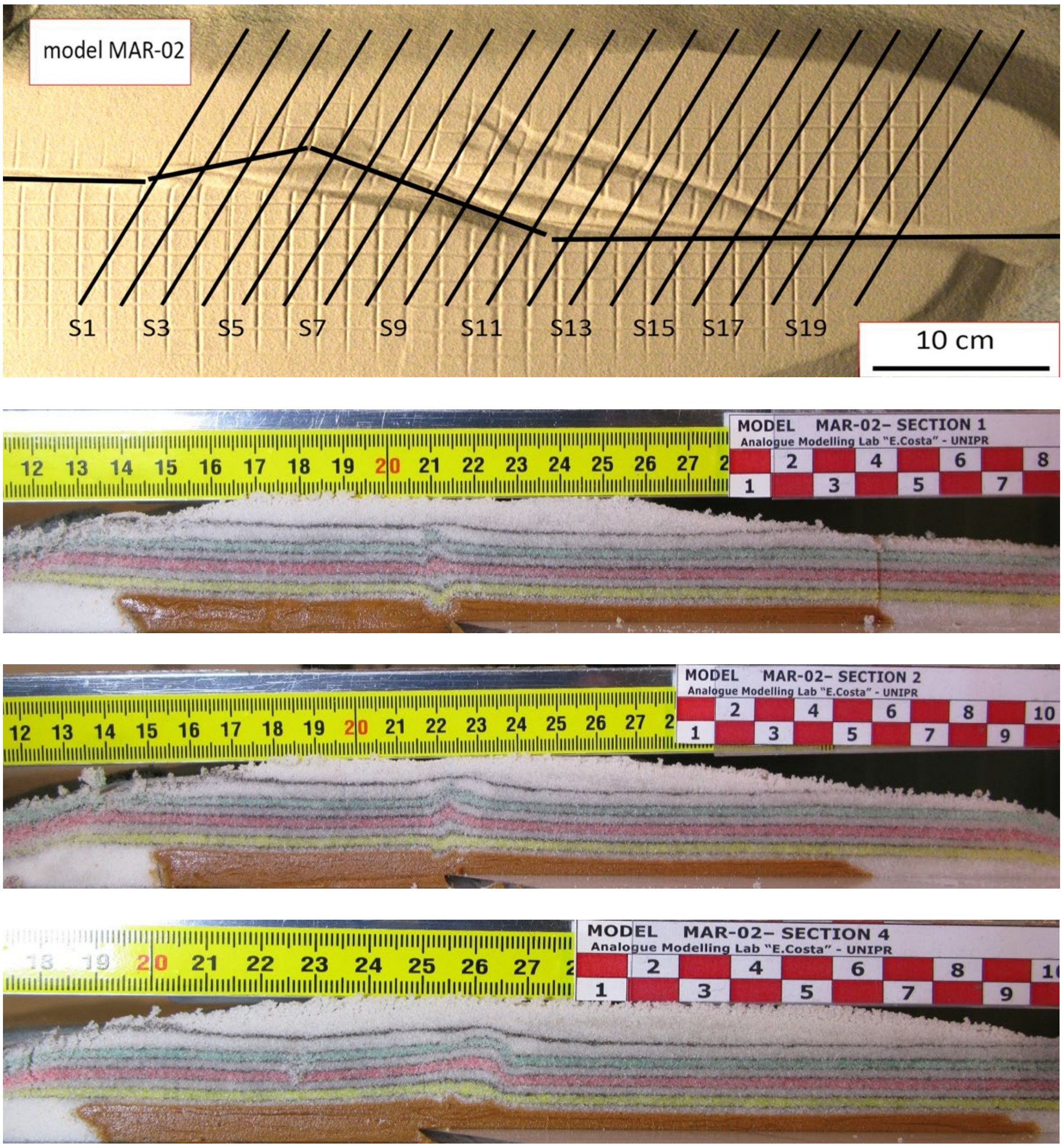


MODEL MAR-02– SECTION 5
Analogue Modelling Lab "E.Costa" - UNIPR


MODEL MAR-02– SECTION 6
Analogue Modelling Lab "E.Costa" - UNIPR

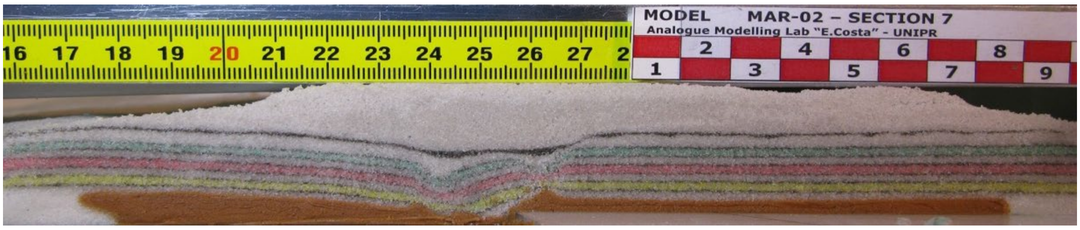
MODEL MAR-02 – SECTION 7
Analogue Modelling Lab "E.Costa" - UNIPR


MODEL MAR-02 – SECTION 8
Analogue Modelling Lab "E.Costa" - UNIPR


MODEL MAR-02– SECTION 9
Analogue Modelling Lab "E.Costa" - UNIPR


MODEL MAR-02– SECTION 10
Analogue Modelling Lab "E.Costa" - UNIPR


MODEL MAR-02– SECTION 11
Analogue Modelling Lab "E.Costa" - UNIPR

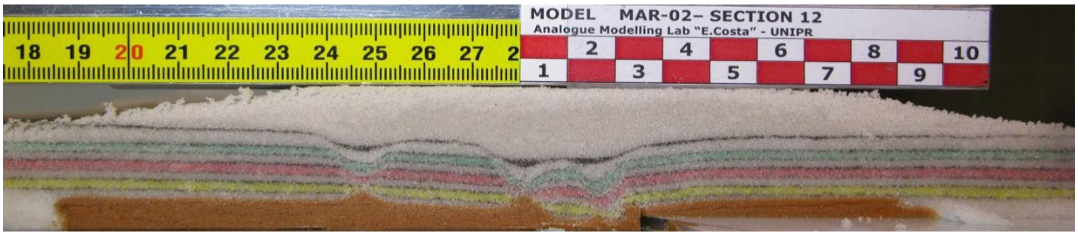
MODEL MAR-02– SECTION 12
Analogue Modelling Lab "E.Costa" - UNIPR

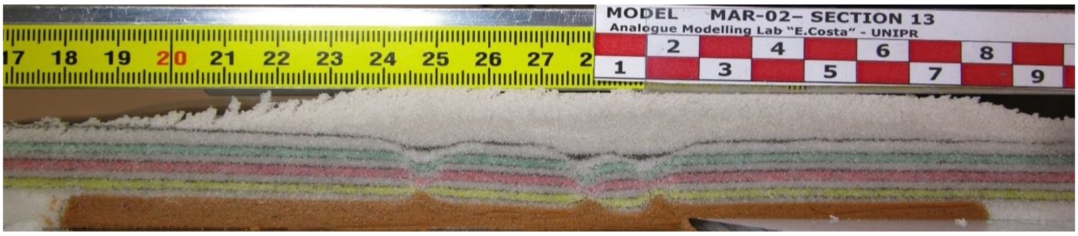
MODEL MAR-02– SECTION 13
Analogue Modelling Lab "E.Costa" - UNIPR

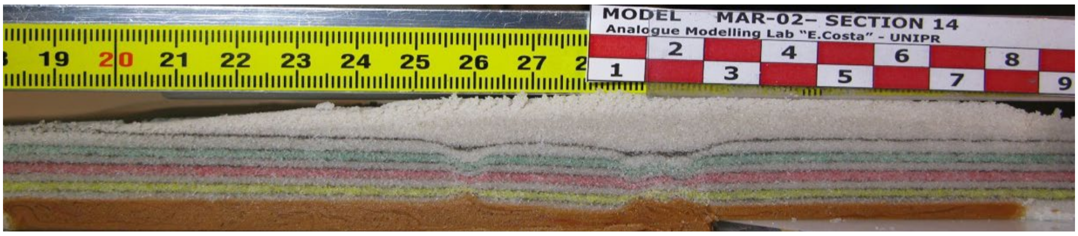
MODEL MAR-02– SECTION 14
Analogue Modelling Lab "E.Costa" - UNIPR

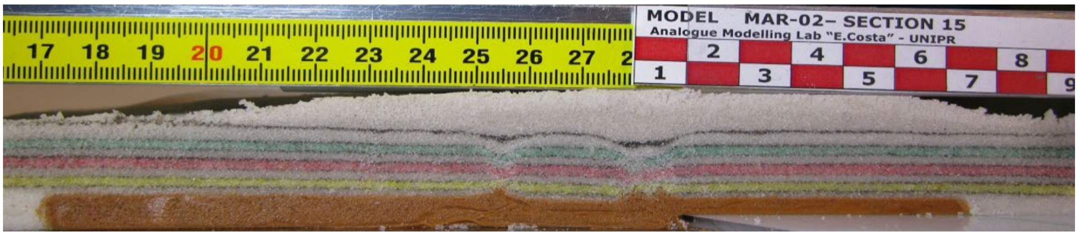
MODEL MAR-02– SECTION 15
Analogue Modelling Lab "E.Costa" - UNIPR


MODEL MAR-02– SECTION 16
Analogue Modelling Lab "E.Costa" - UNIPR

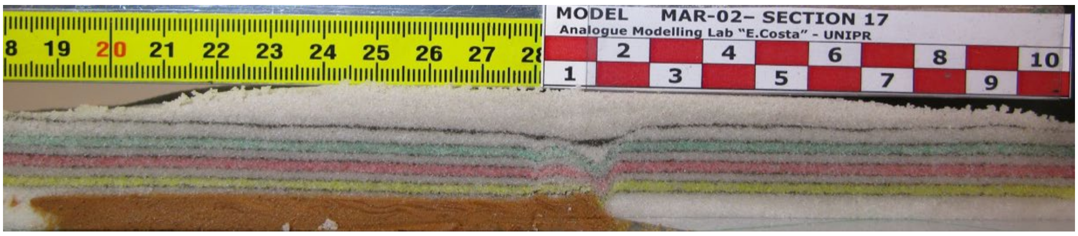
MODEL MAR-02– SECTION 17
Analogue Modelling Lab "E.Costa" - UNIPR


MODEL MAR-02 – SECTION 18
Analogue Modelling Lab "E.Costa" - UNIPR

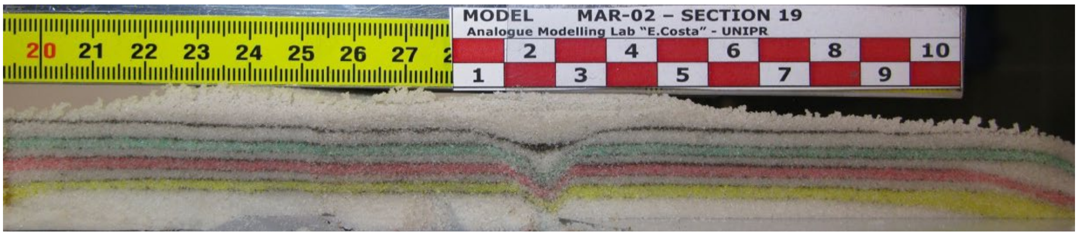

MAR-03, MAR-05, MAR-06

MAR-03, MAR-05, MAR-06 were built to monitor the relationship between the horizontal propagation and the branching of the strike slip fault. The models' geometry was designed to compare the structural and topographic evolution observed during the experiments with examples taken from the western-NAF system.

All the models share the same basal plate geometry formed by two overlaying plexiglass sheets: a lower plate purposely cut to simulate the trace of a strike-slip fault characterised by a releasing bend and an adjacent restraining bend (red polygon in figure 3A), and a rectangular upper plate (black dashed line in figure 3A) and). Both plates were able to slide independently. The silicon putty and the sand pack (green rectangle in figure 3A) were layered on the two basal plates.

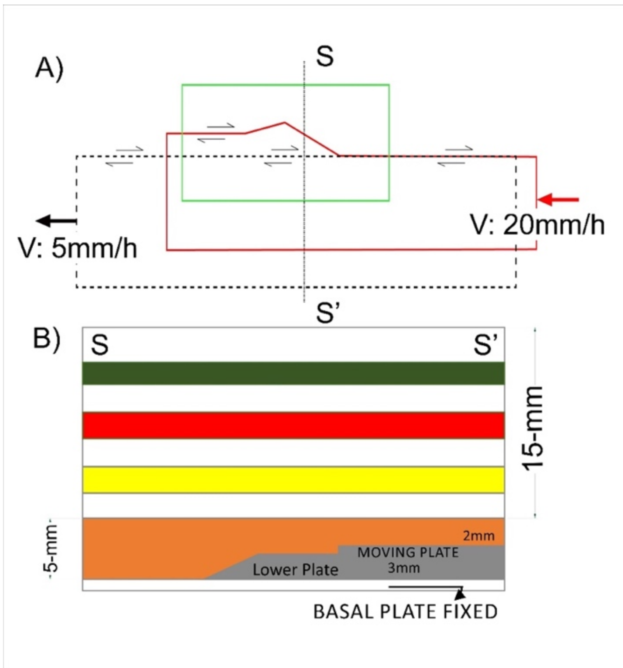

Figure 3 *shows a) the experimental setup for MAR-03. The green rectangle represents the silicone putty layer put on top of the movement plates, the black-dashed lines represents the upper plate; the red polygon represents the lower plate. The arrows represent the direction of the plates' movement. b) Stratigraphic view (S-S' section) of the model setups.*

MAR-03

The layering of **MAR-03** started with 2 mm-thick silicone putty resting on the composite base made of two plexiglass sheets. On the silicone putty layer, we put 15 mm-thick sand pack. Two plates are moving at different velocities in the same direction (see in Fig. 3). In MAR-03 at the 20 mm displacements, the velocity of upper plate was increased from 4 to 6. In this model, the right-lateral displacement was 70 mm.

Figure 4 shows the model photographed each 10 mm of displacement. Figure 5 shows the topographic evolution of the model. Figure 6 shows the cross sections cut at the end of the experiment.

Note that, although the model developed subsidence and uplift in relation to the releasing and restraining bends respectively, the model did not develop faults.

Figure 4: TOP IMAGES OF MAR-03

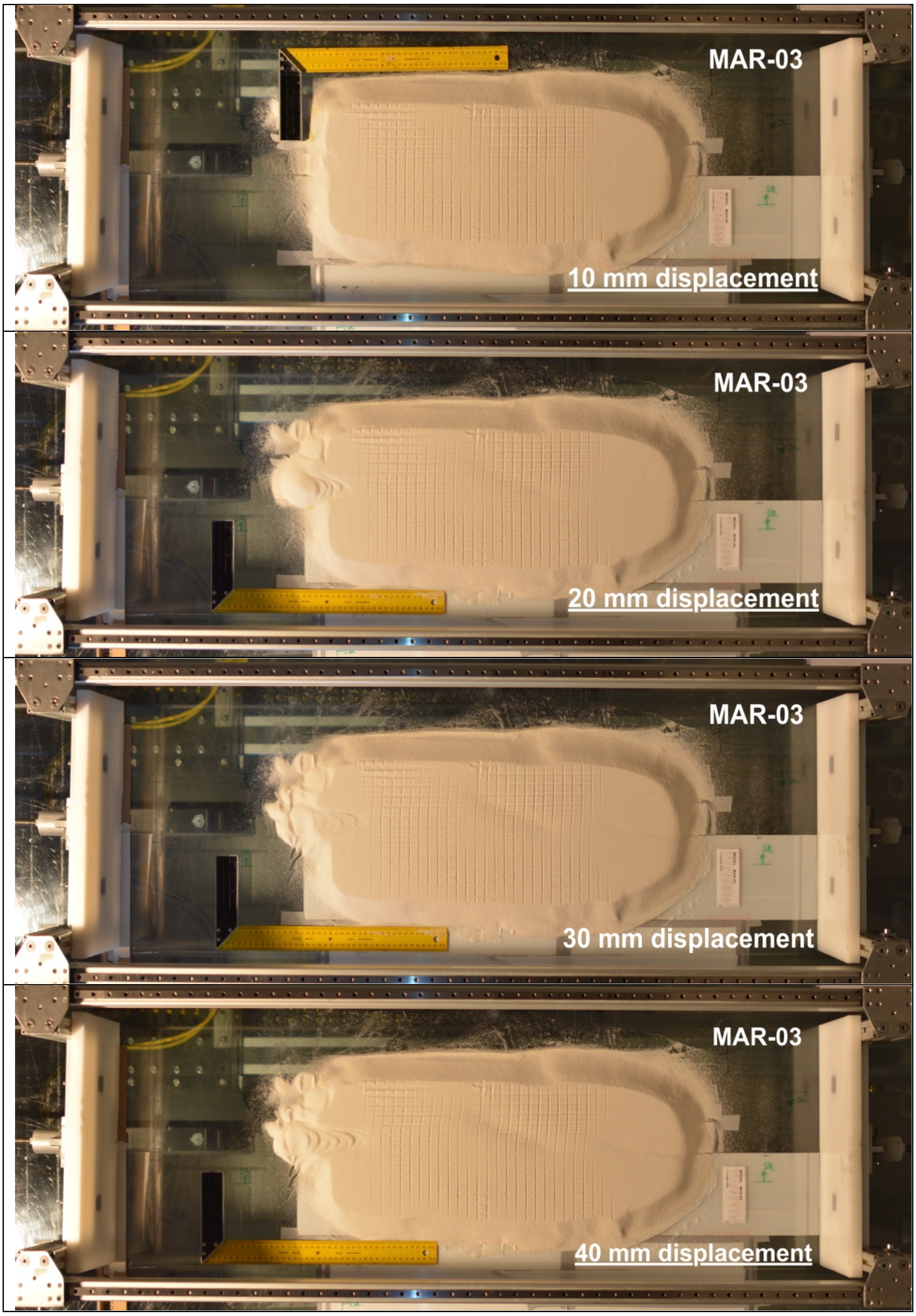

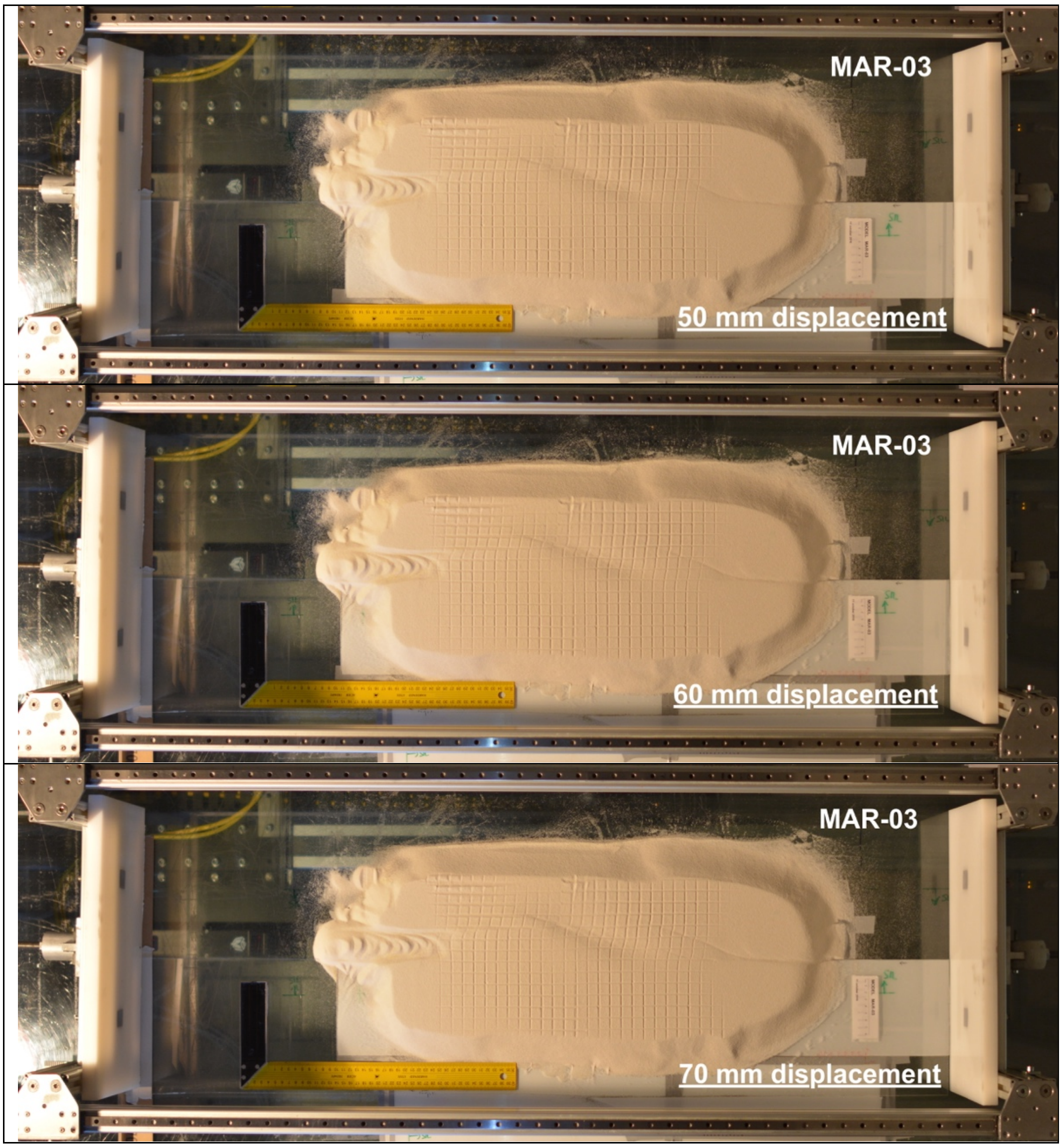
MAR-03
50 mm displacement
MAR-03
60 mm displacement
MAR-03
70 mm displacement

Figure 5: 3D TOPOGRAPHIC EVOLUTION OF MAR-03

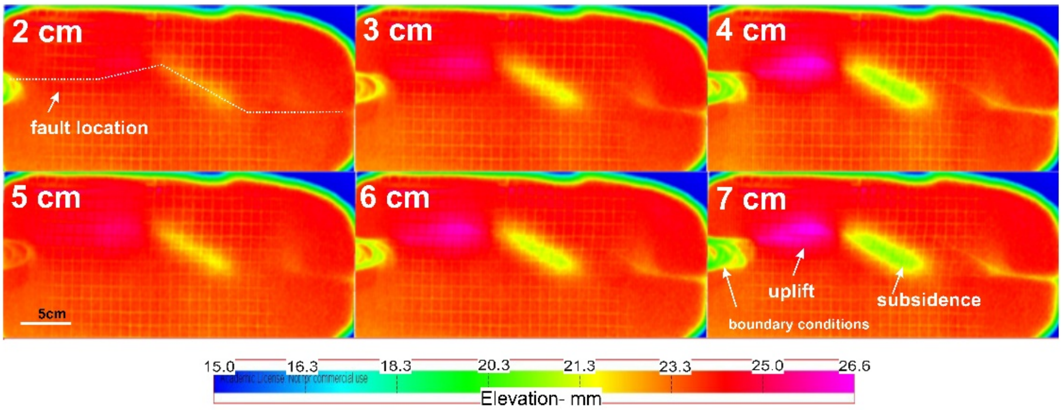

Figure 6: CROSS-SECTIONS OF MAR-03

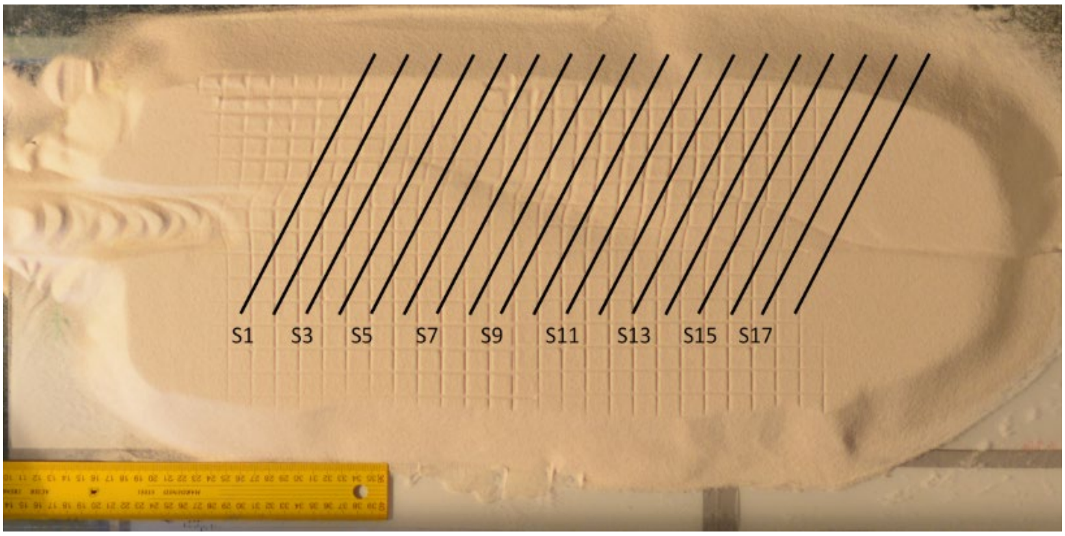

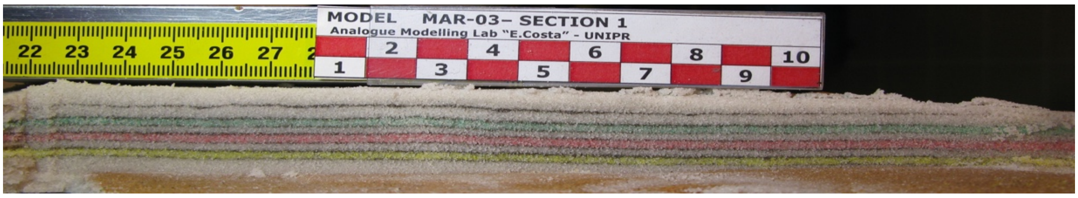

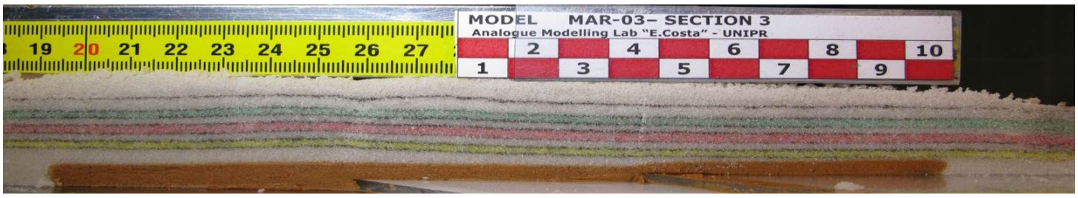
MODEL MAR-03- SECTION 3
Analogue Modelling Lab "E.Costa" - UNIPR

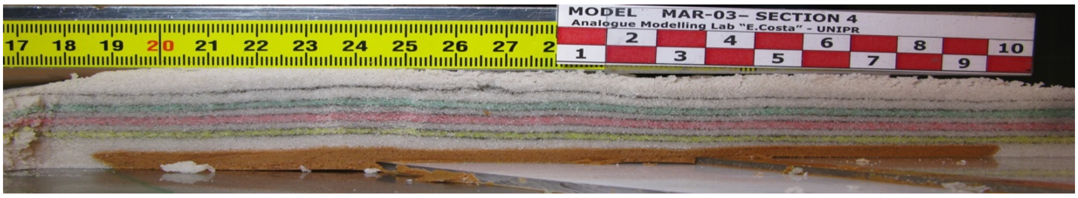
MODEL MAR-03- SECTION 4
Analogue Modelling Lab "E.Costa" - UNIPR

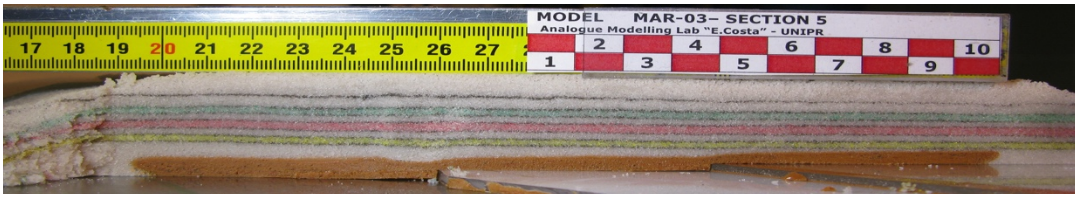
MODEL MAR-03- SECTION 5
Analogue Modelling Lab "E.Costa" - UNIPR

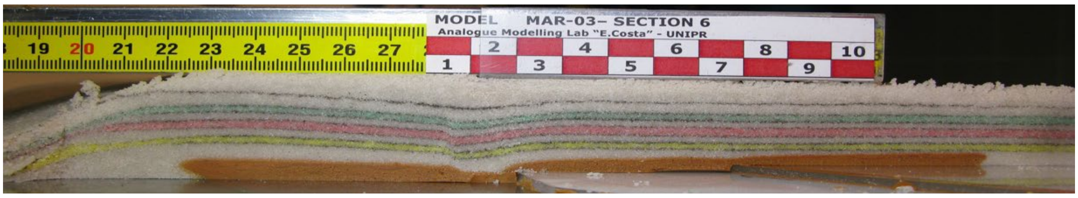
MODEL MAR-03- SECTION 6
Analogue Modelling Lab "E.Costa" - UNIPR

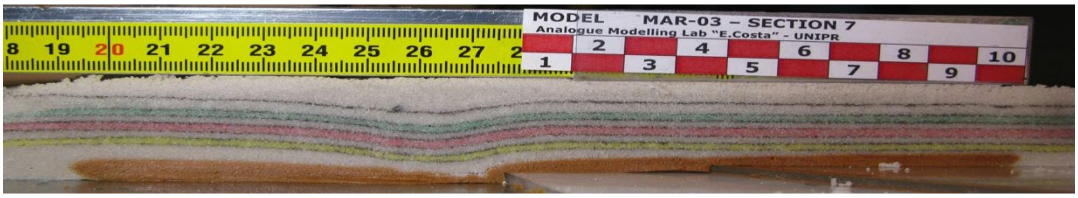
MODEL MAR-03 - SECTION 7
Analogue Modelling Lab "E.Costa" - UNIPR

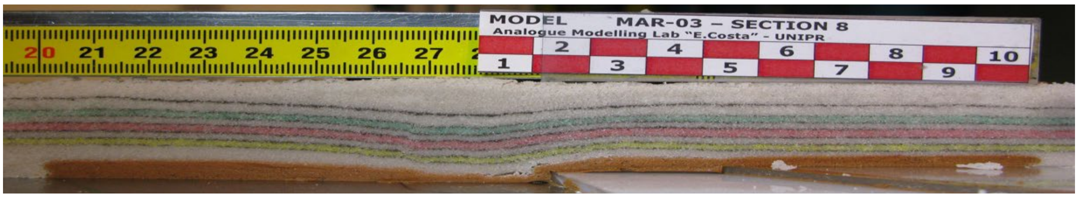
MODEL MAR-03 - SECTION 8
Analogue Modelling Lab "E.Costa" - UNIPR

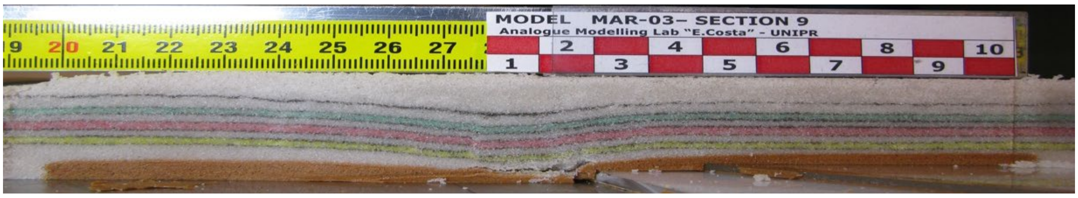
MODEL MAR-03- SECTION 9
Analogue Modelling Lab "E.Costa" - UNIPR

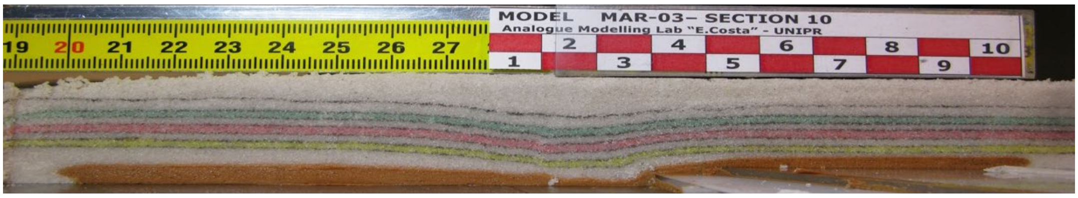
MODEL MAR-03- SECTION 10
Analogue Modelling Lab "E.Costa" - UNIPR

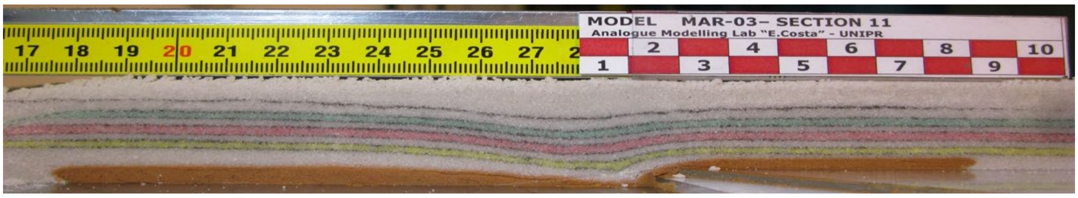
MODEL MAR-03- SECTION 11
Analogue Modelling Lab "E.Costa" - UNIPR

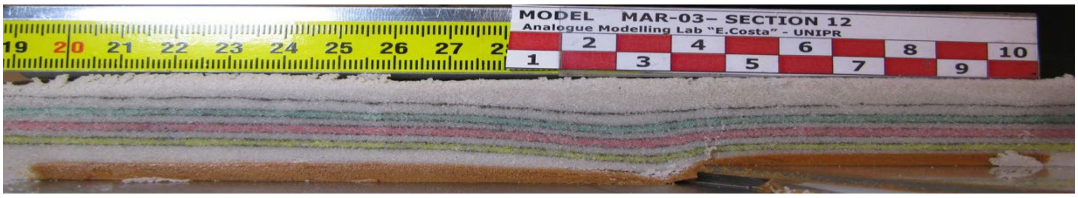
MODEL MAR-03- SECTION 12
Analogue Modelling Lab "E.Costa" - UNIPR

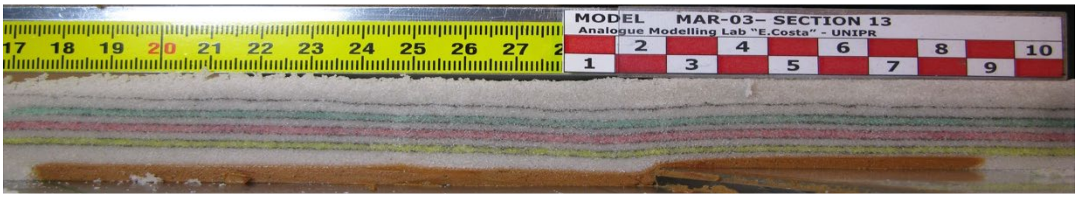
MODEL MAR-03- SECTION 13
Analogue Modelling Lab "E.Costa" - UNIPR

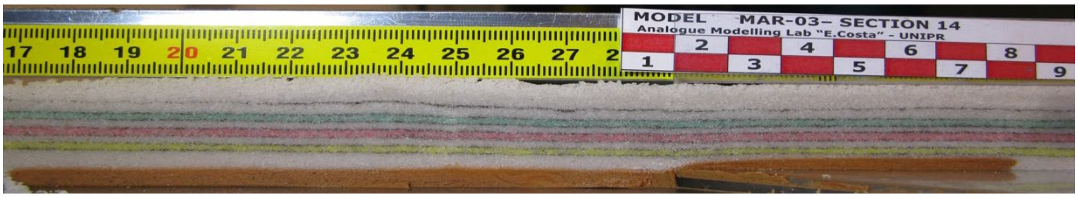
MODEL MAR-03- SECTION 14
Analogue Modelling Lab "E.Costa" - UNIPR

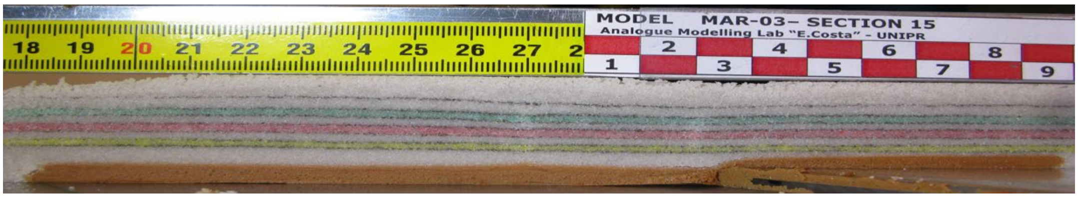
MODEL MAR-03- SECTION 15
Analogue Modelling Lab "E.Costa" - UNIPR

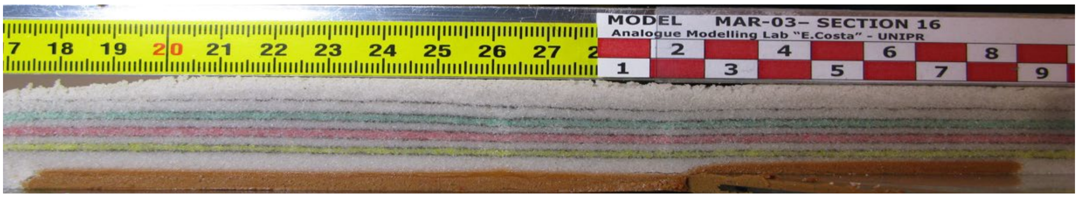
MODEL MAR-03- SECTION 16
Analogue Modelling Lab "E.Costa" - UNIPR

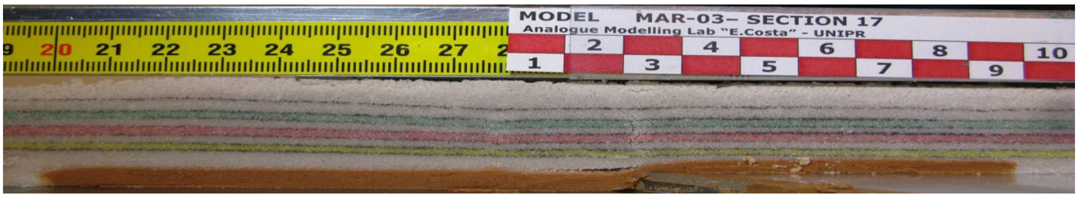
MODEL MAR-03- SECTION 17
Analogue Modelling Lab "E.Costa" - UNIPR


MODEL MAR-03 – SECTION 18
Analogue Modelling Lab "E.Costa" - UNIPR

MAR-05 and MAR-06

The experimental setups of MAR-05 and MAR-06 are the same, except for the velocities of the two plates. From bottom to top the layering of the model started with 1 mm-thick silicone putty below 15 mm-thick sand pack.

In these models, the lower plate and the upper plate were allowed to slide in the same direction, but with different velocities. In both models the lower plate was moving at 20 mm/hr. In MAR-05, after 30 mm of displacement the upper plate started to move at 6 mm/hr. In MAR-06, both lower and upper plates started to slide at the same time but with different velocities: the velocity of lower plate was 12 mm/hr; the velocity of the upper plate was 20 mm/hr. The total displacement was 70 mm for both models.

Figure 7 and 8 show models MAR-05 and MAR-06 respectively photographed each 10 mm of displacement. Figure 9 shows the topographic evolution of the two models.

While during the experiment MAR-05 we observed a secondary branch evolution, MAR-06 did not produce any branching.

Figure 10 Plan view and cross section of MAR-05 to show details of the northern vs. south branch deformation at the end of the experiment.

Figure 11 and 12 show the cross sections of models MAR-05 and MAR-06 cut at the end of the experiments.

Figure 7: TOP IMAGES OF MAR-05

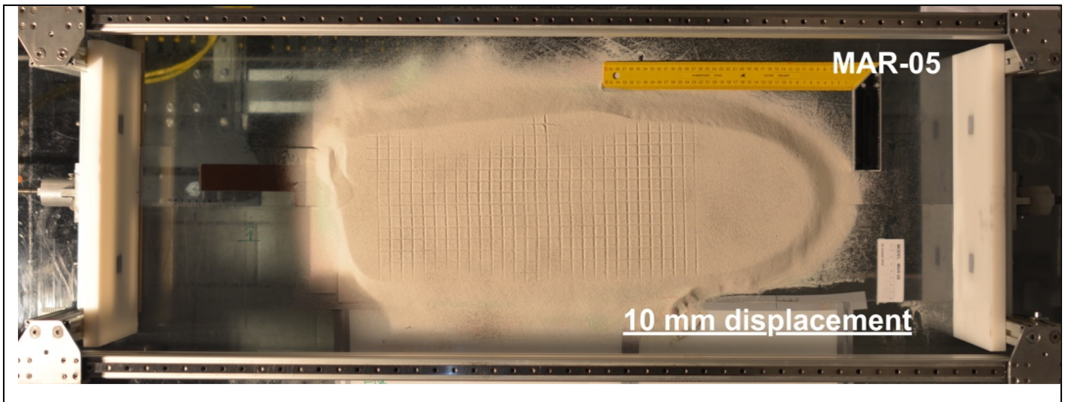

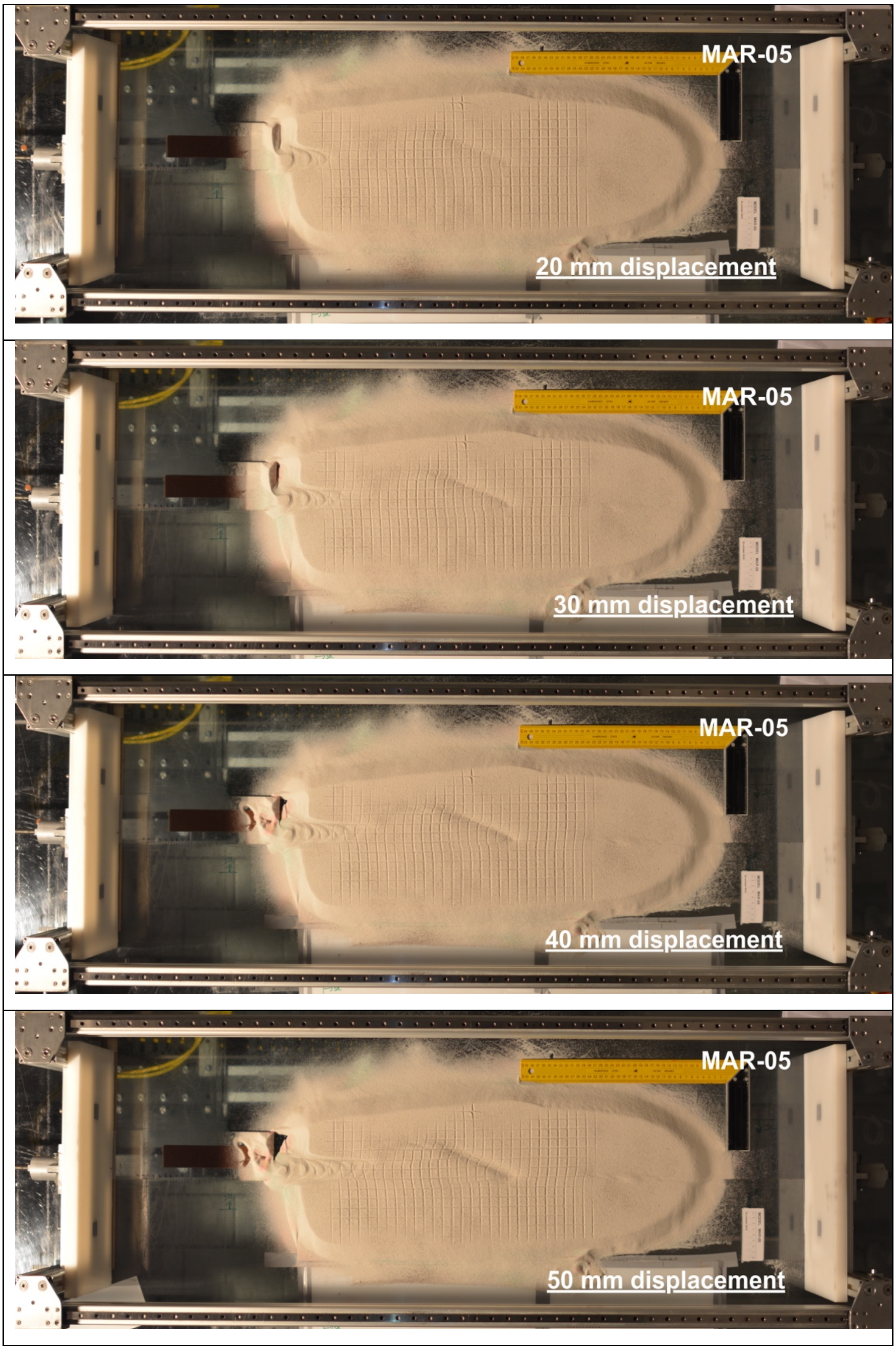
MAR-05
20 mm displacement
MAR-05
30 mm displacement
MAR-05
40 mm displacement
MAR-05
50 mm displacement

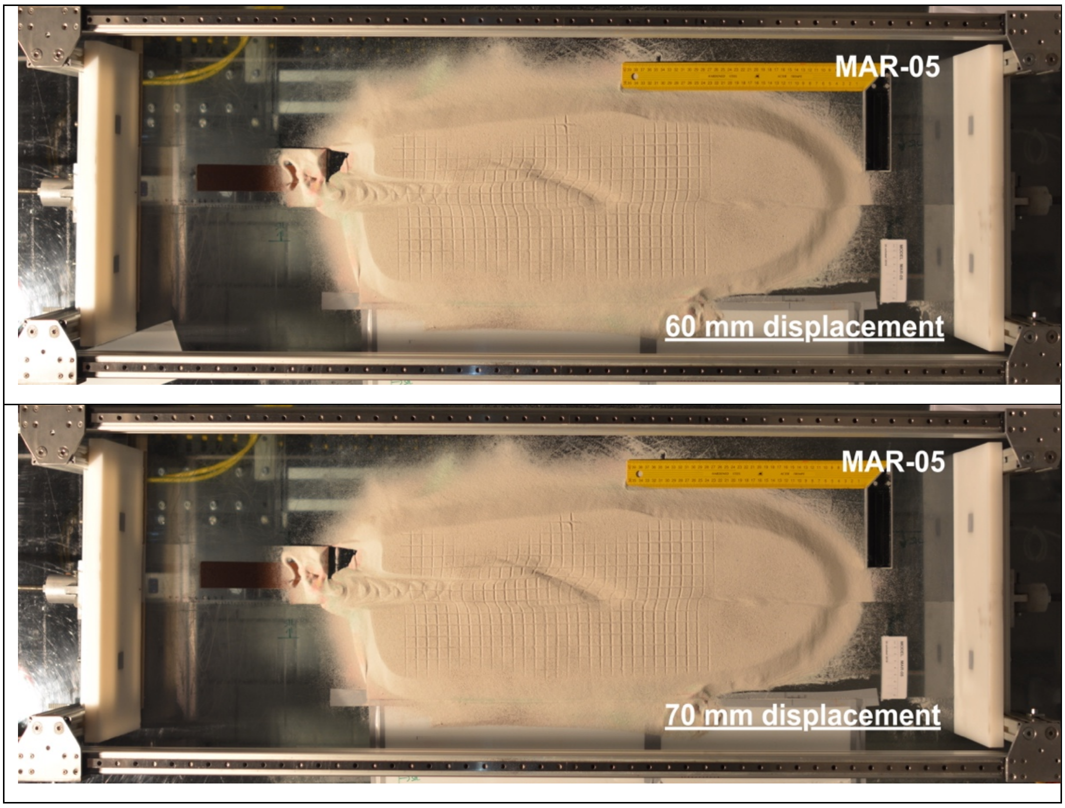

Figure 8: TOP IMAGES OF MAR-06

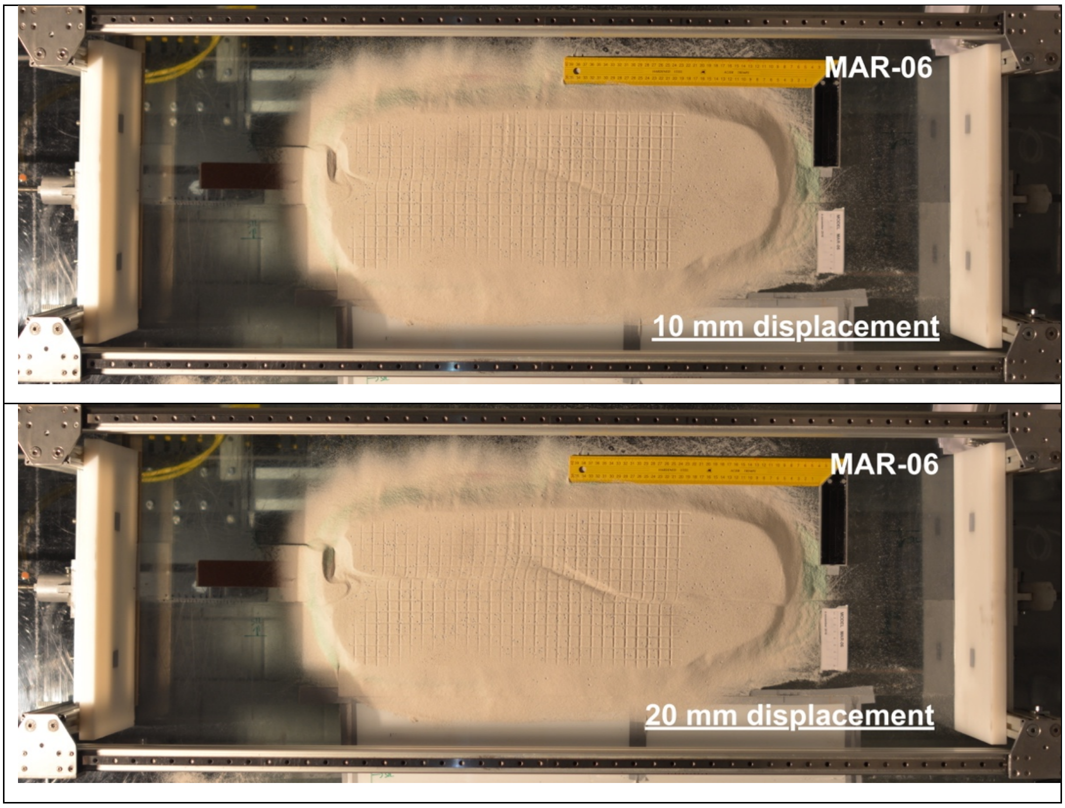

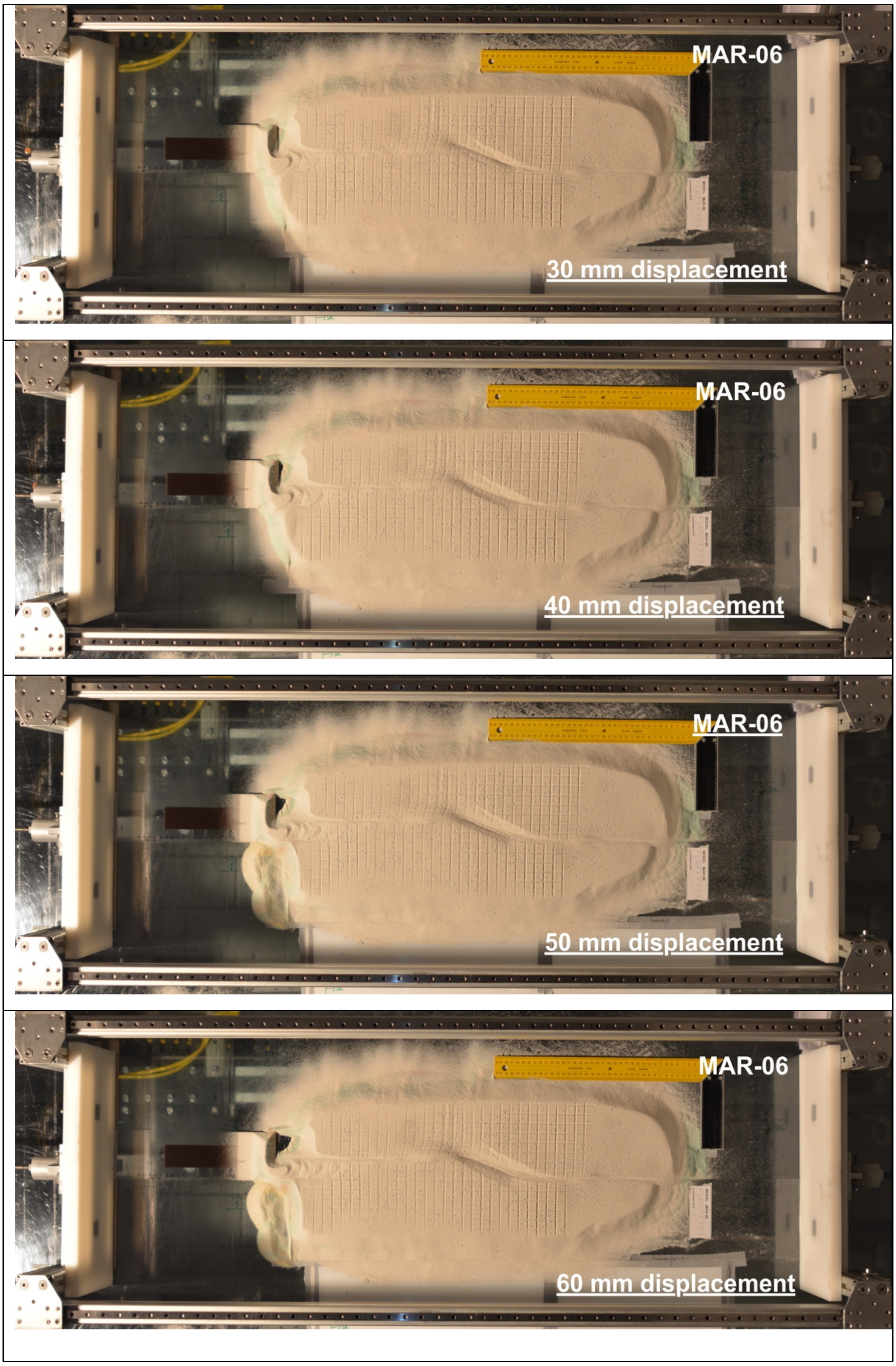
MAR-06
30 mm displacement
MAR-06
40 mm displacement
MAR-06
50 mm displacement
MAR-06
60 mm displacement

Figure 9: 3D TOPOGRAPHIC EVOLUTION OF MAR-05 AND MAR-0

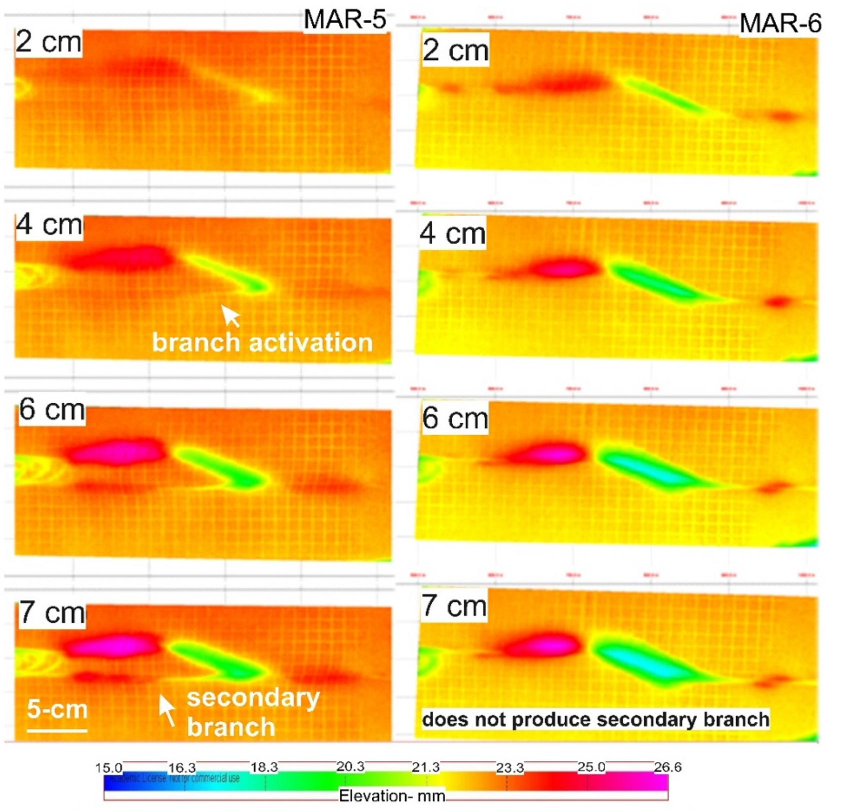

***Figure 9** shows the comparison of the topographic evolution between MAR-05 and MAR-06. The surface topographies of models are derived from scan data. MAR 5 and MAR 6 were set to investigate the branching on the western part of the NAF. An upper plate was added to the model setup, representing the southern branch in the Sea of Marmara (see in Fig. 5.1). The deformation was collected during the experiments through surface scanning.*

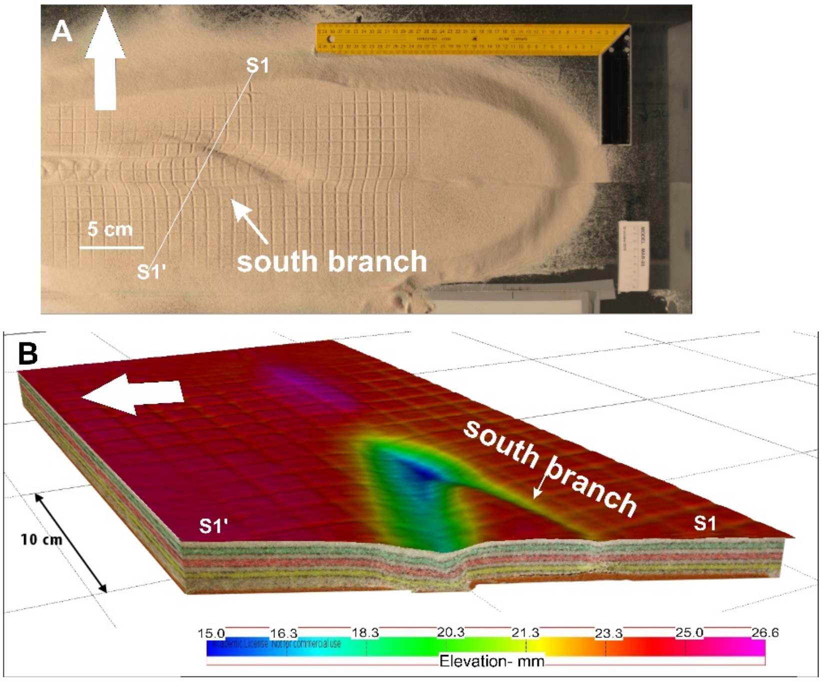

Figure 10 *shows a) Top images of the model at the end of the deformation. The final topography of the model MAR-05, which the south branch is seen clear. b) the final surface topography of model MAR-05 derived from scan data with cross section integrated.*

Figure 11: CROSS SECTIONS OF MAR-05

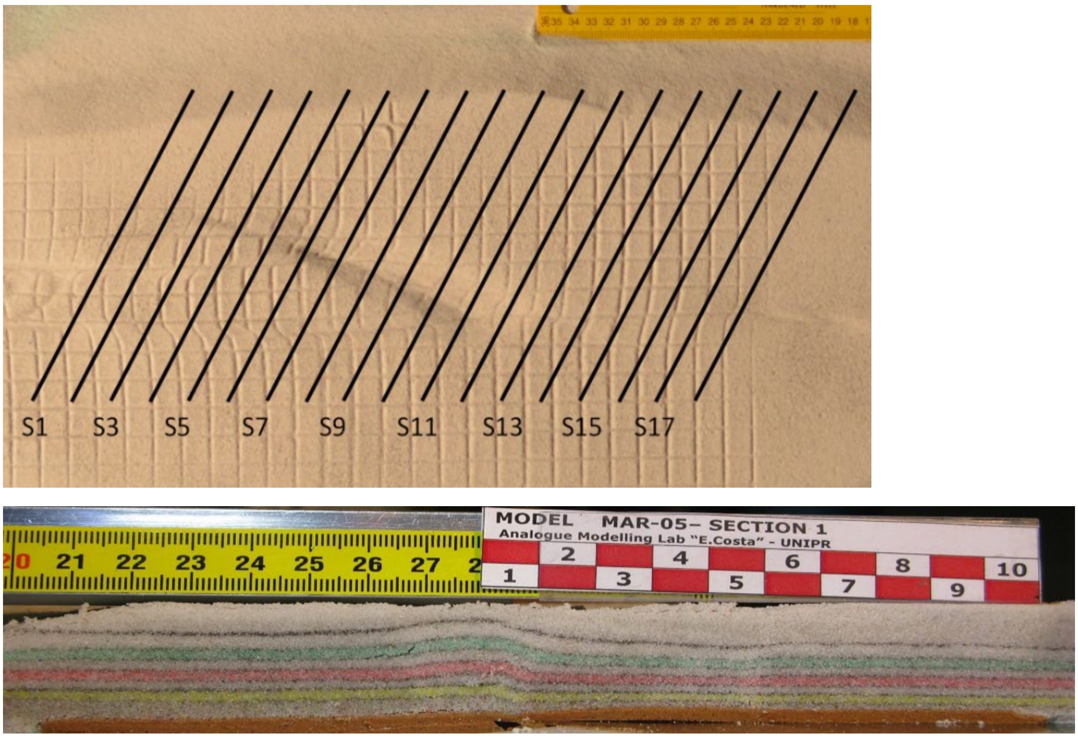

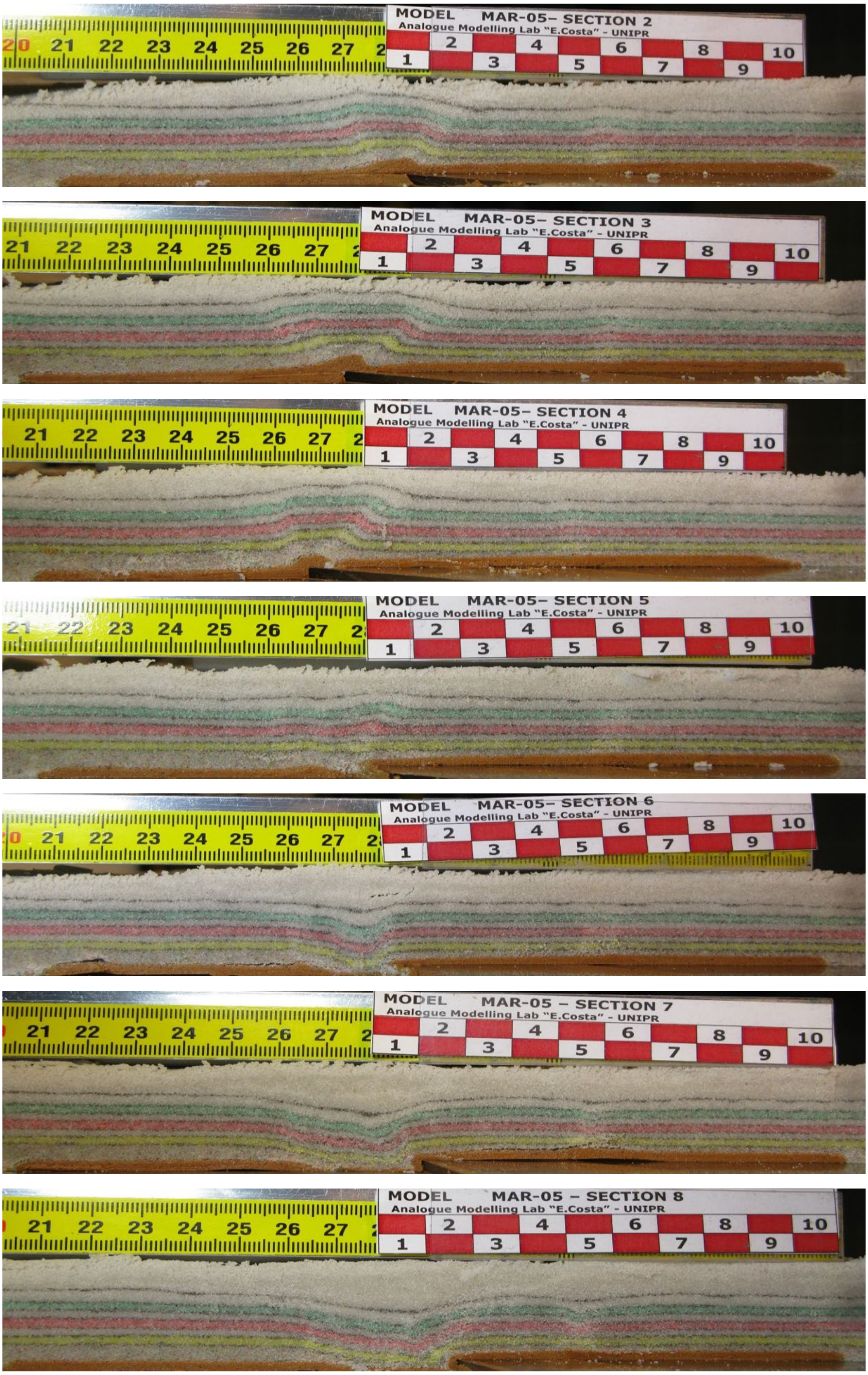
MODEL MAR-05– SECTION 2
Analogue Modelling Lab "E.Costa" - UNIPR
MODEL MAR-05– SECTION 3
Analogue Modelling Lab "E.Costa" - UNIPR
MODEL MAR-05– SECTION 4
Analogue Modelling Lab "E.Costa" - UNIPR
MODEL MAR-05– SECTION 5
Analogue Modelling Lab "E.Costa" - UNIPR
MODEL MAR-05– SECTION 6
Analogue Modelling Lab "E.Costa" - UNIPR
MODEL MAR-05 – SECTION 7
Analogue Modelling Lab "E.Costa" - UNIPR
MODEL MAR-05 – SECTION 8
Analogue Modelling Lab "E.Costa" - UNIPR

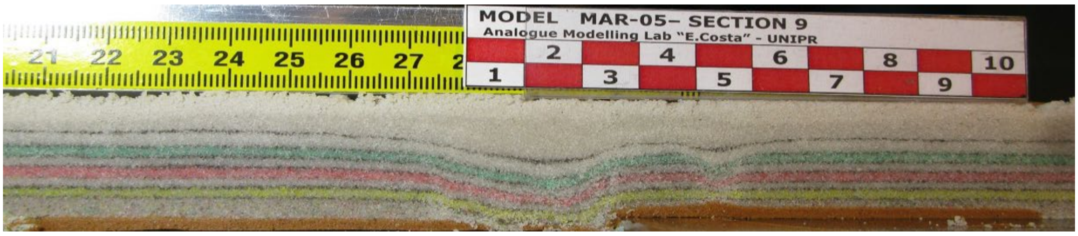
MODEL MAR-05- SECTION 9
Analogue Modelling Lab "E.Costa" - UNIPR

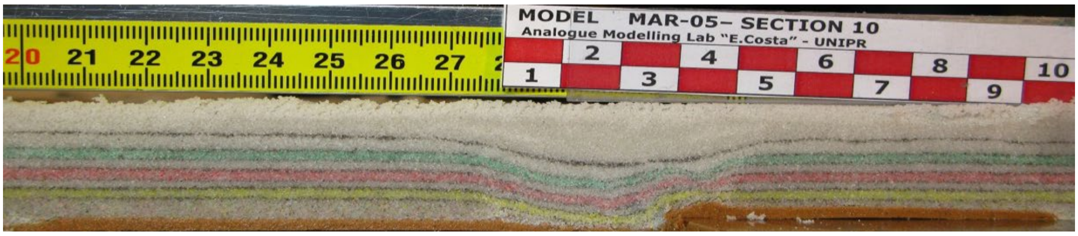
MODEL MAR-05- SECTION 10
Analogue Modelling Lab "E.Costa" - UNIPR

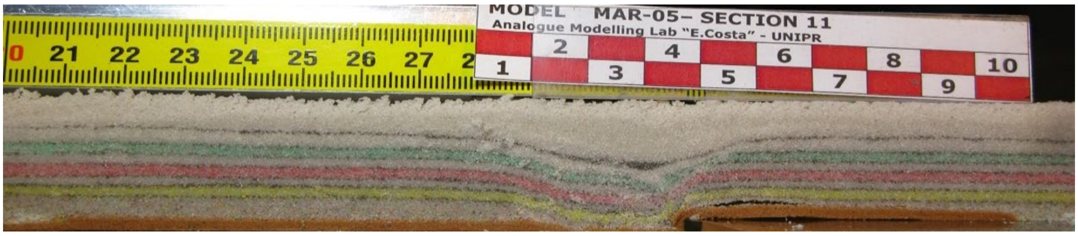
MODEL MAR-05- SECTION 11
Analogue Modelling Lab "E.Costa" - UNIPR

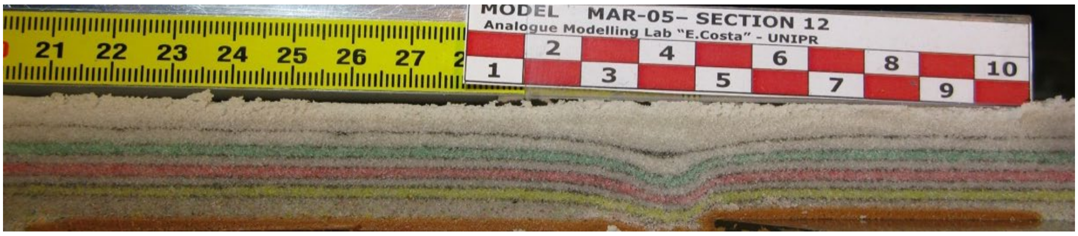
MODEL MAR-05- SECTION 12
Analogue Modelling Lab "E.Costa" - UNIPR

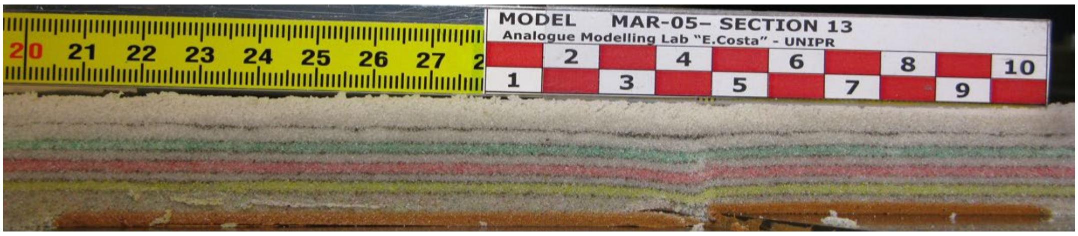
MODEL MAR-05- SECTION 13
Analogue Modelling Lab "E.Costa" - UNIPR

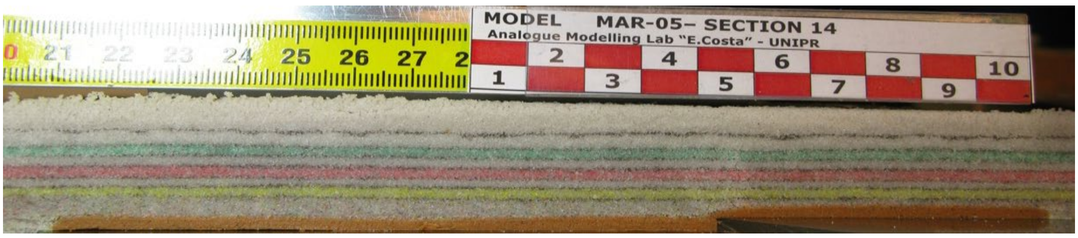
MODEL MAR-05- SECTION 14
Analogue Modelling Lab "E.Costa" - UNIPR

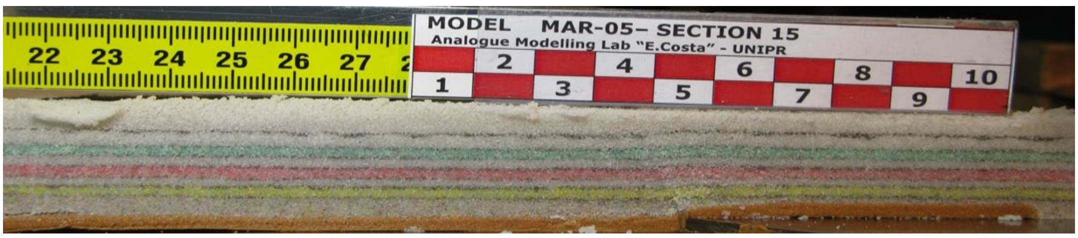
MODEL MAR-05- SECTION 15
Analogue Modelling Lab "E.Costa" - UNIPR

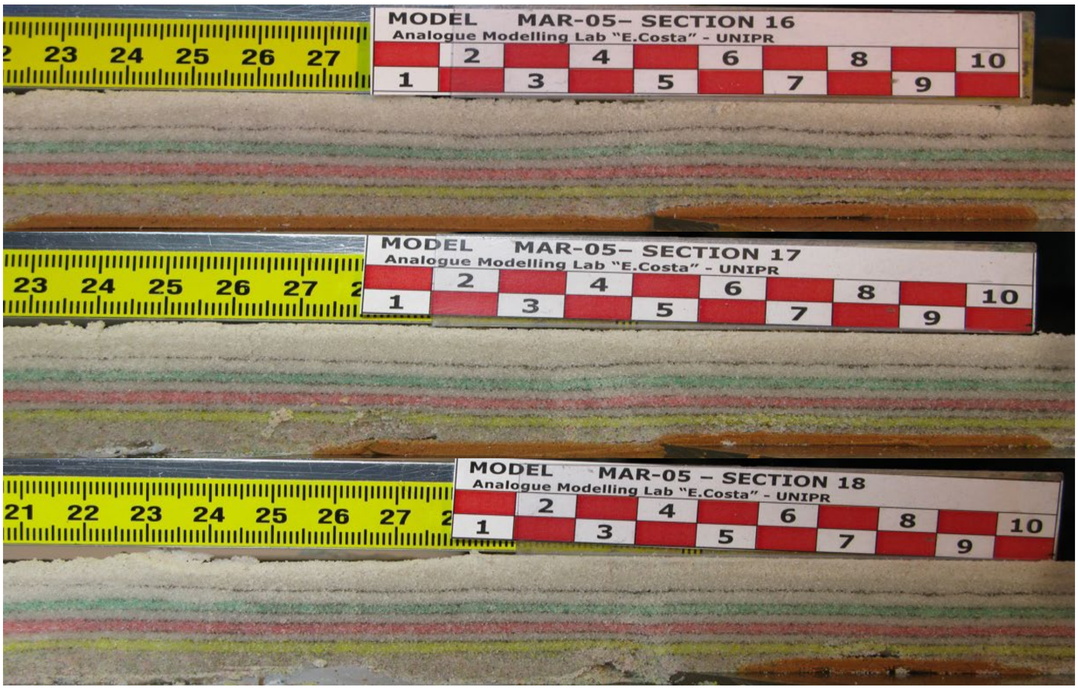

Figure 12: CROSS SECTIONS OF MAR-06

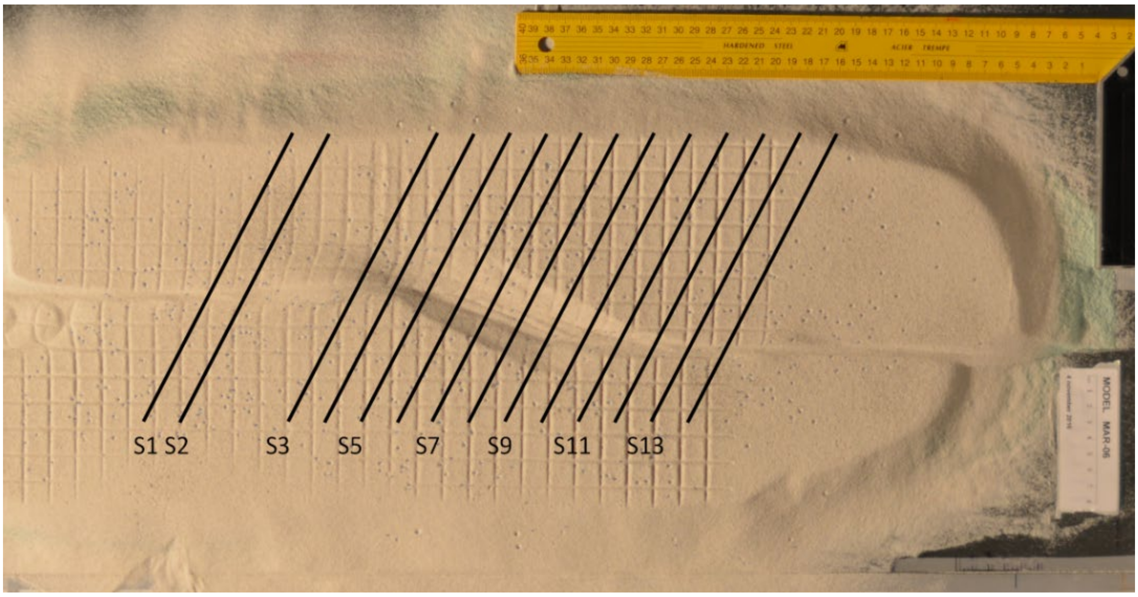

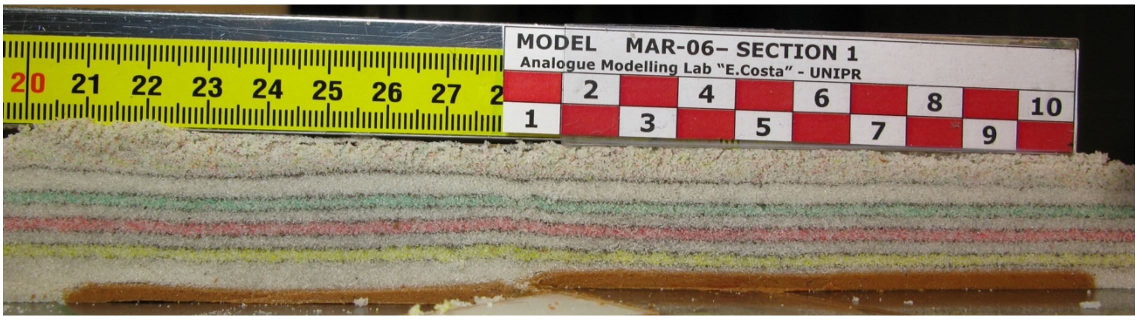
MODEL MAR-06– SECTION 1
Analogue Modelling Lab "E.Costa" - UNIPR

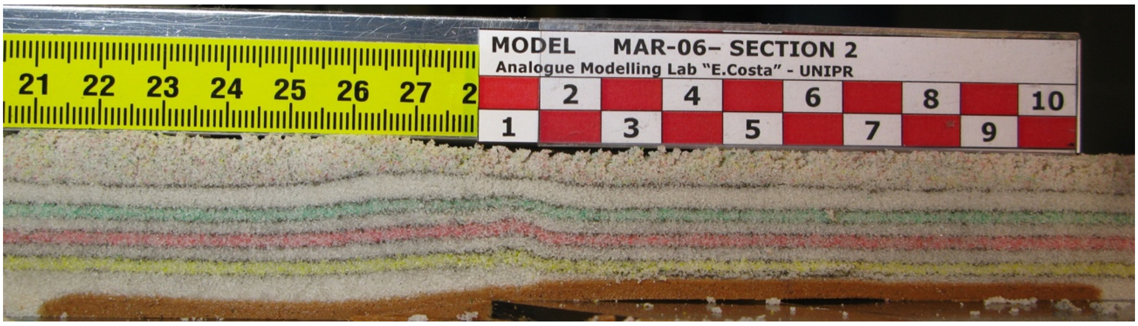
MODEL MAR-06– SECTION 2
Analogue Modelling Lab "E.Costa" - UNIPR

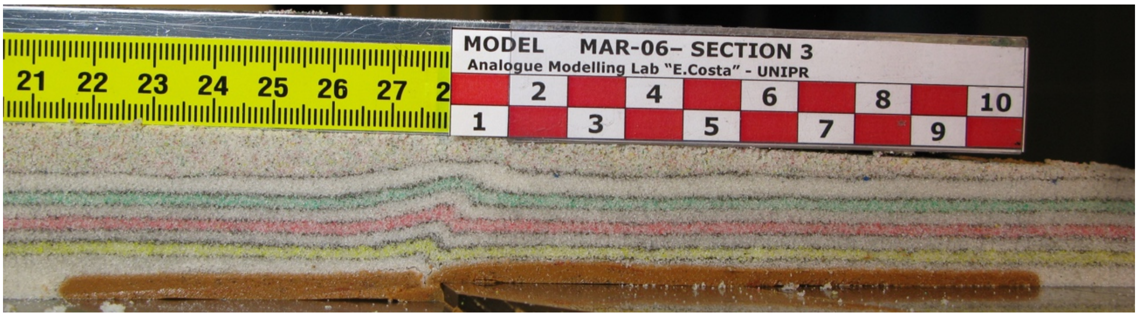
MODEL MAR-06– SECTION 3
Analogue Modelling Lab "E.Costa" - UNIPR

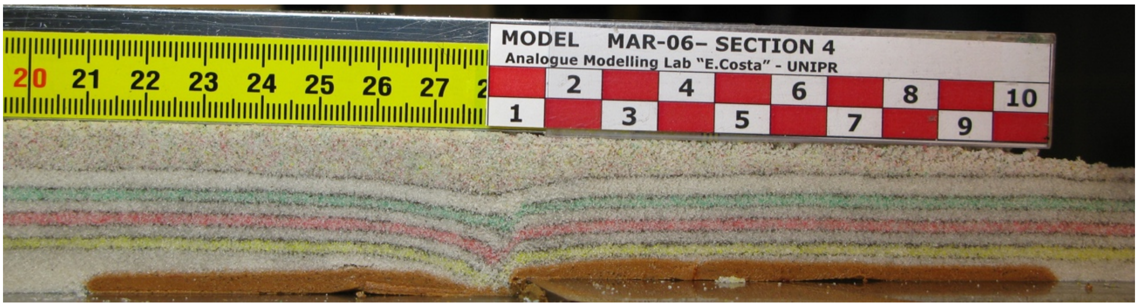
MODEL MAR-06– SECTION 4
Analogue Modelling Lab "E.Costa" - UNIPR

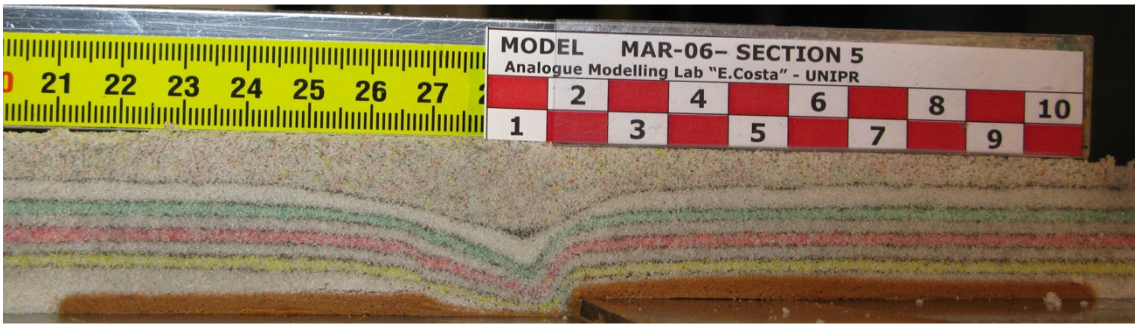
MODEL MAR-06– SECTION 5
Analogue Modelling Lab "E.Costa" - UNIPR

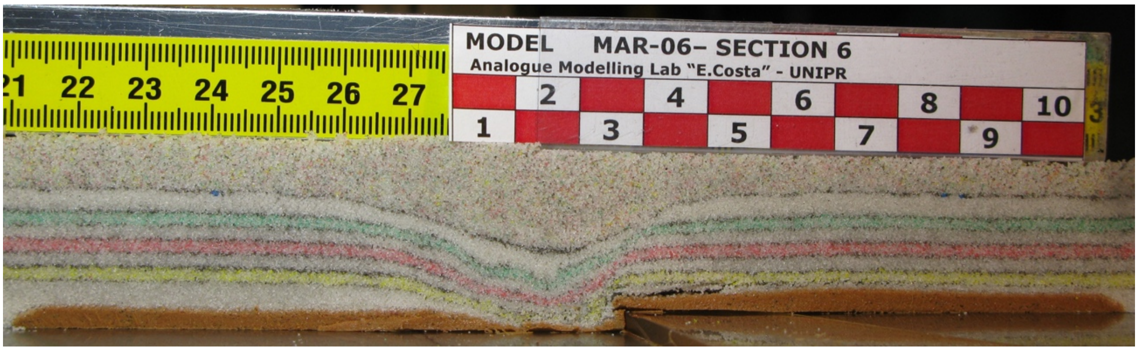
MODEL MAR-06– SECTION 6
Analogue Modelling Lab "E.Costa" - UNIPR

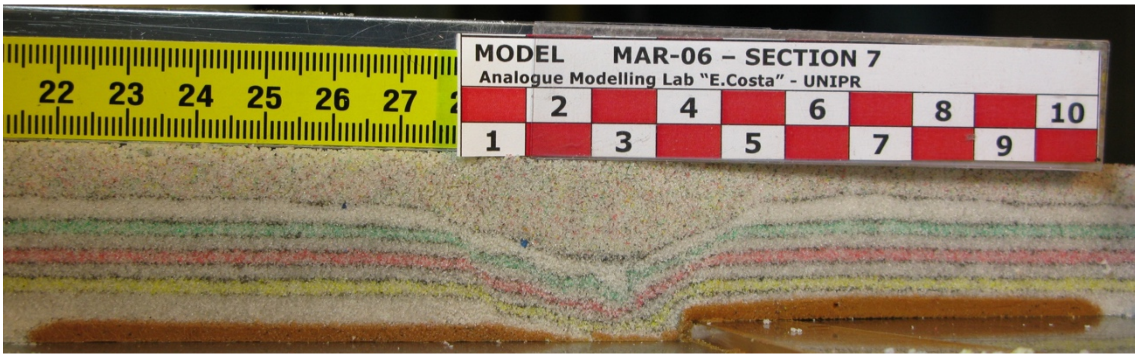
MODEL MAR-06 – SECTION 7
Analogue Modelling Lab "E.Costa" - UNIPR

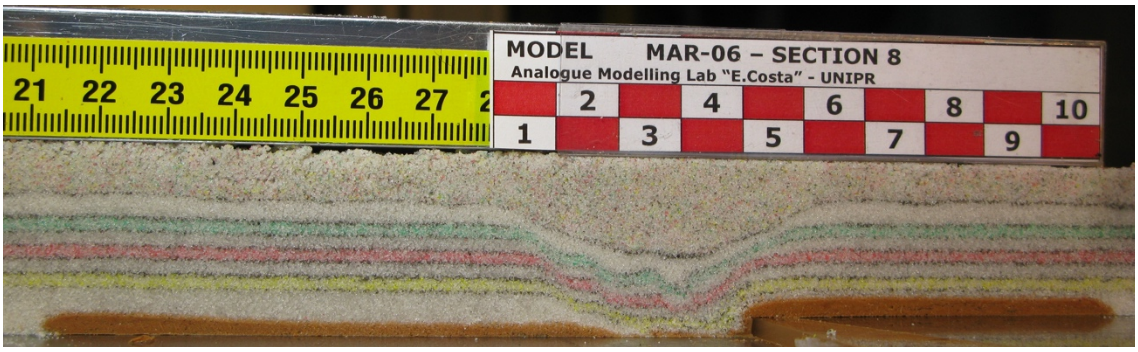
MODEL MAR-06 – SECTION 8
Analogue Modelling Lab "E.Costa" - UNIPR

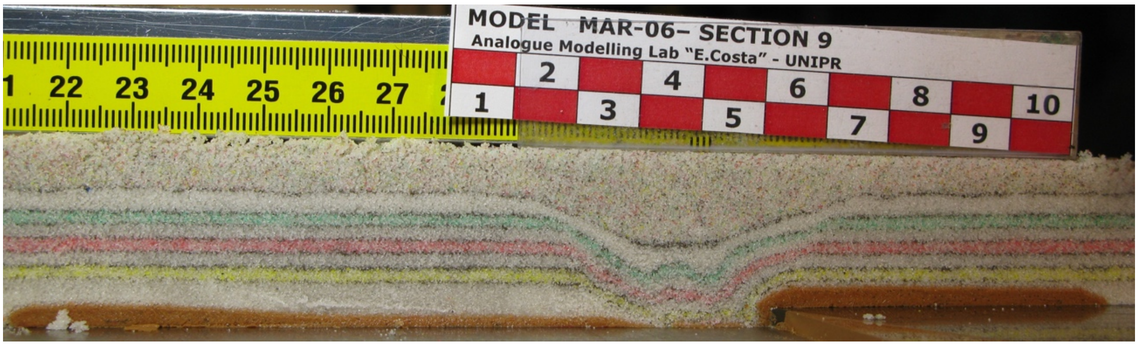
MODEL MAR-06– SECTION 9
Analogue Modelling Lab "E.Costa" - UNIPR

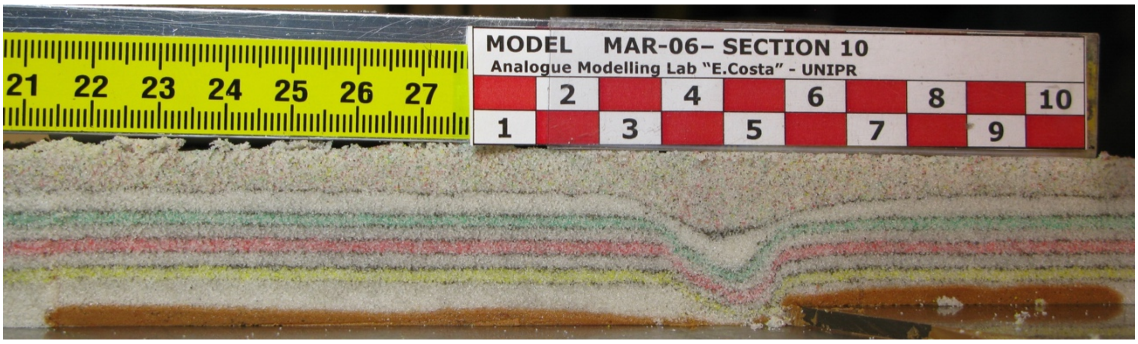
MODEL MAR-06– SECTION 10
Analogue Modelling Lab "E.Costa" - UNIPR

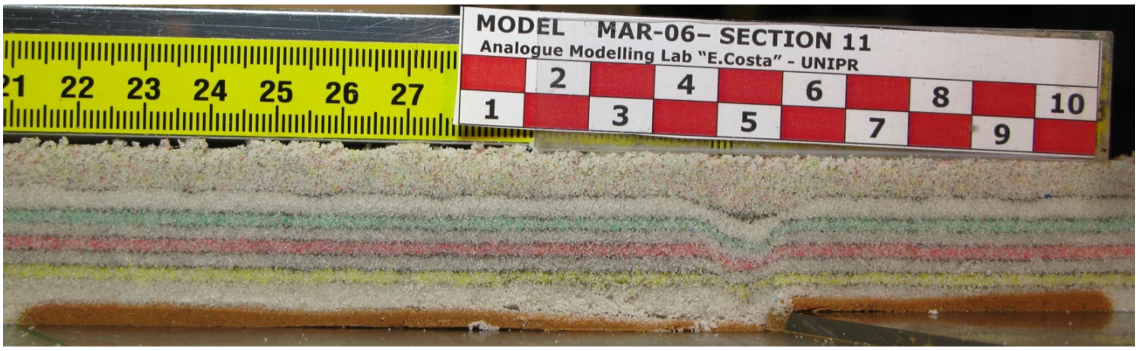

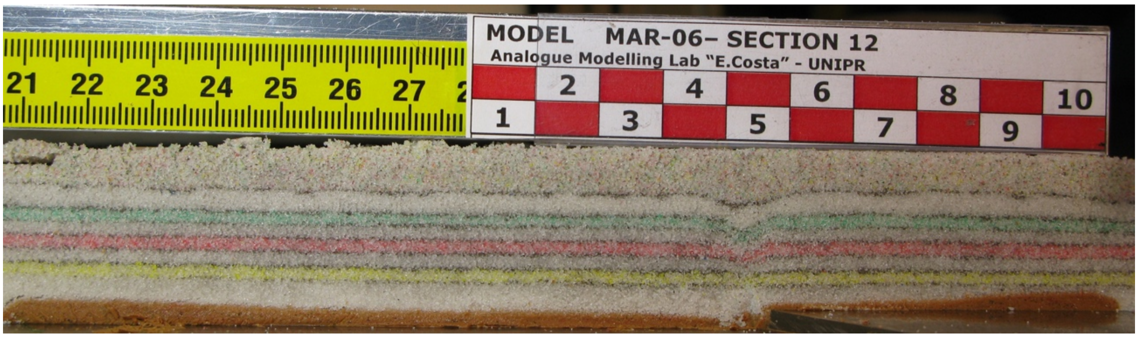

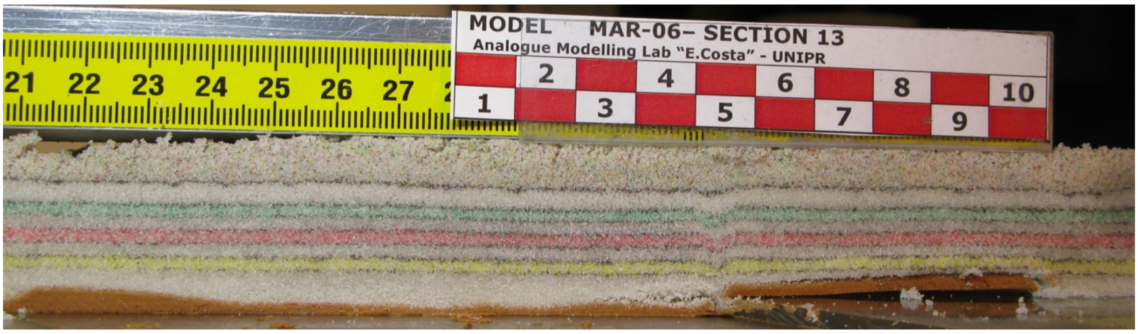

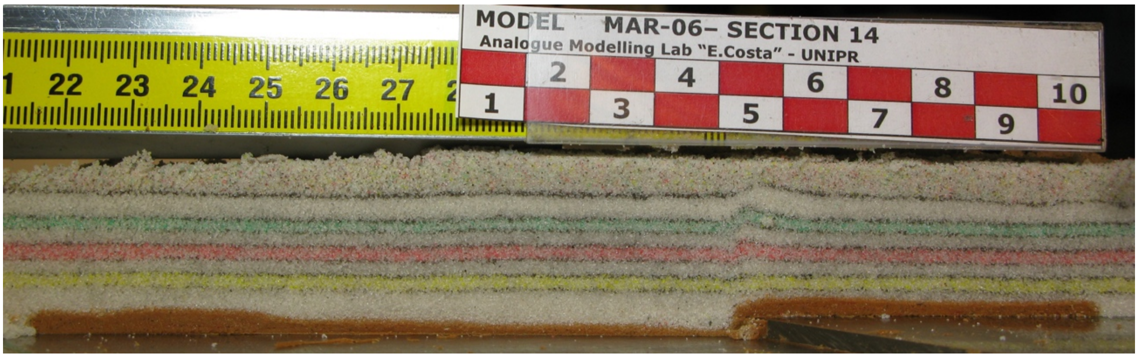

MAR-07 and MAR-08

MAR-07 and MAR-08 were built to investigate the effect of “escape” tectonics on the evolution of transpression and transtension. The models’ geometry was designed to compare the structural and topographic evolution observed during the experiments with examples taken from the western-NAF system with the effect of the Aegean Sea "pulling".

The models share the same silicon putty and sand pack configuration, but they differ in their basal plate geometry: MAR-07 was conceived with only one plate, while MAR-08 used the same basal plate of MAR-07, but also added an upper plate (Fig. 13). The basal plexiglass plate (lower plate in MAR-08) is characterised by a triangular protrusion and in both models is moved at 20 mm/hr, but while on MAR-07 is moved towards the left (and the resulting sense of shear is right-lateral), in MAR-08 is moved toward the right (Fig. 14). MAR-08 added an upper plate purposely cut to simulate lithospheric pulling towards the right of the model (Fig. 13 and 14).

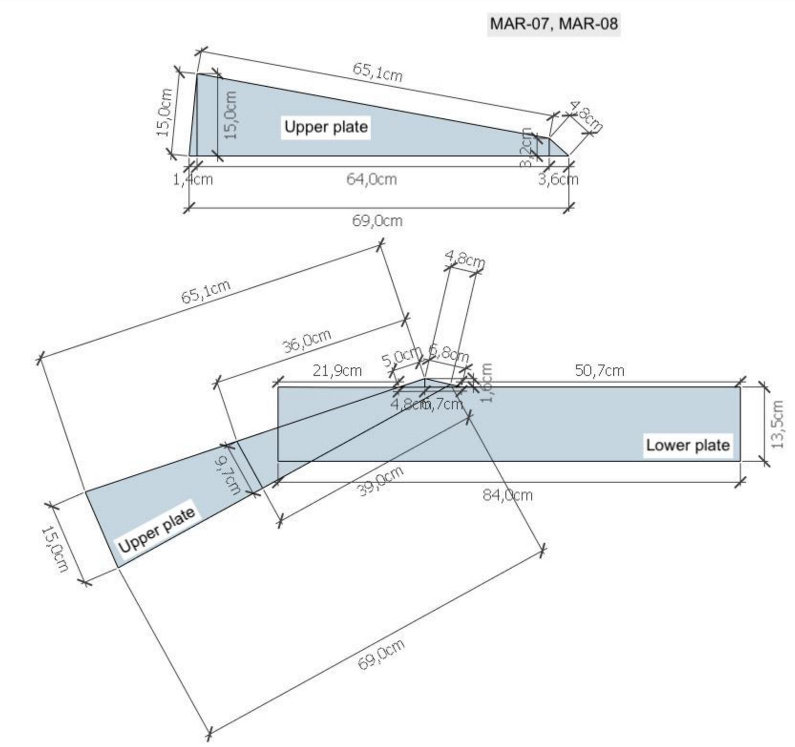

Figure 13 *shows the geometry of the plexiglass plates used during the experiments MAR-07 and MAR-08. MAR-07 was run without upper-plate. MAR-08 was run with two plates, each plate was moved different direction and with different velocities (see also Table 1 and figure 12).*

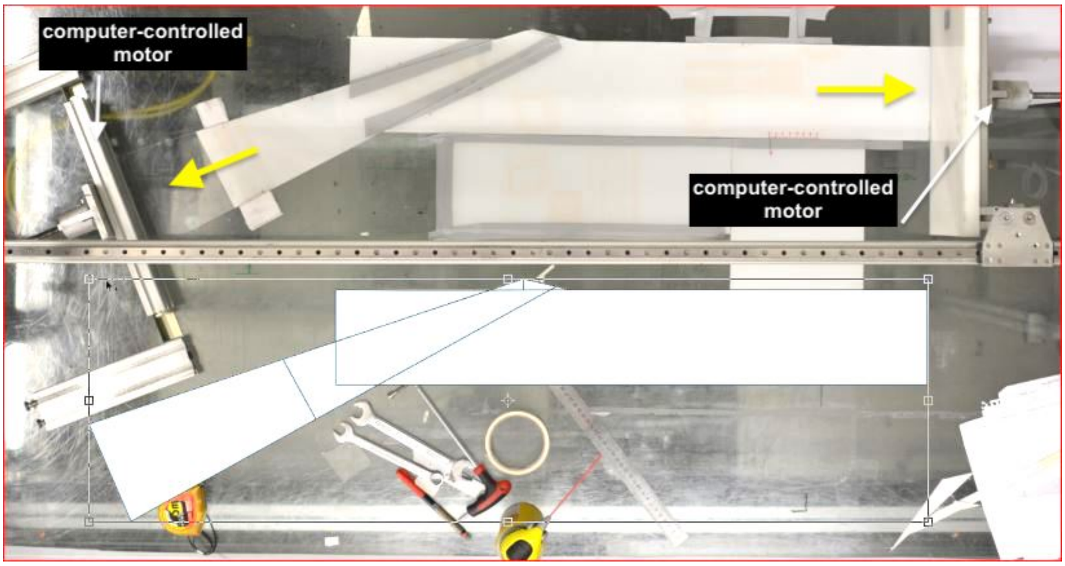

Figure 14 shows the model configuration for MAR-08. Two computer controlled motor used in this experiment. Yellow arrows show the direction of plate-movements.

Figure 15 and 16 show models MAR-07 and MAR-08 respectively photographed each 10 mm of displacement. Figure 15 and 16 show details of the deformation at the end of the experiments, i.e. 7 cm of displacement for MAR-07 and 11 cm of displacement for MAR-08.

Figure 18 and 19 show the cross sections of models MAR-07 and MAR-08 cut at the end of the experiments.

Figure 15: TOP IMAGES OF MAR-07

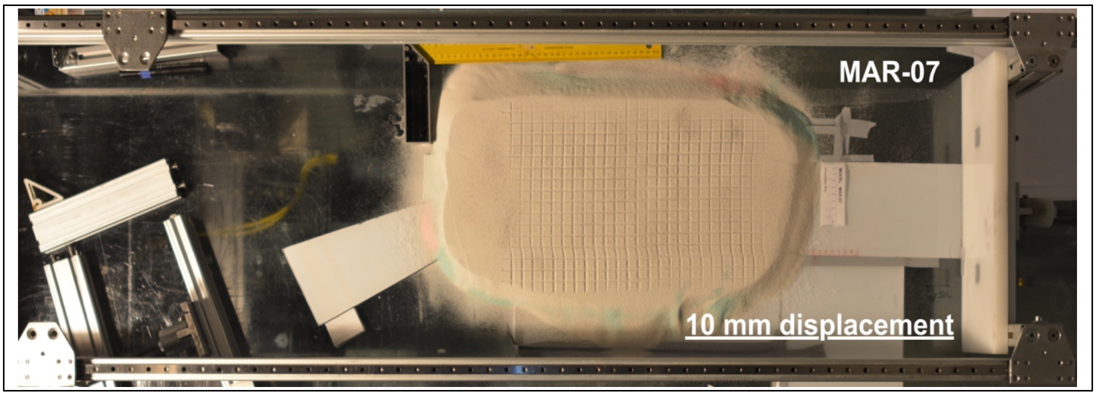

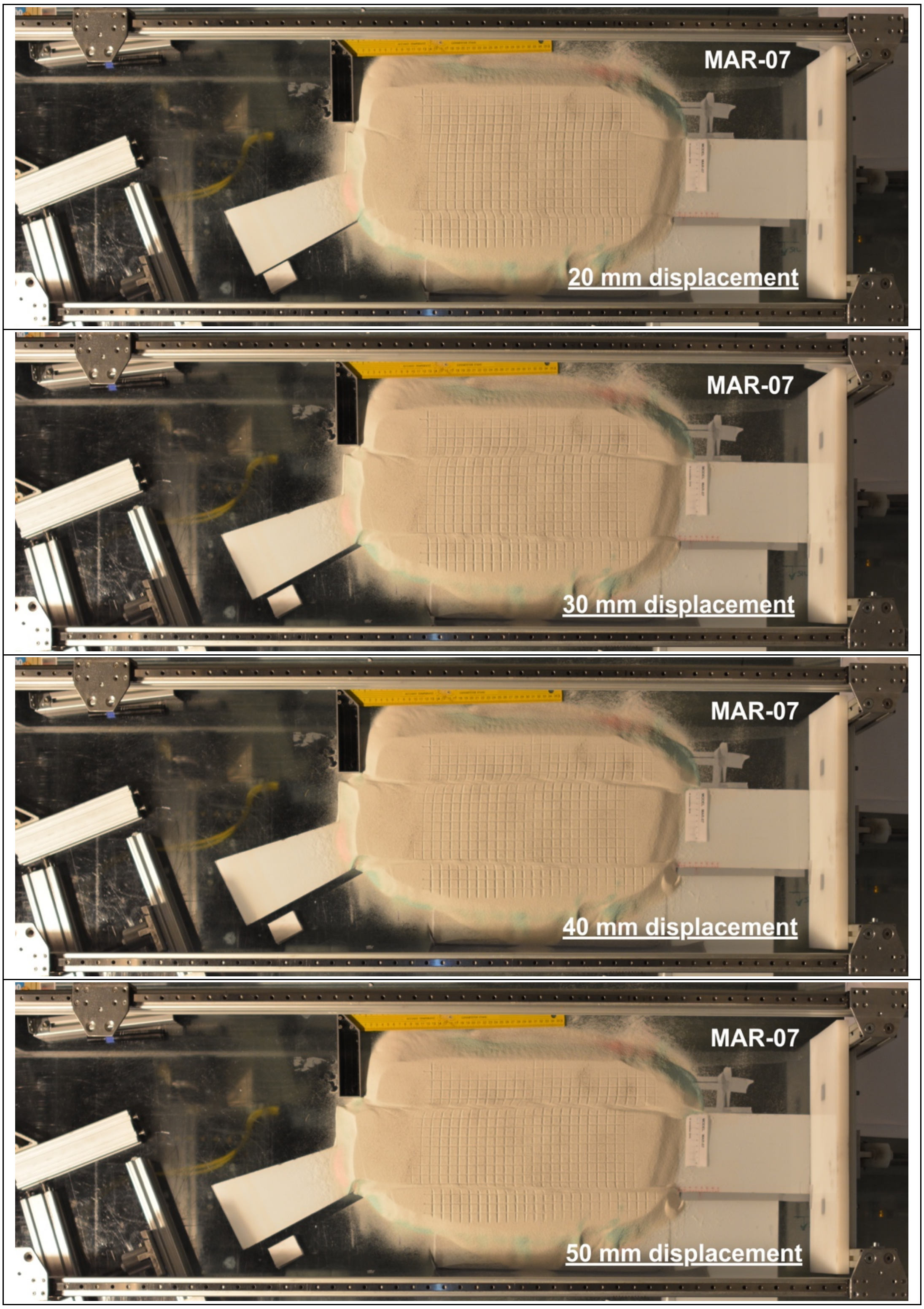
MAR-07
20 mm displacement
MAR-07
30 mm displacement
MAR-07
40 mm displacement
MAR-07
50 mm displacement

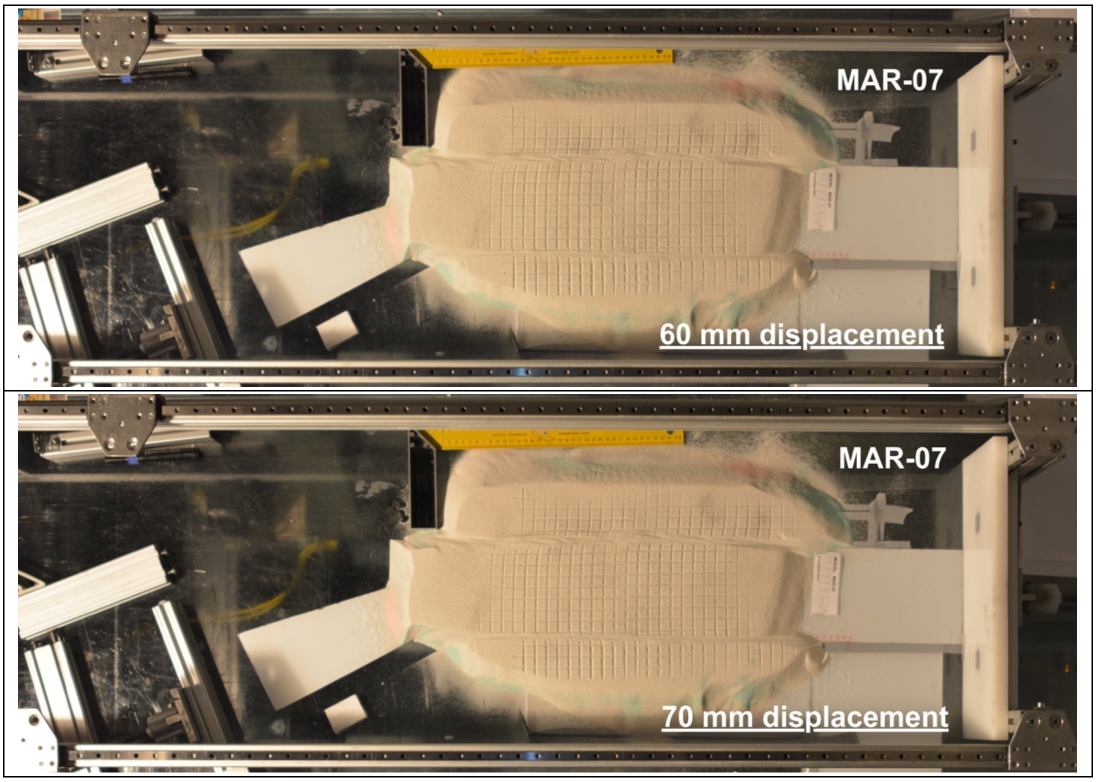

Figure 16: TOP IMAGES OF MAR-08

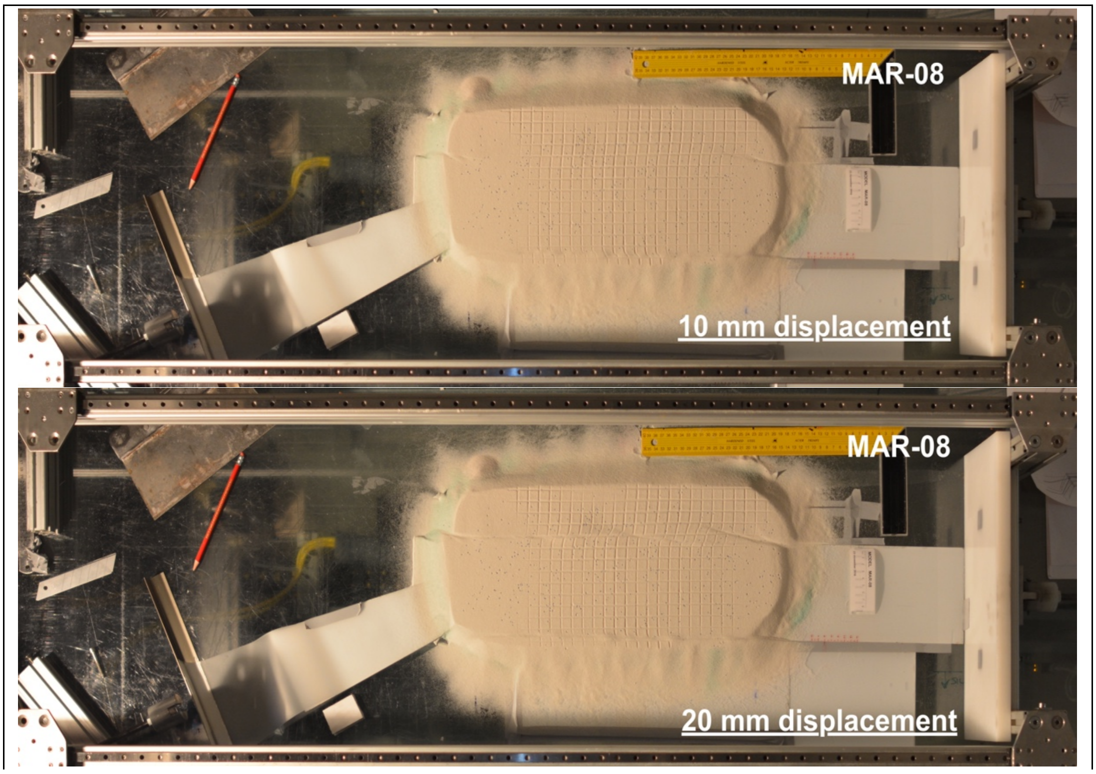

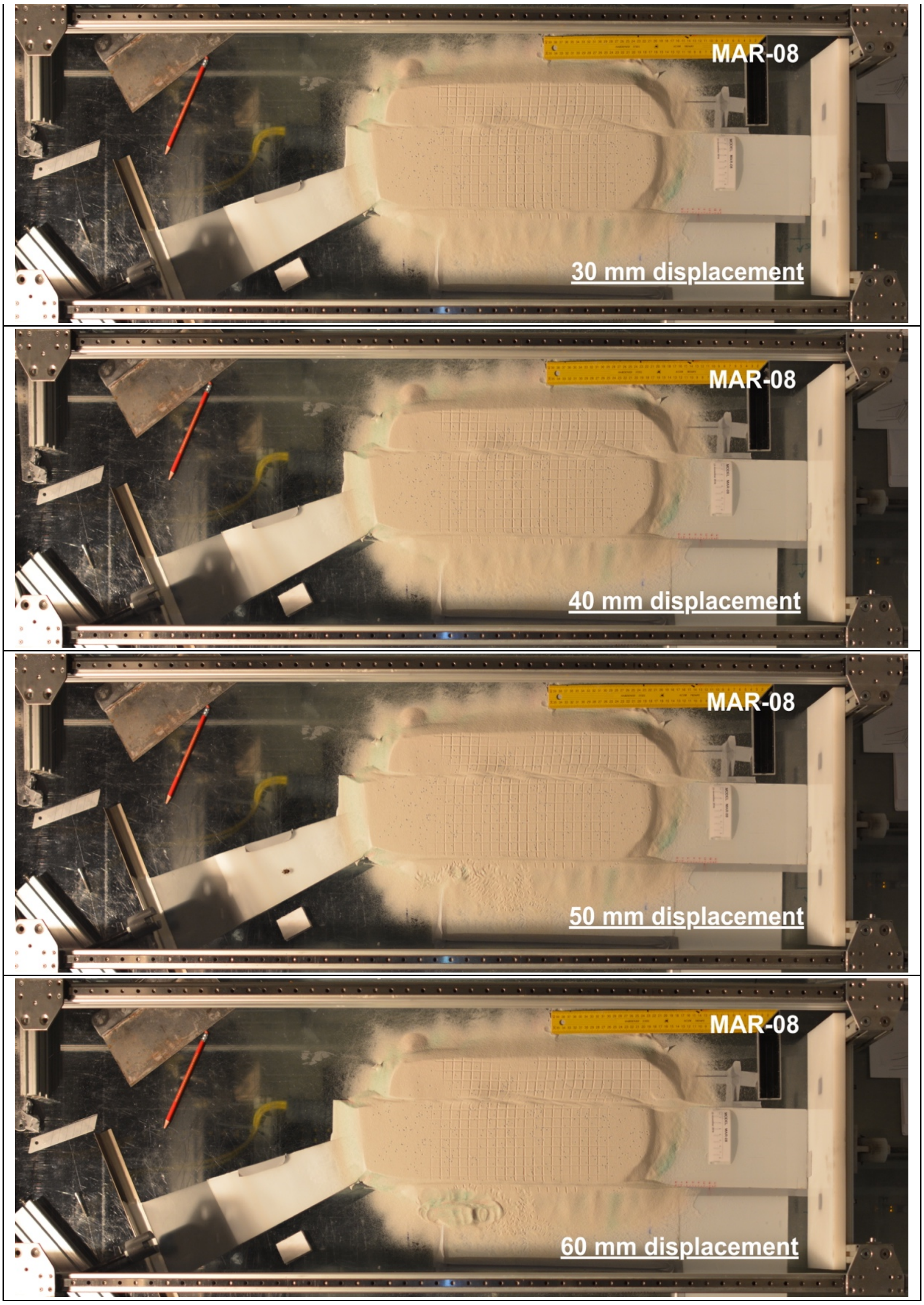
MAR-08
30 mm displacement
MAR-08
40 mm displacement
MAR-08
50 mm displacement
MAR-08
60 mm displacement

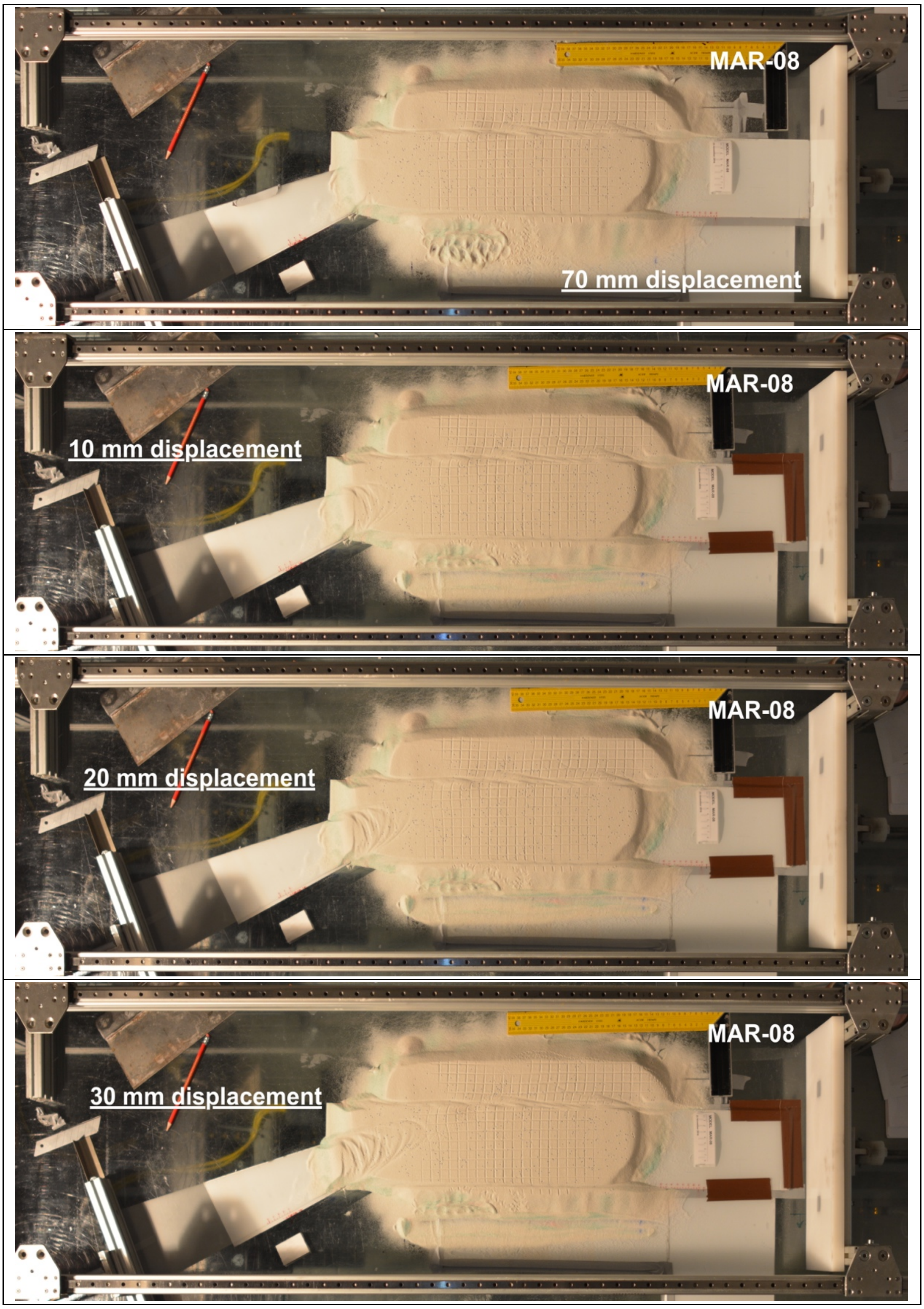

MAR-08
70 mm displacement
MAR-08
10 mm displacement
MAR-08
20 mm displacement
MAR-08
30 mm displacement

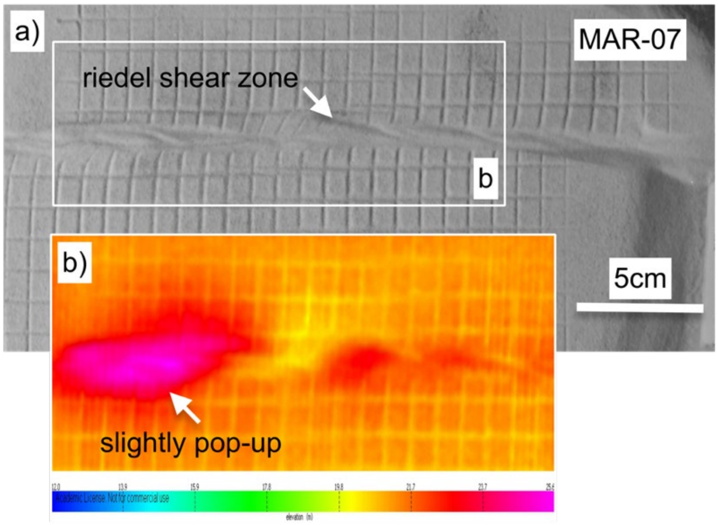

Figure 17 *shows a) top image of the end of deformation (7cm). The deformation dominates by the Riedell shears. b) The surface topography of MAR-07 derived from scan data.*

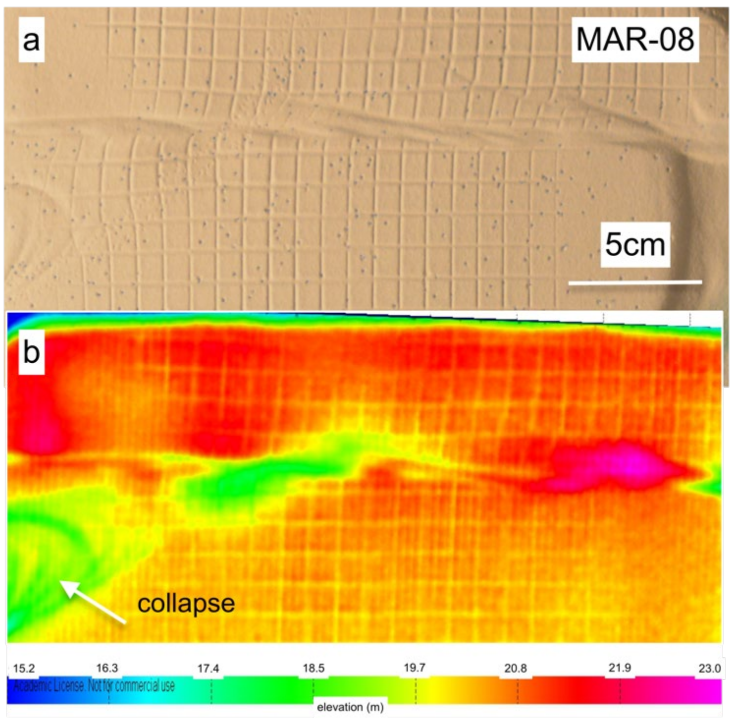

Figure 18 *shows a) top image of the end of deformation (7cm). b) The surface topography of MAR-08 derived from scan data.*

Figure 19: CROSS SECTIONS OF MAR-07

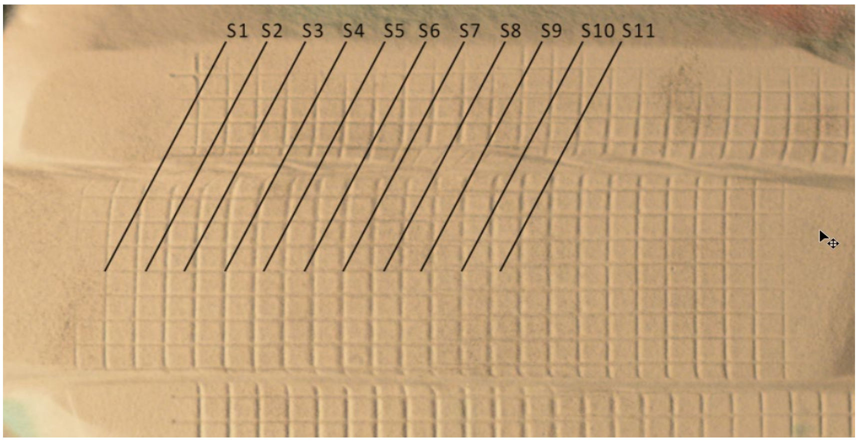

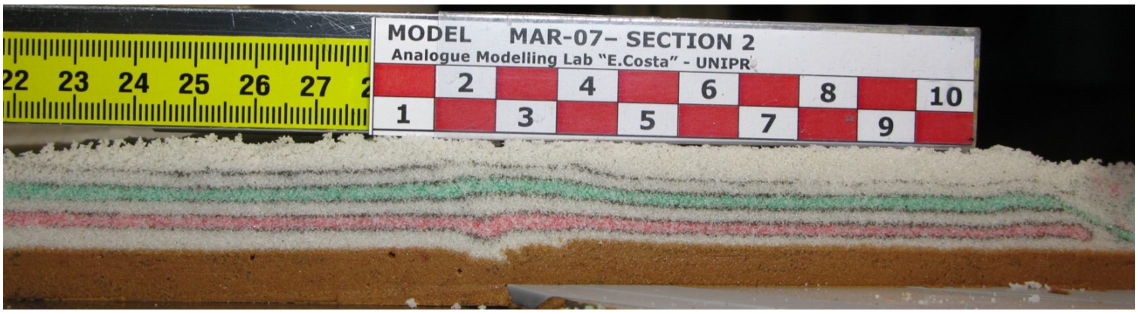

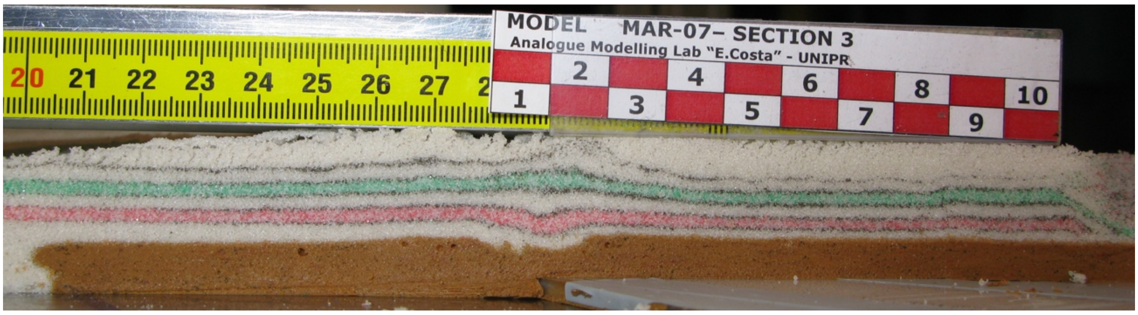

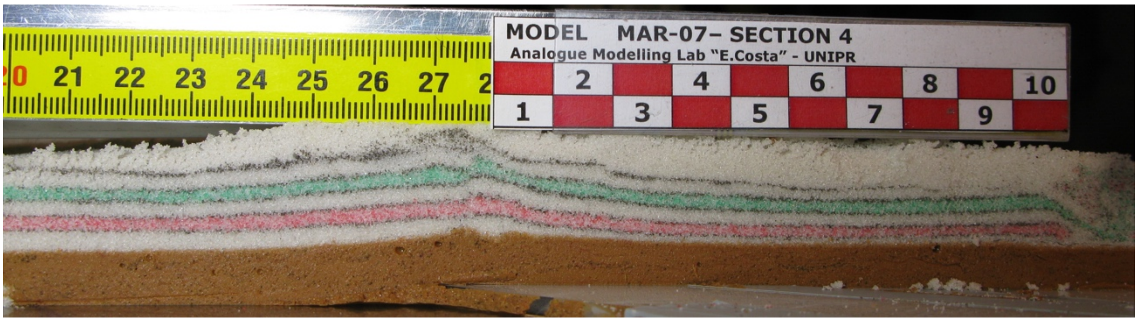
MODEL MAR-07– SECTION 4
Analogue Modelling Lab "E.Costa" - UNIPR

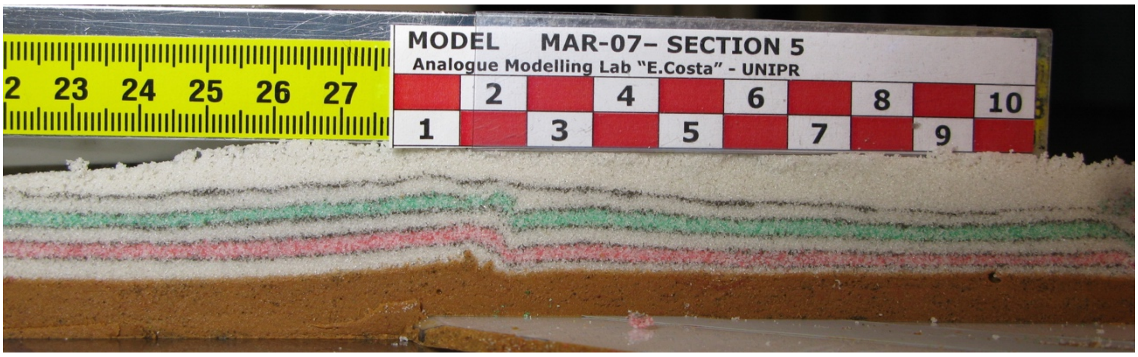
MODEL MAR-07– SECTION 5
Analogue Modelling Lab "E.Costa" - UNIPR

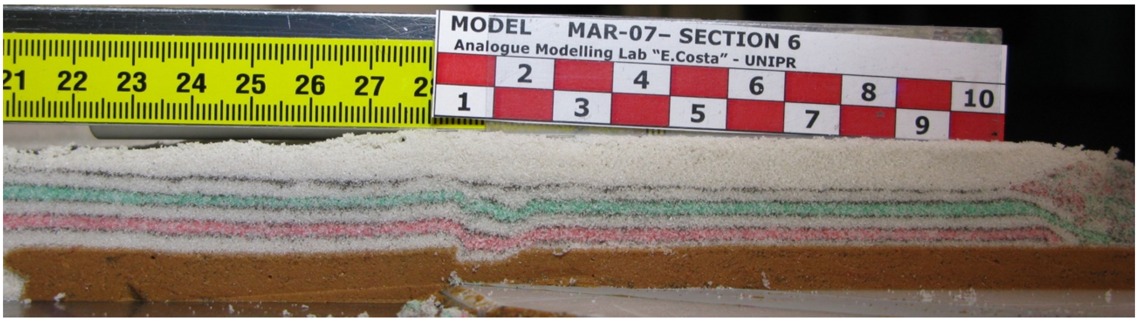
MODEL MAR-07– SECTION 6
Analogue Modelling Lab "E.Costa" - UNIPR

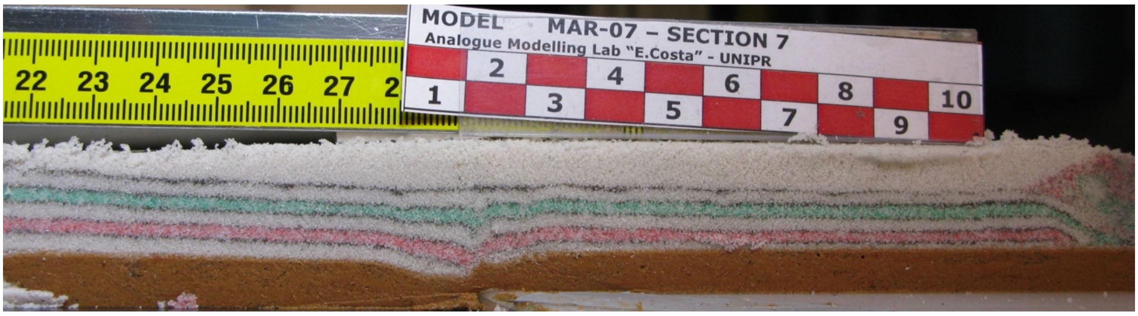
MODEL MAR-07 – SECTION 7
Analogue Modelling Lab "E.Costa" - UNIPR

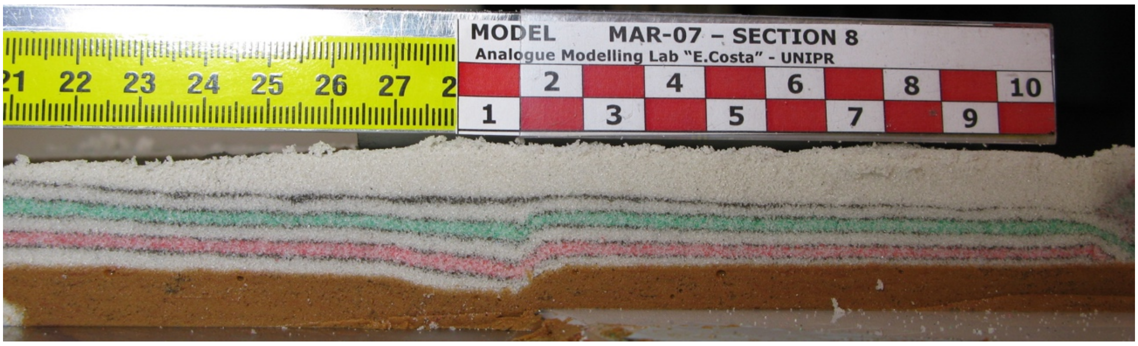
MODEL MAR-07 – SECTION 8
Analogue Modelling Lab "E.Costa" - UNIPR

Figure 20: THE CROSS SECTIONS OF MAR-08

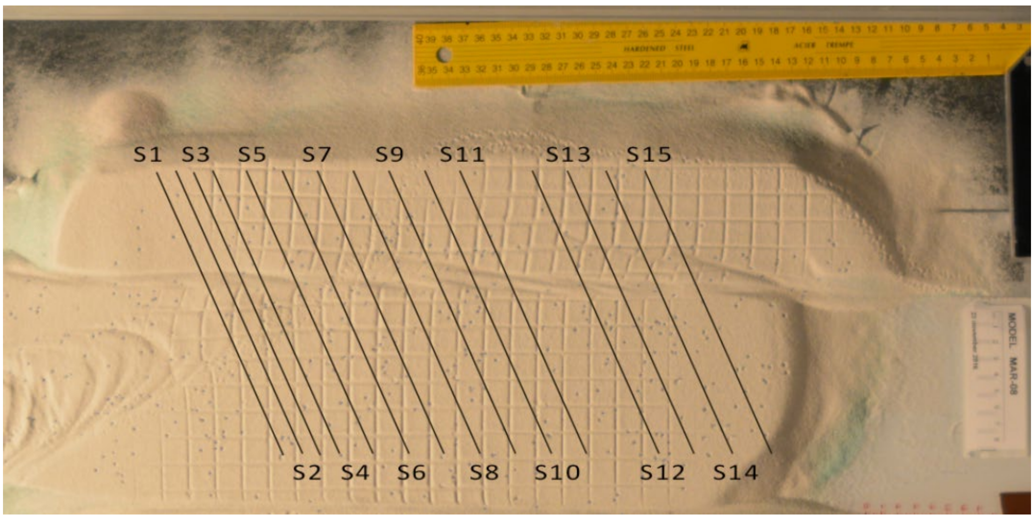

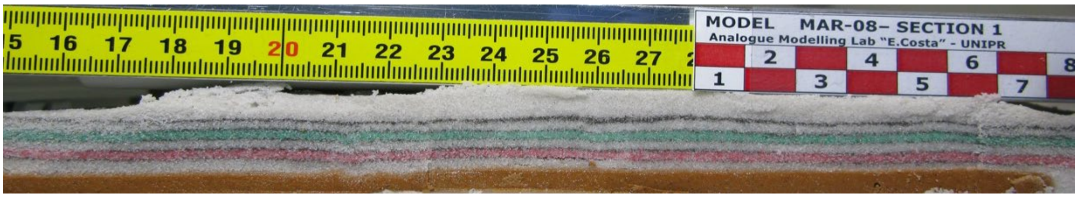
MODEL MAR-08- SECTION 1
Analogue Modelling Lab "E.Costa" - UNIPR

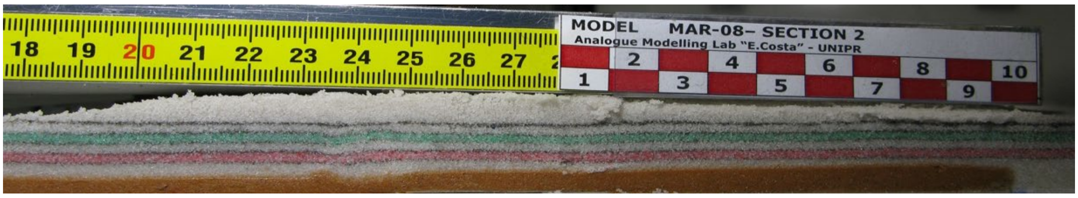
MODEL MAR-08- SECTION 2
Analogue Modelling Lab "E.Costa" - UNIPR

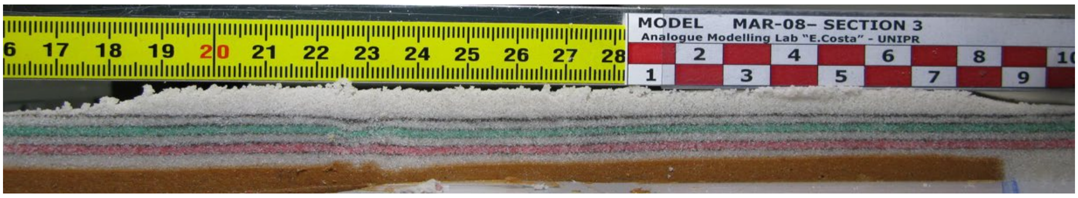
MODEL MAR-08- SECTION 3
Analogue Modelling Lab "E.Costa" - UNIPR

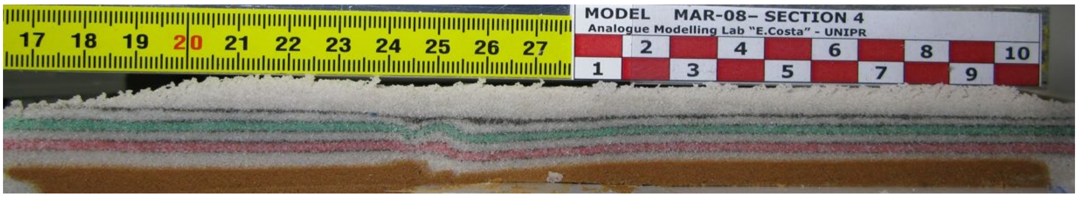
MODEL MAR-08- SECTION 4
Analogue Modelling Lab "E.Costa" - UNIPR

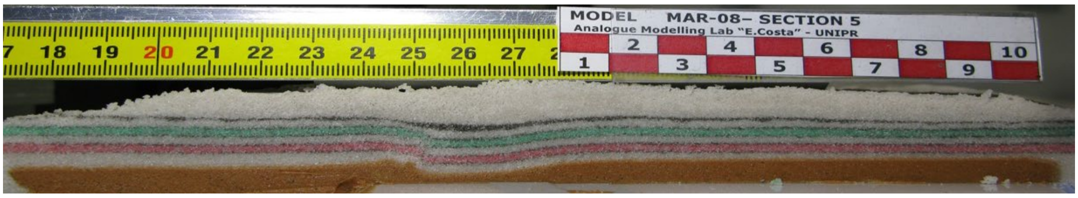
MODEL MAR-08- SECTION 5
Analogue Modelling Lab "E.Costa" - UNIPR

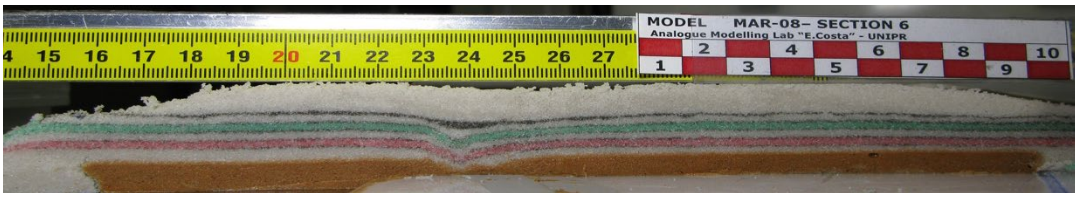
MODEL MAR-08- SECTION 6
Analogue Modelling Lab "E.Costa" - UNIPR

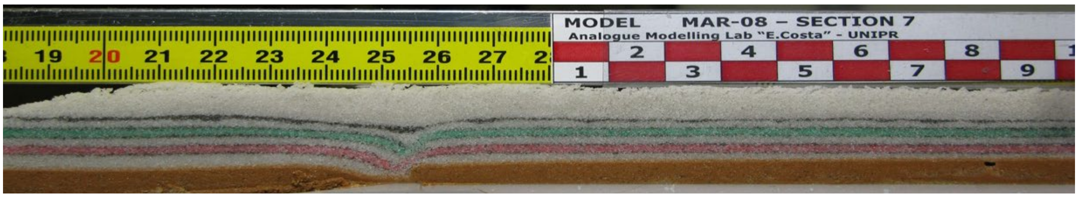
MODEL MAR-08 – SECTION 7
Analogue Modelling Lab "E.Costa" - UNIPR

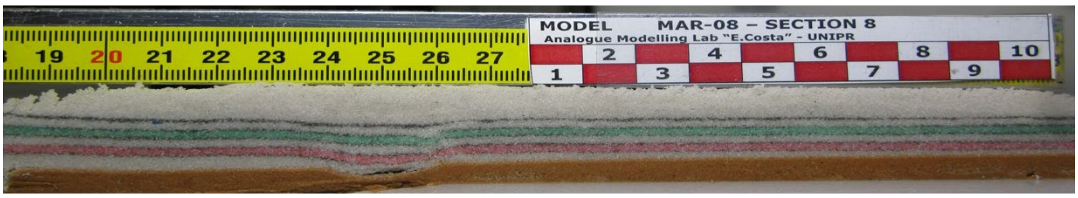
MODEL MAR-08 – SECTION 8
Analogue Modelling Lab "E.Costa" - UNIPR

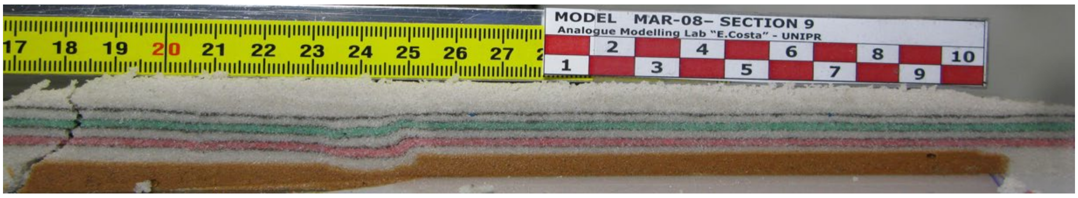
MODEL MAR-08– SECTION 9
Analogue Modelling Lab "E.Costa" - UNIPR

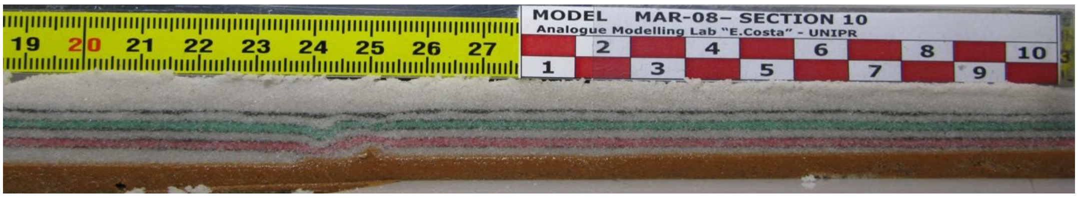
MODEL MAR-08– SECTION 10
Analogue Modelling Lab "E.Costa" - UNIPR

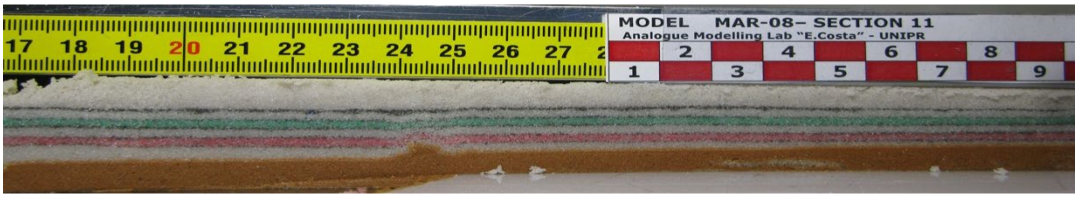
MODEL MAR-08– SECTION 11
Analogue Modelling Lab "E.Costa" - UNIPR

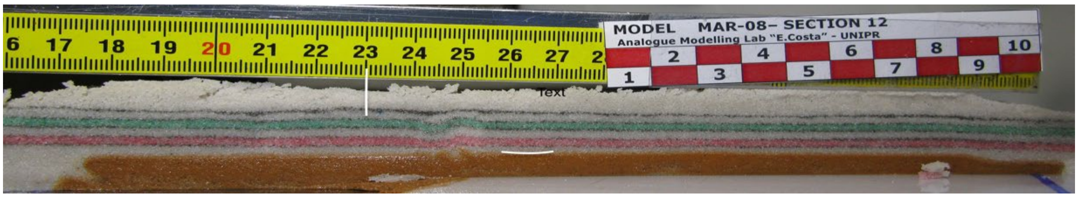
MODEL MAR-08– SECTION 12
Analogue Modelling Lab "E.Costa" - UNIPR

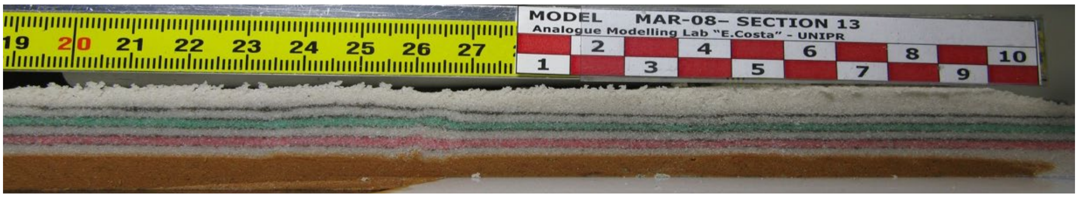
MODEL MAR-08– SECTION 13
Analogue Modelling Lab "E.Costa" - UNIPR


MODEL MAR-08– SECTION 14
Analogue Modelling Lab "E.Costa" - UNIPR

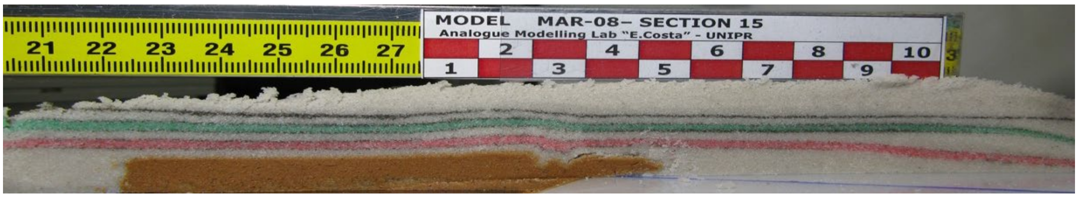
MODEL MAR-08– SECTION 15
Analogue Modelling Lab "E.Costa" - UNIPR

MAR-09 and MAR-10

The purpose for building these models was to investigate the deformation at the big (plate) scale. The shape of the fault cut is the same as the previous models, but the length of the segments is different. In the MAR-09 model the length of the releasing segment is 16 cm, and the length of the restraining segment is 10 cm (see in Fig. 21). However, the effect of the boundary condition was too high, and we suspended the deformation after 40 mm of displacement (Fig. 22).

Similarly, the same configuration was used in MAR-10. Additionally, we added a graphite powder following the boundaries of the two faults on the releasing bend to lower the friction on the fault zones. The purpose was to see multiple sub-basins on the surface. However, we observed that the effect of the boundary conditions was too much on MAR-10 and we suspended the deformation.

Figure 22 show MAR-09 photographed each 10 mm of displacement.

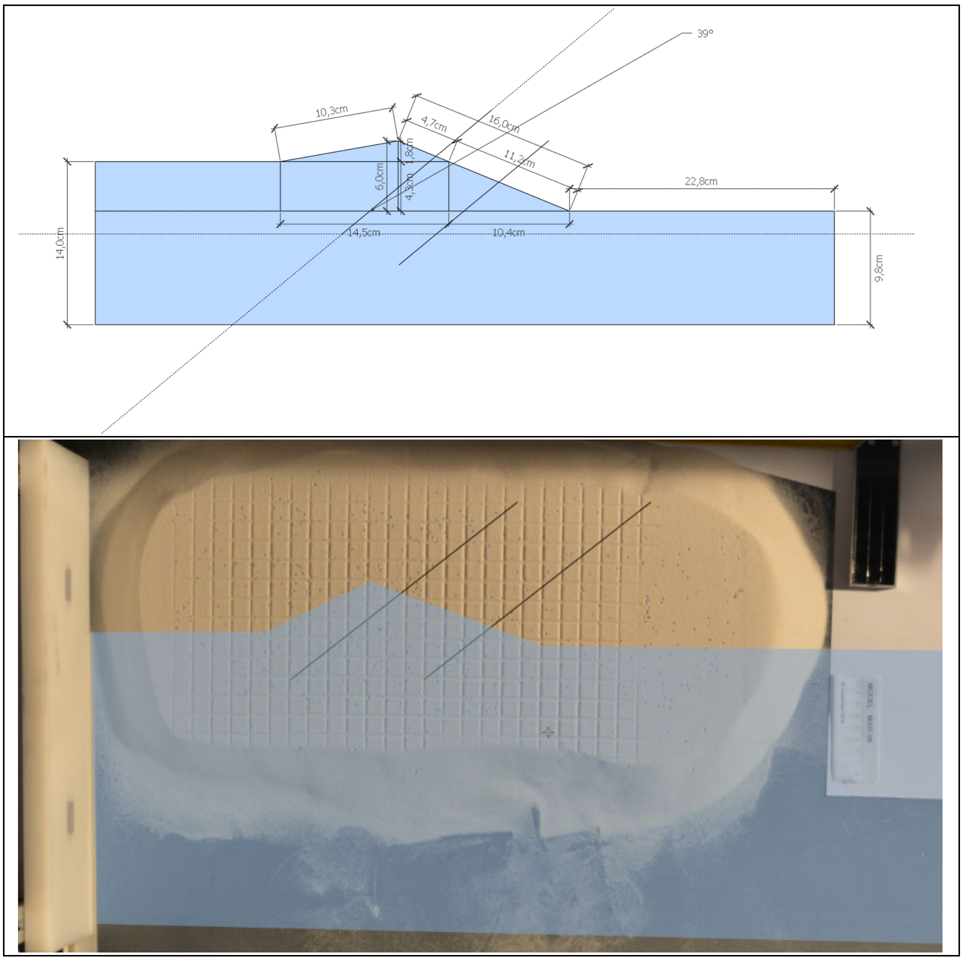

Figure 21 shows the experimental setup for the models MAR-09 and MAR-10. The top image shows the plan view of the experimental setup for the models MAR-09 and MAR-10. The bottom image overlays with shadows the experimental setup on top of the sand pack. The black lines represent the graphite powder insertion on the fault zones in MAR-10.

Figure 22: THE TOP IMAGES OF MAR-09

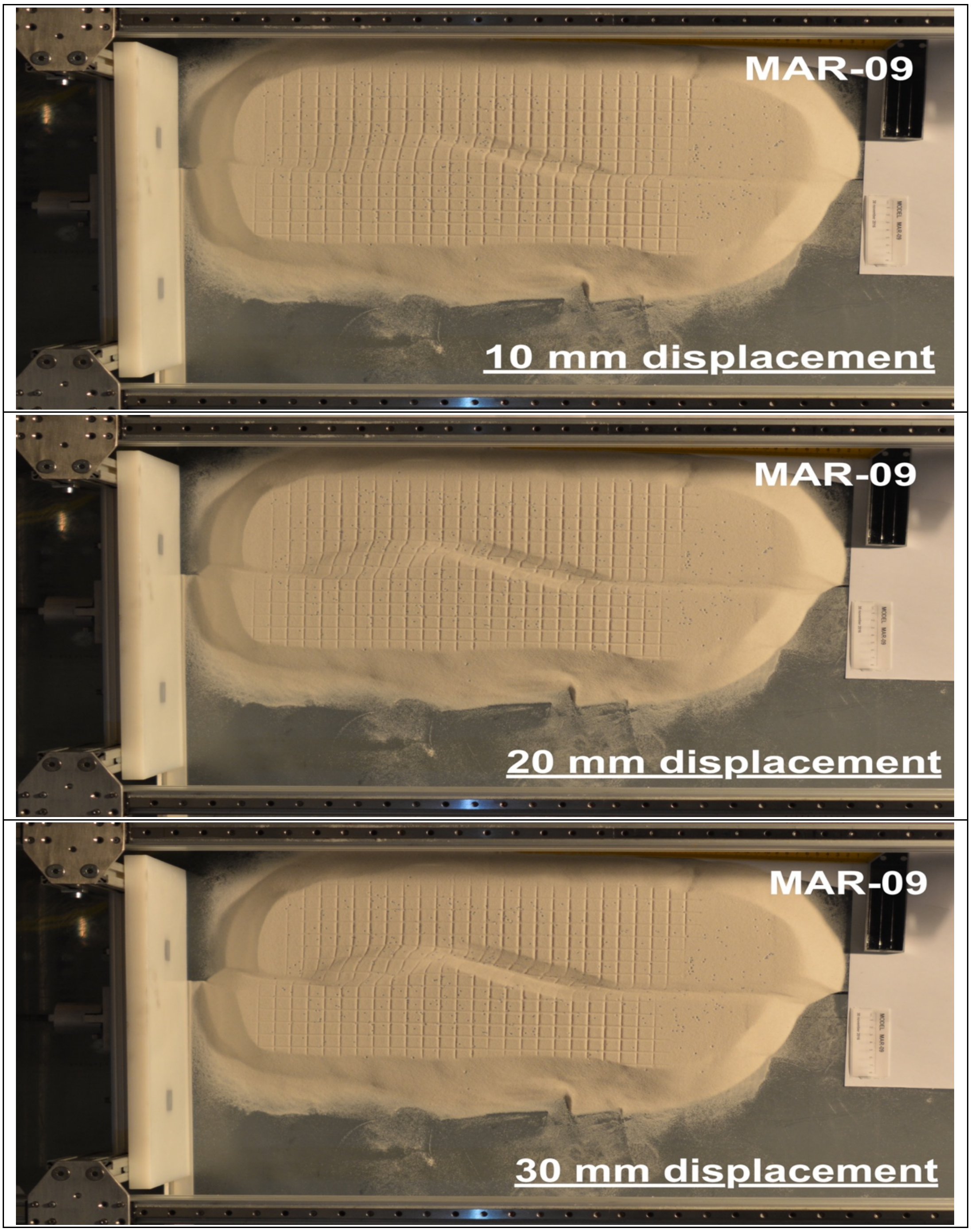

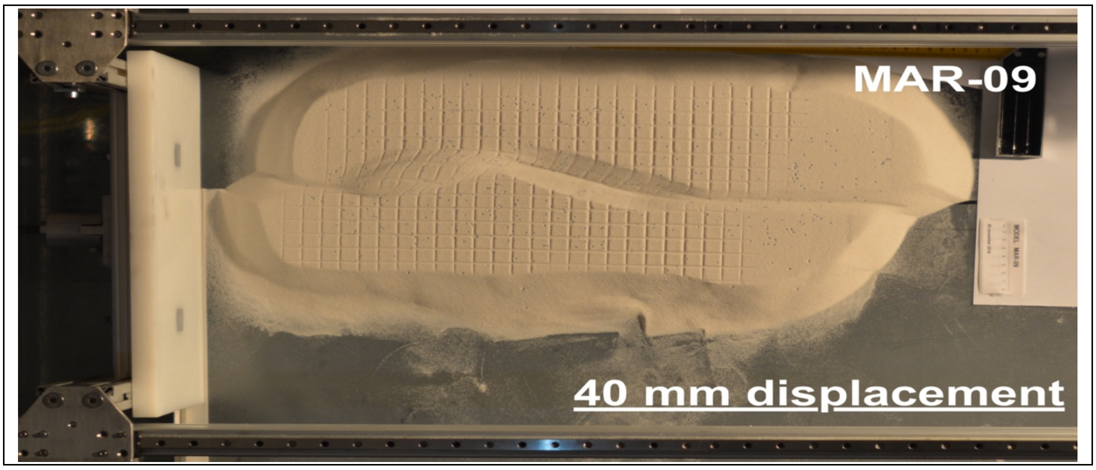

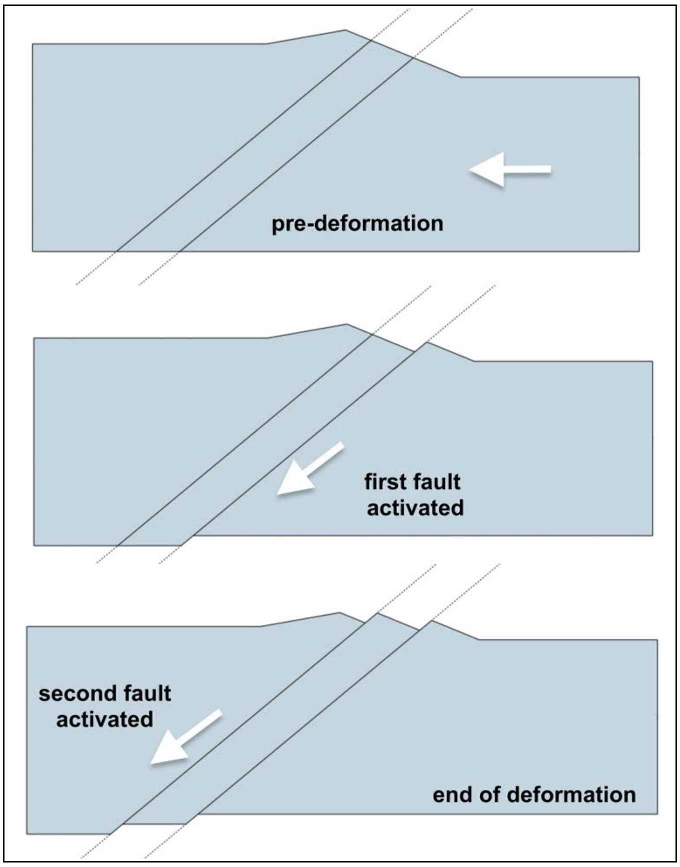

Figure 23 shows the plan view of the experiment setup for MAR-10 and the expected results with the activation of the first fault and activation of the second fault.

MAR 12 and MAR-13

MAR-12 and MAR 13 used a basal plate cut in a similar manner to that of MAR-02. The difference was the relative length of the segments, the silicon putty and the sand pack thickness and the total displacement (Figure 24). These experiments wanted to test the influence of ductile vs. brittle layers as well as the overall geometry of the fault.

MAR 12 used a single plate moved toward the left at 10 mm/hr for a total displacement of 70 mm. MAR 13 used a single plate moved toward the left at 5 mm/hr for a total displacement of 100 mm. Interestingly in these conditions, despite the larger displacement, the models did not develop structures that could be compared to the NAF system.

Figure 25 show model MAR-13 photographed each 10 mm of displacement.

Figure 26, 27 show the cross sections of models MAR-12 and MAR-13 cut at the end of the experiments.

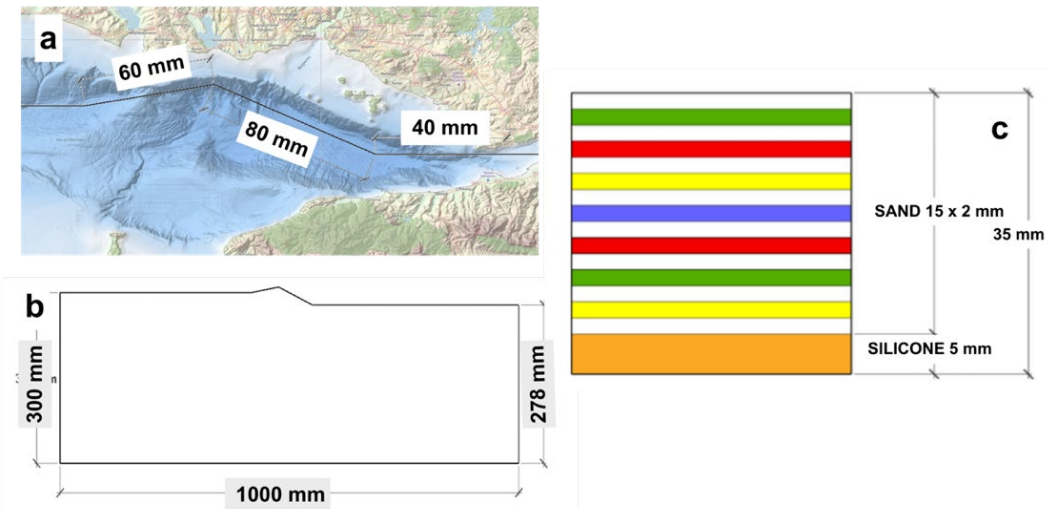

Figure 24 shows the setup configurations of MAR 13. a) the initial fault cut of the MAR-13 on Sea of Marmara-representing the base plate b) the base plate of plexiglass c) shows the stratigraphic view of the MAR-13 setup.

Figure 25: TOP IMAGES OF MAR-13

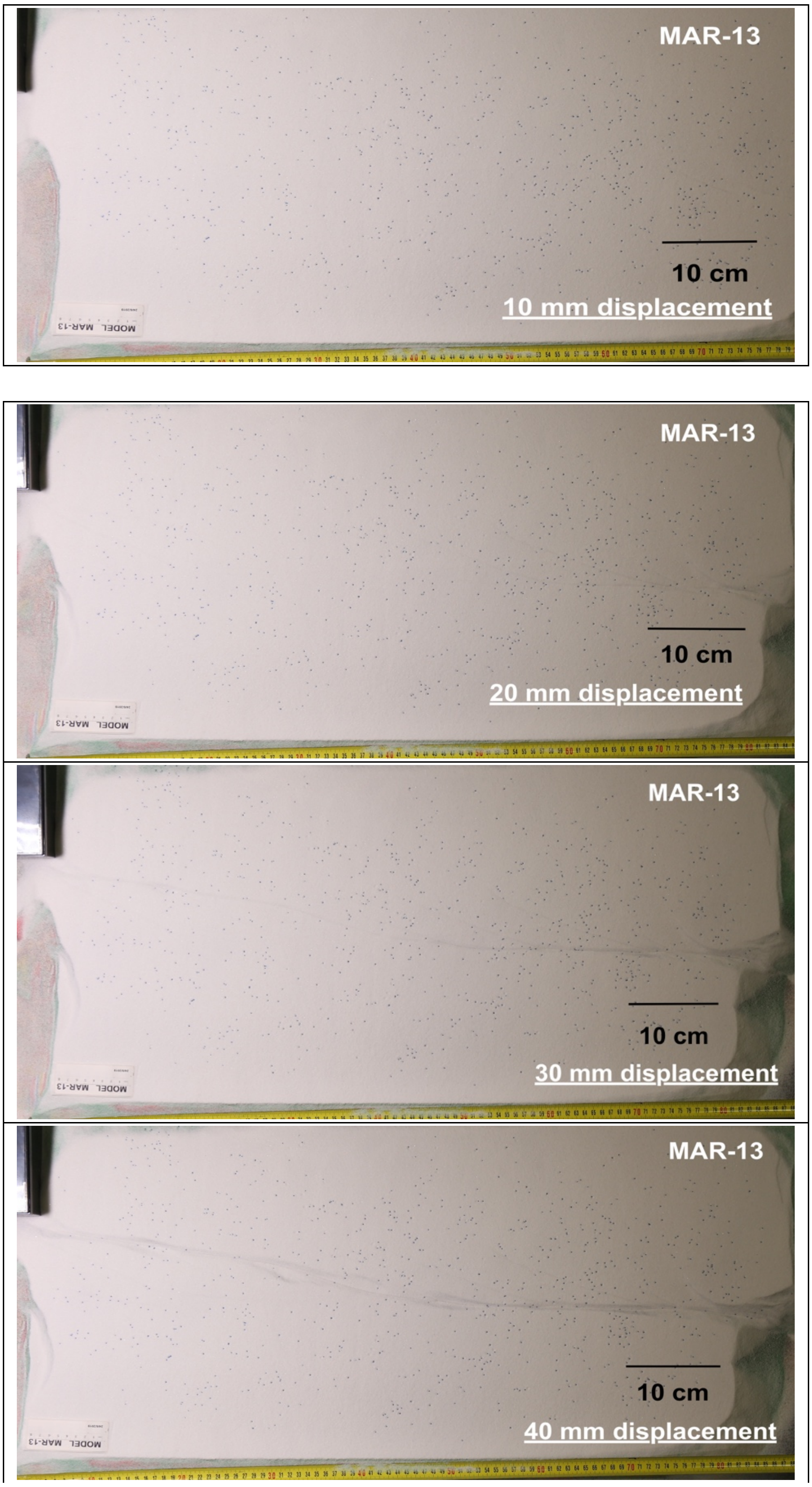

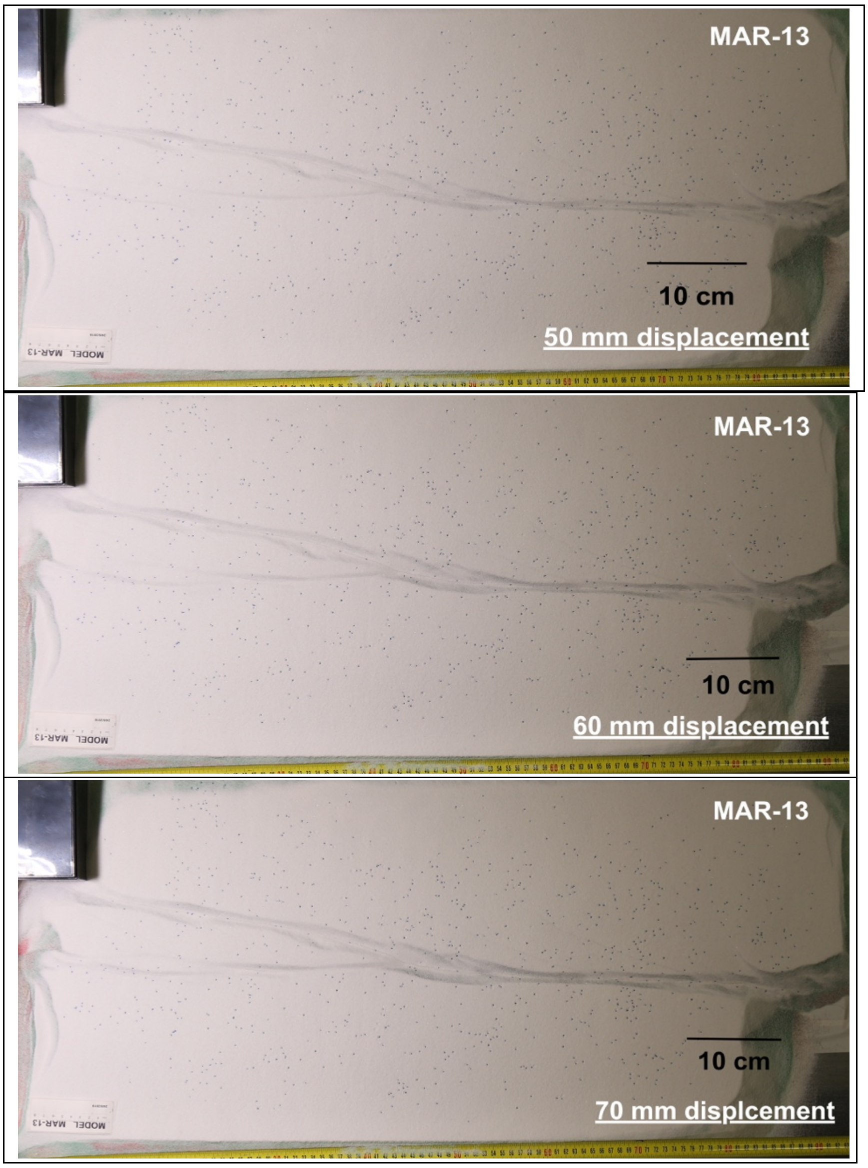

Figure 26: THE CROS SECTIONS OF MAR-12

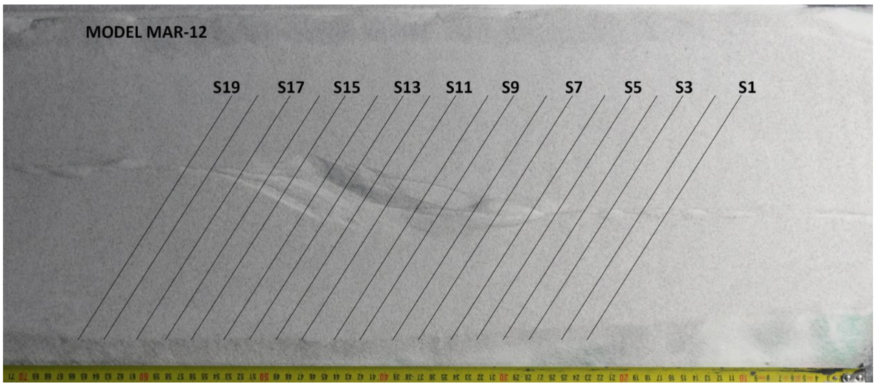

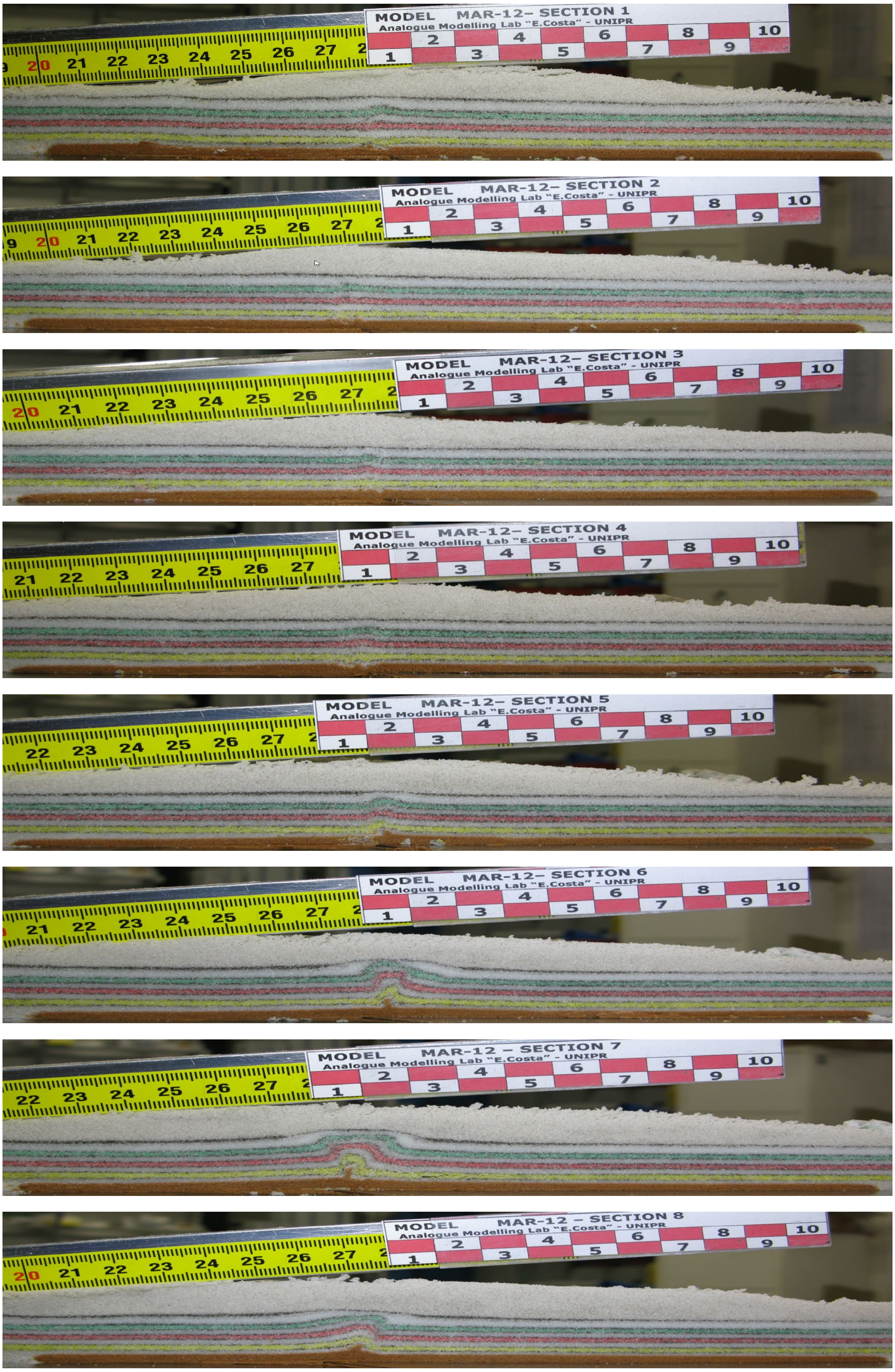
MODEL MAR-12- SECTION 1
Analogue Modelling Lab "E.Costa" - UNIPR
MODEL MAR-12- SECTION 2
Analogue Modelling Lab "E.Costa" - UNIPR
MODEL MAR-12- SECTION 3
Analogue Modelling Lab "E.Costa" - UNIPR
MODEL MAR-12- SECTION 4
Analogue Modelling Lab "E.Costa" - UNIPR
MODEL MAR-12- SECTION 5
Analogue Modelling Lab "E.Costa" - UNIPR
MODEL MAR-12- SECTION 6
Analogue Modelling Lab "E.Costa" - UNIPR
MODEL MAR-12 – SECTION 7
Analogue Modelling Lab "E.Costa" - UNIPR
MODEL MAR-12 – SECTION 8
Analogue Modelling Lab "E.Costa" - UNIPR

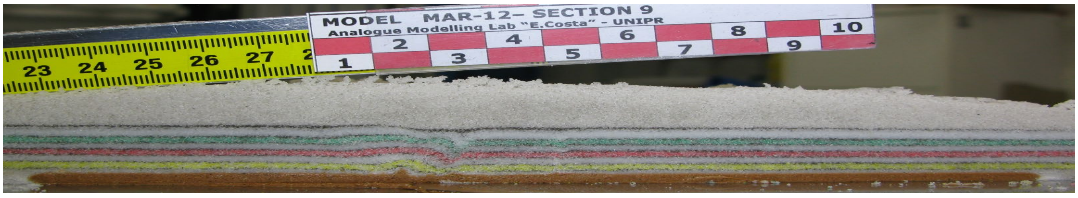
MODEL MAR-12– SECTION 9
Analogue Modelling Lab "E.Costa" - UNIPR

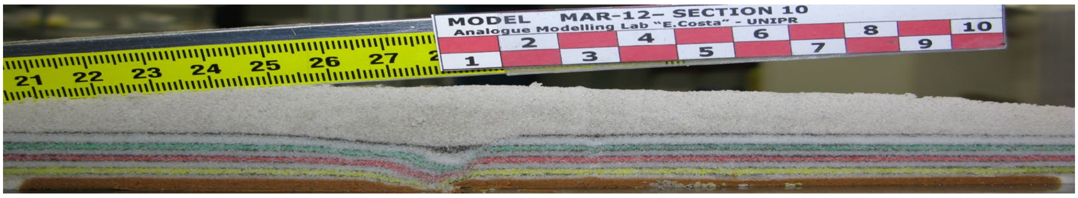
MODEL MAR-12– SECTION 10
Analogue Modelling Lab "E.Costa" - UNIPR


MODEL MAR-12– SECTION 11
Analogue Modelling Lab "E.Costa" - UNIPR


MODEL MAR-12– SECTION 12
Analogue Modelling Lab "E.Costa" - UNIPR

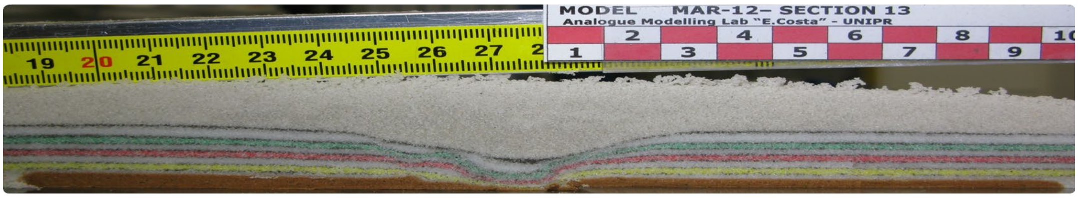
MODEL MAR-12– SECTION 13
Analogue Modelling Lab "E.Costa" - UNIPR

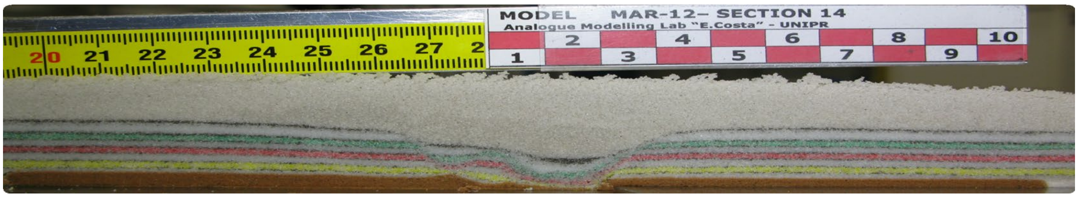
MODEL MAR-12– SECTION 14
Analogue Modelling Lab "E.Costa" - UNIPR

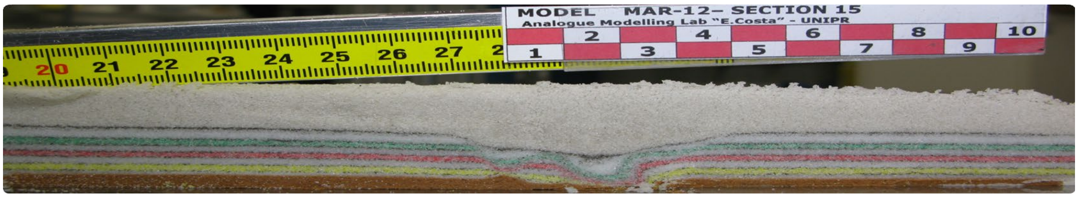
MODEL MAR-12– SECTION 15
Analogue Modelling Lab "E.Costa" - UNIPR

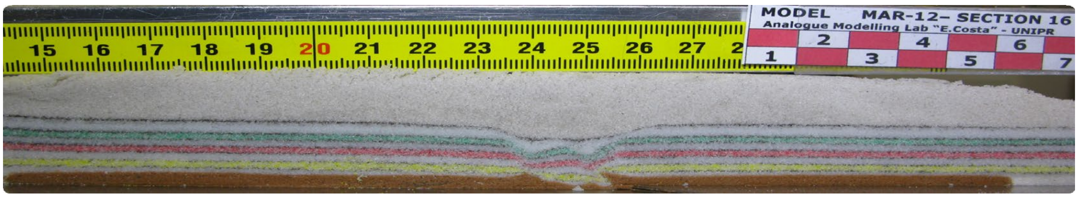
MODEL MAR-12– SECTION 16
Analogue Modelling Lab "E.Costa" - UNIPR

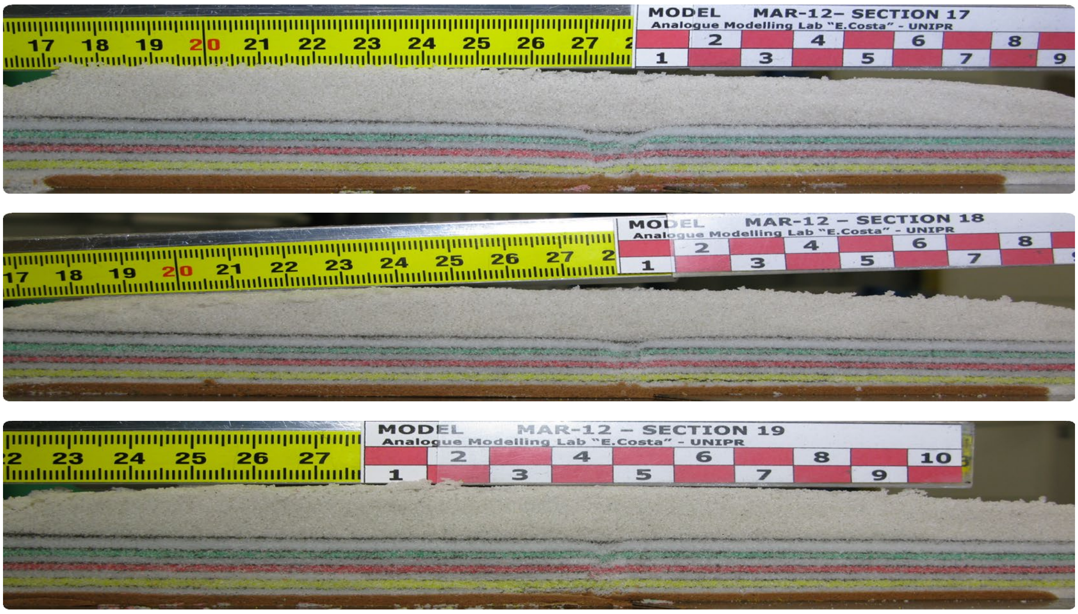

Figure 27: CROSS SECTION OF THE MAR-13

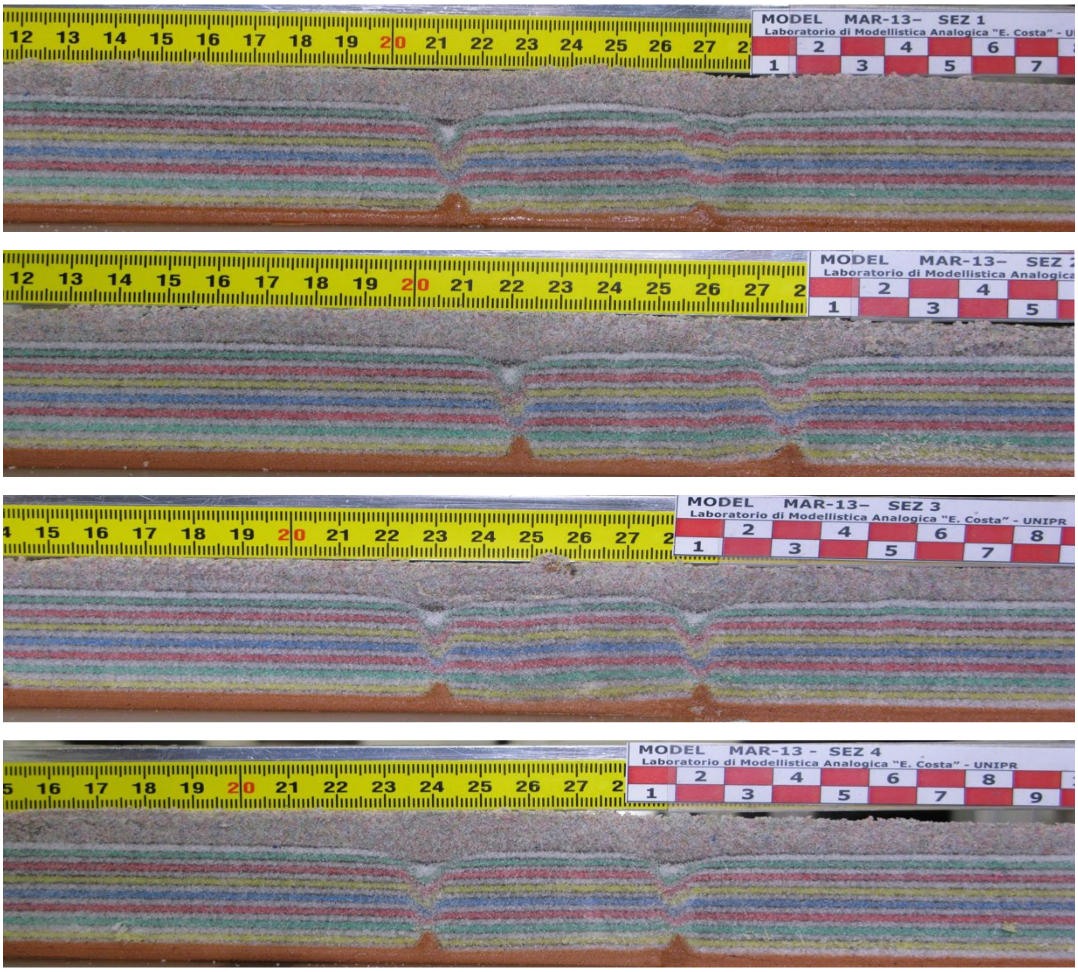


MODEL MAR-13- SEZ 5
Laboratorio di Modellistica Analogica "E. Costa" - UNIPR

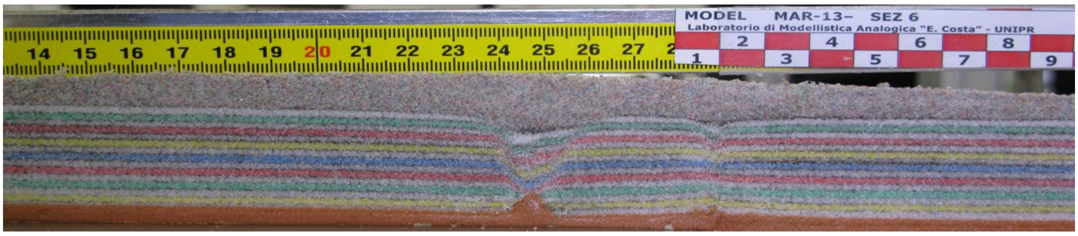
MODEL MAR-13- SEZ 6
Laboratorio di Modellistica Analogica "E. Costa" - UNIPR

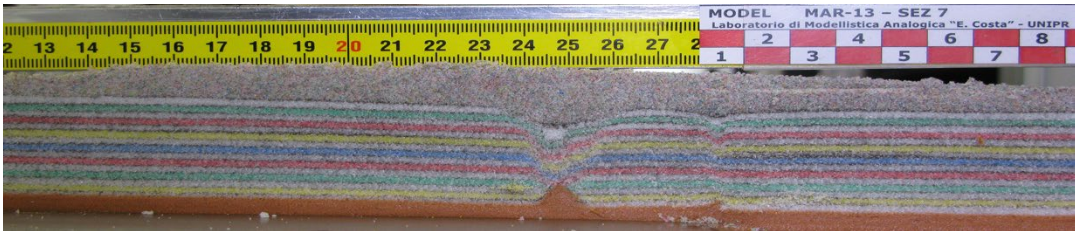
MODEL MAR-13 - SEZ 7
Laboratorio di Modellistica Analogica "E. Costa" - UNIPR

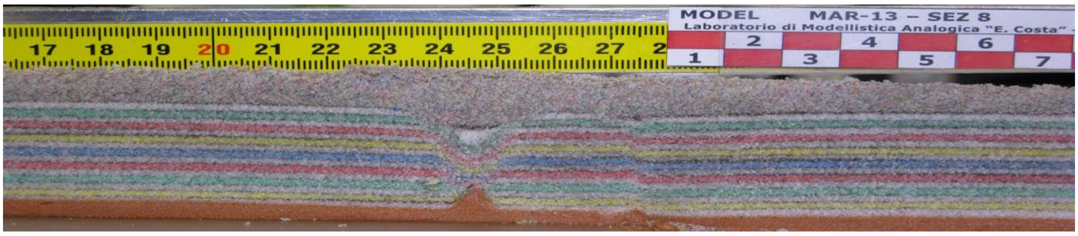
MODEL MAR-13 – SEZ 8
Laboratorio di Modellistica Analogica "E. Costa"

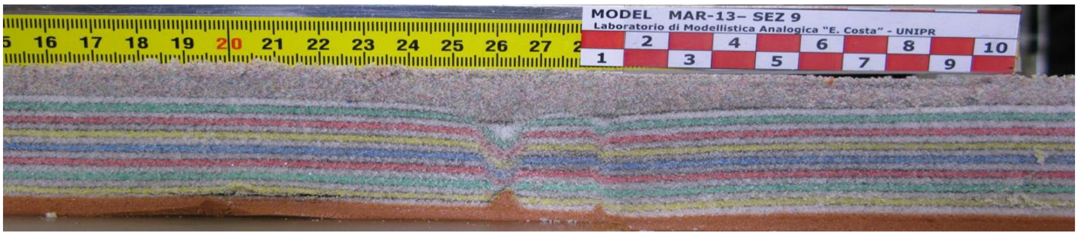
MODEL MAR-13- SEZ 9
Laboratorio di Modellistica Analogica "E. Costa" - UNIPR

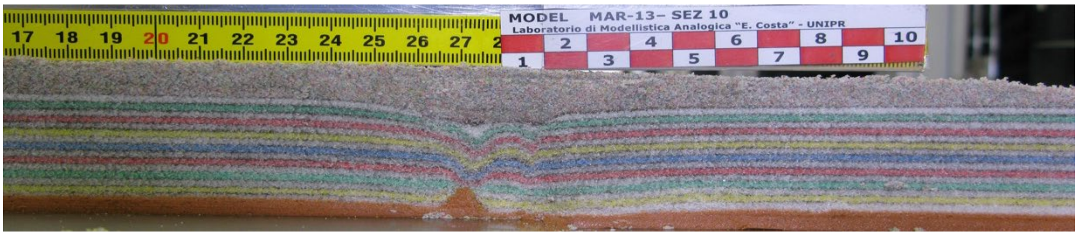
MODEL MAR-13- SEZ 10
Laboratorio di Modellistica Analogica "E. Costa" - UNIPR

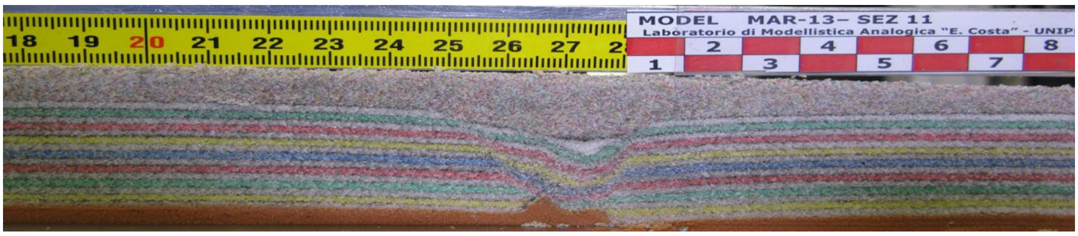
MODEL MAR-13- SEZ 11
Laboratorio di Modellistica Analogica "E. Costa"

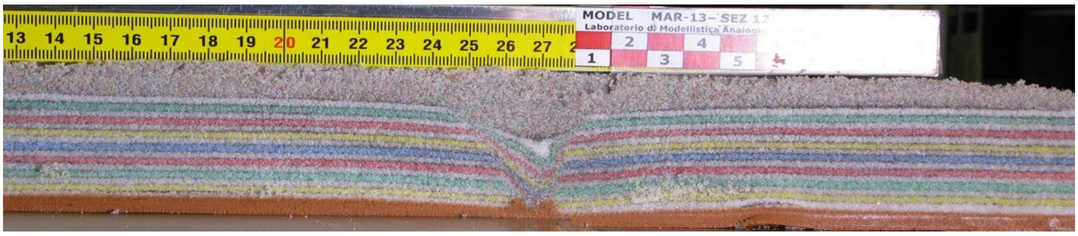

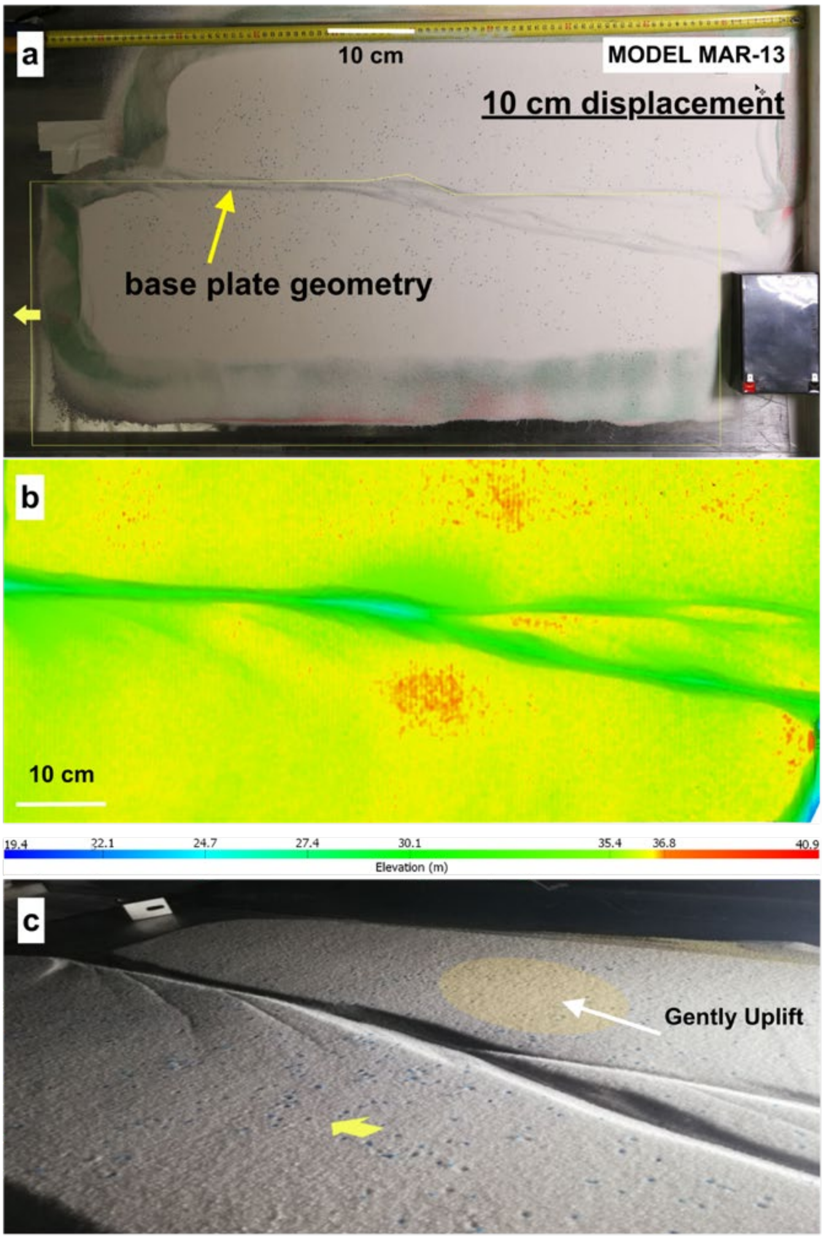

Figure 28 shows the results of MAR-13 at the end of the deformation. a) Top photograph of the model with initial cut of base-plate in yellow. The thick-yellow arrow represents the movement direction of the base-plate. b) the results of the top scan data show the elevation model of MAR-13. c) 3D view of the top photograph indicates the gentle uplift on the model. The yellow arrow represents the movement direction of the base-plate.

Appendix II: GPS Velocities

Table 1 *Observed GPS Velocities in the Eurasian Plate Fixed Frame compiled from Bulut et al. (2019) and Ayhan et al. (2002), *Standard deviation of east–west (σVe) and north–south (σVn) components.*

Site	Lon (°)	Lat (°)	Ve	Vn	σVe *	σVn *	bse	bsn
AKCP	30.761	40.589	-14.3569	-1.3543	0.4376	0.4406	9.739	-0.691
AKGA	30.680	40.538	-18.2563	-0.8075	0.3690	0.3732	5.761	-0.041
ARMT	27.214	40.171	-21.2972	-8.2446	0.4621	0.4765	1.994	-3.061
AVCI	26.910	40.029	-21.0376	-7.7700	0.4619	0.4761	2.019	-2.200
AYKA	29.261	40.200	-22.4655	-1.0979	0.4627	0.4685	0.997	1.479
BAYO	29.143	40.639	-16.9602	1.3262	0.4096	0.4145	7.148	4.053
BIST	26.706	40.739	-5.9191	-2.2361	0.4129	0.4297	-7.756	-1.282
BLKV	29.106	40.270	-22.1578	0.6985	0.4607	0.4668	1.401	3.473
CAKI	27.816	40.400	-21.8386	-2.6235	0.4082	0.4186	1.836	1.794
CALI	28.882	40.481	-19.6786	4.9038	0.6192	0.5912	4.181	7.964
CEIL	29.423	40.821	-8.9881	-0.1851	0.3875	0.3919	-10.650	-2.446
CKOY	29.146	40.460	-21.3802	2.0940	0.4612	0.4667	2.462	4.817
DBEY	28.779	40.167	-21.6922	-2.2134	0.4620	0.4695	1.696	0.978
DIKI	29.514	40.164	-22.7056	0.0002	0.4609	0.4641	0.715	2.254
DOGA	29.908	40.438	-19.0266	-1.6962	0.3639	0.3683	4.817	0.055
GMDR	27.301	40.381	-19.5235	-4.8394	0.4464	0.4597	4.086	0.233
GOKT	30.827	40.735	-9.3525	-0.5956	0.4176	0.4198	-11.188	-4.517
HALP	30.655	40.628	-14.7628	-1.3187	0.3600	0.3627	9.388	-0.521
KABU	30.745	40.652	-12.4534	0.8986	0.4770	0.4821	11.735	1.582
KINI	27.763	40.059	-24.0142	-2.4707	0.4451	0.4579	-0.849	2.014
KKLR	29.889	40.066	-21.9006	-6.2847	0.6612	0.6417	1.390	-4.509
KMLP	29.288	40.485	-17.3571	1.3876	0.5964	0.5642	6.529	3.930
KNRL	26.871	40.601	-14.4883	-3.3071	0.4518	0.4715	9.412	2.312
KOB1	27.960	40.971	1.2729	0.2569	0.3996	0.4072	-0.130	-0.272
MNSA	30.026	40.465	-18.2450	-1.6846	0.4001	0.3987	5.643	-0.084
PAYM	27.586	40.588	-16.5783	-4.9017	0.4682	0.4684	7.359	-0.192
SFRH	29.585	40.667	-14.6272	1.8414	0.4517	0.4552	9.543	4.005
SOKE	30.862	40.555	-18.0523	-0.7878	0.4475	0.4527	5.995	-0.254
TIRE	26.880	40.396	-19.8879	-5.7796	0.4394	0.4587	3.710	-0.172
UADA	30.130	40.745	-9.7323	-0.6294	0.4536	0.4619	-11.536	-3.727
UCTP	30.134	40.690	-14.4872	-0.1694	0.4277	0.4338	9.739	1.294
YAMA	30.804	40.386	-20.8735	-2.0814	0.4062	0.4089	2.922	-1.473
YENF	27.629	40.245	-21.2474	-4.7730	0.4603	0.4733	2.184	-0.118
YKOY	29.141	40.122	-21.2255	-2.2089	0.4093	0.4127	2.115	0.521

YUNT	27.393	40.811	-4.7447	-4.0202	0.4142	0.4237	-6.438	-3.878
ZEYT	28.373	40.398	-20.5356	-0.9657	0.4949	0.4775	3.172	2.743
BOR1	29.635	40.803	-7.2940	1.3306	0.4675	0.4669	-8.989	-1.181
BRUS	29.111	40.165	-23.8762	-1.8212	0.3822	0.3895	-0.473	0.947
GOPE	30.916	40.118	-29.6639	-1.7897	0.7585	0.8102	-6.264	-1.325
GRAZ	30.570	40.028	-27.1864	-1.9864	0.7584	0.8106	-3.930	-1.080
JOZE	30.960	40.600	-13.5098	-1.2700	0.7510	0.7700	10.607	-0.861
KIT3	30.710	40.830	-5.8116	-0.1680	0.8080	0.8141	-7.477	-3.951
KOSG	30.520	40.350	-18.4302	-4.8186	0.8395	0.8455	5.304	-3.848
MATE	30.320	40.610	-19.3897	-0.5775	0.7493	0.7602	4.724	0.648
ONSA	30.300	40.780	-9.7193	2.2572	0.7822	0.7944	-11.464	-1.041
PENC	30.290	41.050	1.3349	-0.7268	1.1139	1.2192	0.064	-4.013
POL2	29.680	40.360	-21.2572	0.6342	0.4104	0.4063	2.461	2.676
POTS	29.620	41.180	-1.7203	-0.2321	0.4721	0.4705	-2.754	-2.726
TRO1	29.070	41.250	-0.6354	3.4868	2.4944	2.9334	-1.543	1.644
VILL	29.060	41.060	-3.5780	1.2099	0.4033	0.4048	-4.819	-0.621
WTZR	29.020	40.170	-24.0255	-2.0502	1.0357	1.0739	-0.620	0.834
ZIMM	29.020	41.100	-3.4506	0.2476	0.4142	0.4195	-4.621	-1.536
ZWEN	28.940	40.300	-15.7101	2.7716	2.4927	2.8245	7.884	5.757
afyn	28.360	41.050	-2.3866	1.2244	0.4719	0.4690	-3.647	0.222
afyo	28.290	41.470	0.0009	0.0002	0.4871	0.4755	-0.522	-0.919
agok	27.910	40.090	-21.7116	-4.5159	0.8388	0.8468	1.510	-0.218
aguz	27.710	40.030	-22.0740	-5.1036	0.7299	0.7737	1.044	-0.551
akhi	26.320	40.260	-22.8840	-8.9708	1.7146	1.8340	0.464	-2.652
aksh	26.170	40.690	-1.8428	-3.9491	1.5001	1.7258	-3.784	-2.361
aksu	29.973	41.033	-0.0167	1.0659	1.3320	1.3738	-1.311	-1.846
alan	27.203	40.054	-19.2353	-6.8659	2.0090	2.0377	3.882	-1.669
alex	28.727	40.987	-4.9521	1.5087	1.0863	1.0116	-6.322	0.071
alse	26.570	40.932	-0.2071	-2.5284	1.3116	1.3903	-1.709	-1.413
aman	27.091	40.203	-18.9574	-6.9683	1.3651	1.4250	4.372	-1.629
ankr	30.404	40.880	-1.4137	1.8396	1.3272	1.4056	-2.985	-1.582
antg	30.462	40.478	-24.7196	-0.6102	1.3607	1.4332	-0.798	0.435
arak	29.243	40.319	-22.8695	-0.4302	1.3427	1.3869	0.768	2.169
astp	27.476	40.266	-19.9353	-4.9233	2.4498	2.5672	3.516	-0.073
ayag	28.536	41.062	-1.7042	-0.4684	2.6520	2.1710	-2.943	-1.679
bah1	29.310	40.927	-1.5832	0.3982	1.4135	1.4652	-3.059	-1.729
bali	27.608	40.159	-19.1221	-4.4736	2.3888	2.5654	4.181	0.208
bcak	29.321	40.866	-2.7689	0.0690	1.3113	1.3379	-4.351	-2.071
bder	29.273	40.834	-4.1950	1.2129	0.9556	0.9639	-5.832	-0.870
bhtl	30.229	41.187	0.0619	2.6495	1.3445	1.4031	-0.968	-0.565

bltp	28.476	41.041	-3.4324	0.9999	2.2474	2.4337	-4.708	-0.140
bodr	29.363	41.017	-0.7262	-0.3548	1.2862	1.3199	-2.043	-2.544
bogo	28.615	40.996	-1.1930	0.5260	1.0587	1.1049	-2.547	-0.779
bozu	28.684	41.030	-2.3108	1.6794	0.9484	1.1994	-3.604	0.294
buck	29.539	40.980	-1.2072	0.1790	1.3218	1.3617	-2.591	-2.219
bucu	30.453	40.351	-25.5220	-0.2770	1.3523	1.4226	-1.789	0.778
burd	29.238	40.917	-1.7089	-0.4431	1.7990	1.8894	-3.202	-2.485
byda	27.696	40.186	-20.6332	-4.2496	1.1935	1.1946	2.716	0.321
bysh	27.563	40.083	-20.1951	-5.3059	1.1826	1.2034	2.992	-0.567
bzkr	26.524	40.126	-18.7381	-7.2968	1.1702	1.2404	4.429	-1.236
cagl	29.118	40.852	-3.0925	1.7337	0.7289	0.7476	-4.698	-0.166
camk	27.997	40.331	-20.0752	-4.2489	1.0742	1.1957	3.510	-0.061
cata	29.093	41.177	-1.3485	0.4597	1.2725	1.2807	-2.384	-1.411
cift	29.977	40.142	-23.4776	-1.5067	1.1053	1.1302	-0.072	0.156
cina	28.782	40.534	-18.5287	-1.8739	1.0686	1.1131	5.405	1.313
cinc	29.145	40.909	-3.3305	0.3193	1.2043	1.6912	-4.837	-1.613
cine	29.372	40.566	-20.4419	-0.0091	1.1063	1.0733	3.568	2.426
cmlk	26.380	40.917	-2.1904	0.5392	1.1211	1.1926	-3.725	1.879
crao	28.832	40.991	-2.1712	1.4089	0.8751	0.8735	-3.533	-0.152
d7du	29.951	40.802	-1.8680	1.4497	0.7187	0.7782	-3.569	-1.436
dlmn	28.683	41.347	-1.1157	0.8306	0.7696	0.7709	-1.853	-0.554
dmir	28.963	41.086	-2.6019	1.4144	1.2130	1.2333	-3.796	-0.302
dion	28.333	40.265	-21.3503	-2.3368	1.0595	1.0646	2.158	1.423
doku	26.999	40.951	-3.4195	-0.8641	1.1658	1.2314	-4.877	-0.256
drag	27.916	41.443	-1.5746	0.7454	1.1153	1.1194	-2.150	0.268
dtas	28.083	41.080	-2.0423	1.2427	1.3938	1.2003	-3.252	0.568
durs	28.974	40.875	-6.2610	1.0382	1.1707	1.1894	-7.827	-0.690
egmi	27.497	40.958	-1.9525	-1.1156	1.1998	1.1568	-3.385	-1.096
ebre	26.486	40.384	-15.4526	-5.8102	1.0642	0.9798	8.094	0.299
elat	26.587	40.468	-13.9584	-5.8722	1.2451	1.4377	9.722	0.108
elmi	26.414	40.111	-24.9730	-1.8730	3.7251	4.3396	-1.837	4.326
1	32.76	39.89	-21.1	0.7	0.1	0.1	0	0
10	31.81	39.56	-20.7	-0.9	0.2	0.3	0	0
36	30.64	38.77	-21.6	-1.6	0.2	0.3	0	0
38	30.64	39.66	-24.4	-1.3	0.3	0.3	0	0
49	29.78	38.73	-22.5	-4.5	0.2	0.2	0	0
56	29.42	39.04	-23	-4.7	0.2	0.2	0	0
59	29.25	39.33	-22.8	-2.5	0.2	0.2	0	0
68	29.04	39.15	-22.9	-3.8	0.2	0.2	0	0
71	28.96	39.42	-24.4	-3.6	0.2	0.2	0	0

73	28.92	39.93	-24.1	-0.2	2	2.3	0	0
74	28.91	38.76	-23.7	-5.9	0.2	0.2	0	0
76	28.86	38.02	-22.5	-9.1	0.2	0.2	0	0
78	28.67	39.05	-22.5	-5.2	0.2	0.2	0	0
79	28.63	39.61	-21.6	-3.3	0.2	0.2	0	0
80	28.48	38.31	-24.4	-9.8	0.8	0.8	0	0
81	28.42	38.73	-23.5	-6.9	0.2	0.2	0	0
82	28.41	39.99	-17.4	-2.9	1	1.2	0	0
86	28.28	38.97	-23.7	-6.4	0.2	0.2	0	0
87	28.24	38.03	-20	-9.8	0.2	0.2	0	0
88	28.14	39.23	-22.7	-5.5	0.2	0.2	0	0
89	28.09	39.92	-20.4	-2.9	0.2	0.2	0	0
90	28	38.25	-21.4	-15.9	1.1	1.1	0	0
93	27.91	39.72	-20.7	-3	0.2	0.2	0	0
94	27.87	39.01	-21.3	-9.6	0.3	0.3	0	0
95	27.86	38.48	-19.5	-15	0.1	0.2	0	0
99	27.78	38.06	-21.2	-12.4	0.2	0.2	0	0
102	27.67	38.68	-20	-11.8	0.1	0.2	0	0
104	27.59	39.29	-22.8	-8.1	0.6	0.7	0	0
106	27.45	38.57	-23.7	-12	0.2	0.2	0	0
107	27.42	39.78	-20.9	-5.4	0.7	0.9	0	0
109	27.32	39.02	-21.1	-12	0.3	0.3	0	0
110	27.31	38.71	-18.9	-13.7	0.1	0.1	0	0
112	27.27	39.58	-19.7	-5.2	0.7	0.8	0	0
113	27.22	39.9	-20	-7.5	0.4	0.4	0	0
114	27.16	38.6	-23.1	-12.5	0.2	0.2	0	0
115	27.13	38.49	-23	-14.4	0.2	0.2	0	0
116	27.11	39.24	-18.1	-10.2	1.8	2	0	0
117	27.08	38.02	-19.7	-17.8	0.4	0.4	0	0
119	26.88	39.01	-21.7	-9.3	0.6	0.7	0	0
122	26.79	38.74	-21.9	-16.6	0.2	0.2	0	0
123	26.73	39.65	-21.4	-5.5	1.8	2	0	0
124	26.72	38.43	-20.7	-18	0.2	0.2	0	0
125	26.71	39.33	-22.1	-9.1	0.7	0.9	0	0
127	26.7	39.31	-18.8	-10.1	0.3	0.3	0	0
129	26.53	39.58	-19.9	-6.6	0.6	0.7	0	0
130	26.38	38.31	-20.3	-20.4	0.2	0.2	0	0
132	26.32	39.78	-18.5	-9.5	1.8	2.1	0	0
133	26.19	39.61	-21	-8.9	0.8	0.7	0	0
134	26.17	39.97	-18.1	-8.4	0.3	0.3	0	0

Appendix III: Pre-seismic Deformation

The 17 August 1999 M7.4 İzmit earthquake (40.76°N, 29.97°E) was a devastating event that occurred on the North Anatolian Fault Zone (NAFZ) and caused many casualties. It was followed by the 12 November 1999 M7.2 Düzce earthquake after 87 days. The İzmit earthquake ruptured over 150 km long section of the NAFZ, from the Sea of Marmara in the west to Düzce in the east.

We evaluated GPS campaigns made before and after the Izmit earthquake to estimate the displacements that accompanied (Fig. 1A) (performed from 1992 to just before the 17 August 1999) and followed (Fig. 1B) the earthquake. We use the data set from Ayhan et al. (2002). We analysed the GPS data using the same method, which was described in detail in this thesis in Chapter 6 - Section 6.2. The pre-seismic GPS data set was given in Appendix II. The process of post-seismic data was explained in Chapter 6.

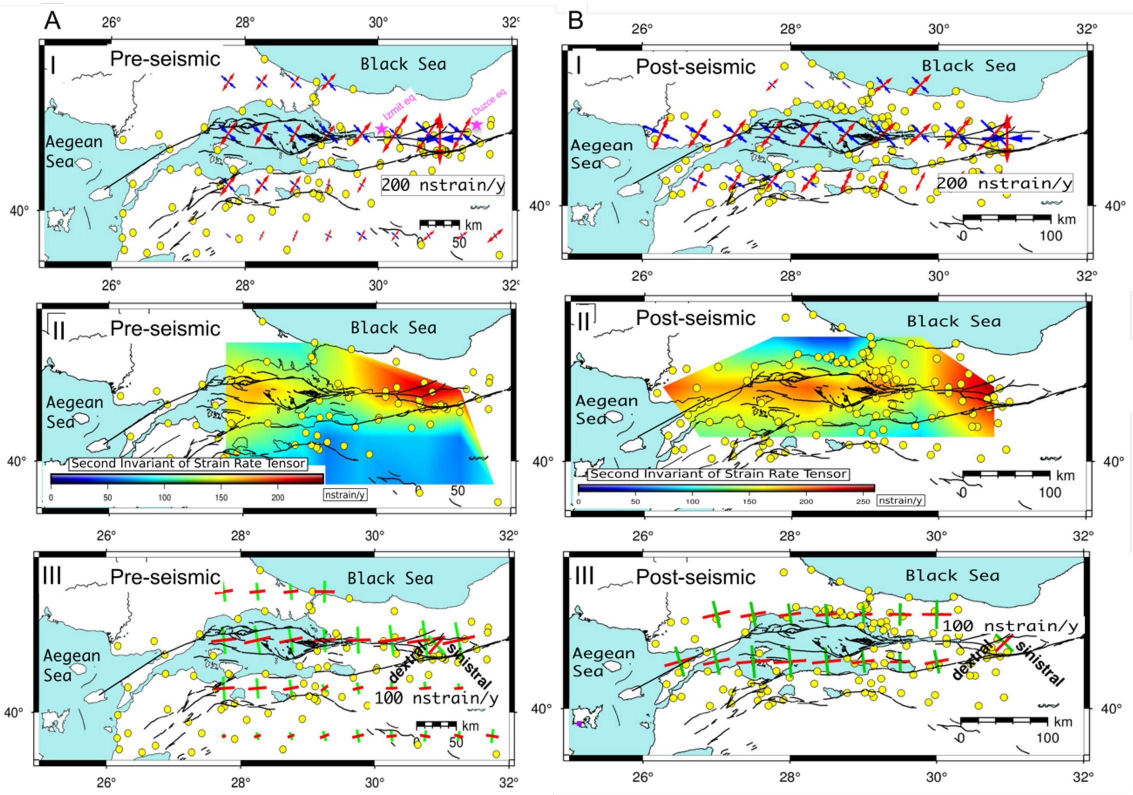

Figure 1 Comparison between pre-seismic deformation and post-seismic deformation (AI-BI) Principal axes of strain rates. Red arrows indicate extension, and blue arrows indicate compression. (AII-BII) Second invariant of

strain-rates in units ofnanostrain/yr. (AIII-BIII) Conjugate line segments show the magnitude and direction of the maximum dextral(red) and sinistral(green) local shear strain rate.

Results & Discussion

Figure 1A showed the GPS-inferred strain-rate pattern around the northern branch of the NAF within the Marmara area. The strain rate along the eastern Marmara is dominated mainly by NE-trending principal tensile strain, accompanied by NW-trending principal compressional strain, and the amplitude of the latter is generally much smaller than that of the former (Fig. 1A). The overall deformation is consistent with the pervasive dextral strike-slip faulting in this region (Fig. 1C) (Korkusuz et al.,2015; Wollin et al., 2019). The comparison of the pre-seismic and post-seismic deformation in the area seems to indicate that there are no noticeable changes in deformation between these two periods.

The analysis shows that the 1999 Izmit Earthquake didn't release much elastic-strain. The horizontal principal strain orientation and their size is not changing in the pre- and post-seismic dataset, so western extension of the 1999 İzmit rupture area presently has low strain accumulation.

Indeed, it is expected that Izmit EQ built up high strain accumulation to the west of the Izmit fault (Armijo et al., 2005; Gasperini et al., 2011, Ergintav et al., 2014). Instead, lower than expected strain here might explain that it reduces the amount of strain accumulation and effects the earthquake cycle which will either cause a delay of the arrival of future events to the west of the Izmit rupture area (Ergintav et al., 2007). Another interpretation is that high number of faults caused a strain partitioning and the Izmit earthquake resulted from failure of only some fault among those that strike within the Cinarcik Basin on its western (Bohnhoff et al., 2006).

On the other side, the pre-post seismic comparison of the second invariant of strain rate showed that after the 1999 Izmit EQ strain migrated to the east from the center of the MMF. The central segment of the MMF that was thought to be a creeping segment does not show evidence of strain accumulation (Ergintav et al., 2014). While our results are not sufficiently accurate for detailed interpretation, the observed strain accumulation might imply the potential for a significant earthquake in the eastern part of the Sea of Marmara.